Correlation of superconducting properties and microstructure in MgB$_2$ using SEM, EPMA and TEM

Dissertation
zur Erlangung des Grades eines Doktors
der Naturwissenschaften
der Fakultät für Mathematik und Physik
der Eberhard-Karls-Universität zu Tübingen

Vorgelegt von

Balaji I. Birajdar

aus Kamjalga, Nanded, India
2008

<u>Summary</u>

MgB_2 is an intermetallic compound, has hexagonal crystal structure and is known for more than five decades. The outstanding superconducting properties of MgB_2 were however discovered only in 2001 by Nagamatsu et al. On the basis of experiments (isotope effect, de Haas-van Alphen effect, specific heat, photo-emission spectroscopy and tunnelling spectroscopy) and band structure calculations, MgB_2 is confirmed to be a phonon mediated BCS superconductor with a s-wave symmetry and a clear example of two band superconductivity. MgB_2 has two dimensional σ-bands and three dimensional π-bands giving rise to superconducting energy gaps of 5-7 meV and 2-4 meV respectively. Superconducting transition temperature (T_c) of MgB_2 is twice that of Nb_3Sn and four times that of Nb-Ti, the two most common commercial superconductors. The upper critical field (B_{c2}) of MgB_2 is anisotropic but variable and can be enhanced by introducing structural disorder by e.g. C-doping and neutron irradiation. Recently $B_{c2}(0)$ of 70 T in thin films and 37 T in bulk samples have been reported. The superconducting coherence length of MgB_2 lies in the range of about 2-10 nm.

Superconducting wires and tapes are hysteretic type II superconductors that are exposed to high magnetic fields and are in the critical (Shubnikov) state. Therefore the critical current density ($J_c (B,T)$) is an exclusively important figure of merit for these superconductors. In MgB_2 J_c is limited by B_{c2}, anisotropy in B_{c2} and the structural granularity introduced by the microstructure. Most of the applied research on MgB_2 is aimed at enhancing the J_c which reached about 1×10^5 Acm^{-2} (at 4.2 K and 12 T).

The MgB_2 samples investigated in this thesis were produced by partner institutes within the HIPERMAG project (EU-FP6) and were thoroughly characterised for their superconducting properties namely T_c, B_{c2} and $J_c(B,T)$ by the partner institutes. Depending on the synthesis technology the J_c's of the MgB_2 wires and tapes were found to vary by a factor of about 100. The reasons for these order of magnitude differences in J_c are crucial for the understanding of the transport properties of the MgB_2 conductors.

Like in $(Bi,Pb)_2Sr_2Ca_2Cu_3O_{10}$ (Bi-2223) superconducting tapes, chemical analysis from μm to nm length scales is essential to understand and improve the superconducting properties of MgB_2. Phase analysis is usually done by x-ray diffraction, which however fails for superconducting wires and tapes. In Bi-2223 superconducting tapes, strong texture of the matrix prevents phase fraction determination, whereas in MgB_2 conductors, x-ray phase analysis fails to detect B-rich secondary phases because of the low x-ray atomic scattering factor of B. Therefore, structural granularity which limits the J_c of MgB_2 wires and tapes can only be explored by quantitative microstructure analysis using advanced electron microscopy and spectroscopy methods as done in this thesis. Conventional scanning (SEM) and transmission electron microscopy (TEM), energy filtered TEM, electron beam spectroscopy and chemical mapping techniques in SEM and TEM were extensively used.

This thesis can be subdivided as follows: (I) Development of the methodology for the advanced electron microscopy and spectroscopy of MgB_2 and thereby assess the performance of two energy-filtered TEMs (Zeiss 912Ω and Zeiss Libra 200FE). (II) Quantitative microstructure analysis of selected MgB_2 samples using advanced electron microscopy and spectroscopy methods. (III) Establishing a microstructure-critical current density model for MgB_2 wires and tapes.

(I) Quantitative electron microscopy and spectroscopy of MgB_2 wires and tapes is challenging because of the following reasons: i) carbon and oxygen contamination artefacts during sample preparation and under the electron beam in the microscope, ii) low fluorescence yield of $B-K_{\alpha}$ x-rays requires highly sensitive detectors for low-energy x-rays, iii) the $B-K_{\alpha}$ and $C-K_{\alpha}$ x-ray peak overlap in energy dispersive x-ray spectroscopy (EDX) has to be corrected during the quantitative evaluation of the spectra, iv) preferential absorption of $B-K_{\alpha}$ x-rays in the sample has to be corrected for the quantitative analysis of B, v) formation of MgB_2 colonies and secondary phases (MgB_{4+x}, MgB_{7+x}, $MgSi_xO_y$, and Mg_2Si) yields structural granularity from μm to nm length scale, which needs to be quantitatively measured.

The methodology of the quantitative electron microscopy and spectroscopy analysis of MgB_2 has been established and involved a combined SEM and TEM analysis with contamination free sample preparation, chemical mapping and advanced chemical quantification of B containing compounds (MgB_2, MgB_4, MgB_7, etc.). Chemical mapping techniques enabled to study the thermodynamics of the MgB_2 phase formation and to investigate the chemical inhomogeneities upto the 10 nm length-scale.

C contamination during SEM sample preparation was significantly minimized by avoiding the use of organic resin as embedding material. Acquisition conditions for the EDX elemental mapping using Jeol JSM 6500F SEM equipped with a field emission gun were established and the reliability and accuracy of quantitative B analysis by SEM-EDX was checked using MgB_2 standards previously characterised by electron probe microanalysis (EPMA). The minimum detectable mole fraction of carbon in MgB_2 for the SEM-EDX analysis was determined to be 1.7 at.%. The volume fraction of the B-rich and Mg_2Si secondary phases was quantitatively determined using the Mg-B and Mg-Si concentration-histograms (CHI).

Diffraction contrast imaging in TEM was used for the analysis of the MgB_2 grain size and crystal defects like grain boundaries, dislocations and precipitates. Chemical mapping in Zeiss 912Ω and Zeiss Libra 200FE TEMs using x-ray microanalysis (STEM-EDX) and electron spectroscopic imaging (ESI) was applied for the analysis on the sub-µm scale.

During quantitative EDX analysis, significant preferential absorption of low energy x-rays from B occured both in SEM and TEM samples. EDX detector efficiency was carefully monitored over time and no degradation by ice build-up was detected. Parameterless x-ray absorption correction was applied for the quantitative TEM-EDX analysis of MgB_2 tapes. The B-K_α Cliff-Lorimer factor was determined as 8.71 with respect to Mg-K_α. TEM-EDX spectroscopy was found to be essential for a reliable interpretation of ESI elemental mapping.

(II) Three kinds of representative and selected samples, which were well characterised by their normal and superconducting properties by partner institutes were investigated using advanced electron microscopy and spectroscopy methods and the results were correlated with their superconducting properties. These samples are (a) MgB_2 bulk samples alloyed with Al (b) long length (1 km) MgB_2 tapes (c) MgB_2 ceramics and tapes synthesised by mechanical alloying.

(IIa) Al-alloyed MgB_2 ceramics were prepared with a nominal composition of $Mg_{1-x}Al_xB_2$, with x = 0, 0.1, 0.2, 0.3 and actual composition determined using EPMA. The B-rich secondary phases constitute less than 4% of the total sample volume. The actual Al mole fraction in the MgB_2 matrix was found to be less than the nominal Al mole fraction and the difference increased with increasing Al mole fraction. Al is incorporated into MgB_2 grains of ~1 µm size by substitution of Mg atoms causing T_c and c lattice parameter to decrease at a rate of 1.56 K and 1.15 pm per at.% of Al alloying. In comparison the a lattice parameter decreased at a lower rate of 0.17 pm/at.%. This data may be used to determine the actual Al mole fraction in Al-alloyed MgB_2 samples by diffraction methods. Precipitation of Al was not detected upto highest Al mole fractions but Al was found to be distributed inhomogenously which explained the broadening of the superconducting transition width (ΔT_c) with increasing Al mole fraction.

(IIb) Multifilamentary Ni sheathed Cu-stabilised MgB_2 tapes with a critical current density of 2.0×10^5 Acm^{-2} (at 20 K and 1 T) were prepared by a powder in tube technique, using pre-reacted MgB_2 powders. Colony formation, i.e. an arrangement of several well connected, oxygen-poor, ~ 0.5 µm large MgB_2 grains was found in the MgB_2 filaments and the colony size was between 1 to 6 µm. The B to Mg mole fraction ratio in the MgB_2 colonies was close to 2 and O mole fraction was less than 1 at.%. MgO precipitates of the size of 15-70 nm were found in the MgB_2 grains. Long straight dislocations with a density of 1×10^{10} cm^{-2} were observed. Non-superconducting oxide layers were found on the surface of the MgB_2 colonies, yielding structural granularity and reduction in J_c. Intermetallic reaction layers were formed at the MgB_2-Ni interface with a composition of $MgB_2Ni_{2.9}$ and $MgB_{3.3}Ni_{10}$, and a width of 5 µm each.

(IIc) The quality of the B precursor powders significantly affect the superconducting properties of MgB_2 conductors and its influence on the microstructure was investigated in detail. The

nominal purity specified by the B-powder suppliers considers only metallic impurities which was found to be inadequate. Oxygen impurities and the grain size of the B precursor powder were found to affect T_c and the microstructure of the MgB_2 tapes. MgB_2 precursor powder was prepared by mechanical alloying which resulted in a small 20-60 nm MgB_2 grain size in bulk samples and tapes. Boron precursor powder with small grain size and small fraction of metallic impurities yielded bulk samples with highest MgB_2 phase fraction and a critical current density of 4.7 x 10^4 A/cm^2 (at 20K, 1T). Such powder also yielded compact tapes with a J_c of 5.0 x10^4 A/cm^2 (at 20K, 3T) and required lower annealing temperatures for the MgB_2 phase formation. The high J_c of these tapes, without additives like SiC, is attributed to the enhanced grain boundary pinning because of the small size of MgB_2 grains and shows the importance of mechanical alloying for enhancing the critical current density of MgB_2 tapes.

(III) In order to establish a microstructure-J_c correlation model, about 10 MgB_2 wires and tapes were prepared by using either pre-reacted MgB_2 (ex-situ) or a mixture of Mg + 2B (in-situ) as the precursor powders and analysed with respect to their microstructure. In some wires the precursor powders were mixed with SiC. Ex-situ wires showed dense oxygen-poor MgB_2 colonies embedded in a porous matrix. The MgB_2 grains in the porous matrix are surrounded by $MgSi_xO_y$ layers yielding structural granularity. In-situ wires are generally more dense, but show inhibited MgB_2 phase formation with significantly higher fraction of B-rich secondary phases in comparison to the ex-situ wires. The MgB_2 grain size was 20-100 nm in in-situ and 200-1000 nm in ex-situ samples. The smaller MgB_2 grain size resulted in significantly enhanced pinning properties for in-situ samples.

The large, order of magnitude, differences in the J_c's of MgB_2 wires and tapes could be explained using microstructure- critical current density model which contains the following microstructure parameters: 1) MgB_2 grain size, 2) oxygen mole fraction, 3) volume fraction of B-rich secondary phases and 4) colony size. The J_c curves of superconducting MgB_2 wires and tapes were parameterised by straight lines in the logarithmic $J_c(B)$ diagrams. The parameters of these line were correlated with the four quantitatively determined parameters of the microstructure-J_c model. Results of the microstructure-J_c model are discussed with respect to the percolation model presented by Eisterer and Weber.

The microstructure analysis of MgB_2 using a 200 kV Zeiss-Libra FEG TEM (SESAM II microscope), carried out in this thesis also aided in assessing the analytical performance of this microscope. The Sub-Electron Sub-Angstrom Microscope (SESAM)- project is a joint effort of the University of Tuebingen and Max Planck Institute for metal research, Stuttgart.

Based on this thesis, the following investigations are highly recommended for the future: (i) MgB_2 grain boundaries are observed to be efficient pinning centres. Structural analysis of the MgB_2 grain boundaries would be helpful in understanding the mechanism of grain boundary pinning in MgB_2. (ii) The microstructure analysis of MgB_2 wires and tapes synthesised at different annealing temperature and annealing times has began with this thesis but is incomplete at the present stage. Advanced electron microscopy and spectroscopy of these samples would yield understanding of the thermodynamics of Mg-B-O and Mg-B-Si-C-O system about which little is known in the literature, but is necessary to control the phase and microstructure formation in these systems.(iii) The successfully established quantitative B analysis using TEM-EDX should be applied to determine the exact chemical composition of B-rich secondary phases smaller than 1 μm. (iv) The technique of quantitative phase analysis established here for SEM-EDX should be applied also to ESI and EDX elemental maps acquired in the STEM.

Zussamenfassung

MgB_2 ist eine intermetallische Verbindung, hat eine hexagonale Kristallstruktur und ist seit über fünfzig Jahren bekannt. Die außergewöhnlichen supraleitenden Eigenschaften von MgB_2 wurden aber erst 2001 durch Nagamatsu und Mitarbeiter entdeckt. Auf Grundlage experimenteller Ergebnisse (Isotopeneffekt, de Haas-van Alphen Effekt, spezifische Wärme, Photoemissionsspeltroskopie und Tunnellspektroscopie) und Bandstrukturrechnungen wurde gezeigt, dass MgB_2 ein BCS-artiger Supraleiter mit s-Wellensymmetrie ist und Phononen zur attraktiven Wechselwirkung führen. Außerdem ist MgB_2 ein Zweiband-Supraleiter, bei dem zwei unterschiedliche Bänder an der Fermikante auftreten, zweidimensionale σ-Bänder und dreidimensionale π-Bänder. Die den Bändern zugeordneten Energielücken betragen 5-7 meV und 2-4 meV. Die supraleitende Übergangstemperatur T_c von MgB_2 ist mehr als doppelt so hoch wie die von Nb_3Sn und mehr als viermal so hoch wie die von Nb-Ti, die beiden meist verwendeten Materialien für supraleitende Anwendungen. Das obere kritische Feld B_{c2} von MgB_2 ist anisotrop und kann durch strukturelle Unordnung wie C-Dotierung oder Neutronenbestrahlung erhöht werden. Es wurden extrapolierte Werte des oberen kritischen Feldes von bis zu 70 T bei Dünnfilmen und bis zu 37 T in Volumenmaterialien gemessen. Die supraleitende Kohärenzlänge von MgB_2 liegt zwischen 2 und 10 nm.

Supraleitende Drähte und Bänder sind harte Typ-II Supraleiter, die hohen Magnetfeldern ausgesetzt werden und sich dann in der Shubnikov Phase befinden. Deshalb ist die kritische Stromdichte j_c (B,T) für solche Supraleiter eine wesentliche Gütezahl. In MgB_2 wird j_c durch das obere kritische Feld B_{c2}, die Anisotropie von B_{c2} und durch die Granularität der Mikrostruktur bestimmt. Der Großteil der angewandten Forschung an MgB_2 zielt auf eine Erhöhung der kritischen Stromdichte ab, die zur Zeit maximale Werte von 10^5 Acm^{-2} bei 4,2 K und 12 T erreicht.

Die MgB_2 Proben, die in dieser Arbeit untersucht wurden, wurden durch Partner innerhalb des HIPERMAG Projektes (EU-FP6) hergestellt und wurden sorgfältig bezüglich der supraleitenden Eigenschaften, d.h. T_c, B_{c2} and $J_c(B,T)$, charakterisiert. Abhängig vom Herstellungsverfahren wurden bei den kritischen Stromdichten zwischen den Leitern Unterschiede bis zu einem Faktor 100 gefunden. Die strukturellen und chemischen Ursachen für diese deutlich verschiedenen Werte für j_c sind wesentlich, um die Transporteigenschaften von MgB_2 Leitern zu verstehen.

Wie auch in $(Bi,Pb)_2Sr_2Ca_2Cu_3O_{10}$ (Bi-2223) Supraleiter-Bändern ist es auch in MgB_2 wichtig, die Mikrostruktur auf Längenskalen von µm bis nm zu messen, um die supraleitenden Eigenschaften zu verbessern. Phasenanalysen werden gewöhnlich mittels Röntgenbeugung durchgeführt, jedoch versagt dieses Verfahren für diese Verbindungen. In Bi-2223 verursacht dies die starke Textur der Matrix, hingegen ist in MgB_2 der geringe atomare Streufaktor von B ausschlaggebend und B-reiche Phasen können nicht empfindlich genug nachgewiesen werden. Auch deshalb kann eine Analyse der Granularität der Mikrostruktur, die zu einer Beschränkung von J_c in MgB_2 führt, nur mit den hier beschriebenen quantitativen elektronenmikroskopischen und spektroskopischen Methoden durchgeführt werden. Konventionelle Raster- (REM) und Transmissionselektronenmikroskopie (TEM), energiegefilterte TEM, Elektronenstrahlspektroskopie und abbildende chemische Methoden wurden im REM und TEM angewandt..

Diese Arbeit ist wie folgt gegliedert: (i) Methodische Arbeiten für die quantitativen elektronenmikroskopischen und -spektroskopischen Verfahren für MgB_2, bei denen auch zwei energiegefilterte TEMs (Zeiss 912 Omega und Zeiss Libra 200 FE) bezüglich ihrer Leistungsfähigkeit beurteilt wurden, (ii) Mikrostrukturbestimmungen ausgewählter MgB_2 Leiter, bei denen die quantitativen Methoden angewandt wurden, (iii) Erstellen eines Mikrostruktur-kritische Stromdichte Modells für MgB_2 Drähte und Bänder.

(I) Quantitative Elektronenmikroskopie und -spektroskopie von MgB_2 Drähten und Bändern ist wegen der folgenden Gründe anspruchsvoll: (i) Kohlenstoffkontaminations-Artefakte müssen vermieden werden, die bei der Probenpräparation und unter dem Elektronenstrahl auftreten, (ii) die geringe Fluoreszenzausbeute von B erfordert hochempfindliche Detektoren für weiche, niederenergetische Röntgenstrahlung, (iii) mit der $B-K_\alpha$ und $C-K_\alpha$ Peaküberlagerung in EDX-Spektren muss bei der quantitativen EDX-Analyse geeignet verfahren werden, (iv) die bevorzugte Absorption von Röntgenstrahlung muss bei quantitativer Messung geeignet berücksichtigt werden, (v) strukturelle Granularität muss quantitativ gemessen werden.

Quantitative elektronenmikroskopische und spektroskopische Methoden wurden etabliert und umfassen eine kombinierte REM und TEM Analyse mit kontaminationsfreier Probenpräparation, chemische Abbildung und fortschrittlicher Verfahren zur quantitativen Bestimmung der chemischen Zusammensetzung von B-haltigen Verbindungen. Elementverteilungsbilder mittels Röntgenmikroanalyse und energiegefilterter Abbildung erlaubt die Thermodynamik der MgB_2 Phasenbildung zu studieren und die strukturellen und chemischen Inhomogenitäten bis zu der 10 nm Längenskala zu untersuchen.

Kohlenstoff-Kontamination konnte bei der Probenpräparation verhindert werden, indem keine organischen Einbettmittel zur Anwendung kamen. Die Akquisitionsbedingungen wurden für EDX Elementverteilungsbilder an einem Jeol JSM 6500F REM ausgerüstet mit einer Felde-missionsquelle festgelegt und die Genauigkeit der quantitativen B-Analyse durch REM-EDX wurde überprüft, indem Standards vermessen wurden, deren chemische Zusammensetzung zuvor mittels Elektronenstrahl-Mikrosonde bestimmt wurde. Die Nachweisgrenzen von Kohlenstoff in MgB_2 wurden für REM-EDX als 1,7 at% festgestellt. Der Volumenanteil B-reicher Sekun-därphasen und Mg_2Si wurden quantitativ durch Mg-B und Mg-Si Konzentrationshistogramme (CHI) bestimmt.

Beugungskontrastabbildung im TEM wurde für die Analyse der MgB_2 Korngröße und Kristallbaufehler wie Korngrenzen, Versetzungen und Ausscheidungen verwendet. Elementver-teilungsbilder im Zeiss 912 Omega und dem Zeiss Libra 200 FE TEM wurden mittels Röntgen-mikroanalyse (STEM-EDX) und energiegefilterter Abbildung (ESI) für die sub-µm Längenskala verwendet.

In der quantitativen EDX-Analyse tritt sowohl im REM als auch im TEM bevorzugte Ab-sorption der weichen Röntgenstrahlung von B auf. Die Detektoreffizienz für B wurde über die Zeit überwacht und es trat keine Degradation infolge Vereisung auf. Ein parameterloses Korrek-turverfahren für die Röntgenabsorption wurde für die quantitative TEM-EDX Analyse von MgB_2 Bändern angewandt. Der Cliff-Lorimer k-Faktor für B-K_α Röntgenstrahlung wurde als 8,71 bezo-gen auf Mg-K_α ermittelt. Die quantitative EDX-Spektroskopie ist für eine zuverlässige Interpreta-tion von energiegefilterten Elementverteilungsbildern unabdingbar.

(II) An drei verschiedenen repräsentativen und ausgewählten Proben wurden die normal- und supraleitende Eigenschaften durch Partnerinstitutionen untersucht und die Mikrostruktur mittels quantitativer elektronenmikrskopischer und spektroskopischer Verfahren vermessen. Mikrostruk-turergebnisse und supraleitende Eigenschaften wurden korreliert. Diese Proben sind (a) Al-le-giertes MgB_2 , (b) MgB_2 Bänder, die in langen Längen (1 km) hergestellt werden und (c) MgB_2 Keramik und Bänder, die mittels mechanischem Legieren hergestellt wurden.

(IIa) Al-legierte MgB_2 Keramik wurde mit Zusammensetzungen $Mg_{1-x}Al_xB_2$, mit x = 0, 0.1, 0.2, 0.3 hergestellt. Die B-reiche Sekundärphase enthält weniger als 4% Volumenanteil. Der tat-sächlich eingebaute Al-Atomzahlanteil der MgB_2 Matrix war geringer als der nominelle, eingewo-gene Anteil und der Unterschied stieg mit steigendem Al-Anteil an. Es wurde mittels Röntgen-mikroanalyse nachgewiesen, dass Al in die Kristallstruktur von MgB_2 eingebaut wird, indem Al Mg substituiert. Dabei wird die kritische Temperatur und die *c* Gitterkonstante um 1,56 K bzw. 1,15 pm pro at% Al verringert. Die *a* Gitterkonstante verringert sich lediglich um 0,17 pm pro at % Al. Mit Hilfe dieser Ergebnisse kann die tatsächliche chemische Zusammensetzung von Al- le-giertem MgB_2 über Beugungsmethoden bestimmt werden. Ausscheidungsbildung wurde selbst bis zum höchsten Al-Anteil der Probenserie nicht beobachtet. Jedoch wurden Inhomogenitäten in der Al-Verteilung mittels Röntgenmikroanalyse im TEM nachgewiesen, die die beobachtete Ver-breiterung des supraleitenden Phasenübergangs (ΔT_c) der Proben bei zunehmendem Al-Atomzah-lanteil erklären.

(IIb) Ni umhüllte, Cu stabilisierte MgB_2-Multifilamentbandleiter, die eine kritische Stromdi-chte von 2.0×10^5 Acm^{-2} (at 20 K and 1 T) aufweisen, wurden über eine Pulver-im-Rohr Techno-logie hergestellt, wobei vorreagiertes MgB_2 Pulver verwendet wurde. Koloniebildung, d.h. eine Anordnung von mehreren sauerstoffarmen, ohne Zwischenlagen verbundenen Körnern mit Korngrößen von 0,5 µm, wurde nachgewiesen, die Kolonien hatten Durchmesser von 1-6 µm.

Das B zu Mg Atomzahlanteilsverhältnis wurde als nahezu 2 bestimmt und der Sauerstoffanteil war kleiner 1 at%. MgO-Ausscheidungen mit Durchmessern von 15-70 nm wurden in den MgB_2-Körner gefunden. Einzelne, gerade verlaufende Versetzungen wurden mit einer Dichte von 10^{10} cm^{-2} beobachtet. Normalleitende Zwischenphasen wurden an den Grenzen der Kolonien beobachtet und führen zu Granularität und Verringerung der kritischen Stromdichte j_c. Intermetallische Zwischenschichten mit bis zu 5 µm Breite wurden an der MgB_2-Ni-Grenzfläche beobachtet mit einer Zusammensetzung von $MgB_2Ni_{2.9}$ und $MgB_{3.3}Ni_{10}$.

(IIc) Die Qualität der B Ausgangspulver beeinflusst maßgeblich die supraleitenden Eigenschaften von MgB_2 Leitern und der Einfluss auf die Mikrostruktur wurde detailliert untersucht. Die nominelle Reinheit der Pulver, wie sie durch die Hersteller spezifiziert wird, erfasst nur metallische Verunreinigungen und ist deshalb unzureichend. Oxidische Verunreinigungen und die Korngröße der B Körner beeinflussen maßgeblich T_c und die supraleitenden Eigenschaften der MgB_2 Bänder. MgB_2 Ausgangspulver wurde über mechanisches Legieren erzeugt und lieferte Korngrößen von 20-60 nm in MgB_2 Volumenproben und Bändern. B Ausgangspulver mit kleinen Korngrößen und geringen Anteilen metallischer Verunreinigungen lieferte Volumenproben, die sich durch einen hohen Phasenanteil MgB_2 und Stromdichten von 4.7 x 10^4 A/cm² (bei 20K, 1T) auszeichneten. Dasselbe Pulver lieferte Bänder mit Stromdichten von 5.0 x10^4 A/cm² (at 20K, 3T) und erforderte geringere Glühtemperaturen zur Phasenbildung. Die hohe kritische Stromdichte dieser Bänder, die ohne Additive wie z.B. SiC hergestellt wurden, ergibt sich durch die hohen Verankerungskräfte für magnetische Flußschläuche an Korngrenzen bedingt durch die geringen Korngrößen. Damit wird das Potential des mechanischen Legierens für die Herstellung der MgB_2 Bändern mit hoher Stromdichte dokumentiert.

Um das Mikrostruktur-j_c Modell zu erstellen wurden 10 MgB_2 Drähte und Bänder hergestellt, indem entweder vorreagiertes MgB_2-Ausgangspulver (ex-situ) oder Ausgangspulver aus elementaren Mg und B (in-situ) verwendet wurde, und bezüglich der Mikrostruktur vermessen. Für einige Proben wurde nanokristallines SiC zugegeben. Ex-situ Proben zeigten dichte MgB_2 Kolonien, die in einer granularen Matrix eingebettet waren. MgB_2 Körner in der granularen Matrix waren von $MgSi_xO_y$ Zwischenphasen umgeben, die zu Granularität führen. In-situ Proben wiesen eine höhere Dichte auf, aber zeigen, dass die MgB_2 Phasenbildung nicht vollständig erfolgte und enthielten hohe Anteile B-reicher Sekundärphasen. Die MgB_2 Korngößen in in-situ Proben waren 10-100 nm, hingegen betrugen die Korngrößen in ex-situ Proben 200-1000 nm. Die Flußlinien-Verankerung war wegen der kleineren Korngrößen in in-situ Proben deutlich erhöht.

Die großen Unterschiede in der kritischen Stromdichte dieser Proben konnten durch ein Mirkostruktur-kritische Stromdichte-Modell erklärt werden. In diesem Modell wurden die folgenden Mirkostrukturgrößen eingeführt: (1) MgB_2 Korngröße, (2) Sauerstoffanteil in der MgB_2 Matrix, (3) Durchmesser der Kolonien und (4) Volumenanteil der B-reichen Sekundärphasen. Die j_c Kurven der untersuchten MgB_2 Drähte und Bänder konnten in logarithmischen $j_c(B)$ Diagrammen durch Geraden parametrisiert werden. Die Parameter der Geraden wurden mit den experimentell Größen der Mikrostruktur korreliert. Die Ergebnisse des Mikrostruktur-kritische Stromdichte-Modells wurden in Bezug auf das Perkulationsmodell von Eisterer diskutiert.

Die Mikrostruktur-Untersuchungen von MgB_2, die auch mittels des Zeiss-Libra FEG TEM (SESAM II Mikroskop) bei 200 kV im Rahmen dieser Arbeit durchgeführt wurden, ermöglichten auch, die Leistungsfähigkeit dieses Gerätes zu beurteilen. Das Subelektron-Subangström-Mikroskop (SESAM)-Projekt ist ein von der Universität Tübingen und dem Max Planck Institut für Metallforschung getragenes Projekt.

Auf der Grundlage dieser Arbeit ergeben sich folgende Prioritäten für weiterführende Arbeiten: (i) MgB_2 Korngrenzen wurden als effektive Flußlinien-Verankerungszentren nachgewiesen, die Struktur dieser Korngrenzen sollte mittels Hochauflösung im TEM untersucht werden. (ii) Die Untersuchung der Mikrostruktur von MgB_2 Proben, die bei unterschiedlichen Glühtemperaturen und -dauern hergestellt wurden, wurde mit dieser Arbeit begonnen, sollte aber weiter auf Probenserien angewandt werden, für die diese Größen systematisch variiert werden, um die Thermodynamik in den Systemen Mg-B-O und Mg-B-Si-C-O quantitativ zu erfassen, über die in der Literatur wenig bekannt ist. (iii) die erfolgreich etablierte, quantitative B-Analyse im TEM sollte

angewandt werden, um die exakte chemische Zusammensetzung der B-reichen Fremdphasen mit Korngrößen kleine 1 µm zu bestimmen. (iv) die Methoden der quantitativen Phasenanalyse, die hier für REM-EDX etabliert wurde, sollte auch für STEM-EDX und energiegefilterte Elementverteilungsbilder (ESI) angewandt werden.

Chapter preview

Chapter 1 summarises the important physical properties of MgB_2 like its thermodynamical phase diagram, crystal structure and electronic structure. Various aspects of supercoductivity in MgB_2 like two-band superconductivity, electron-phonon coupling, upper critical field and its anisotropy, and critical current density will be briefly described. Various routes for the synthesis of MgB_2 wires and tapes are summarised. Importance of MgB_2 superconductor for commercial applications will be discussed.

Chapter 2 briefly describes the principles of advanced electron microscopy and spectroscopy methods. These include EDX spectroscopy and quantitative phase analysis using EDX chemical mapping in SEM, and EDX spectroscopy, STEM-EDX chemical mapping and ESI chemical mapping in TEM. Then the SEM (Jeol 6500F) and two TEMs (Zeiss 912Ω and Zeiss 200FE Libra), which have been used in this work are described. Carbon contamination free sample preparation which is of crucial importance for the microstructure analysis of MgB_2 samples, is also included.

Chapter 3 describes the challenges in the quantitative microstructure analysis of MgB_2 and the application of advanced electron microscopy and spectroscopy methods to MgB_2. By advanced electron microscopy we mean a combined SEM and TEM analysis with contamination free sample preparation, chemical mapping with good counting statistics and advanced chemical quantification (Figure 3.1(a)). The importance of electron microscopy and spectroscopy methods in the understanding of the thermodynamics of phase formation in MgB_2 as well as in improving the synthesis technology and the superconducting properties of MgB_2 wires and tapes is described.

Chapter 4 describes the Quantitative TEM-EDX analysis of B. B-K_α x-ray absorption in TEM samples is demonstrated. parameterless methods of absorption correction, which do not required the explicit sample thickness measurement, are reviewed. Application of Eibl's method of absorption correction to MgB_2 is demonstrated.

In chapter 5, the microstructure of MgB_2 bulk samples, alloyed with Al, are investigated using SE imaging, EPMA-WDX and TEM-EDX. The actual Al mole fraction alloyed into the MgB_2 lattice is determined. The influence of microstructure on the residual resisitivity and superconducting properties like B_{c2}, T_c and ΔT_c is discussed.

In chapter 6, the microstructure of long length, commercial, 14-filament MgB_2 tapes is investigated. Structural granularity which arises not only from voids but also from oxygen rich layers surrounding the MgB_2 grains is analysed using SEM. The reaction zone between the MgB_2 filament and the Ni-sheath is analysed using EPMA. TEM diffraction contrast imaging is used to determine MgB_2 grain size and, the density of dislocations and precipitates. The influence of oxide layers and the crystal defects on J_c is discussed.

Chapter 7 is concerned with the MgB_2 ceramics and tapes synthesised by mechanical alloying. First the chemical impurities, grain size and crystallinity of precursor boron powder was determined. Then the voids, cracks and B-rich secondary phases in MgB_2 bulk and tapes were investigated using secondary electron imaging and EDX in SEM. Effect of precursor powder quality and the annealing temperature on the microstructure and superconducting properties of MgB_2 bulk and tapes is discussed.

In chapter 8, a microstructure-critical current density model is given to explain thee large differences in the J_c's of different MgB_2 wires and tapes. Based on the advanced electron microscopy of well characterised MgB_2 wires and tapes, following microstructure parameters were extracted: 1) MgB_2 grain size, 2) oxygen mole fraction, 3) volume fraction of B-rich secondary phases and 4) colony size. The influence of these parameters on the J_c is discussed.

Contents

Chapter 1

1   Physical properties and synthesis of MgB$_2$

1.1   Introduction

MgB$_2$ was known at-least since 1953 [1], however, the superconductivity in MgB$_2$ was discovered only in 2001 by Nagamtsu et al.[2]. A summary of the important physical properties of MgB$_2$ like phase diagrams, crystal structure, electronic structure, two band superconductivity and state of the art values of the superconducting properties like T$_c$, B$_{c2}$ and J$_c$ are given in this chapter. The synthesis and technological importance of MgB$_2$ wires and tapes will also be given.

1.2   Thermodynamical phase diagrams

1.2.1   Mg-B system

Experimental phase diagrams of MgB$_2$ are not available so far primarily because phase analysis by x-rays is not feasible because of the poor diffracted signals from B-rich secondary phases like MgB$_4$ and MgB$_7$. A hypothetical temperature-composition phase diagram at Atmospheric pressure, proposed by Spear [3] is reported in compilation of Predel [4]. Recently Liu et al. [5] published calculated temperature-composition, pressure-composition and pressure-temperature phase diagrams which agree with the phase diagram of Spear. The historical development of the identification of phases in Mg-B system is reviewed by Braccini [6].

The temperature-composition phase diagram (Figure 1.1) at atmospheric pressure indicates that MgB$_2$ phase can exist with Mg rich solid, liquid and gas phases for temperatures upto 1545 °C and for B/Mg mole fraction ratios smaller than 2. Above this temperature MgB$_2$ decomposes into MgB$_4$ and gaseous Mg. The magnesium rich phases are more likely to react with residual oxygen forming MgO precipitates. For B/Mg mole fraction ratios between 2 and 4 and temperature less than 1545 °C, MgB$_2$ and MgB$_4$ phases coexist.

Brutti et al.[7] have carried out MgB$_2$ and MgB$_4$ vaporisation experiments using knudsen effusion-mass spectrometry. They determined the MgB$_2$ and MgB$_4$ decomposition temperatures at atmospheric pressures to be 1615 ±124 °C and 1615± 69 °C respectively which are in close agreement with the values calculated by Liu et al. indicating the reliability of their calculated phase diagrams[5].

However, the phase diagram of Liu et al. does not allow the simultaneous existence of MgB$_2$ and MgB$_7$ phases which is inconsistent with the EPMA analysis of MgB$_2$ ceramics [8] [9][10] which show MgB$_{7+\delta}$ secondary phases in the matrix of MgB$_2$.

Grivel et al [11] investigated the MgB$_2$ phase formation in Fe sheathed tapes by in-situ x-ray diffraction with hard synchrotron radiation (90 keV). From the variation of the Mg, MgB$_2$ and MgO x-ray diffraction peak intensities as a function of annealing temperature, they found the MgB$_2$ phase formation to begin at 575°C which is below the melting point of Mg (650°C). The intensity of the Mg reflections was found to decrease from temperatures as low as 100°C, reasons for which were not clearly understood. MgO was reported to form at a temperature of 450°C, which is lower compared to the temperature of MgB$_2$ formation.

1.2.2   Mg-Si system

Mg-Si phase diagram is important to understand the formation of Mg$_2$Si phase in in-situ MgB$_2$ samples with SiC additives. Using the experimental phase diagrams of previous researchers,

1

Nayab-Hashemi et al [12] constructed an assessed phase diagram of Mg-Si, which is used to draw the phase diagram of the Mg-Si system [13] given in Figure 1.2. In the Mg rich section (Mg-1.16 at.% Si) the eutectic temperature is at 637.8 °C, i.e. slightly below the melting point of Mg (650 °C).
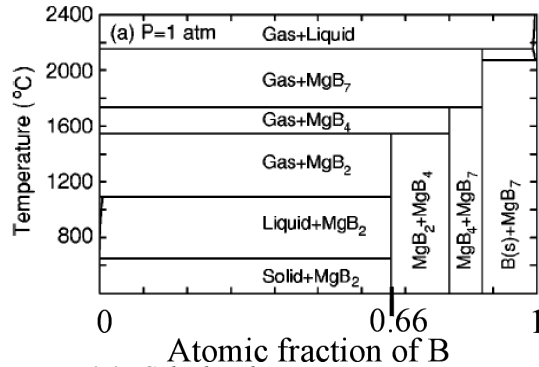

Figure 1.1: Calculated Temperature-composition phase diagram of Mg-B binary system(Liu et al. [5])
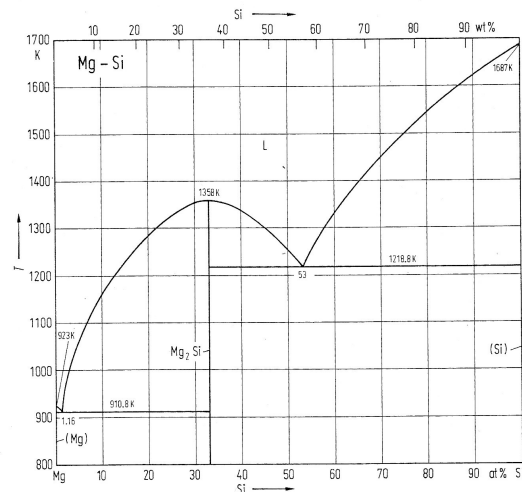
Figure 1.2: Temperature-composition phase diagram of Mg-Si system [13].

1.3   Crystal structure

MgB_2 is an intermetallic compound with hexagonal crystal structure (Figure 1.3 [14])of the AlB_2 type and was determined as early as 1953 [1]. The Mg atoms are at the positions (0,0,0) forming hexagonal close packed Mg-layers and the B atoms are at the positions (1/3,2/3,1/2) and (2/3,1/3,1/2) forming graphite like B-layers. The centre of the hexagonal boron ring lies both directly above and below each Mg atom. Its space group is P6/mmm and the space group number as given in the international tables of crystallography [15] is 191. MgB_2 thus has primitive crystal structure. The crystallographic direction [001] has a six-fold symmetry of rotation, while [100] and [1-10] each has two-fold symmetry of rotation. Each of these axis also has a mirror plane of symmetry perpendicular to it.

After the discovery of superconductivity, the structural properties of MgB_2 were investigated in much more detail. Jorgenson et al [16] measured the variation of lattice constants with temperature and pressure using neutron powder diffraction. $^{11}MgB_2$ samples were prepared by reacting isotopically enriched ^{11}B and Mg at a temperature of 1073 K under an argon atmosphere of 50 bar for 1.5 hours. The linear thermal expansion coefficients along a and c axes (α_a, α_c), Debye-Waller factors in the basal plane (U11) and perpendicular to the plane (U33) for B and Mg, and the bulk modulus [$V_0(\Delta P/\Delta V)$] were determined by them. The values of the structural parameters at 297 K are given in Table 1.1 [16]. The thermal expansion coefficient and Debye-Waller factor for B are substantially higher along the c axis than the a axis. This anisotropy is among the highest for AlB_2 type compounds and was attributed by Jorgenson et al.[16] to the weaker B-Mg bond. Such a structure facilitates the formation of two-dimensional-like electronic structure which is thought to be important in understanding the two gap superconductivity, high T_c, and and the anisotropy in B_{c2} [17].

Apart from MgB_2, three other higher borides of Mg exist: MgB_4, MgB_7 and MgB_{20}. The crystal structure of MgB_4 and MgB_7 have been determined by Naslain et al [18] and Guette et al [19] respectively using x-ray diffraction and are listed in the compilation of Predel et al.[13], while MgB_{20} has been recently discovered and investigated by Brutti et al. [20] using x-ray diffraction. The structural parameters of these higher borides are given in Table 1.2 . A fourth boride, MgB_{12}

is also suggested in the literature [21], but conclusive results concerning its crystal structure and stoichiometry could not be obtained [22].

Table 1.1: Structural parameters of MgB$_2$ at 297 K

Crystal structure	Space group	a (Å)	c (Å)	a_a (K^{-1})	a_c (K^{-1})
hcp	P6/mmm	3.08489	3.52107	5.4x10^{-6}	11.4x10^{-6}

U_{11}(Mg) (Å^2)	U_{33}(Mg) (Å^2)	U_{11}(B) (Å^2)	U_{33}(B) (Å^2)	$[V_0(\Delta P/\Delta V)]$ (GPa)
0.00545	0.00559	0.00454	0.00648	147.2

Table 1.2: Crystal structures and lattice parameters of higher borides (MgB$_4$, MgB$_7$ and MgB$_{20}$)

	Crystal system	Space group	a(Å)	b(Å)	c(Å)
MgB$_4$	Orthorhombic	Pnam	5.464	7.472	4.428
MgB$_7$	Orthorhombic	Imam	5.970	8.125	5.240
MgB$_{20}$	Trigonal	R3m	10.9830 (hexagonal cell)		24.1561 (hexagonal cell)

1.4   Electronic structure

MgB$_2$ like graphite has sp$_x$p$_y$ (sp^2) bonding. Each B atom in the graphite like (honeycomb) B layer is joined to three others by strong covalent σ bonds, between the sp^2 hybrid orbitals. The remaining p$_z$ orbital which have lobes above and below the B layer create π bonds. The electrons in the σ bonds are localised in the B planes, while those in the π bonds are delocalised throughout the crystal.

Band structure calculations of MgB$_2$ have been carried out by e.g. Kortus et al. and Mazin et al. [23]. The energy bands in the MgB$_2$ are shown in Figure 1.4 and the Fermi surface (FS) is shown in Figure 1.5. Two bonding σ bands derived from Boron p$_x$ and p$_y$ orbitals cross the Fermi level in the section Γ−A of the Brillouin zone. These two σ bands form cylindrical sheets (hole-like) of the FS around Γ−A line and possess nearly two-dimensional (2-D) character. These conducting, covalent σ bands are an unique feature of MgB$_2$. One bonding π band and one antibonding π band derived from Boron p$_z$ oribitals cross the Fermi level just after point K and at point M of the Brillioune zone respectively. The bonding and antibonding π bands form holelike (blue) and electronlike (red) tubular networks in FS. The π and σ bands contribute 58% and 42 % of the total density of states at the Fermi level and both are important for the electronic properties of MgB$_2$ [24][25].

The results of the band structure calculations agree with the experimental studies of FS e.g. de Hass-van Alphen effect [26][27][28] and angle-resolved photoemission spectroscopy (ARPES) [29][30].

1.5   Superconducting properties of MgB$_2$

The superconducting and normal state properties of MgB$_2$ are given in Table 1.3. The values are taken either from review articles of Buzea et al [14] and Muranaka et al [31] or from the single crystal studies of Eisterer et al [32].

Table 1.3: Normal and superconducting state properties of pure MgB$_2$

Critical temperature (T$_c$)	39-40 K	Superconducting coherence length in the ab plane ($\xi_{ab}(0)$)	10.2 nm
Total isotope effect (α_T)	0.32	Superconducting coherence length along c axis ($\xi_c(0)$)	2.3 nm
Resistivity near T$_c$ (ρ (40K))	0.4-16 $\mu\Omega$ cm	Penetration depth in the ab plane ($\lambda_{ab}(0)$)	82 nm
Upper critical field parallel to the ab plane (B$_{c2ab}$ (0))	14.5 T	Penetration depth along c axis ($\lambda_c(0)$)	370 nm
Upper critical field parallel to c axis (B$_{c2c}$ (0))	3.18 T	Superconducting energy gap on σ band (Δ_σ)	5.8-7.7 meV
Lower critical field parallel to the ab plane (B$_{c1ab}(0)$)	22 mT	Superconducting energy gap on π band (Δ_π)	1.8 – 3 meV
Lower critical field parallel to the c axis (B$_{c1c}(0)$)	63 mT		

1.5.1   Isotope effect, T$_c$ and two gap superconductivity

The T$_c$ (39 K) of MgB$_2$ is extraordinarily high- the next highest T$_c$ among other intermetallic superconductors being that of Nb$_3$Ge (T$_c$ =23 K). Experimental observations of other superconducting properties like isotope effect coefficient (α), average electron phonon coupling strength (λ) and the superconducting energy gaps cannot be adequately described by the standard BCS model. A convincing understanding of the superconductivity in MgB$_2$ can be obtained by considering the anisotropy in λ and the anharmonicity in the lattice vibrations[33]. Physics of the superconductivity in MgB2 has been beautifully explained by Canfield and Crabtree [34]. These aspects will be briefly reviewed.

The isotope effect coefficient (α_i) of element i in a multicomponent system is defined by

$$\alpha_i = \frac{-d \ln T_c}{d \ln M_i},$$

where M$_i$ is the atomic mass of element i . Budko et al.[35] Measured the B isotope coefficient (α_B) to be 0.26 which is significant and indicated that phonons associated with B vibrations play a major role in the superconductivity in MgB$_2$. Hinks et al [36] measured the Mg isotope effect (α_{Mg}) to be 0.02 and the total isotope effect coefficient (α_t) to be 0.32, which is significantly smaller than the BCS value of 0.5 for a conventional superconductor.

The specific heat of MgB$_2$ at low temperatures (<50 K) has been measured by e.g. Wang et al [37] , Bouquet et al [38]and Yang et al.[39]. The electronic contribution to the specific heat divided by temperature shows a large hump at about 10 K. Tunnelling [40] and photoemission[41] spectra and point contact spectroscopy [42] show excitations at two energies close to 2.5 meV and 7 meV. These results indicate two superconducting energy gaps in MgB$_2$.

Significant understanding of the nature of superconductivity in MgB$_2$ was obtained by Midgal-Eliashberg type calculations based on the band structure calculations. Midgal-Eiashberg theory is a generalisation of BCS theory and allows to take into consideration the anisotropy in λ and the anharmonicity in the lattice vibrations. These band structure calculations have been reviewed by Dahm [25].

According to isotropic Eliashberg theory the T$_c$ and α_t can be calculated [36][43][44][45] in terms of the material properties: electron-phonon coupling strength (λ), the repulsive electron-electron interaction (μ^*) and the logarithmic average frequency ($\omega_{\ln}$). Hinks et al [36] argued that the reduced isotope effect is due to large λ and μ^*. They further pointed out that the reduced α_t could also be due to the complex dimensional effects of FS and anharmonic lattice vibrations.

They predicted that the cause of the reduced α_t may in some way be related to the high T_c in MgB_2.

Liu et al [46] investigated the anisotropy in λ on the FS. λ on σ bands was found to be significantly higher because of its preferential coupling with the E_{2g} phonon mode of the in-plane vibrations of the boron atoms, than the λ on π bands. They showed that the effective λ relevant for superconductivity (λ_{sc}) is enhanced from its dirty limit value (0.77) to an effective clean limit value of 1.01. Together with ω_{ln}=56.2 meV and a realistic μ^* value of 0.13, the higher T_c of 40 K could be explained. However, these values of μ^* and λ_{sc} could not explain the reduced α_t , which they attributed to the anharmonicity of the lattice vibrations and a possible two-phonon coupling.

Correct explanation of both the high T_c and reduced α_t was given by Choi et al.[33] by solving Eliashberg equations in which the anisotropy of electron-phonon interaction and the anharmonicity of the phonons was considered. They concluded that anisotropy in MgB_2 increases T_c, while anharmonicity decreases T_c, yielding a resultant T_c of 39 K. The reduced α_t was attributed primarily to the phonon anharmonicity.

In an extended work Choi et al [47] evaluated the superconducting energy gap on the FS at 4 K, which was found to have s-wave symmetry, but the size of gap differed significantly on different part of the FS (Figure 1.6). The average value of the gap was 6.8 meV for σ bands and 1.8 meV for π bands, which is consistent with the experimental observations [37] [38] [39] [40] [41] [42].

In a two gap superconductor like MgB_2, T_c is expected to decrease with increase in residual resistivity because of interband impurity scattering [48]. However, experimentally, the T_c of MgB_2 is seen to be essentially independent of the residual resistivity [49]. Mazin et al [50] explained this discrepancy by considering the disparity between the σ and π bands. The σ bands derived from boron $p_{x,y}$ orbitals are mainly symmetric with respect to the boron plane, while the π bands derived from p_z orbitals are mainly antisymmetric. Due to the disparity of σ and π bands, the superconducting energy gaps at these gaps bands are stable against impurity scattering, which explains the high T_c of MgB_2 sample, even when their residual resistivity is large.

Apart from impurity scattering, the residual resistivity can also be dominated by the structural granularity (i.e. reduced connectivity)[49], introduced by the microstructure in the form of cracks, voids, grain boundary secondary phases and is discussed in detail in chapters 3 and 8.

1.5.2   Upper critical fields and their anisotropy

Measurements of the upper critical fields of MgB_2 samples in the form of bulk, wires and single crystals have been reviewed by Buzea et al [14]in 2001 and more recently by Muranaka et al [31]. The upper critical field at zero kelvin ($B_{c2}(0)$) of different samples was found to lie between 2.5 to 32 T. Thin films with a low T_c of 31 K even showed a $B_{c2}(0)$ of 39 T [51].

B_{c2} of MgB_2 single crystals has been investigated by [52] [53] [54] [55] using magnetisation, magnetotransport and specific heat measurements. The B_{c2} showed anisotropy which decreased with increasing temperature. $B_{c2ab}(0)$ (B_{c2} parallel to the boron plane) was 14-19 T, while $B_{c2c}(0)$ (B_{c2} perpendicular to the boron plane) was 3-4 T yielding an anisotropy ratio of about 5 at 0 K. Near T_c, $B_{c2ab}(T)$ showed a positive curvature while $B_{c2c}(T)$ showed a linear temperature dependence, yielding significantly decreased anisotropy ratio of about 2 [54] [25] [31].

Recent experiments on single crystals, bulk and wires showed that it is possible to enhance $B_{c2ab}(0)$ and decrease anisotropy ratio by introducing structural disorder in the form of carbon doping [56] or neutron irradiation [57] [58].

Theoretical calculations of B_{c2} and its anisotropy ratio for structurally ideal two gap superconductors like MgB_2 have been reviewed by Dahm [25]. These are based on Eilenberger theory which is a generalisation of the BCS theory to inhomogenous superconducting states. In the clean limit (i.e. neglecting impurity scattering) Dahm and Schopohl [59] explained the strong temperature dependence of the anisotropy ratio as follows. At low temperature and high magnetic field the anisotropic σ bands dominates the behaviour of B_{c2} because of its larger superconducting energy

gap leading to a strong anisotropy in B_{c2}. At temperature close to T_c (and the concurrently reduced magnetic fields) the influence of more isotropic π bands become significant yielding a reduced anisotropy. Dahm and Schopohl show that intermediate interband pairing interaction is essential for strong temperature dependence of B_{c2} anisotropy. Too strong or too weak interband pairing interaction was shown to result in an effective single gap behaviour.

Even in the best MgB_2 samples, impurity scattering is believed to affect the temperature dependence of MgB_2. Calculations considering general impurity scattering have not been given so far. However, "dirty limit theories" in which intraband scattering rate is larger than superconducting gaps and the intraband impurity scattering is negligible, have been given by Gurevich [60] and Golubov et al [61]. The physical explanation for the temperature dependence of B_{c2} anisotropy according to dirty limit theories is similar to that in the clean limit theory: an intermediate interband pairing interaction together with the strong anisotropy of Fermi velocities in σ bands which result in a strong anisotropy of the diffusivities in σ bands. The theoretical models of Dahm and Schopohl as well as Gurevich have been able to explain the positive (upward) curvature of $B_{c2\ ab}$ (T). Gurevich predicted that such an upward curvature can yield $B_{c2ab}(0)$ of upto 70 T by suitable manipulation of scattering centeres in σ and π bands for example by C and Al alloying [62] [62]. Extrapolated $B_{c2ab}(0)$ of 70 T has recently been observed in MgB_2 thin films alloyed with C [63].

1.5.3   Critical current density

Critical current density (J_c) is the most important figure of merit for applied superconductors [64]. J_c is microstructure dependent and might be influenced by weak links (structural granularity), B_{c2} and its anisotropy, and pinning centres [64]. In $(Bi,Pb)_2Sr_2Ca_2Cu_3O_{10}$ (Bi-2223), the J_c is primarily limited by thermally activated flux flow, because of its extreme two-dimensional (layered) crystal structure. In $Yba_2Cu_3O_x$ (YBCO) the J_c is primarily limited by the weakly coupled grain boundaries [64].

Bulk (intergrain) J_c's of $\sim 4 \times 10^5$ Acm^{-2} (at 10K and 1 T) [65] and 2×10^5 Acm^{-2} (at 10K and 0 T) [66] were found from the magnetic measurements on untextured bulk samples of MgB_2, which indicated strongly coupled grain boundaries in MgB_2. Kambara et al [66] showed that the remnant magnetization in the hysteresis loops decreased by a factor of 50 when the bulk sample was ground into a fine powder and re-measured under similar conditions, indicating dramatic reduction in the current loop size. The intragrain J_c in the powder was however found to be comparable to the intergrain J_c in the bulk sample. Furthermore the remnant magnetization in bulk sample was found to increase continuously as a function of the maximum applied field external magnetic field, without showing any steps. These results clearly demonstrated the presence of strongly coupled grain boundaries in polycrystalline MgB_2, which enables high J_c in wires and tapes prepared by the relatively simple powder in tube technique.

MgB_2 with its relatively large coherence length (~ 10 nm) offers significant scope to optimise its microstructure. The synthesis processes (to be described in next section) are adjusted to obtain optimum microstructure yielding highest J_c.

Dou et al [67] reviewed the recent developments in the J_c of MgB_2 single crystals, bulk, wires and tapes. The influence of various additives like C, nano-SiC, Si, Silicides (WSi_2, $ZrSi_2$, $MgSi_2$, Mg_2Si and SiO_2), metals (Fe, Mo, Cu, Ag, Z), oxides (Y_2O_3, ZrO_2) as well as other compounds like BN and Si_3N_4 is discussed. Nano-SiC was found to be the most effective additive in enhancing the Jc. This was attributed to i) enhanced B_{c2} because of C and Si alloying at the B sites of the MgB_2 lattice and ii) to enhanced flux pinning due to nanoscale impurities like Mg_2Si, BC, BO_x, $SiBO_x$ introduced by SiC addition.

Recently in 2007, Dou et al.[56] proposed a "dual reaction model" to explain the enhancement of J_c, B_{irr} (irreversibility field), and B_{c2} of MgB_2, by various kinds of carbon containing nanoaddtives. In this work the nano-SiC added MgB_2 wires showed a J_c of 1×10^5 Acm^{-2} at 4.2 K and 12 T, which was the best in-field J_c reported till then. The high effectivity of nano SiC in enhanc
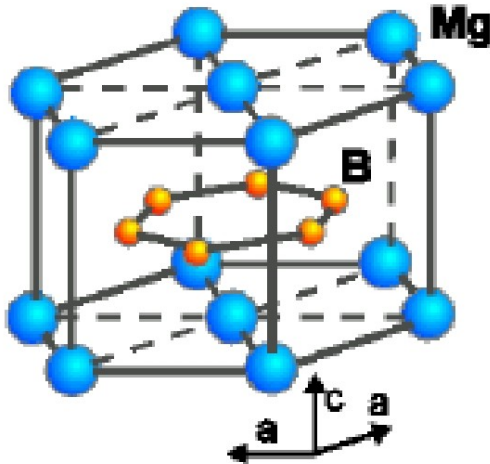
Figure 1.3: The crystal structure of MgB_2 containing graphite type boron layers separated by hexagonal close packed layers of Mg [14].
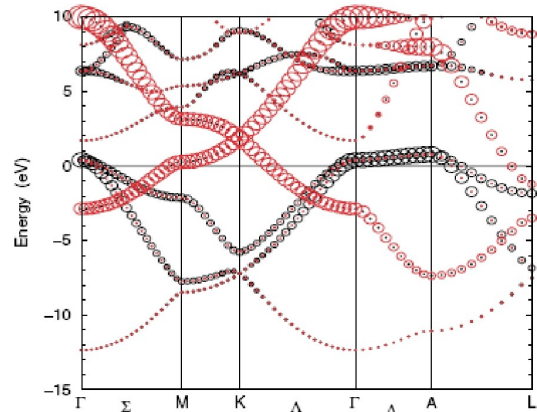

Figure 1.4: Band structure of MgB_2 with B p character. The radia of the red (black) circles are proportional to the B p_z (B $p_{x,y}$) character [23].
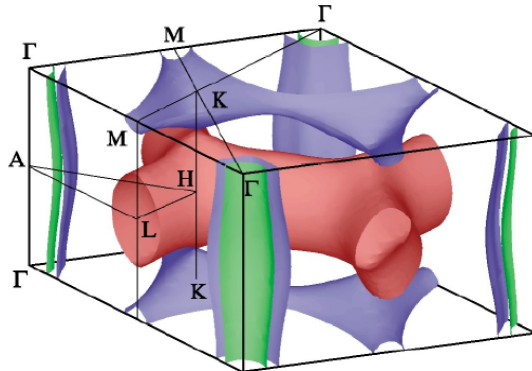

Figure 1.5: Fermi surface of MgB_2. The green and blue cylinders (holelike) come from B $p_{x,y}$ bands, the blue tubular network (holelike) from bonding p_z bands and the red tubular network (electronlike) come from the antibonding p_z band [23].
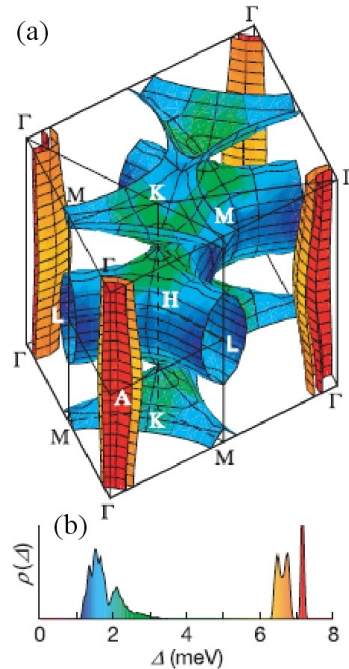

Figure 1.6: (a) The superconducting energy gap on the FS at 4 K using colour scale, (b) the distribution of gap values at 4 K [47]

ing the J_c of MgB_2 wires was attributed to its high reactivity with elemental Mg to form Mg_2Si. The free carbon released in the process was considered to be doped into the MgB_2 lattice during the subsequent formation of MgB_2 phase. Currently the J_c at 20 K of best MgB_2 samples with SiC additives is comparable to that of Nb-Ti at 4.2 K and to that of Bi-2223 at 20 K and low fields [68].The electron microscopy results obtained in this thesis, support the aforementioned "dual reaction model" proposed by Dou et al.[56].

A statistical analysis of the $J_c(B)$ data in the literature published between 2003 and 2006 has been given in chapter 3 of van Weeren's thesis [69]. Three parameters were used to assess the trends of the influence of the MgB_2 conductor development routes on the J_c: i) J_{c0} i.e. critical current density at zero field and is influenced by grain connectivity, ii) B_p i.e. magnitude of inverse slope of the log J_c versus B plot and is influenced by pinning and iii) B^*, i.e. magnetic field at a J_c of 10^4 Acm^{-2} which is influenced by the first two parameters as well as B_{c2} and is technologically the most relevant parameter. Weeren concluded that most progress has been done in B^* which

gauges the field retention of the J_c. From this point of view, in-situ samples were found to be better than the ex-situ samples.

In the present work J_c of about 10 MgB$_2$ samples in the form of bulk, wires and tapes are reported. The J_c's of wires and tapes were determined by transport measurements using 1 μVcm^{-1} criteria. J_c's of some bulk samples were determined by magnetic measurements using Beans model [70]. Depending on the synthesis technology, the J_c's of wires and tapes varied by a factor of upto 100. The highest J_c of 4x 10^3 Acm^{-2} was obtained in mechanically alloyed MgB$_2$ without any additives. Microstructure of these wires and tapes showed substantial structural granularity. In chapter 8, a microstructure- J_c correlation model is given to explain this large variation in the J_c of MgB$_2$ wires and tapes. The high J_c of MgB$_2$ wires, inspite of the substantial structural granularity, can be attributed to the unique features of superconductivity in MgB$_2$: the 10 nm coherence length, variable B_{c2} and the anisotropy in B_{c2}. The large variations in the J_c of MgB$_2$ wires and tapes could be attributed to the variations in the microstructure affecting the structural granularity (connectivity) and pinning[71] [72].

1.6   Synthesis of MgB$_2$ superconductors

Synthesis of MgB$_2$ bulk, wires and tapes involves the following thermodynamical parameters of freedom: Mg/B stoichiometry, SiC and other additives, annealing temperature and annealing time. There are also some technological parameters like precursor powder processing and deformation process in the case of wires and tapes. By varying these parameters one can control the resulting microstructure to yield optimal superconducting properties.

In an ex-situ synthesis, a pre-reacted MgB$_2$ powder and a annealing temperature of about 900°C is used, where as in an in-situ synthesis, elemental powders of Mg and B or suitable precursor like MgH$_2$ are annealed at a relatively lower temperature of about 650°C. In a third type of synthesis called mechanical alloying (MA) [73], which is actually a intermediate between in-situ and ex-situ synthesis, the precursor powders are mixed together using planetary ball mill at high speed. In the process grains in the precursor are broken down and also partially react to form a highly reactive mixture of unreacted precursor elements and MgB$_2$. The annealing temperature in MA is similar to that in in-situ synthesis. The melting points of Mg and B are 650 and 2076°C respectively and the equilibrium vapour pressure of Mg is very high. Therefore the MgB$_2$ phase formation in in-situ and MA samples takes place by diffusion of gaseous or liquid Mg into boron grains in solid phase. MgB$_2$ bulk, wires and tapes can be prepared by any of the above three methods: ex-situ synthesis, in-situ synthesis and mechanical alloying.

Bulk samples are prepared by sintering under pressure using techniques like hot pressing [73], hot isostatic pressing [74] or resistive sintering [75]. Sintering under pressure is essential to achieve strong connectivity between the MgB$_2$ grains [31].

A simple method of preparing MgB$_2$ wires is to react Mg vapour with boron wires at a temperature of about 900°C for few hours [76]. Because of the high equilibrium pressure of Mg vapour, this kind of wire synthesis as well as the bulk synthesis described earlier has to be carried out in sealed metal cells or under well controlled Mg vapour pressure[31]. Such kind of wires are very dense and therefore suitable to study the basic properties of MgB$_2$ but are not suitable for applications as there is no metal sheath around them.

The wires and tapes are usually prepared by powder-in-tube (PIT) technology. A schematic of steps involved in such a synthesis are a given in Figure 1.7 [77]. The precursor powder is put into a metal tube followed by deformation into monocore wire or tape of desired dimensions using different techniques like rolling, drawing, swaging, hydrostatic extrusion [78], two-axial rolling [79], continuous tube forming and filling (CTFF)[80] [81], and then annealed in a furnace. In case of multifilament wires and tapes, either many monocore wires or tapes are bundled together and inserted into a tube or the precursor powder is put into a tube with many holes drilled into it. The subsequent deformation and annealing procedure is similar to that for a monocore wire or tape.
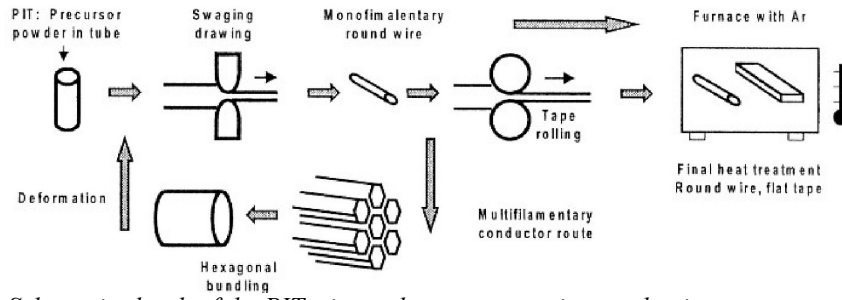
Figure 1.7: Schematic sketch of the PIT wire and tape preparation mechanism

1.7   Technological importance of MgB₂ superconductors

The favourable superconducting properties of MgB_2 have important and mostly positive technological implications. The 39 K T_c of MgB_2 which is four times the T_c of Nb-Ti (Table 1.4), would result in an operating temperature close to 20 K, which could be easily and economically achieved using liquid hydrogen or close cycle cryostats (chapter 1 of [69]).

The precursor powders of Mg, or MgH_2 and B are cheap, abundant and light in weight. The MgB_2 synthesis is relatively simple. The large (~10 nm) coherence length of MgB_2 yields strong coupling between the MgB_2 grains, and the existing PIT technology can be used to synthesise wires and tapes of MgB_2 which is a great simplification. In addition MgB_2 is essentially a line compound i.e. it has fixed stoichiometry [82][31], which results in reproducible T_c's.

In pristine MgB_2 B_{c2} and J_c are low and B_{c2} is anisotropic. However due to the two gap superconductivity in MgB_2, theoretical predictions [60] as well as experiments [63] suggest that a B_{c2}(0) close to ~70 T could be obtained by introducing structural disorder. Already MgB_2 wires with nano-SiC additives have shown a J_c of 10^5 Acm^{-2} at 20 K and 3 T, which exceed the J_c of the state of the art Ag/Bi-2223 tapes [67]. Moreover, as the subsequent electron microscopy analysis reported in this thesis will show, there is still a tremendous scope to improve and optimise the microstructure of MgB_2 wires and tapes, specially the in-situ ones, by controlling the MgB_2 grain size, C-doping and the distribution of secondary phases, and to enhance the already competitive J_c's.

One of the most extensive application of superconducting MgB_2 wires and tapes is the superconducting magnet in the MRI machines, which require a moderate field of about 1 T [31]. MRI machines with MgB_2 magnets have already been built and first MRI images of the human brain have been acquired [83].

Table 1.4: Comparison of T_c and B_{c2} of MgB_2 and other metallic and high-Tc oxide superconductors[84]

	Nb-Ti	MgB₂	Nb₃Sn	Nb₃(Al,Ge)	Bi-2223	YBCO
T_c (K)	9.8	39	18	20	92	110
B_{c2} (T) at 4.2 K	11.5	Anisotropic and variable	25	43	>100	>100

Chapter 2

2   Electron microscopy methods, microscopes and sample preparation

2.1   Introduction

Electron microscopy (EM) methods in SEM, EPMA and TEM have been used in this work to investigate the microstructure of MgB_2 superconductors. Principles of these EM methods, electron microscopes and sample preparation methods are described in this chapter. Application of conventional TEM to MgB_2 is described in detail. Application of other advanced electron microscopy techniques like chemical mapping using SEM-EDX, STEM-EDX, EFTEM-ESI and quantitative analysis using SEM-EDX, EPMA-WDX (wavelength dispersive x-ray spectroscopy) and TEM-EDX to MgB_2 is described in chapters 3 and 4.

2.2   SEM and EPMA

Principles of SEM and EPMA can be found e.g. in [85][86][87] and [88][87] respectively. SEM, because of its short sample preparation and analysis time has been extensively used to analyse the microstructure of a large number of MgB_2 wires and tapes on μm scale. EPMA has been used for a precise quantitative analysis of a few selected samples.

2.2.1   SEM-EDX chemical mapping and quantitative phase analysis

In SEM, a focussed electron beam is scanned on an array of points on the sample and the response signal of the sample (SE, BSE, or x-ray photons) is measured by a detector (SE, BSE or EDX). A SE image, BSE image or an EDX-elemental map is then formed by associating to each of the array points on the sample, a 8-bit pixel with a grey value proportional to the magnitude of the response signal.

To acquire an EDX-elemental map of a particular element, an energy window is set at the characteristic x-ray line of the element and the x-ray intensity detected in this window is used as a signal. Background x-ray intensity is not subtracted and the elemental map is used to qualitatively study the spatial distribution of the particular element. The characteristic x-ray lines used for the acquisition of B, C, O, Mg and Si elemental maps and for quantitative analysis are given in Table 2.1.

Table 2.1: Characteristic x-ray lines used for the SEM-EDX elemental mapping and quantification of B, C, O, Mg and Si

	B	C	O	Mg	Si
X-ray line	$B\text{-}K_\alpha$	$C\text{-}K_\alpha$	$O\text{-}K_\alpha$	$Mg\text{-}K_\alpha$	$Si\text{-}K_\alpha$
X-ray energy (eV)	183.3	277.0	524.9	1536	1740

A RGB image is formed by assigning red, green, and blue channels to, for example, Mg, O and B elemental maps respectively, acquired from the same sample area and then overlaying them on each other. Such a false colour overlay of Mg (red), O (green) and B (Blue) elemental maps will henceforth be referred to as RGB(Mg-O-B) image. A SE image of a MgB_2 sample (sample 5 of chapter 3) and the corresponding Mg elemental map, B elemental maps and RGB(Mg-O-B)

images are shown in Figure 2.1(a-d). RGB images enable to study the spatial distribution of different chemical phases.
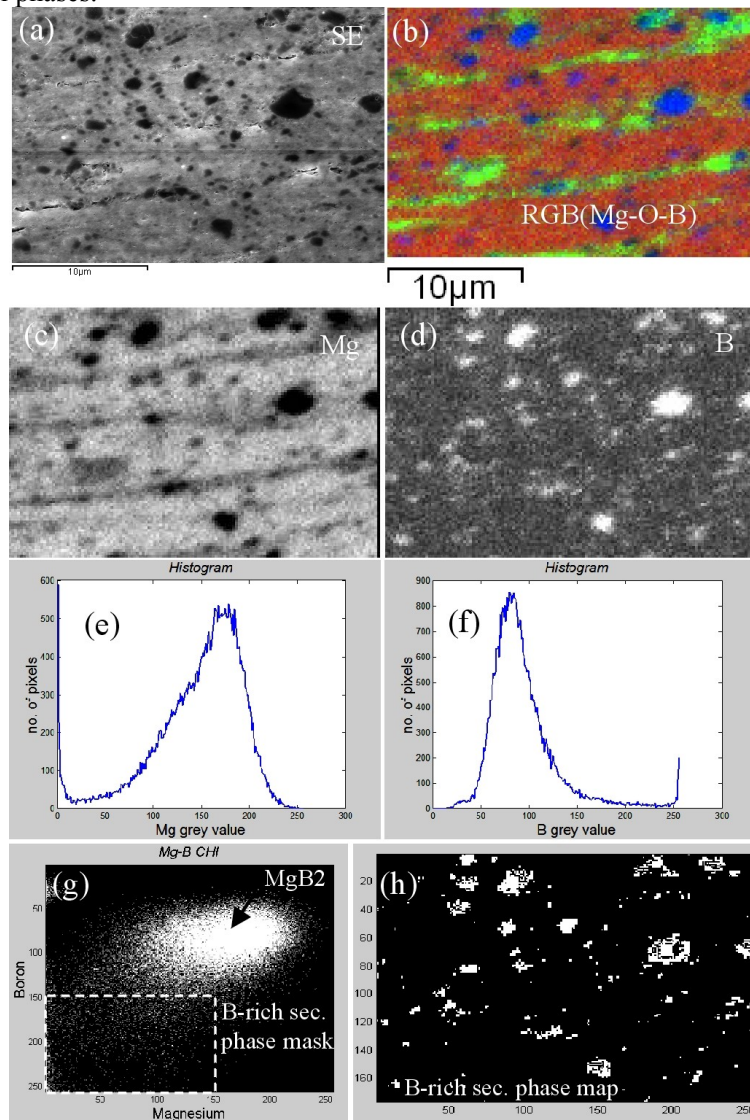

Figure 2.1: (a) SE image, (b) RGB-(Mg-O-B) image, (c-d) Mg and B elemental maps, (e-f) histograms of Mg and B elemental maps, (g) CHI of B and Mg elemental maps, (h) Synthetic phase map of B-rich secondary phases

Volume fraction of the chemical phases can be determined by quantitative phase analysis which is described in detail in [89]. A brief summary of the application of this technique to determine volume fraction of B-rich secondary phases in MgB_2 will be described here. The Mg and B elemental maps are converted into an 8-bit images using corel photopaint 8. Further image analysis was carried out using Matlab script given in section (9.2.1) of appendix. The grey values (0-255) in the Mg elemental map (henceforth called as Mg-grey values) are read pixel by pixel and stored in the form of a matrix. A one -dimensional histograms giving number of pixels with a particular Mg-grey value is shown in Figure 2.1(e). A similar histogram for B-elemental map is given in Figure 2.1(f). A two-dimensional histogram, called as concentration histogram (CHI) , with Mg-grey values on x-axis and B-grey values on y-axis is shown in Figure 2.1(g). The intensity in the CHI is proportional to the number of pixels with a particular combination of Mg-grey value and B-grey value. Different regions in the CHI correspond to different chemical phases. The brightest region corresponds to the MgB_2 matrix. A region shown by rectangular mask with high B-grey values and low Mg-grey values correspond to B-rich secondary phases (MgB_4 and MgB_7). A synthetic phase map of B-rich secondary phases (Figure 2.1(h)), which is a 2-bit image, is cre-

ated by assigning a grey value 1 to pixels with B and Mg grey values lying inside the mask and 0 to pixels lying outside the mask. Good agreement is seen between the synthetic phase map and the B-rich secondary phases which show up as blue in RGB(Mg-O-B) image. The volume fraction of the B-rich secondary phases is determined by counting the number of pixels whose B and Mg grey values lie inside the mask. In the present case the volume fraction of B-rich secondary phases is 1.4%.

2.2.2 SEM-EDX and EPMA-WDX quantification

ZAF method:

Quantitative x-ray microanalysis of bulk samples is usually carried out using a ZAF method:

$$\frac{I_A^{sample}}{I_A^{stnadard}} = c_A ZAF \quad,$$

where, I_A^{sample} and $I_A^{standard}$ are the x-ray intensities of element A obtained under similar experimental conditions (beam current, acquisition time, x-ray take-off angle etc.) from sample whose composition is to be determined and from a pure element standard. C_A is the weight fraction of element A in the sample. Z, A and F are the atomic number, absorption and fluorescence correction factors, essential because the sample and specimen are obviously different. Z, A and F themselves depend on the chemical composition, therefore the final composition C_A is determined iteratively. Z, A and F together with the depth distribution of x-ray generation ($\phi(\rho z)$) are described below.

Depth distribution of x-ray generation (Phi (rho-z)):

$\phi(\rho z)$ is of crucial importance in the calculation of atomic number and absorption correction. $\phi(\rho z)$ is written as a function of "mass thickness" that is a product of density and thickness, to make it independent of the physical state of the material. It gives the distribution of x-ray intensity induced by primary ionisation as a function of mass-thickness (ρz) of the sample. It is defined as the x-ray intensity generated per unit mass thickness at mass-thickness (ρz) of the sample normalised with respect to the x-ray intensity generated per unit mass thickness in a similar sample of infinitesimally small thickness ([88], p.48).

$\phi(\rho z)$ can be determined experimentally by tracer method, and by monte-carlo calculations. However tracer method can be applied only to pure element systems and both, the tracer method and monte-carlo simulations, are time consuming.

Philibert [90] derived an analytical expression for $\phi(\rho z)$ by considering the physical processes of electron scattering and ionisation occurring in the sample,

$$\phi(\rho z) = \exp(-\sigma \rho z)[4 - (4 - \phi(0)) \exp(-\sigma \rho z / h)].$$

He used Lenard's [91] exponential law for attenuation of electron density and Bothe's [92] law to determine the diffusion depth of electron in the sample. The ionisation cross section was assumed to be independent of energy. Further, the surface ionization function $\phi(0)$ was set to 0 to obtain a simplified Philibert formula,

$$\phi(\rho z) = 4 \exp(-\sigma \rho z)[1 - \exp(-\sigma \rho z / h)],$$
$$with, \; h = 1.2 \; A/Z^2, \;\; \sigma = Lenard \; constant = 4.5 \times 10^5 / (E_0^{1.65} - E_c^{1.65})$$

where, A is atomic weight, Z is atomic number, E_0 is the primary energy and E_c is the ionisation energy. In case of multi-element samples, average value of h is taken. An experimental and the simplified Philibert $\phi(\rho z)$ curves are shown in Figure 2.2 (a) and (b) respectively. While the shape of the simplified philibert $\phi(\rho z)$ resembles the experimental $\phi(\rho z)$, the agreement is not exact, specially near the surface of the sample.

Atomic number correction:

Atomic number correction ([88], p.148) takes into account the difference in the characteristic x-ray intensity of element A in the specimen and in the standard. It can be expressed in terms of $\phi(\rho z)$,

$$Z = \frac{\left[\int\limits_0^\infty \phi(\rho z)\,d\rho z\right]_A^{sample}}{\left[\int\limits_0^\infty \phi(\rho z)\,d\rho z\right]_A^{standard}}.$$

Calculation of $\phi(\rho z)$ from first principles, as in the case of simplified philibert model, is inaccurate. Consequently, the Z is usually calculated using

$$Z = \frac{[R/S]_A^{sample}}{[R/S]_A^{standard}}; \quad \frac{1}{S} = \int\limits_0^{E_c} \frac{Q}{dE/d\rho z}\,dE \quad,$$

where, R is the backscatter loss factor, S is the stopping power factor and Q is the ionisation cross section of element A.

Absorption correction:

Absorption correction factor takes into account the difference in the absorption of the characteristic x-ray intensity of element A in the specimen and in the standard. It can be expressed in terms of $\phi(\rho z)$ as,

$$A = \frac{[f]_A^{sample}}{[f]_A^{standard}}; \quad f = \frac{\int\limits_0^\infty \phi(\rho z)\exp(\mu\,cosec\,\theta)\,d\rho z}{\int\limits_0^\infty \phi(\rho z)\,d\rho z} \quad,$$

where, μ is the mass absorption coefficient of the characteristic x-rays of element A and θ is the x-ray take-off angle. Either the experimental or calculated $\phi(\rho z)$ is used. Because the term $\phi(\rho z)$ occurs both in numerator and denominator, acceptable absorption correction of heavy element ($z>12$) x-rays [93] can be obtained even with an approximate $\phi(\rho z)$ like that of the simplified philibert model.

Fluorescence correction:

Fluorescence correction factor takes into account the difference in the contribution of Fluorescence x-rays to the characteristic x-ray intensity of element A in the specimen and in the standard. It is written ([88], p.58) as

$$F = 1 + \gamma + \delta \quad,$$

where, γ is the ratio of intensity of fluorescence emission caused by characteristic x-rays to the intensity of primary characteristic x-rays of element A, and δ is the corresponding ratio for continuum fluorescence contribution.

Phi-rho-z methods:

It has not been possible to determine, based upon the physical process of electron scattering and ionisation, expression for $\phi(\rho z)$ which agrees sufficiently accurately with the experimental $\phi(\rho z)$. Fortunately however the general shape of all the experimentally determined $\phi(\rho z)$ curves are similar. Therefore an empirical or semi-empirical approach is used, in which exponential or gaussian functions are used to match to the shape of the $\phi(\rho z)$ curve and curve parameters like area under the curve, gradient, peak height, etc. are expressed as functions of sample composition and analysis conditions, to get an exact fit to the experimental $\phi(\rho z)$ curves. Such curve fitting methods, e.g. Gaussian model, Quadrilateral model [93], parabolic (PAP) model [94], Exponential (XPP) model[94], are called phi-rho-z methods (see Figure 2.2). Since $\phi(\rho z)$ methods model the experimental $\phi(\rho z)$ curves accurately, they yield accurate analysis of light elements. Additionally, unlike in ZAF methods, the atomic number and absorption corrections in $\phi(\rho z)$ methods can be combined:

$$ZA = \frac{[\int\limits_0^\infty \phi(\rho z)\exp(\frac{\mu}{\rho}cosec\,\theta)d\rho z]_A^{sample}}{[\int\limits_0^\infty \phi(\rho z)\exp(\frac{\mu}{\rho}cosec\,\theta)d\rho z]_A^{standard}}.$$

For example in XPP method [94], which is a phi-rho-z method, the $\phi(\rho z)$ is modelled by the following expression consisting of two exponentials,

$$\phi(\rho z) = A\,\exp(-a\rho z) + [B\rho z + \phi(0) - A]\exp(-b\rho z)\;,$$

where the coefficients A,a,B and b are determined from,

  i)   F: area under the $\phi(rz)$curve
  ii) G: the gradient of $\phi(\rho z)$ curve as ρz tends to 0
  iii) $\overline{\rho z}$:mean depth of x-ray generation
  iv) $\phi(0)$: surface ionisation,

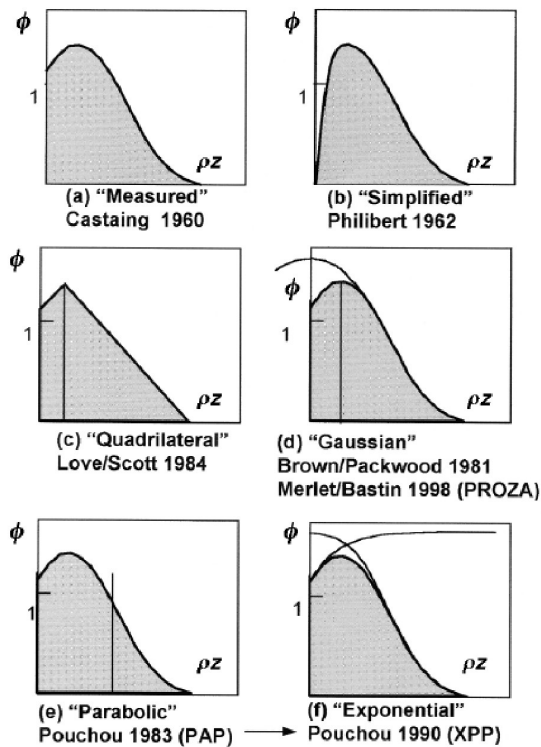which are themselves functions of primary energy (E_0) and the specimen composition.

Figure 2.2: Various models for representing depth distribution φ(ρz): (a) as measured by Castaing; (b)-(f) mathematical models capable of calculation for a given radiation, target atomic number and incident beam energy [95].
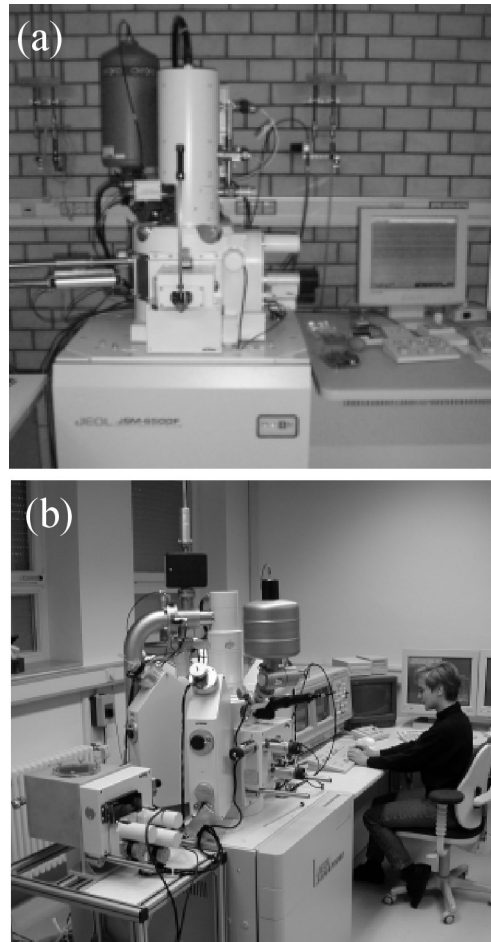
Figure 2.3: Photographs of the SEM and EPMA

2.2.3   SEM and EPMA used

Jeol JSM 6500F SEM (Figure 2.3(a)) equipped with field emission gun, SE detector and Si(Li) EDX detector (with an ultra thin window :ATW2) of the Oxfords instruments, was used at an operating voltage of 10 kV. The EDX-detector was able to detect B-K_α x-rays with a peak to background ratio of 11. The EDX spectra, EDX elemental maps and SE images were acquired and processed using INCA software of the Oxford instruments.

Jeol Superprobe 8900 RL EPMA (Figure 2.3(b)) equipped with a thermionic emission gun and an WDX detector system was operated at 15 kV. Following crystals were used: LDEB for B-K_α x-rays, TAP for Mg-K_α and Al-K_α x-rays, and LDE1H for O-K_α x-rays.

Further specifications of the SEM and EPMA instruments, and the acquisition conditions used for the analysis of MgB_2 samples, are summarised in Table 9.1 of the appendix.

2.2.4   Sample preparation

Metallographic SEM sample preparation:

About 3mm x 3mm x 1 mm piece of MgB_2 ceramic was cut using diamond wire saw and embedded in epoxy resin. The sample is than mounted on a tri-pod holder (Figure 2.4 (b)) and its surface was mechanically polished using diamond foils (Figure 2.4(a)) with grain size from 30 μm to 1 μm followed by ultrasonic cleaning in ethanol bath for 15 minutes. Some MgB_2 bulk samples degraded on contact with water possibly due to the reaction of unreacted residual Mg with water to from MgO and $Mg(OH)_2$. Therefore ethanol instead of water was used during mechanical polishing of such MgB_2 samples. The sample surface is then cleaned by etching with 4 kV Ar^+ ions in a Gatan Duo Mill, at an angle of 12.5° for 30 minutes. The SEM sample is rotated but not cooled during etching. The different ion etching rates of the different microstructural phases in the sample help to enhance the contrast in the secondary electron images. The sample surface was then coated by carbon or gold to improve electrical conductivity and immediately brought into EPMA and SEM.

This method yields extremely flat and polished samples and was used to prepare EPMA samples of Al-alloyed MgB_2 bulk. However, this method is not suitable for small (< 1 mm) MgB_2 samples because of carbon contamination from the surrounding organic resin (Figure 2.6 (b)). Moreover, such samples require conducting coating which leads to additional absorption of B-K_α x-rays.
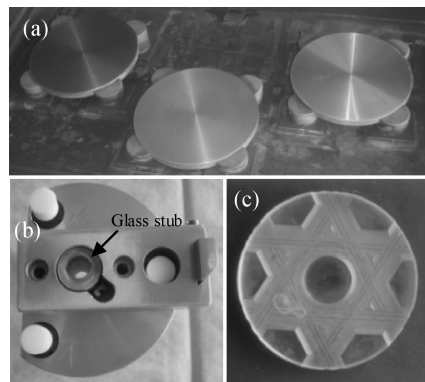

Figure 2.4: Photograph of the (a) diamond foils (b) Tri-pod holder and (c) Star holder used to prepare electron microscopy samples

SEM sample preparation without using resin:

To avoid carbon contamination and the use of conducting coating, MgB_2 samples were prepared without embedding them in the organic resin. About 3 mm long piece of MgB_2 tape was glued to Si-wafer as a support (Figure 2.5(a)) and the cross-section surface was polished using diamond foils. SEM samples of MgB_2 wires and bulk samples can also be polished in a similar manner. The sample is then ultrasonically cleaned , ion etched for 30 minutes and mounted on a metallic sample holder using Al-tape coated with a conducting adhesive. Al-tape contacts as shown in (Figure 2.5(b)) were sufficient to avoid charging effects in SEM in bulk samples. For tapes and wires, the metallic sheath automatically acted as conducting contacts. Apart from the above method, resin-free SEM samples could also be prepared by mechanically thinning to a thickness about 30 μm, like in a conventional TEM sample preparation (see the inset of Figure 2.6(a)), followed by ion etching for 30 minutes. The carbon contamination in SEM samples was drastically minimised by such resin-free sample preparation methods (Figure 2.6(a)).
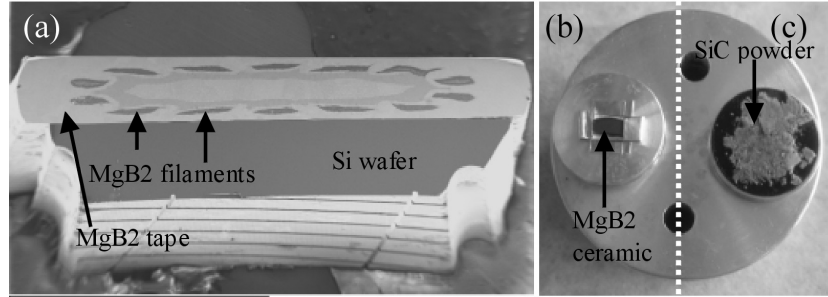
Figure 2.5: (a) overview SEM image of 14-filament MgB$_2$ tape and (b-c) photographs of a MgB$_2$ ceramic and SiC powder ready to be inserted in the SEM.
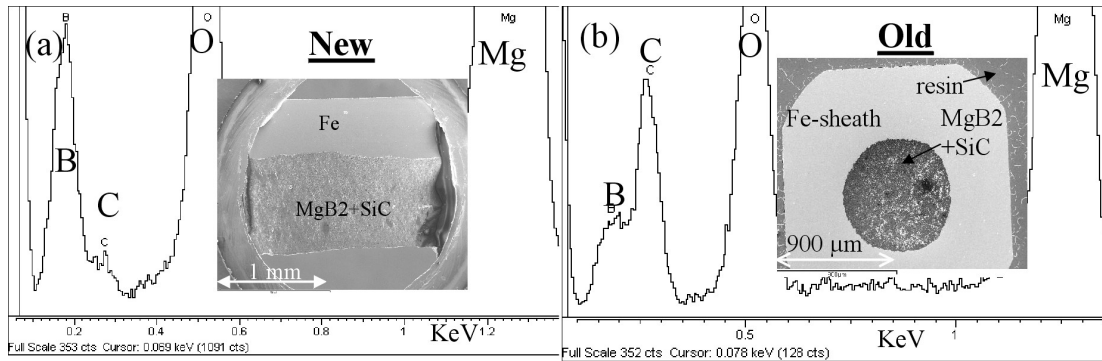

Figure 2.6: SEM-EDX spectra and secondary electron images (shown in the inset) of sample 2 prepared by (a) resin-free sample preparation method and (b) conventional method using organic resin.

SEM samples of B, MgH$_2$ and SiC Powder:

SEM samples of B, MgH$_2$ and SiC powders were prepared by spreading a thick layer of powder on a carbon foil and pressing it. The powders were than coated with a gold using Ar ion sputtering unit to avoid charging under electron beam in SEM. The sputtering time was 12 s (estimated gold film thickness ~ 12 nm) for B powder and 20 s (estimated gold film thickness 20 nm) for MgH$_2$ and SiC powders. Photograph of a SEM sample of SiC powder ready to be inserted in the SEM is shown in Figure 2.5(c).

2.3   TEM

TEM has been used for the microstructure analysis on nm scale. Unlike SEM, which gives information from only the top surface of the sample, TEM gives three-dimensional information of a thin sample.

2.3.1   Conventional Transmission Electron Microscopy

Conventional transmission electron microscopy (CTEM) means selected area diffraction and diffraction contrast imaging. Diffraction contrast imaging included bright-field and dark-field imaging usually carried out under nearly two-beam conditions. The principles of conventional TEM are described, for example in [96][97][98][99][100].

2.3.1.1   Diffraction patterns and Kikuchi maps in MgB$_2$

Selected area diffraction patterns were acquired with a 290 mm camera length, mainly to determine the orientation of the MgB$_2$ crystallites with respect to the electron beam, which was important for the analysis and interpretation of diffraction contrast images. They also gave quick measure of the crystallinity of the MgB$_2$ phase: ring patterns corresponding to nanocrystalline MgB$_2$ and spot patterns corresponding to polycrystalline MgB$_2$.

The diffraction patterns were indexed using 3-index (hkl) system, by matching the experimentally determined interplanar spacing and angles with the calculated ones. The experimental interplanar spacing (d_{hkl}) is given by,

$$d_{hkl}\, R_{hkl} = (camera\, length)\, \lambda$$

where, R_{hkl} is the length of the $\mathbf{g}_{hkl}$ diffraction vector and λ is the wavelength of electrons with an energy of 120 keV. If the R_{hkl} was measured in pixels, the camera length was determined to be 22193 pixels. The calculated interplanar spacing is given by

$$\frac{1}{d_{hkl}^2} = \frac{4(h^2 + hk + k^2)}{3a^2} + \frac{l^2}{c^2}$$

The angle ϕ between the ($h_1 k_1 l_1$) and ($h_2 k_2 l_2$) lattice planes is given by

$$\cos\phi = \frac{h_1 h_2 + k_1 k_2 + \frac{1}{2}(h_1 k_2 + k_1 h_2) + \frac{3}{4}\frac{a^2}{c^2}l_1 l_2}{\left[(h_1^2 + k_1^2 + h_1 k_1 + \frac{3}{4}\frac{a^2}{c^2}l_1^2)(h_2^2 + k_2^2 + h_2 k_2 + \frac{3}{4}\frac{a^2}{c^2}l_2^2)\right]^{1/2}}$$

Furthermore the $\mathbf{g}_{hkl}$ vectors should satisfy the vector law of addition. MgB$_2$ has a primitive hexagonal Bravais lattice, as a consequence all the hkl diffraction spots are allowed in the diffraction pattern. The pole of the diffraction pattern was determined using zone law. As a convention, the pole direction was opposite to that of the beam direction. In the case of diffraction patterns of a MgB$_2$ crystal acquired at two different poles, the indexing of the common diffraction spot was carried over from one pattern to another and experimentally determined angles between the poles were matched to the corresponding calculated angles between the poles. The indexing of the [001] and [0-10] poles acquired from two different MgB$_2$ single crystals is described in Figure 2.7 and in Table 2.2.

Apart from hkl diffraction spots, dark -h-k-l Kikuchi line and bright hkl Kikuchi line (together called as Kikuchi band) are also observed in the diffraction pattern. Kikuchi lines are formed due to the exact Bragg diffraction of the inelastically scattered electrons. They represent approximately the projection of hkl lattice planes on the screen and are of great help in tilting the sample from one pole to another and in establishing two-beam conditions with different excitation error s. A Kikuchi map consists of Kikuchi bands and the poles at the intersections of the Kikuchi bands. An experimental Kikuchi map obtained at the TEM by tilting two different single crystallites of MgB$_2$ around the [001] and [0-10] poles is shown in Figure 2.8.
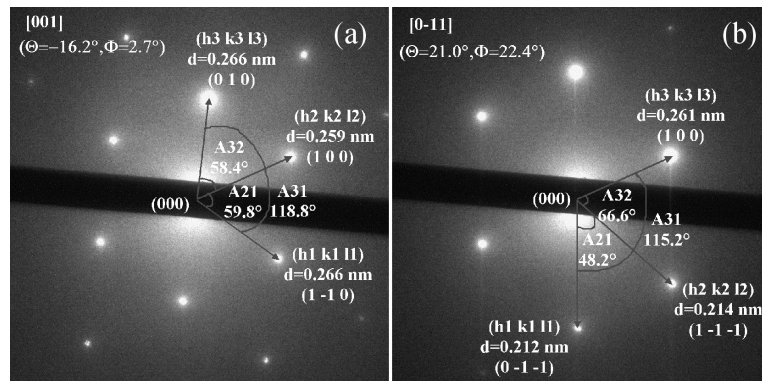

Figure 2.7: TEM diffraction patterns obtained from a MgB$_2$ single crystal in the (a) [001] and (b) [0-10] pole.
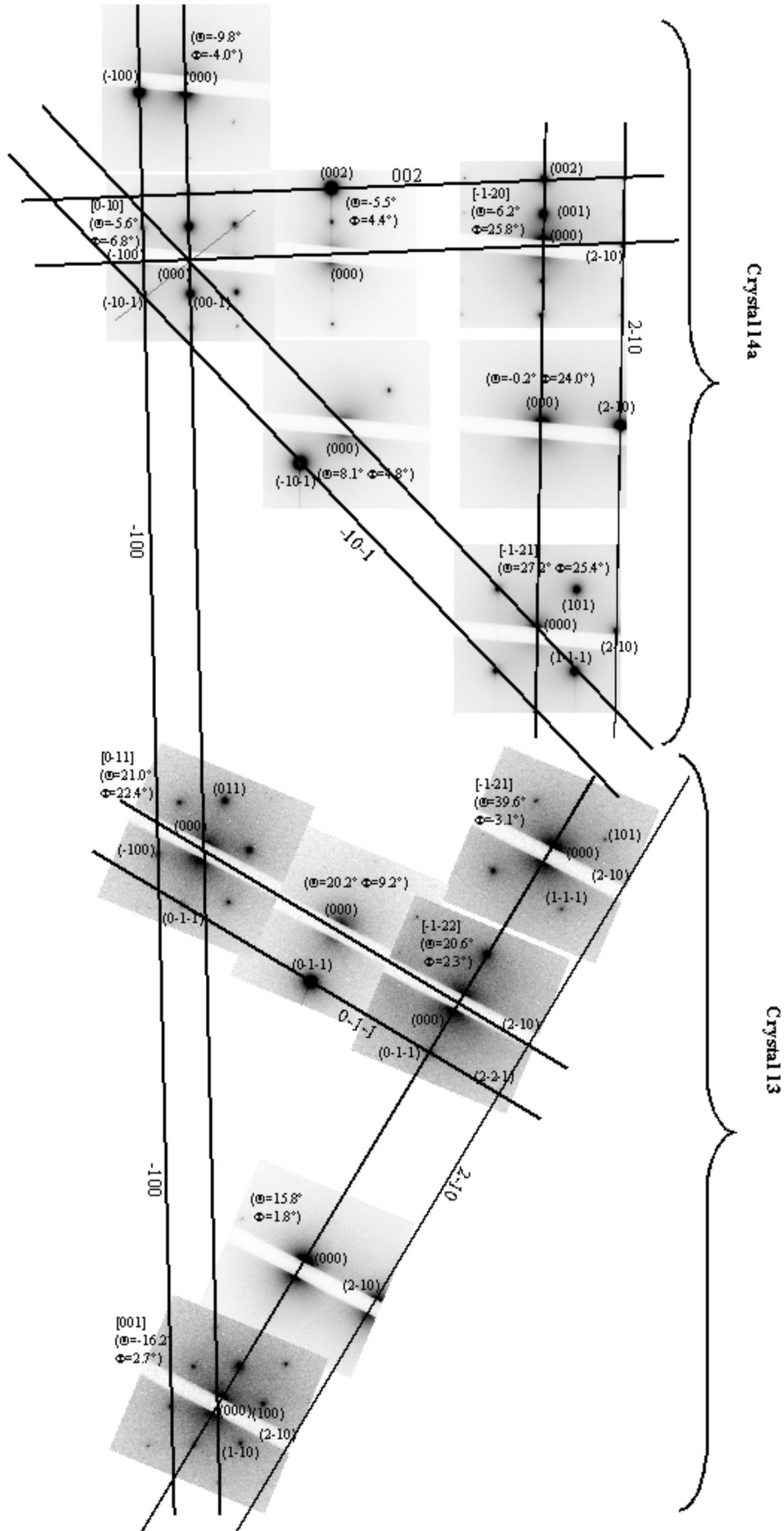
Figure 2.8: Experimental Kikuchi map of MgB₂ obtained at the TEM

Table 2.2: Indexing of TEM diffraction patterns (Figure 2.7) acquired in low index zone axis: lattice spacings and angles yield a unique indexing.

	dhkl (expt) (nm)	dhkl (Calc.) (nm)	Equivalent planes {hkl}	Enclosed angle (expt) (°)	Enclosed angle (Calc.)(°)	(hkl)
			crystallite in the [001] pole			
(h1 k1 l1)	0.212	0.21	(011), (0-11), (1-11), (101), (-101), (-111), (0-1-1), (01-1), (-11-1), (-10-1), (10-1), (1-1-1)	A_{31}=115.2	113.5	(0-1-1)
(h2 k2 l2)	0.214	0.21	(011), (0-11), (1-11), (101), (-101), (-111), (0-1-1), (01-1), (-11-1), (-10-1), (10-1), (1-1-1)	A_{32}=66.6	66.5	(1-1-1)
(h2 k3 l3)	0.261	0.27	(-100), (0-10), (010), (100), (1-10), (-110)			(100)
			crystallite in the [0-10] pole			
(h1 k1 l1)	0.266	0.267	(-100), (0-10), (010), (100), (1-10), (-110)			(1-10)
(h2 k2 l2)	0.259	0.267	(-100), (0-10), (010), (100), (1-10), (-110)	A_{21}=59.8	60	(100)
(h2 k3 l3)	0.266	0.267	(-100), (0-10), (010), (100), (1-10), (-110)	A_{31}=118.8	120	(010)

2.3.1.2   Diffraction contrast Imaging of MgB$_2$

The diffraction contrast images are almost always formed close to two-beam condition. In a two beam condition the sample is oriented in such a way that only the directed beam and one another Bragg diffracted beam G$_{hkl}$ are strongly excited in the diffraction pattern. Under this condition only the (hkl) lattice planes perpendicular to the **g**$_{hkl}$ are in Bragg diffraction condition. The interpretation of the images is then easier because only one set of lattice planes which is in Bragg diffraction condition contributes to the image. Bright/dark-field images under different two beam conditions together with their corresponding **g**$_{hkl}$ diffraction vectors (after correcting for rotation of diffraction pattern with respect to image) enable to characterise the defects in the crystal.

The kinematical structure factors and extinction lengths [96] for a few low-index reflections of MgB$_2$ were calculated using the empirical formula proposed by Doyle et al [101] and are given in Table 9.10 of the appendix. MgB$_2$, because of the light elements in it, has smaller kinematical structure factors and longer extinction lengths, in comparison to materials containing heavy elements. Therefore, the diffraction contrast imaging of MgB$_2$ was carried out using the {011}, {002} and {110} reflections which have the shortest extinction lengths.

Diffraction contrast images were formed by using elastically scattered electrons using an energy slit aperture in combination with an in-column spectrometer to remove the inelastically scattered electrons from the final image. The inelastic scattering increases the background intensity thereby reducing the contrast in the diffraction contrast images specially in thicker regions of the sample.

The acquisition conditions used for the diffraction contrast imaging of MgB$_2$ are summarised in Table 9.5.

In this thesis, diffraction contrast imaging has been used to determine the size of MgB$_2$ grains, size and density of precipitates and the density of dislocations in MgB$_2$ ceramics (chapter 5), wires and tapes (chapter 6). It has also been used to determine the grain size of precursor boron powder (chapter 7) and the agglomerate size of SiC additives [102].

2.3.1.3   Dynamical theory of diffraction contrast

References to dynamical theories of diffraction contrast imaging are described in[97] [103] [98]. According to the dynamical theory of diffraction, the rate of change of amplitudes in the diffracted and direct beam with the respect to the thickness z of the sample is given by the coupled differential equations of the first order:

$$\frac{d}{dz}\begin{pmatrix} \phi_g(z) \\ \phi_0(z) \end{pmatrix} = i\pi \begin{pmatrix} \left(\frac{1}{\xi_0}\right) & \left(\frac{1}{\xi_g}\right) e^{-2\pi i(\vec{g}+\vec{s})\cdot\vec{r}} \\ \left(\frac{1}{\xi_g}\right) e^{2\pi i(\vec{g}+\vec{s})\cdot\vec{r}} & \left(\frac{1}{\xi_0}\right) \end{pmatrix} \cdot \begin{pmatrix} \phi_g(z) \\ \phi_0(z) \end{pmatrix},$$

where, ξ_0 and ξ_g are the extinction lengths for the direct and diffracted beams respectively. $\vec{s}$ is the excitation error defined as,

$$\vec{s} = (\vec{k}' - \vec{k}) - \vec{g},$$

where, $\vec{k}'$ and $\vec{k}$ are incident and diffracted wavevectors and $\vec{g}$ is the diffraction vector. Thus the rates of change of diffracted and direct beam amplitudes are each proportional to the amplitudes of the diffracted and direct beam. These equations consider the diffraction of diffracted beam back to the direct beam as the beam travels through the sample. These equations are called Howie-Whelan equations. On solving these equations, intensities in the diffracted and direct beams, under two beam conditions are given by

$$\left| \phi_g \right|^2 = \left(\frac{\pi t}{\xi_g} \right)^2 \left(\frac{\sin^2(\pi t s_{eff})}{(\pi t s_{eff})^2} \right)$$

where ,

$$\xi_g = \text{Extinciton length} = \frac{\pi V_c \cos(\theta_B)}{\lambda F_g};$$

$$V_c = \text{Volume of unit cell};$$

$$\theta_B = \text{Bragg angle};$$

$$F_g = \text{Kinetmatical structure factor of the material at angle } \theta_B;$$

$$s_{eff} = \frac{\sqrt{s^2 \xi_g^2 + 1}}{\xi_g} = \text{Effective excitation error}$$

and

$$\left| \phi_0 \right|^2 = 1 - \left| \phi_g \right|^2.$$

The above equations explain the thickness fringes (occurring due to periodicity with respect to t) and bend contours (occurring due to variation of excitation error) in the sample. However, they cannot explain the non-complementarities observed in TEM bright field and dark field images, because inelastic scattering and absorption of scattered electrons by objective aperture are not considered. Both the above effects can be considered phenomenologically, by adding the complex terms, i/ξ_0' and i/ξ_g' to the terms $1/\xi_0$ and $1/\xi_g$, in the Howie-Whelan differential equations:

$$\frac{d}{dz} \begin{pmatrix} \phi_g(z) \\ \phi_0(z) \end{pmatrix} = i\pi \begin{pmatrix} \left(\frac{1}{\xi_0} + \frac{i}{\xi_0'} \right) & \left(\frac{1}{\xi_g} + \frac{i}{\xi_g'} \right) e^{-2\pi i(\vec{g}+\vec{s})\cdot\vec{r}} \\ \left(\frac{1}{\xi_g} + \frac{i}{\xi_g'} \right) e^{2\pi i(\vec{g}+\vec{s})\cdot\vec{r}} & \left(\frac{1}{\xi_0} + \frac{i}{\xi_0'} \right) \end{pmatrix} \cdot \begin{pmatrix} \phi_g(z) \\ \phi_0(z) \end{pmatrix}.$$

After suitably transforming the the functions ϕ_g , ϕ_0 and the unit of length, and by approximating $\xi_0' = \xi_g'$, the above Howie-Whelan equations can be written as,

$$\frac{d}{dz} \begin{pmatrix} \phi_g(z) \\ \phi_0(z) \end{pmatrix} = \begin{pmatrix} (-A + 2iw) & (i-A) \\ (i-A) & (-A) \end{pmatrix} \cdot \begin{pmatrix} \phi_g(z) \\ \phi_0(z) \end{pmatrix}$$

Here the anomalous absorption coefficient is defined as $A = \xi_g/\xi_g'$ and the excitation error parameter is defined as $w = s \cdot \xi_g = \cot\beta$. The intensity of the diffracted and direct beam can then be determined analytically,

$$\left| \phi_g \right|^2 = \left| -\cos(\beta/2)\sin(\beta/2)\left(e^{-iXz} - e^{iXz} \right) e^{-\pi z/\xi_0'} \right|^2$$

$$\left| \phi_0 \right|^2 = \left| \left(\cos^2(\beta/2) e^{-iXz} + \sin^2(\beta/2) e^{iXz} \right) e^{-\pi z/\xi_0'} \right|^2$$

where,

$$X = \frac{\pi \sqrt{1+w^2}}{\xi_g} + \frac{\pi i \sqrt{1+w^2}}{\xi_g'}$$

An ideal TEM sample (uniformly thin and perfectly flat) from a defect free crystallite would not show any variation in the intensity in its image. Real crystals however contain defects, e.g. dislocations. They cause local displacement $R(\vec{r})$ of the atoms from their positions in the crystal with perfect translation symmetry. Such a displacement causes bending of the lattice planes and therefore variation in local s values throughout the sample. This gives rise to variation in the intensities in the image. The Howie-Whelan equations for such a distorted crystal, considering absorption due to inelastic scattering are written as,

$$\frac{d}{dz}\begin{pmatrix} \phi_g(z) \\ \phi_0(z) \end{pmatrix} = i\pi \begin{pmatrix} \left(\frac{1}{\xi_0}+\frac{1}{\xi_0'}\right) & \left(\frac{1}{\xi_g}+\frac{1}{\xi_g'}\right)e^{-2\pi i(sz+\vec{g}\cdot\vec{R})} \\ \left(\frac{1}{\xi_g}+\frac{1}{\xi_g'}\right)e^{2\pi i(sz+\vec{g}\cdot\vec{R})} & \left(\frac{1}{\xi_0}+\frac{1}{\xi_0'}\right) \end{pmatrix} \cdot \begin{pmatrix} \phi_g(z) \\ \phi_0(z) \end{pmatrix}.$$

Similar to the ideal crystal, after suitably transforming the the functions ϕ_g, ϕ_0 and the units of length, the above Howie-Whelan equations can be written as,

$$\frac{d}{dz}\begin{pmatrix} \phi_g(z) \\ \phi_0(z) \end{pmatrix} = \begin{pmatrix} \left(-A+2i\left(w+\pi\,\vec{g}\cdot\frac{d\vec{R}}{dz}\right)\right) & (i-A) \\ (i-A) & (-A) \end{pmatrix} \cdot \begin{pmatrix} \phi_g(z) \\ \phi_0(z) \end{pmatrix}.$$

On comparing this equation with the corresponding equation for the defect crystal the effective excitation parameter for the distorted crystal is defined as

$$w_{eff} = w + \pi\,\vec{g}\cdot\frac{d\vec{R}}{dz}$$

In general the Howie-Whelan equations in distorted crystals cannot be solved analytically because of the term $g\cdot\frac{d\vec{R}}{dz}$, but can be solved numerically [104].

2.3.2   STEM-EDX chemical mapping of MgB$_2$

The principles of STEM-EDX chemical mapping are described in [105][86], and are similar to SEM-EDX chemical mapping described in section 2.1.1. A major advantage of STEM-EDX chemical mapping over SEM-EDX chemical mapping is its improved lateral resolution because of the smaller beam spread in thin TEM samples. Difficulties due to multiple scattering, as in ESI, are not encountered for STEM-EDX chemical mapping. Difficulties of STEM-EDX chemical mapping are the lower counts per pixel (particularly for light elements like B) and the carbon contamination of the sample under the electron beam.

Acquisition conditions for the STEM-EDX elemental mapping of MgB$_2$ using Zeiss 200FE (Libra) are given in Table 9.7. Application of the STEM-EDX elemental mapping to MgB$_2$ is given in chapter 3. Application of STEM-EDX chemical mapping to Bi-2223 is given by [89], [106].

2.3.3   EFTEM-ESI chemical mapping of MgB$_2$

The principles of EFTEM-ESI elemental mapping are described in [107] and [98]. A schematic diagram of an energy loss spectrum with a core-loss edge is given in Figure 2.9. In EFTEM it is possible to form images using electrons of definite energy loss range. This is used to form EF-

TEM-ESI elemental maps and are particularly suitable for the chemical mapping of light elements like boron, carbon and oxygen.

An example of EFTEM-ESI elemental mapping using three-window-difference method is shown in Figure 2.10. The TEM bright field image is formed by electrons with an energy loss in the range of (0-20 eV). B-K_3 is a post-edge ESI image of boron obtained using the electrons with an energy loss in the range (200-220 eV). Apart from this, two pre-edge ESI images, B-K_1 and B-K_2, are obtained using electrons in the energy loss range (150-170 eV) and (178-198 eV) respectively. The intensities in B-K_1 and B-K_2 are fit to a power law, pixel by pixel, and interpolated to calculate the B-K_3-background image due to the background signal in the energy range (200-220 eV). EFTEM-ESI elemental map of B is then obtained by subtracting the B-K_3- background image from the B-K3 image. EFTEM-ESI elemental maps of C and O are obtained in a similar manner. A RGB(BCO) image is created by overlaying the B, C and O ESI elemental maps as described in section 2.1.1.

Following difficulties are usually encountered during EFTEM- ESI chemical mapping.

(i) multiple scattering in thick samples, as a consequence inelastically scattered electrons cannot be correctly associated to a single inelastic scattering process.

(ii) inaccuracies in background subtraction

(iii) low signal for high energy core loss edges like Mg-K

(iv) low signal to background ratio for low energy core loss edges like B-K

(v) specimen drift during TEM analysis

The acquisition conditions for the EFTEM-ESI elemental mapping of B,C and O using Zeiss 912Ω and Zeiss 200FE (Libra) are given in Table 9.8. The EFTEM-ESI images shown in Figure 2.10 were obtained from a MgB$_2$ tape at a magnification of 12.5 K using Zeiss 912Ω. Mean pixel intensity in the B elemental map of MgB$_2$ region, at a distance of about 200 nm from the from the edge of the sample, is about 400 cts. The signal to background ratio is 0.15.
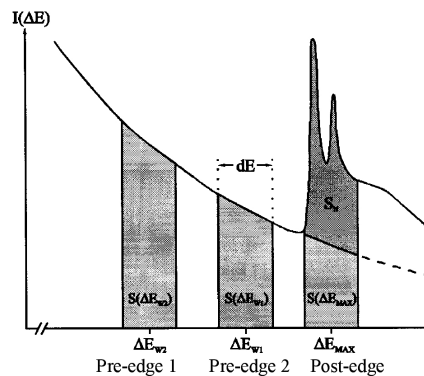

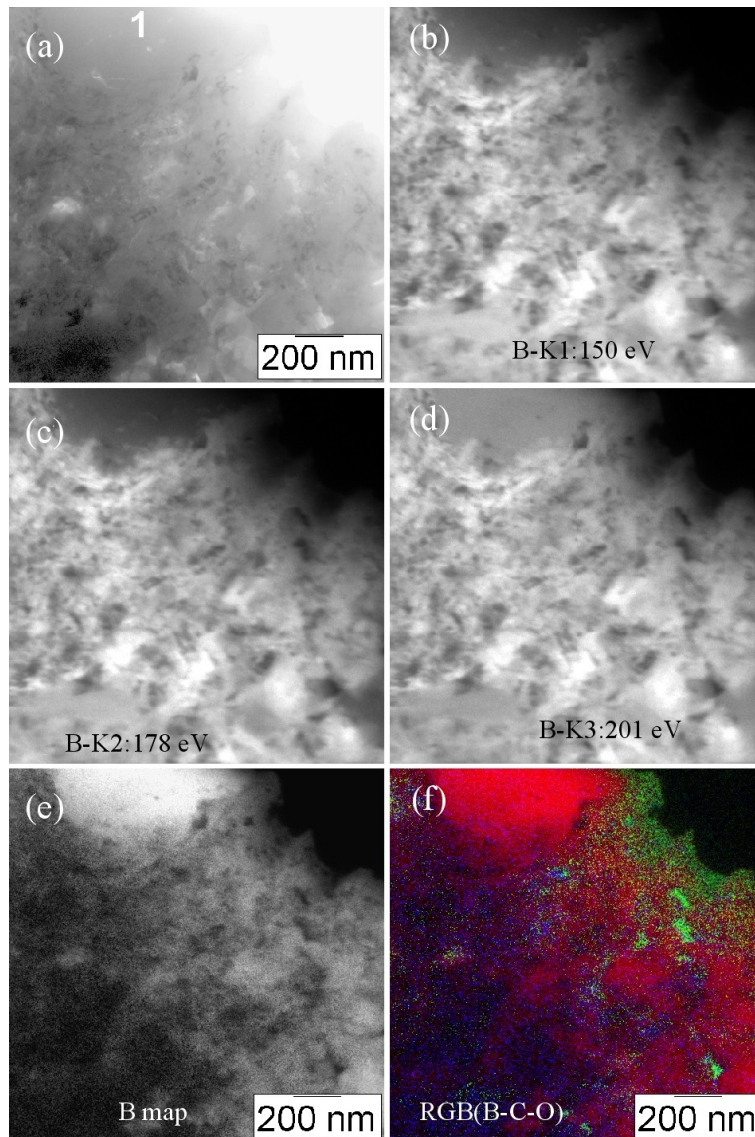*Figure 2.9: A schematic diagram of an energy loss spectrum with a core-loss edge*

Figure 2.10: (a) TEM bright-field image, EFTEM-ESI images (b) B-K1, (c) B-K2, (d) B-K3, (e) B-K elemental map and (f) RGB overlay of EFTEM-ESI elemental maps of B,C and O obtained using Zeiss-912.

2.3.4   Transmission electron microscopes used

Two different TEMs, 912Ω (here after referred as Zeiss-912) and LIBRA 200FE (here after referred as Zeiss-Libra) from ZEISS have been used. Photographs of the two TEMs are given in Figure 2.11. A comparison of their specifications is given in Table 9.4.
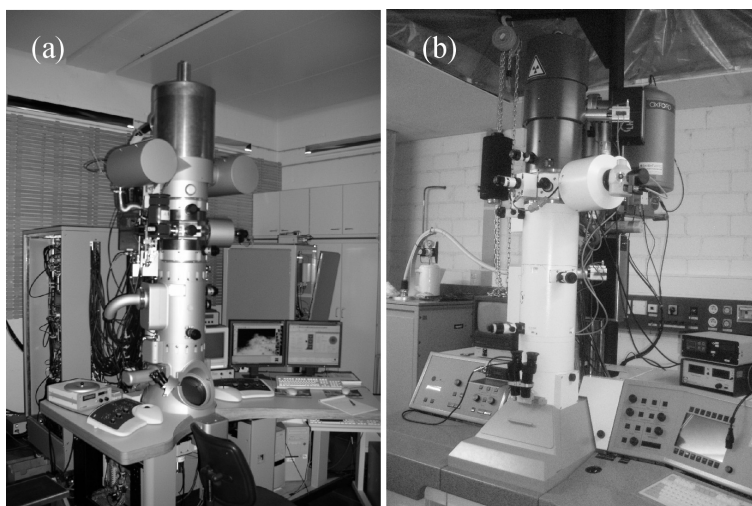
Figure 2.11: Photographs of the TEMs (a) Zeiss-912Ω and (b) Zeiss-Libra

2.3.4.1 *Zeiss-912Ω (Zeiss-912)*

The following description of Zeiss-912 TEM is mainly summarised from the operating manual of Zeiss-912 [108]. A ray diagram of the Zeiss-912 in image mode (dashed lines) and diffraction mode (continuous line) is shown in Figure 2.12. A detailed ray diagram of the spectrometer is shown in Figure 2.13. Zeiss-912 has a LaB_6 thermionic emission gun and an accelerating voltage of 120 kV. In TEM mode, the illuminating system consisting of three condenser lenses, condenser aperture in the third condenser lens and objective pre field lens, illuminates the sample homogeneously and parallely using Kohler principle. The sample is located symmetrically between the objective prefield lens and the objective lens.

Objective lens, first projector lens system, omega energy spectrometer, and second projector lens system constitute the imaging system. The first projector lens system achieves different magnifications. In the image mode the first projective lens system images the first intermediate image in the entrance image plane of the spectrometer and the back focal plane of the objective lens (diffraction pattern) in the entrance crossover of the spectrometer. In diffraction mode the first projective lens system images the back focal plane of the objective lens in the entrance image plane of the spectrometer and first intermediate image in the plane of the entrance crossover of the spectrometer.

The spectrometer generates in its exit image plane an achromatic 1:1 image of its entrance image plane. At the same time it produces a spectrally dispersed image of entrance cross over in the energy dispersive plane. A slit aperture of variable width is centred around the optic axis in the energy dispersive plane. Electrons which have lost a definite range of energy in the sample are selected by this aperture and used for further imaging.

In the image mode of the spectrometer, the second projector lens group images the exit image plane onto the viewing screen to produce energy selected image or diffraction pattern. In spectrum mode of the spectrometer, the second projective lens group images the energy dispersive plane on the viewing screen to produce EELS spectrum.

A fluorescent screen is used to view, and a CCD camera (14 bit, 1kx1k) is used to acquire the BF/DF images, ESI images and EELS spectra using ESIVISION software.

A Si(Li) EDX detector (with an ultra thin window: ATW2) of the Oxford Instruments is used to acquire EDX spectra using INCA software.

High vacuum (8×10^{-8} mbar) in the sample region was obtained using turbo molecular pump and ion getter pump, after cooling the anti-contaminator (which acted as a cryo pump) to liquid nitrogen temperature.
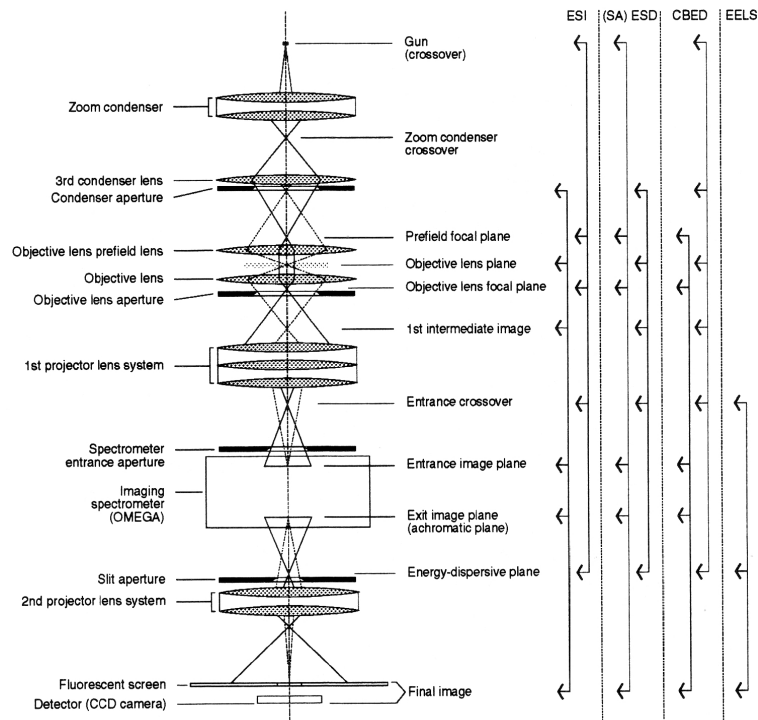
Figure 2.12: Schematic diagram showing the imaging and illuminating ray diagrams of Zeiss-912Ω. Conjugate planes for different operating modes are indicated on the right.

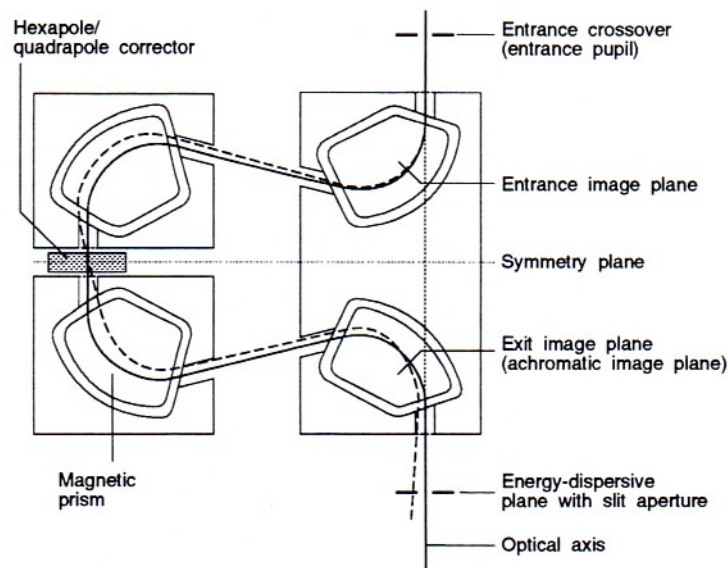

Figure 2.13: Schematic diagram of the Omega in-column spectrometer.

2.3.4.2   Zeiss-Libra (Zeiss-Libra 200F: A SESAM II microscope)

Zeiss-Libra is SESAM II microscope equipped with a field emission gun operated at 200 kV. It is also equipped with a high angle annular dark field (HAADF) detector and a STEM unit. The SESAM (Subelectron Sub-Angstrom Microscope) is a joint effort of the University of Tuebingen and Max Planck Institute for metal research, Stuttgart.

The illuminating lens system, Imaging lens system and the in-column spectrometer in Zeiss-Libra are similar to those in Zeiss-912.

BF/DF images and ESI images and EELS spectra are acquired using Digital Micrograph software of GATAN.

An EDX detector from EDAX was used to acquire EDX spectra and STEM-EDX elemental maps using EDAX-Genesis software.

Ultra high vacuum (1.74×10^{-9} mbar) in the field emission gun region was obtained using turbo molecular pump and ion getter pumps, after cooling the anti-contaminator (which acted as a cryo pump) to liquid nitrogen temperature. The vacuum around the sample region was poor (1.58×10^{-7} mbar) in comparison to Zeiss-912.

ESI and STEM-EDX elemental mapping of MgB_2 using Zeiss-Libra, and ESI and EDX spectroscopy of MgB_2 using Zeiss-912, described in chapter 3, enabled to assess the performance of these two microscopes:

1. Using Zeiss-Libra ESI elmental maps of B,C and O could be acquired at magnification >50 k, while the corresponding ESI imaging in Zeiss-912 was limited to magnification upto 12.5 k. This is because of the high brightness of the field emission gun and lower in-elastic scattering due to high accelerating voltage (200 kV) of electron gun in Zeiss-Libra.

2. Zeiss-Libra which was equipped with STEM unit was useful for the STEM-EDX elemental mapping of O, Si and Mg. Unfortunately the STEM-EDX detector could not detect $B-K_\alpha$ x-rays. Zeiss-912 is not equipped with a STEM unit.

3. The EDX detector in Zeiss-912, was able to detect $B-K_\alpha$ x-rays with a signal to background ratio of 19 and enabled quantitative TEM-EDX analysis of boron. Detector performance was carefully monitored over time and no degradation by ice build-up was detected.

4. In Zeiss-912 carbon contamination of the sample was less in comparison to Zeiss-Libra because of the better vacuum in the specimen chamber of Zeiss-912.

2.3.5   TEM sample preparation

TEM sample preparation for MgB_2 ceramics, wires and tapes:

TEM samples from ceramics, tapes and wires were prepared using the conventional method. 3 mm x 3 mm piece of sample is cut using diamond wire saw or cutter. The sample is then mechanically thinned to about 290 μm thickness using SiC foils and further to about 25 μm thickness using diamond foils of decreasing grain size (30 μm to 1 μm). In the case of tapes, the metal sheaths are polished out exposing the MgB_2 core from both sides.

Further thinning of the sample down to 100 nm thicknesses is achieved by ion etching, using 4 kV Ar^+ ions incident at an angle of 13° to the sample surface in a GATAN Duo Mill or Baltec ion etching machine. Sample is rotated during ion etching to achieve radially symmetric ion thinning. At the end of about 10 hours a hole is formed in the center of the sample. Wedge shaped regions at the boundary of the hole are thin enough (less than 100 nm thickness) to be electron transparent and are used for transmission electron microscopy. Extremely thin samples are essential to avoid the effects of multiple in-elastic scattering during EELS and ESI.

As an example, a detailed stepwise procedure followed during the preparation of multifilamentary tapes is given below. The tape consists of 14 MgB_2/Fe filaments surrounding a copper core embedded in Ni matrix (Figure 2.5(a)).

1. A hexagonal piece of 3 mm diameter is cut out from the tape and glued on a glass plate using yellow wax. The thickness of the tape is about 680 μm which is thinned from one side using SiC foils untill the MgB_2 filaments are just exposed.

2. The sample is then glued on a glass stub (without overturning) using yellow wax and thinned using a Tri-pod holder and diamond foils till about 4 MgB_2 filaments are exposed.

3. The sample is then overturned and glued to a glass plate using yellow wax. It is then thinned till half of the copper core is polished away and the end thickness of the sample is about ~290 μm.

4. The sample and the silicon dummies are then glued on the star holder(without overturning) using white wax and thinned till the same MgB_2 filaments are exposed from the other side and the end thickness of the sample is about 40 μm.

5. An Aluminium ring of 2mm inner diameter is glued to the sample using M-bond and left un-disturbed for about 4 hours till the M-bond hardens. After that sample (together with the star holder) is kept in acetone for about 2 hours. The white wax between the holder and sample is dissolved in acetone and the sample together with the Al ring is detached from the star holder.

6. This sample is then etched in the Duo ion mill for about 10 hours till a tiny hole is formed with its boundary partially going across the Ni-MgB$_2$ interface (Figure 2.14(a)). The thin regions in the MgB$_2$ as well as the MgB$_2$-Ni interface can then be investigated in TEM.

TEM sample preparation for MgB$_2$ single crystals and powders of B, MgH$_2$ and SiC:

Conventional TEM samples cannot be prepared from the MgB$_2$ single crystals because of their small size ~400 μm. TEM powder samples are therefore prepared by crushing about 4 clean single crystals using a mortar in ethanol to produce suspension sub-micrometer sized crystallites. A few drops of this suspension are transferred onto the holey carbon film supported by a copper grid. After about 15 minutes the ethanol is evaporated while the MgB$_2$ crystallites remain attached to the carbon film because of the Van der Waals forces. TEM samples of powders of MgB$_2$, B, MgH$_2$ and SiC can be prepared similarly.

The sample is inserted into the microscope and the positions of thin crystallites lying on the holes in the carbon film(Figure 2.14(b)) are noted. Such crystallites were than used for electron microscopy analysis. This method of sample preparation is rapid, but only a few thin crystallites accidentally lying on the holes in the carbon film can be used for microscopy. Secondly the crystallites showed the tendency of getting contaminated with carbon from the surrounding foil.
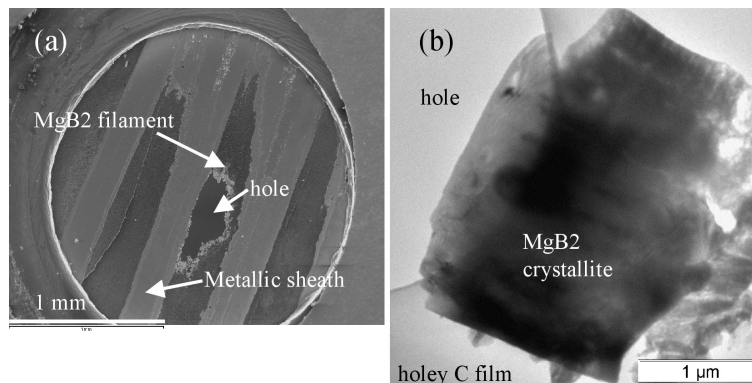

Figure 2.14: (a) SEM images of the TEM samples of MgB$_2$ 14-filament tape and (b) Overview TEM bright-field image of the MgB$_2$ crystalllite on a holey-carbon film.

Chapter 3

3 Application of advanced electron microscopy to MgB$_2$ [109]

3.1 Introduction

Electron microscopy and spectroscopy of MgB$_2$ wires and tapes is challenging because of the following reasons: i) carbon and oxygen contamination artefacts during sample preparation and under the electron beam in microscope ii) low fluorescence yield of B-K$_\alpha$ x-rays iii) B-K$_\alpha$ and C-K$_\alpha$ x-ray peak overlap in EDX iv) preferential absorption of B-K$_\alpha$ x-rays in the sample v) formation of MgB$_2$ colonies and secondary phases (MgB$_{4+x}$, MgB$_{7+x}$, MgSi$_x$O$_y$, and Mg$_2$Si), yielding structural granularity from μm to nm length scale.

Phase analysis is usually done by x-ray diffraction. In Bi(Pb)-2223 superconducting tapes, x-ray phase analysis is of no relevance, because of the strong texture of the matrix and the minimum detectable phase fraction is irrelevantly large. Similarly in the MgB$_2$, x-ray phase analysis is not able to detect B-rich secondary phases like MgB$_4$ and MgB$_7$ due to poor diffracted signals because of the low x-ray atomic scattering factor of B. Also, the spatial distribution of chemical phases cannot be studied using XRD. With rapid developments in the technology of EDX-detectors, digital pulse processors and energy filters, electron beam techniques are able to detect light elements with high signal to background ratio (see for example the TEM-EDX spectra in chapter 4). Chemical mapping techniques like EDX and ESI elemental mapping have become powerful imaging tools in commercial electron microscopes. Therefore electron beam spectroscopy and chemical mapping techniques are suitable for the quantitative chemical analysis of light elements like B, C and O.

Chemical analysis from μm to nm length scales is essential to understand and improve the superconducting properties of wires and tapes. STEM-EDX [89] [106] and ESI [110] chemical mapping was applied to (Bi,Pb)$_2$Sr$_2$Ca$_2$Cu$_3$O$_{10}$ high-temperature superconducting tapes to study the phase formation and microstructure of the final conductors. Unfortunately chemical mapping techniques have not been extensively applied to superconductors, particularly MgB$_2$. So far, SEM-EDX elemental mapping by Pachla et al. [111], STEM-EDX elemental mapping by Hata et al[112] and Yeoh et al. [113], and ESI chemical mapping by Eyidi et al. [8][114] and Sosiati et al. [115] have been reported. Quantitative analysis of MgB$_2$ using EPMA and SEM-EDX is reported in [9][116]. Recently Zhu et al. [117] reported Z-contrast and STEM EDX elemental mapping. EELS analysis of MgB$_2$ has been reported in [118][119][120][121][122][123]. Qualitative TEM-EDX analysis has been reported in [124][116]. A combined SEM, TEM analysis of MgB$_2$ wires and tapes by chemical mapping and quantitative EDX has not been reported previously.

In this chapter the methodology of the advanced electron microscopy and spectroscopy analysis of MgB$_2$ is established by meeting the challenges mentioned above. By advanced electron microscopy we mean a combined SEM and TEM analysis with contamination free sample preparation, chemical mapping with good counting statistics and advanced chemical quantification (Figure 3.1(a), [125]. The methodology was applied to in-situ and ex-situ wires and tapes prepared by different processing techniques. The limitations and strengths (in terms of the spatial resolution and accuracy) of the various electron microscopy methods for the microstructure analysis of MgB$_2$ wires and tapes are discussed. The importance of electron microscopy methods in the understanding of the thermodynamics of phase formation in MgB$_2$ as well as in improving the synthesis technology and the superconducting properties of MgB$_2$ wires and tapes is described.

Depending on the synthesis technology, J$_c$'s of MgB$_2$ wires and tapes differ by orders of magnitude [126]. To understand this large variation of J$_c$, the microstructure of a large number of

MgB$_2$ wires and tapes was systematically studied [126][116][73][127], using the advanced electron microscopy methods and the following microstructure parameters were extracted: 1) MgB$_2$ grain size, 2) oxygen mole fraction, 3) volume fraction of B-rich secondary phases and 4) colony size. Using these microstructure parameters a J$_c$-microstructure correlation model is established which will be presented in chapter 8.
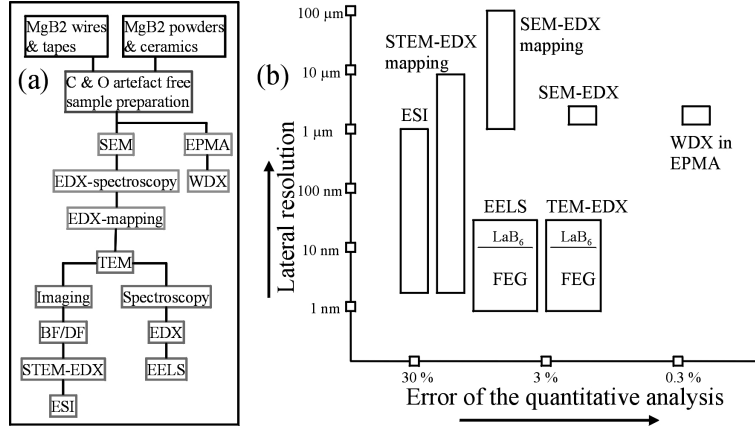

Figure 3.1: (a) Schematic diagram of strategy for the microstructure analysis of MgB$_2$ (b) Lateral resolution and accuracy (in terms of error of the quantitative analysis) for different electron microscopy methods.

3.2   Experimental

The MgB$_2$ wires and tapes were prepared by different variants of the powder in tube (PIT) technique. The deformation technique, precursor powders, annealing temperatures, superconducting transition temperature (T$_c$) , upper critical field (B$_{c2}$) and critical current density (J$_c$) of samples 1-6 are given in Table 3.1. Sample 1 and 2 are ex-situ monofilament wires prepared using a mixture of MgB$_2$ and 1.5 mol. % SiC nano-particles. The deformation was carried out using hydrostatic extrusion (HE) for sample 1 and HE followed by two-axial rolling (TAR) for sample 2. Sample 3 is an in-situ 4-filament wire prepared by RWIT (rectangular wire in tube) technique using a mixture of Mg+ 2B+ 11.3 mol % of SiC with a deformation process similar to that of sample 2 [127][79]. Sample 4 is a commercial, 14-filament, ex-situ MgB$_2$ tape produced over long length scales [116]. Sample 5 is a monofilament tape prepared using a mechanically alloyed [73] mixture of Mg +2B. It may be noted that annealing temperatures in the ex-situ wires are about 300 °C higher than the in-situ wires (~ 650 °C). Sample 6 is prepared by hot isostatic pressing of a ball-milled mixture of MgH$_2$+ 2B+ 6 mol % of SiC.

The T$_c$ was determined by resistivity (ρ) versus temperature (T) measurements. The upper critical field (B$_{c2}$) was determined from the ρ(T) measurements carried out at different magnetic fields. The J$_c$ were measured by transport measurements using the 1 μVcm^{-1} criteria. These measurements were carried out by partner institutes within the HIPERMAG project.

Sample preparation for electron microscopy is described in chapter 2. The names of the electron microscopes are given in Table 3.2 and are described in detail in chapter 2. Acquisition conditions for the electron microscopy are given in detail in section (9.1) of the appendix. The acquisition conditions were optimised to yield large B signal.

Table 3.1: preparation technique, precursor powders, annealing temperature and time, T_c, B_{c2} and J_c for samples 1-6.

#	Synthesis technique	precurosr powder	Ann. Temp. / time	T_c (K)	B_{c2} (T)	J_c (Acm^{-2})
1	HE	MgB$_2$ (aa) +1.5 mol.% SiC	950 °C/ 0.5 h	39.1	14.5	1.29 x 10^4 (@4.2 K & 5 T)
2	HE+TAR	MgB$_2$ (aa) +1.5 mol.% SiC	950 °C/ 0.5 h	38.7	16.0	5.8 x 10^3 (@4.2 K & 5 T)
3	RWIT	Mg (aa) +2B (Geneva) + 11.3 mol.%SiC(aa)	650 °C/ 0.5 h	33.7		1.0 x 10^4 (@4.2 K & 8.9 T)
4	14-filament	MgB$_2$ (Lamia)	980 °C	36.5		2 x 10^5 (@ 20 K & 1 T)
5	MA	Mg (goodfellow)+2B (fluka)	600 °C/ 3 h	36.5		5.5 x 10^4 (@ 20 K & 3 T)
6	HIP	MgH$_2$+2B+6 mol% of SiC	1050 °C/ 2 h			

Notes: HE(Hydrostatic extrusion) [78]; TAR (Two axial rolling) [111]; RWIT(rectangular wire in tube) [79] [127]; 14-filament (see reference [116]); MA (Mechanical Alloying) [73]; HIP (Hot isostatic pressing) ; aa (Alpha Aesar); abcr (ABCR GmbH)

Table 3.2: Intensity of the signal (s) and the relative statistical error (σ) in the quantitative analysis of MgB$_2$ using different electron microscopy methods.

Method	Microscope description	Signal name	s	σ (%)
EPMA-WDX	Jeol Superprobe 8900 RL	B-K$_\alpha$ integrated x-ray cts.	25000	0.6
SEM-EDX	Same as for SEM-EDX mapping	B-K$_\alpha$ integratedx-ray cts.	4820	1.4
TEM-EDX	Zeiss 912 Ω with Si(Li) EDX detector (Oxford), 120 kV	B-K$_\alpha$ integratedx-ray cts.	5300	1.4
SEM-EDX mapping	JEOL 6500F with field emission gun & Si(Li) EDX detector (Oxford)	Mg-K$_\alpha$ x-ray cts per pixel	600	4.1
STEM-EDX mapping	Zeiss Libra 200FE with Si(Li) EDX detector (EDAX), 200 kV	Mg-K$_\alpha$ x-ray cts per pixel	100	10.0
EFTEM-ESI	Same as for STEM-EDX mapping	B-K$_\alpha$ edge intensity per pixel	700	3.8

3.3 Results

Samples 1-3 have been used to study the spatial distribution of secondary phases formed by the addition of SiC in MgB$_2$ wires using chemical mapping in SEM and TEM. Sample 6 is used to determine the minimum detectable mole fraction of carbon in MgB$_2$ using SEM-EDX. Sample 4 is used as a standard sample to establish quantitative analysis of boron using EDX in SEM and TEM (Chapter 4).

3.3.1 SEM EDX elemental mapping and quantitative phase analysis

SE image acquired at 1000x magnification and the corresponding Si SEM-EDX elemental map of the ex-situ sample (sample 1) are shown in Figure 3.2(a, b). While the SE image does not give information about the distribution of Si, the Si-EDX elemental map clearly shows the Si rich and Si deficient regions. SE image of the Si rich region at 5000x magnification and the corresponding Si SEM-EDX elemental map as well as the RGB (Mg-O-B) and RGB(Mg-Si-B) images are shown in Figure 3.2(c-f). From these images three different chemical phases can be identified in the ex-situ sample (sample 1):

1. Pure MgB$_2$ phase: It appears red in the RGB(Mg-O-B) image. It is dark in Si and O elemental maps which indicates that it contains less Si and O. This phase exists in the form of MgB$_2$ colonies; a colony is a dense arrangement of MgB$_2$ grains.

2. B-rich secondary phases: It appears blue in RGB(Mg-O-B) image and dark in Si and O elemental maps.

3. O and Si containing MgB$_2$ matrix: It appears green in RGB (Mg-O-B) image and bright in Si and O elemental maps.

The volume fraction of the pure MgB_2 phase and B-rich secondary phase (determined using the quantitative phase analysis described in (2.2.1) is summarised in Table 3.5.

SE image acquired at 1000x magnification and the corresponding Si SEM-EDX elemental map of in-situ sample (sample 3) are shown in Figure 3.3(a-b). Unlike for the ex-situ wires 1-2 the Si-EDX elemental maps did not show 100 μm sized Si-rich and Si-poor regions in the MgB_2 matrix. The SE image acquired at 5000x magnification and the corresponding Si and C SEM-EDX elemental maps, and the RGB(Mg-Si-B) image are shown in Figure 3.3(c-f). From these images three different chemical phases can be identified in the in-situ sample (sample 3):

1. Mg_2Si secondary phases: It appears yellow in the RGB(Mg-Si-B) image and bright in Si elemental map. They exists in the form of submicrometer to 20 μm long elongated grains (SEM) along the length of the wire.
2. B-rich secondary phases: They appears blue in RGB(Mg-Si-B) image and the grain size lies between submicrometer to about 3 μm.
3. MgB_2 matrix: It appears red in the RGB(Mg-Si-B) image. From the O EDX elemental map not shown here, oxygen was found to be concentrated at the cracks and voids.

The volume fraction of the Mg_2Si and B-rich secondary phases in sample 3 is given in Table 3.6.
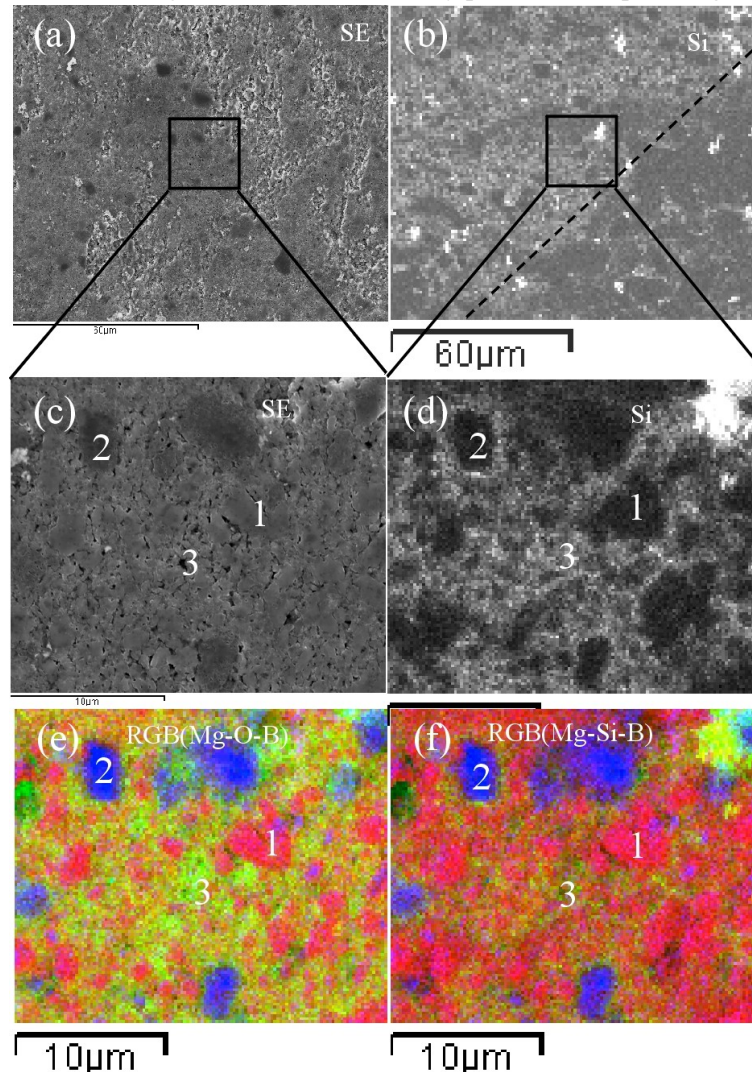
Figure 3.2: sample 1. (a) secondary electron image at 1000x magnification and corresponding (b) Si-EDX elemental map . (c) secondary electron image at 5000x magnification and corresponding (d) Si-EDX elemental map (e) RGB(Mg-O-B) image and (f) RGB (Mg-Si-B) image
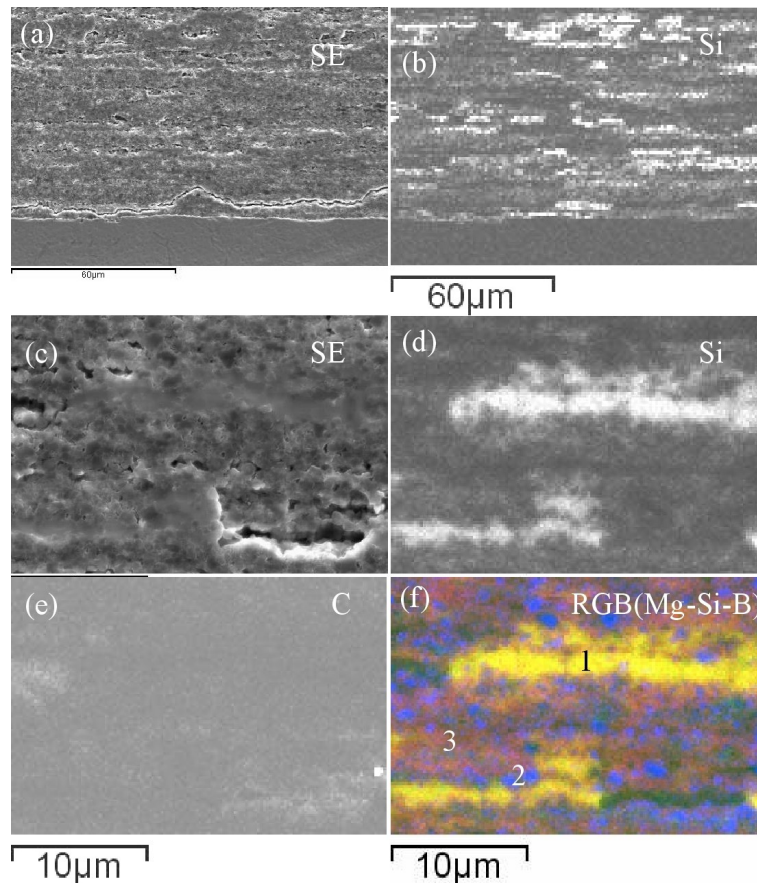
Figure 3.3: sample3. (a) secondary electron image at 1000x magnification and corresponding (b) Si-EDX elemental map. (c) secondary electron image at 5000x magnification and corresponding (d) Si-EDX elemental map (e) C-EDX elemental map and (f) RGB(Mg-Si-B) image.

3.3.2 SEM EDX and EPMA-WDX quantification

A reliable, accurate and standard-based analysis of B by EPMA has been well established [9][10]. A crucial step in the EPMA analysis of B was to use the "area intensity measurement mode" [9]. In this mode, the WDX signal is measured at various positions across the B-K_α peak and the total WDX signal is used for the B quantification. This overcame the difficulties due to B-K_α peak shift and peak shape alterations and simultaneously improved the counting statistics in the B signal.

The EPMA analysis is however time consuming. Therefore, a standard-less, quick and reliable method of B-quantification using EDX in SEM has been established, for the analysis of MgB_2 wires and tapes. The SEM-EDX detector efficiency was calibrated for B-K_α x-rays by the manufacturer [128] using metallic boron as standard. Table 3.3 gives B, O and Mg mole fractions obtained by SEM-EDX and EPMA-WDX measurements on ~ 5 μm large MgB_2 colonies like those in Figure 3.4(a). Due to the modified method of electron microscopy sample preparation SEM-EDX spectra do not contain carbon contamination peak. SEM-EDX measurements carried out on day 1 and after 5 months yield reproducible results which shows the reproducibility of the EDX-detector system. Similar mole fractions were obtained by EPMA, which shows that the SEM-EDX quantification is reliable.

A tilting series was done to show the effect of sample tilt with respect to (towards) the detector. B-K_α x-ray peaks of these spectra after normalisation at the Mg-K_α peak are shown in Figure 3.4(c). The intensity of the B-K_α x-ray peak increases with increasing sample tilt. The tilt could not be incorporated in the quantitative analysis and the B/Mg mole fraction ratios increases with increase in sample tilt. This can be explained by the preferential absorption of low-energy B-K_α x-rays in the specimen. In a tilted sample, the specimen surface is closer to the electron beam-speci-

men interaction volume and greater number of B-K$_\alpha$ x-rays are emitted out of the specimen without being absorbed in the sample, yielding an anomalous increase in the calculated B-Mg mole fraction ratio. For quantitative analysis the amount of sample tilt with respect to the plane perpendicular to the electron beam has to be checked precisely.
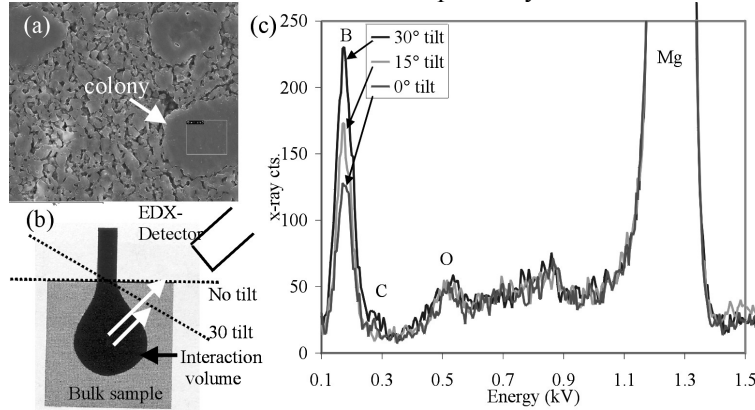
Figure 3.4: (a) Secondary electron image of sample 4, (b) schematic diagram showng x-ray path length in sample for 0 and 30 degree sample tilt and (c) SEM-EDX spectra at different sample tilts (towards the detector)

Table 3.3: Comparison of the SEM-EDX and EPMA-WDX quantification of the MgB$_2$ colonies in sample 4. The tilting was done towards the EDX detector.

	B at.%	O at.%	Mg at.%	B at.% /Mg at.%
SEM-EDX measurements on day 1				
Colony 1	65.21	1.14	33.64	1.94
Colony 2	64.33	1.06	34.61	1.86
Colony 3	65.84	0.74	33.43	1.97
Colony 4	66.8	0.69	32.51	2.05
mean	65.55	0.91	33.55	1.96
SEM-EDX measurements after 5 months				
Colony 5	66.91	0.4	32.69	2.05
Colony 6	67.07	0.87	32.06	2.09
Colony 7	67.16	0.79	32.05	2.10
mean	67.05	0.69	32.27	2.08
EPMA-WDX measurements				
Colony 8	65.87	0.79	33.34	1.98
Colony 9	66.70	0.56	32.75	2.04
Colony 10	66.56	0.15	33.29	2.00
Colony 11	67.49	0.16	32.34	2.09
Colony 12	66.32	0.49	33.19	2.00
mean	66.59	0.43	32.98	2.02
Effect of sample tilt on SEM-EDX quantification				
Tilt 0°	67.16	0.79	32.05	2.10
Tilt 15°	71.45	0.75	27.8	2.57
Tilt 30°	74.58	0.53	24.89	3.00

SEM-EDX spectra acquired from three different places in sample 6 are shown in Figure 3.5 and the corresponding quantitative analysis is given in Table 3.4 which show that Si and C are not distributed homogeneously in the sample. This is used to estimate the minimum detectable mole fraction of carbon in MgB$_2$ for SEM-EDX. Spectrum 1 shows very small Si-K peak and as expected SEM-EDX quantification gives only 0.3 at.% of Si. The C peak is hardly detectable, still the quantification gives 4.2 at.% of C which is a systematic error. The FWHM (Full Width Half Maximum) of the B-K$_\alpha$ peak is about 68 eV (depending on the process time and the objective aperture), while the energy difference between the B-K$_\alpha$ and C-K$_\alpha$ x-ray peaks is 93 eV. B-K$_\alpha$ and C-K$_\alpha$ x-ray peak overlap is therefore unavoidable and in MgB$_2$ samples with trace amounts of C,

some B-K_α x-rays contribute to the C-K_α peak, introducing a systematic error in the carbon quantification. The true C- mole fraction is determined by subtracting this systematic error in C-quantification. In this way, spectrum 3 contains 1.7 at.% of C and the C-K_α peak is just detectable. This then is the minimum detectable mole fraction of carbon in MgB_2 for our SEM-EDX analysis. However, this systematic error is likely to depend on the acquisition parameters like process time and the objective aperture. The relative C mole fraction in a MgB_2 sample with a non-homogenous distribution of C are however accurate, as the systematic error is then automatically subtracted.
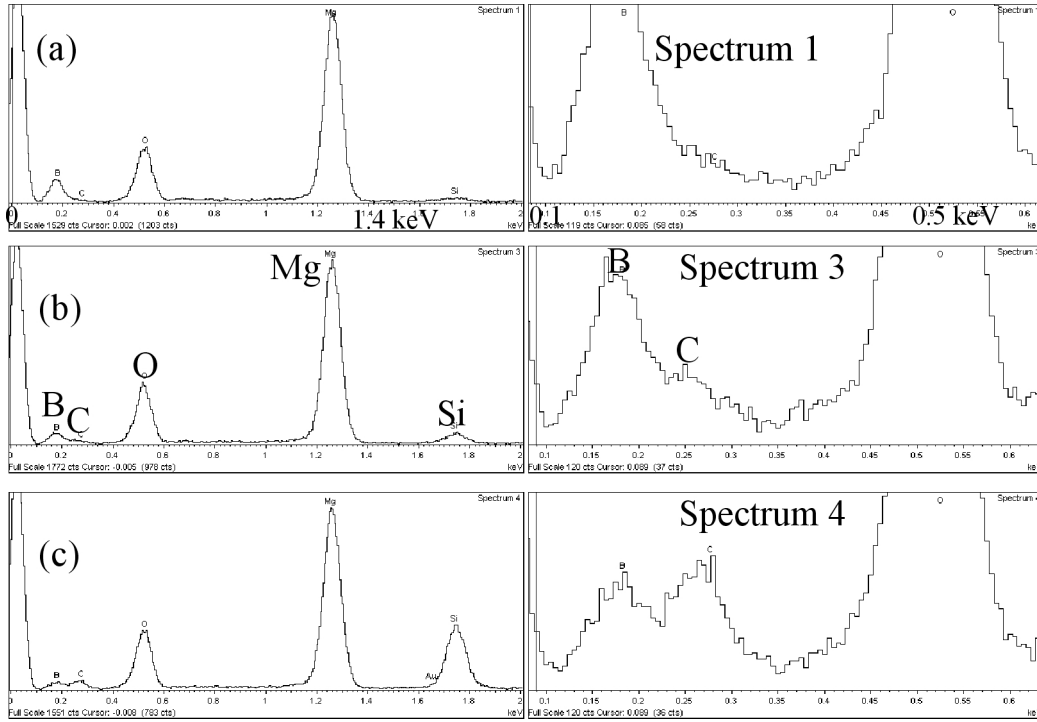
Figure 3.5: Sample 6; SEM-EDX spectra from a hot isostatically pressed in-situ MgB_2 sample with a inhomogenous distribution of Si and C showing (a) 0.3 at.% of Si (b) 1.3 at.% of Si (c) 7.7 at.% of Si. Portion around C-K_α peak is blown up and shown on the right for each spectrum. Dominant elements are marked by bold letters.

Table 3.4: Sample 6; Quantitative analysis of the SEM-EDX spectra shown in Figure 3.5

Spectrum	B at.%	C at.%	O at.%	Mg at.%	Si at.%	corrected C at.%
Spectrum 1	66.0	4.2	14.7	14.8	0.3	0.0
Spectrum 3	53.8	5.9	19.6	19.5	1.3	1.7
Spectrum 4	41.7	13.3	19.7	17.6	7.7	9.1

The quantitative analysis (Table 3.5) of the chemical phases indicated in Figure 3.2 (c-f) of sample 1 (ex-situ) was determined from the SEM-EDX spectra (Figure 3.6) acquired at these phases. The MgB_2 matrix shows B/Mg mole fraction ratio smaller than 2 and contains about 5 at.% of C, 15.6 at.% of oxygen and 1.7 at.% of Si. The pure MgB_2 phase in sample 1 has a B/Mg mole fraction ratio of 2.1. and contains about 3 at.% of carbon and 3 at.% of oxygen. In B-rich secondary phases the B/Mg mole fraction ratio is greater than 5 and contains less than 1 at.% of carbon and about 2 at.% of O. Both the pure MgB_2 phase and the B-rich secondary phase contain less less than 0.2 at.% of Si.

The EDX spectra from the Mg_2Si (region 1 of Figure 3.3(f)), B-rich secondary phases (region 2 of Figure 3.3(f)) and the MgB_2 matrix region similar to region 3 of Figure 3.3(f) of sample 3 (in-situ) are shown in Figure 3.7. The corresponding chemical quantification is given in Table 3.6.

The MgB$_2$ matrix shows a higher B/Mg mole fraction ratio and smaller O mole fraction than in sample 1. The carbon mole fraction (4 at.%) in the MgB$_2$ matrix is significantly higher than in the B-rich secondary phase and Mg$_2$Si secondary phase. In B-rich secondary phases the B/Mg mole fraction ratio is greater than 7. The Mg$_2$Si secondary phases have a Mg/Si mole fraction ratio of 2.2. B-K$_\alpha$ peak is not present in the spectrum from Mg$_2$Si.
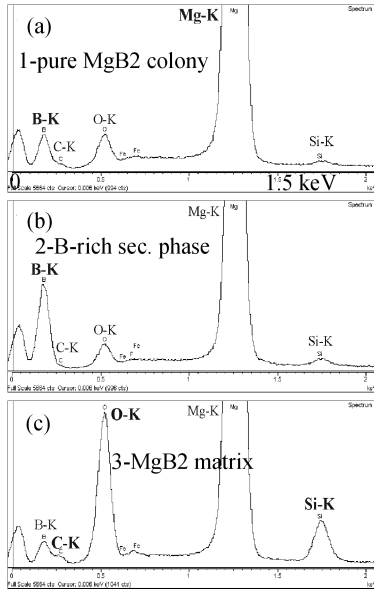

Figure 3.6: sample 1; Representative EDX spectra of phases indexed as 1-3 in Figure 3.2(c), (a) 1- pure MgB$_2$, (b) 2-B-rich secondary phases, (c) 3-O and Si-rich MgB$_2$ matrix. Dominant elements are marked by bold letters.
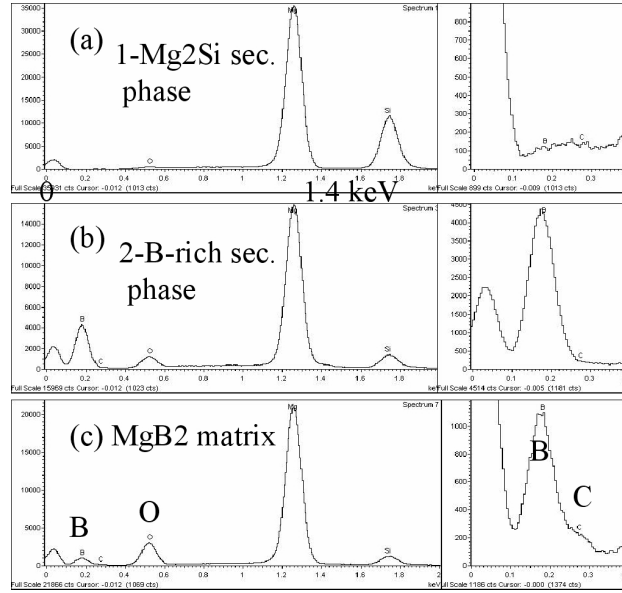
Figure 3.7: sample 3; Representative EDX spectra of phases indexed as 1-3 in Figure 3.3(f), (a) 1- Mg$_2$Si secondary phase, (b) 2-B-rich secondary phases, (c) 3-MgB$_2$ matrix. Portion around B-K$_\alpha$ peak is blown up and shown on the right for each spectrum. Dominant elements are marked by bold letters.

Table 3.5: sample 1; Quantitative analysis of the SEM-EDX spectra shown in Figure 3.6

Phase	B (at %)	C (at %)	O (at %)	Mg (at %)	Si (at %)	Vol. fraction (%)
1-Pure MgB$_2$ (spec. 3)	63.45	3.14	3.08	30.16	0.17	2.6
2-B-rich sec. Phases (spec. 2)	81.46	0.87	2.13	15.35	0.19	1.6
3-O & Si containing MgB$_2$ matrix (spec. 7)	49.3	4.93	15.63	28.45	1.69	

Table 3.6: Sample 3; Quantitative analysis of the SEM-EDX spectra shown in Figure 3.7

Phase	B at.%	C at.%	O at.%	Mg at.%	Si at.%	Vol. fraction (%)
1-Mg$_2$Si (spec 1)	15.93	2.14	1.81	54.7	25.41	5.4
2-B-rich sec. Phase (spec 3)	84.91	1.53	2.93	9.69	0.95	3.7
MgB$_2$	61.96	4.02	11.18	21.34	1.5	

3.3.3   STEM-EDX elemental mapping

The idea for the preparation of the samples 1 and 2 was to introduce SiC in the MgB$_2$ grains as pinning active defects, which would have the scale of the superconducting coherence length. Conventional TEM was applied and the bright-field image (Figure 3.8(a)) was obtained. It shows dense grains and by diffraction their lattice spacings were confirmed to correspond to MgB$_2$.

However, between the grains porous regions are identified, which appear brighter than the grains. Similar to secondary electron images in the SEM these overview images contain no information regarding the chemical composition and phase fractions.

Therefore, chemical mapping with high lateral resolution was done by EDX elemental mapping in the STEM. Figure 3.8(b-f) show STEM dark-field image and the corresponding Mg, O, Si EDX elemental maps and RGB(Mg-O-Si) image of sample 2. The MgB_2 grains appear bright in the Mg elemental map and red in the RGB (Mg-O-Si) image. The grain size of the MgB_2 varies between 200 and 500nm. At the grain boundary Si rich and O-rich phases appear. They show a bright contrast in the Si and O elemental maps and appear blue (Si) and green (O) in the RGB (Mg-O-Si) overlay. The majority of these secondary phases are oxygen rich and not Si rich. Also in pre-characterisation by x-ray diffraction, oxide phases were identified. The size of the Si rich secondary phases is about 50 nm. The chemical composition of these phases was confirmed by the EDX point spectra shown in Figure 3.9.
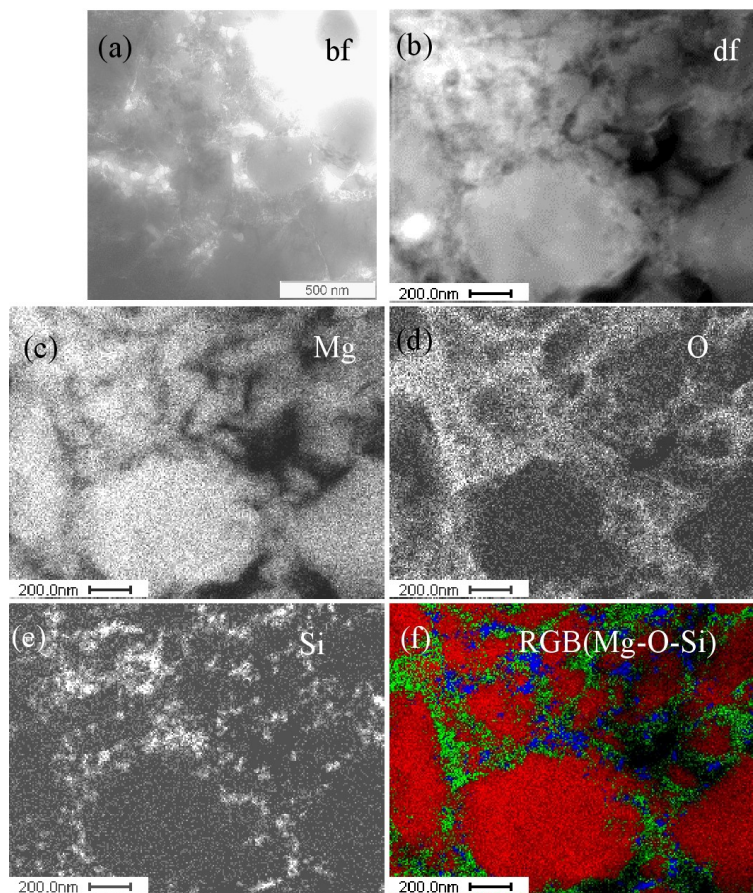
Figure 3.8: Sample 2. (a) Overview TEM-bright-field image. (b) STEM dark-field image, (c-f) Mg, O, Si EDX elemental maps and RGB(Mg-O-Si) image.
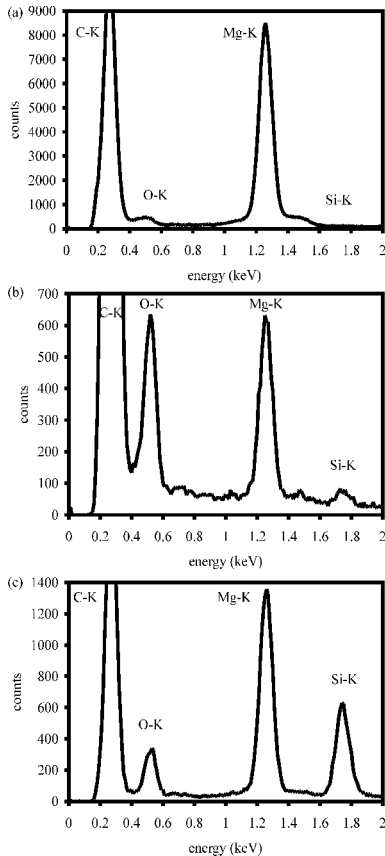
Figure 3.9: sample 2; EDX point spectra acquired in the STEM at (a) MgB$_2$ grains, (b) oxygen-rich secondary phases, presumably MgO and (c) Si and O rich secondary phases (MgSi$_x$O$_y$)
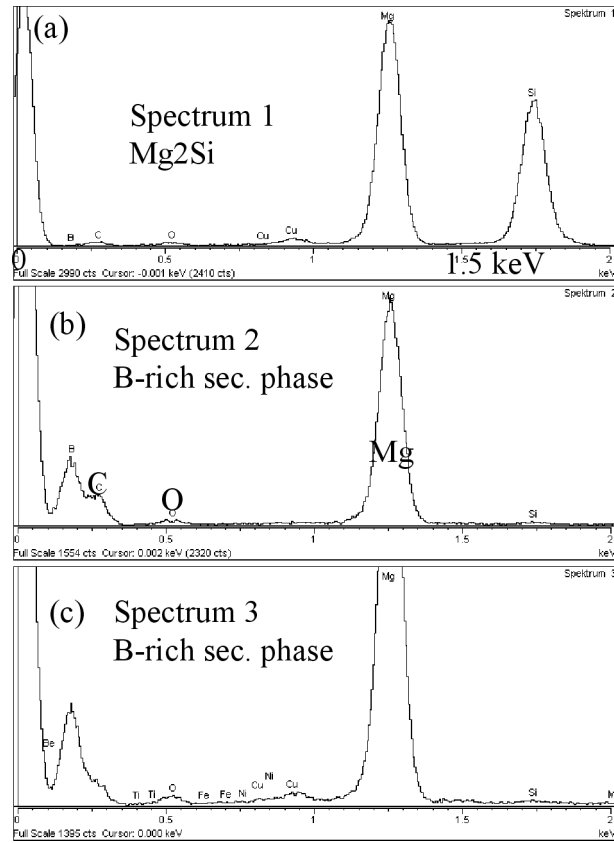
Figure 3.10: sample 3; EDX point spectra acquired in Zeiss-912 at (a) Mg$_2$Si grains, (b-c) B-rich secondary phases(MgB$_4$, MgB$_7$)

3.3.4   EFTEM-ESI elemental mapping

Since the EDX detector used in the STEM (Zeiss-Libra) was not able to fully detect B, it remained open whether the grain boundary phases in sample 2 contained B. For analysing these phases, ESI elemental maps for B, C and O were acquired by "three-window ratio" technique and RGB(B-C-O) images were generated. A TEM bright-field image, corresponding elemental maps and RGB(B-C-O) image are shown in Figure 3.11. It shows the large amount of oxygen rich secondary phases. From the B elemental map it becomes evident that the grain boundary phases contain no or only a small fraction of B.

TEM bright-field image and the corresponding RGB(B-C-O) and RGB(B-Si-O) images of sample 3, acquired by "three-window power law difference technique" in Zeiss-912 are shown in Figure 3.12(a-c). The RGB(B-C-O) image shows B-rich secondary phase of size 200-300 nm. RGB(B-Si-O) image shows Mg$_2$Si secondary phase of size 200-300 nm.

TEM dark-field images, corresponding to the bright field image in Figure 3.12(a) are shown in Figure 3.12(d and f) at two different diffraction conditions. A dark field image of the area marked in Figure 3.12(d) at higher magnification is shown in Figure 3.12(e). They show 20-50 nm large MgB$_2$ grains surrounding the B-rich and Mg$_2$Si secondary phases. The ring in the diffraction pattern shown in the inset was indexed to be due to MgB$_2$. Figure 3.12(f) shows a crystalline Mg$_2$Si secondary phase with grain size of about 400 nm. The spots in the diffraction pattern shown in the inset were indexed to be due to Mg$_2$Si. The chemical composition of these phases was further confirmed by the EDX point spectra shown in Figure 3.10.
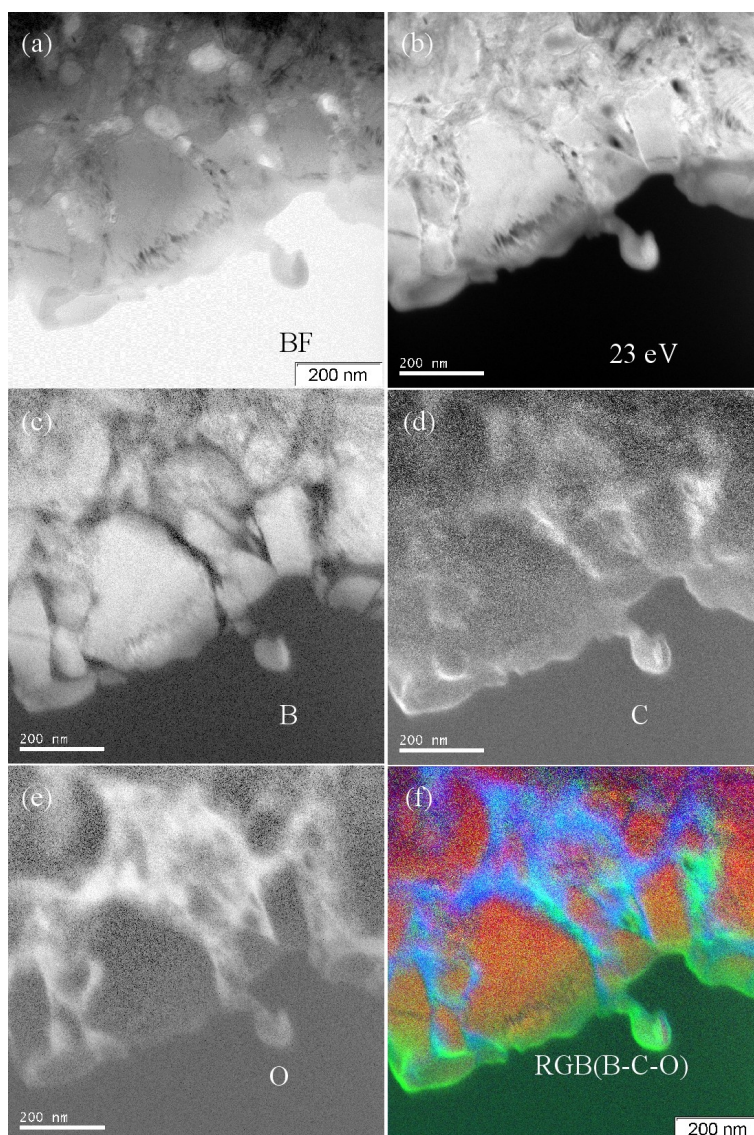
Figure 3.11: Sample 2; (a) Bright-field image, (b) ESI image with an energy loss of 23 eV , (c-e) ESI elemetal maps of B, C and O obtained by three-window ratio technique and (f) RGB (B-C-O) image.
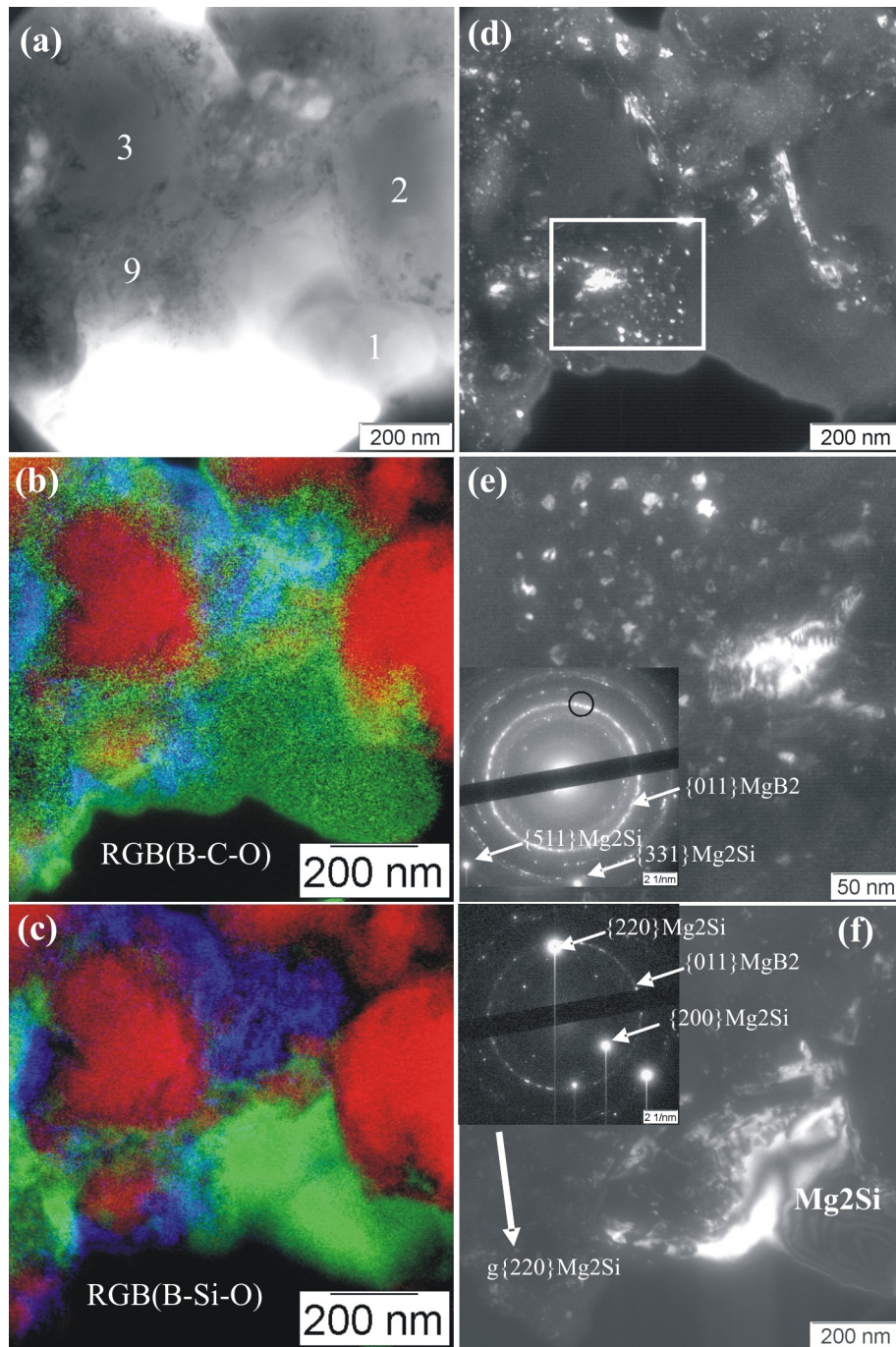
Figure 3.12: Sample 3. (a) TEM bright-field image containing Mg2Si grain (marked as 1) and B-rich secondary phases (marked as 2 and 3), (b-c) the corresponding RGB(B-C-O) and RGB(B-Si-O) images acquired by three-window power law difference technique, (d and f) corresponding TEM dark-field images at two different diffraction conditions. (e) TEM dark field image of the region marked in (d) at higher magnification. The diffraction pattern corresponding to (d) and (e) is shown as inset in (e) and diffraction pattern corresponding to (f) is shown as inset in (f).

3.4 Discussion

3.4.1 Thermodynamics of the phase formation in MgB_2 system

It is well known that understanding and controlling the thermodynamics of phase and microstructure formation is the key for the technology of superconducting materials. The microstructure of

superconducting materials appropriate for applications has to fulfil various requirements, e.g. high density, small grain size, small fraction of secondary phases and distribution of pinning relevant crystal defects. The used precursors [73] and the thermodynamics govern the microstructure evolution.

In MgB_2 the two constituents have very different thermodynamic properties, i.e. melting points, diffusion properties etc. Mg melts at 922 K, and B at 2600 K [129] at 1 bar of pressure. The Mg-B phase diagram and the reaction to MgB_2 today is still far from being well understood [4] [5] [7] and not accurate and specific enough for being used for superconducting materials research. MgB_2 is known to be a line compound [82] and slight variations in stoichiometry yield secondary phases.

The phase diagram of the Mg-Si system is given in [13]. In the Mg rich section (Mg-1.16 at. % Si) the eutectic temperature is at 637.8 °C, i.e. slightly below the melting point of Mg (650 °C).

The chemical phases found in the ex-situ and in-situ MgB_2 samples discussed in this chapter are summarised in Table 3.7. These phases were identified in this work and in our recent papers dealing with these samples [116][73][126][127].

In the ex-situ wires and tapes, O free MgB_2 colonies (a colony is a 3-10 μm large dense arrangement of MgB_2 grains) are embedded in a granular matrix of porous MgB_2 grains (or small MgB_2 colonies) surrounded by oxide layers (Figure 3.2(e) and Figure 3.8(f)). This is found to be a universal feature of all ex-situ MgB_2 samples [116] [126]. In addition small ($< 2\%$) volume fraction of B-rich secondary phases with a composition of $MgB_{4+\delta}$ or $MgB_{7+\delta}$ were also observed (Figure 3.2(e) and Table 3.5). It is not clear at present why these two distinctly different microstructural features (colonies and granular matrix) within one sample are formed and what the reason of the formation of the porous matrix really is? However various oxidation mechanisms like surface oxidation [130] [131] and internal oxidation [114] have been reported in the literature.

In the ex-situ samples with SiC additives, additional 50 nm sized $MgSi_xO_y$ phases are found at the MgB_2 grain boundaries (Figure 3.8)probably formed by the reaction of SiC with the oxide layers around the MgB_2 grains.

In the in-situ samples significant volume fraction (up to 6 % [126]) of B-rich secondary phases is found in the MgB_2 matrix. As reported in section 3.3.2, the B/ Mg mole fraction ratio in the B-rich secondary phases in the in-situ sample, sample 3, is higher than the B-rich secondary phases in the ex-situ sample, sample 1. The oxygen in the matrix of in-situ samples is concentrated at the voids or cracks, probably arising from the oxidation of unreacted Mg on contact with air. These features indicate incomplete formation of MgB_2 phase in the in-situ samples like sample 3. The size and volume fraction of B-rich secondary phases in in-situ samples is found to decrease with increasing annealing temperature [73].

In the in-situ samples with SiC additives, a Mg_2Si secondary phase is formed (Figure 3.3 and Figure 3.12) before the diffusion of Mg into the boron grains to form MgB_2, because the melting point of Mg-1.16 at.% Si is lower than the melting point of Mg. Such a mechanism of Mg_2Si phase formation accompanied by release of free carbon has been recently proposed to explain the substitution of carbon in the MgB_2 lattice in SiC [56] added MgB_2 samples.

Table 3.7: Chemical phases identified by advanced electron microscopy techniques in ex-situ and in-situ MgB_2 wires and tapes.

Ex-situ MgB_2 (sample 4)	Ex-situ MgB_2 with SiC (samples 1, 2)	In-situ MgB_2 (sample 5)	In-situ MgB_2 with SiC (sample 3)
MgB_2 matrix	MgB_2 matrix	MgB_2 matrix	MgB_2 matrix
B-rich secondary phases ($MgB_{4+\delta}$ or $MgB_{7+\delta}$)	B-rich secondary phases ($MgB_{4+\delta}$ or $MgB_{7+\delta}$)	B-rich secondary phases ($MgB_{7+\delta}$)	B-rich secondary phases ($MgB_{7+\delta}$)
Pure MgB_2 colonies	Pure MgB_2 colonies		
Oxide layers in matrix	Oxide and $MgSi_xO_y$ layers in matrix	Oxide layers in matrix	Oxide layers in matrix
			Mg_2Si secondary phase

3.4.2   Relevance and application of the advanced electron beam methods for MgB_2 analysis

The difficulties in the microstructure analysis of MgB_2 superconductors were listed in the introduction and the advanced electron microscopy methods were essential to overcome these difficulties. Advanced electron microscopy involves a combined SEM and TEM analysis with contamination free sample preparation, chemical mapping with good counting statistics and advanced chemical quantification. A schematic diagram of the steps involved in the microstructure analysis of MgB_2 wires and tapes is shown in Figure 3.1(a).

Carbon contamination is a common artefact introduced mainly during sample preparation. It causes serious problems for the boron EDX analysis in MgB_2 samples because of the B and C peak overlap and for C analysis in SiC added MgB_2 wires and tapes. The problem of C contamination was significantly minimized by avoiding the use of organic resin during SEM sample preparation as described in section 2.1.

Because of its high reactivity, any unreacted Mg in MgB_2 wires and tapes is rapidly oxidised on contact with air. To minimise these oxidation artefacts, electron microscopy samples were immediately transferred to electron microscopes after the ion etching by Ar ions.

MgB_2 wires and tapes with small (<1mm) MgB_2 filaments surrounded by metallic sheath did not yield charging during sample analysis. Therefore conducting coating which would have resulted in significant absorption of B-K_α x-rays was not required.

Structural granularity in MgB_2 arises not only from the cracks and voids, but also due to formation of colonies and secondary phases. Chemical mapping techniques are essential to study these phenomena related to thermodynamics.

The lateral resolution and the accuracy (in terms of the error in the quantitative analysis) of the different electron microscopy techniques is given in Figure 3.1(b). The accuracy in the quantitative analysis is based on the statistical error in the MgB_2 analysis (Table 3.2). It is seen from Figure 3.1(b) that an accurate chemical analysis of MgB_2 wires and tapes on different length scales is not possible with a single electron microscopy technique and therefore a combination of electron microscopy techniques is essential.

The SEM-EDX elemental maps allow to study the chemical phases on the scale of 100 to 1 μm (The spatial resolution of the SEM-EDX elemental maps is about 1 μm). Since a significant cross-section of the MgB_2 filament is covered by such an analysis, volume fraction of the different chemical phases can be estimated, which is representative of the entire MgB_2 filament. SEM-EDX elemental maps, especially those of B are noisy because of the low x-ray counts per pixel. On an average about 20 B-K_α and 600 Mg-K_α x-ray counts per pixel are obtained for an acquisition time of about 1000 s, which corresponds to a statistical error of 22.5 and 4 % respectively. Nevertheless, it is seen from Figure 3.2 and Figure 3.3 that SEM-EDX elemental maps are suitable for the qualitative analysis of the spatial distribution of various secondary phases.

SEM-EDX point spectra have to be acquired for the precise chemical analysis of the different chemical phases identified by SEM-EDX elemental mapping. For a acquisition time of 2 minutes about 5000 B-K_α x-ray counts are obtained which corresponds to a statistical error of only 1.4 %. The quantitative analysis is carried out using an XPP [132] matrix correction approach based on the phi-rho-z method [88], and is particularly suitable for the analysis of light elements. The MgB_2 matrix as well as the Mg_2Si and B-rich secondary phases listed in Table 3.7 were investigated by SEM-EDX analysis.

SEM- EDX analysis is however not suitable for the quantitative analysis of chemical phases smaller than about 2 micrometer because of its limited spatial resolution. For example SEM-EDX cannot be used to identify the sub-micrometer sized oxide phases in the MgB_2 matrix of ex-situ wires and tapes described in section 3.1.

EDX analysis in TEM is required for the analysis of MgB_2 wires and tapes on the nm scale. Since the TEM samples are less than 100 nm thick, the beam spreading in the samples is small. The spatial resolution of STEM-EDX spectroscopy and elemental mapping is therefore drastically improved in comparison to SEM-EDX [86]. From the STEM-EDX elemental maps in Figure 3.8, it was possible to identify the Si and O rich secondary phases at the MgB_2 grain boundaries. The counting statistics in the STEM-EDX elemental maps is however poor in comparison to SEM-EDX elemental maps. For an acquisition time of 14 minutes, which is comparable to the acquisition time of SEM-EDX elemental map, only 100 Mg x-ray counts per pixel (CPP) are obtained, which corresponds to a statistical error of 10 %. The CPP would be an order of magnitude lower for the TEM-EDX elemental maps of light elements like B, C and O and in our case the STEM-EDX detector could not detect the B-K_α x-rays.

For light elements, it was advantageous to acquire ESI elemental maps (Figure 3.11) which require very short acquisition times (2 s for B and C, and 3.2 s for O). For Mg, ESI elemental mapping using Mg-K_α edge usually yields a poor signal, while use of Mg-L23 edge (52 eV) leads to artefacts due to overlap with multiple inelastic plasmon (19 eV) scattering. The noise in the elemental maps of B, C, O obtained by "three-window difference" difference technique arose mainly because the maximum CPP in the ESI images acquired with CCD camera was limited to about 10000. After the background subtraction, a significantly lowered count rate of about 1000 CPP is obtained in the B elemental map at a distance of about 200 nm from the edge of the sample which corresponds to a statistical error of only 3.8 %. However, the background subtraction in ESI elemental maps introduces significant additional systematic error. ESI elemental mapping is restricted to thin regions of the sample because of the effects of multiple scattering. Therefore a combination of these complementary techniques -STEM-EDX for Mg elemental mapping and ESI for B, C and O elemental mapping- is essential for a reliable analysis of MgB_2 superconductors.

The effects of multiple inelastic scattering can be minimised by using higher accelerating voltage, and the signal can be enhanced by using TEM, equipped with field emission gun which has high brightness. Zeiss-Libra TEM which is equipped with a 200 kV field emission gun, was able to obtain ESI images of magnification greater than 50k (Figure 3.11), while magnification in the ESI images acquired by Zeiss-912 were limited to 12.5 k (Figure 3.12).

3.4.3   Importance of advanced electron beam techniques for the improvement of synthesis technology

Generally, the following synthesis parameters are systematically varied to enhance the J_c of MgB_2 wires and tapes.

1. Precursor powders (including additives like SiC, carbon nano-tubes, nano-carbon, nano diamond, etc.) of different quality, grain size, and stoichiometry
2. Thermodynamic parameters like annealing temperature, annealing time and cooling conditions
3. Deformation techniques like rolling, swaging, drawing, extrusion
4. Sheath material like Fe, Nb, Ti.

5. Conductor designs like 14-filament configuration, 4-filament configuration etc. with provisions for thermal stability [116].

In the process, a large number of samples have to be prepared and investigated for superconducting properties and microstructure. Many of the microstructure features relevant for the synthesis technology are on the micrometer scale and can be efficiently studied by SEM analysis which includes SE imaging, EDX elemental mapping and EDX spectroscopy. Additionally SEM analysis is less demanding in terms of efforts and time and thus suitable for the analysis large number of samples.

The chemical phases in ex-situ sample 1 and in-situ sample 3, identified from the SEM-EDX elemental maps and SEM-EDX spectra in section 3.1 and 3.2 are summarised in Table 3.7 In the ex-situ samples (sample 1) Si rich phase is found to be inhomogenously distributed on the scale of 100 micrometer. In in-situ sample (sample 3) Mg_2Si secondary phases with a size upto 20 μm are found with an volume fraction of 5.4%. Such an information of the spatial distribution of chemical phases gives hints about the ways to optimise the synthesis parameters like annealing temperature, annealing time, precursor powder quality etc.

3.4.4 Importance of advanced electron beam techniques for the understanding and improvement of superconducting properties

The superconducting properties of MgB_2 wires and tapes are influenced by i) Structural granularity from micrometer to nanometer length scale caused by cracks, voids and secondary phases, ii) carbon doping and iii) flux pinning crystal defects. These microstructure features can be uniquely studied using the advanced electron microscopy techniques described in section 3.4.2, which is essential to understand and improve the superconducting properties of MgB_2 wires and tapes. A J_c -microstructure correlation model is established to explain the large variation of J_c of MgB_2 wires and tapes, which will be presented in chapter 8.

The importance of SEM analysis on the micrometer scale, in understanding the technological aspects of MgB_2 wires an tapes was discussed in the previous section. These microstructure features in turn influence its superconducting properties. For example, the elemental maps (Figure 3.2) and SEM-EDX spectra (Figure 3.6) of sample 1 (ex-situ sample) show pure MgB_2 colonies embedded in a granular MgB_2 matrix rich in O. Increasing the volume fraction of MgB_2 colonies, which are dense, pure and constitute a well formed MgB_2 phase, would increase the J_c of ex-situ wires like sample 1. In-situ sample (sample 3) shows a significant (3.7 %) volume fraction of B-rich secondary phases (Figure 3.3). J_c in a in-situ wire like sample 3 can be improved by reducing the phase fraction of B-rich secondary phases, leading to complete formation of well connected MgB_2 phase. The J_c of in-situ samples with SiC can also be improved by dispersing the Mg_2Si phase (Figure 3.3) in the form of nano-inclusions to act as pinning centres [124].

The lack of correlation between Si and C SEM-EDX elemental maps (Figure 3.3) and SEM-EDX spectra (Figure 3.7) of sample 3 (in-situ wire with SiC additives) indicates that almost the whole of Si is consumed by Mg_2Si secondary phases, while the C is homogenously distributed in the MgB_2 lattice. The decrease in T_c of sample 3 because of the possible C doping[133] [56] is thus understandable. However, a clear evidence for the co-substitution of Si (together with C) into the MgB_2 lattice was not found. Co-substitution of Si was proposed by Dou et al. [124] to explain the reduced effect of SiC doping on T_c suppression. Carbon doping is known to enhance the B_{c2} of MgB_2 [63] [134], which in turn can enhance the J_c.

Microstructure features on the scale of coherence length of MgB_2 (~10 nm) can be studied using TEM. These features have a direct influence on the superconducting properties of MgB_2. For example the 50 nm wide non superconducting $MgSi_xO_y$ phases at MgB_2 grain boundaries in sample 2, identified in the STEM-EDX elemental maps and ESI maps in section 3.4, yield poor connectivity between grains which limits the J_c of this sample. Crystal defects like grain boundaries, dislocations and precipitates, can be determined from the diffraction contrast imaging in TEM. For example, the TEM dark field images show MgB_2 grains with a size of 50-250 nm in sample 2 (Figure 3.8.) and 20-50 nm in sample 3 (Figure 3.12(e)) These crystal defects have been

reported to enhance the J_c of MgB_2 wires and tapes, due to enhanced pinning [116],[73],[126] [124].

3.5   Summary and conclusions

Methodology of quantitative microstructure analysis of MgB_2 wires and tapes is described which is essential to understand and improve their superconducting properties. Quantitative microstructure analysis of MgB_2 is challenging because of the boron analysis, carbon and oxygen contamination, and structural granularity from the μm to nm scale arising not only from porosity but also from the formation of large number of secondary phases. These difficulties have been overcome by using advanced electron microscopy which involves, combined SEM and TEM analysis with artefact free sample preparation, chemical mapping and advanced chemical quantification. Chemical maps were obtained by using SEM-EDX, TEM-EDX or ESI in EFTEM. Considering the low fluorescence yield of B-K_α x-rays, SEM-EDX acquisition conditions were optimised to obtain maximum B-K_α x-ray counts. The absorption of B-K_α x-rays in the specimen during TEM-EDX was corrected using a parameterless method to be described in chapter 4.

The methodology was applied to in-situ and ex-situ MgB_2 wires with and without SiC additives. Ex-situ wires show oxygen-free MgB_2 colonies (a colony is a dense arrangement of several MgB_2 grains) embedded in a porous and oxygen-rich matrix. In comparison, in-situ wires are generally more dense, but show inhibited MgB_2 phase formation with significantly higher fraction of B-rich secondary phases. SiC added MgB_2 wires contained additional secondary phases. In the ex-situ wires Si was found to be in-homogeneously distributed in the granular matrix from the 100 μm and 1 μm scale. On the nanometer scale Si and O were found in the 50 nm layers along the MgB_2 grain boundaries. In the in-situ wires most of the Si was found in the form of Mg_2Si secondary phases while carbon was homogeneously distributed in the MgB_2 matrix, which suggests the substitution of C into the MgB_2 lattice.

Such an advanced electron microscopy and spectroscopy analysis is helpful in understanding the thermodynamics of the phase formation in MgB_2 and helps in improving the synthesis technology by optimising the synthesis parameters like annealing temperature, annealing time and the precursor powder. The advanced electron microscopy techniques have been used to extract the following microstructure parameters like MgB_2 grain size, oxygen mole fraction, volume fraction of B-rich secondary phases and colony size which are essential in establishing a correlation between the microstructure and superconducting properties like T_c, B_{c2} and J_c (see chapter 8). In summary, it was demonstrated in this chapter that, conventional secondary electron imaging and diffraction contrast imaging alone are by far not sufficient and advanced electron microscopy and spectroscopy methods are essential for the analysis of superconducting MgB_2 wires and tapes.

Chapter 4

4   Quantitative TEM-EDX analysis of Boron

4.1   Introduction

Superconducting materials like MgB_2, YBCO [135], Bi-2223, contain light elements like B, C, O. Quantitative analysis of light elements is therefore essential to understand and improve the microstructure and superconducting properties (T_c, Bc_2, J_c) of these materials.

TEM-EDX has a good lateral resolution, comparable to the size of the electron beam (about 10 nm) and unlike EELS, is relatively straightforward to use. TEM-EDX analysis in combination with other imaging techniques like diffraction contrast imaging, STEM-EDX mapping and ESI mapping turns out to be very useful for the microstructure analysis of materials like MgB_2 which contain light elements and many secondary phases.

Quantitative TEM-EDX analysis is challenging mainly because of the preferential absorption of light element x-rays in the TEM sample. In this chapter various methods of absorption correction are briefly summarised and then applied for the quantitative TEM-EDX analysis of B in MgB_2.

4.2   Principles of Quantitative analysis using TEM-EDX

4.2.1   Cliff-Lorimer ratio technique

For TEM-EDX, absorption and fluorescence effects can be neglected in many cases and the quantitative analysis is usually carried out using the Cliff-Lorimer equation (chapter 35 of [96])

$$\frac{C_A}{C_B} = k_{A-B} \frac{I_A}{I_B} \ldots \ldots (4.1),$$

where, C_A and C_B are the wt. fractions of elements A and B, and I_A and I_B are the measured characteristic x-ray intensities of elements A and B. k_{A-B} is the Cliff-Lorimer factor.

The Cliff-Lorimer factor k_{A-B} is related to the atomic number correction factor Z of the x-ray microanalysis of bulk samples (see section 2.2.2 and p. 610 of [96]). k_{A-B} can be calculated theoretically using,

$$k_{A-B} = \frac{Q_B \omega_B a_B \varepsilon_A}{Q_A \omega_A a_A \varepsilon_B} \ldots \ldots (4.2),$$

where, Q is the ionisation cross section, ω is the fluorescence yield of characteristic x-rays, a is the relative probability for the K_α transition and ε is the EDX detector efficiency for characteristic x-rays of elements A and B written as subscripts A and B in each case. The ionisation cross sections and the detector efficiencies cannot be determined accurately. As a result calculated values of k_{A-B} can have inaccuracies up-to 20% relative [96]. Accurate values of Cliff-Lorimer factors are therefore determined experimentally by measuring (I_A/I_B) of a standard sample for which (C_A/C_B) is known.

During TEM-EDX analysis of light elements significant preferential absorption of light element x-rays occurs, which needs to be corrected. The Cliff-Lorimer equation suitable for light element analysis is,

$$\frac{C_A}{C_B} = k_{A-B} \frac{I_{A0}}{I_{B0}} \ldots \ldots (4.3),$$

where I_{A0} and I_{B0} are absorption corrected x-ray intensities.

In principle I_{A0} can be calculated from I_A. Consider the schematic diagram (Figure 4.1) of the sample – EDX detector geometry in the TEM. Sample of thickness t is tilted by angle α with respect to the normal to the optic axis and the detector take-off angle is β. The x-rays are emitted throughout along the electron beam path of length z in the sample, some of which are collected by the EDX detector. The following relation holds,

$$I_A = I_{A0} \frac{\int_{t=0}^{t=t} \exp(-(\sum_i \rho c_i \mu_i) t f) dt}{t} = I_{A0} \frac{1 - \exp(-(\sum_i \rho c_i \mu_i) t f)}{(\sum_i \rho c_i \mu_i) t f} \quad ......(4.4),$$

where C_i is the wt. fraction of element i, ρ is the density of the sample, μ_i is the mass absorption coefficient in $cm^2 g^{-1}$ of element i for x-rays from element A, t is the specimen thickness in cm, and $f = 1/\sin(\alpha+\beta)$ is the geometry factor which on multiplying with t yields x-ray path length in the sample. I_{B0} can be calculated similarly and equation 4.3 can be written as

$$\frac{C_A}{C_B} = k_{A-B} \frac{I_A}{I_B} ACF ......(4.5),$$

where, Absorption correction factor (ACF) is given by,

$$ACF = \frac{(\sum_i \rho c_i \mu_i)^A t f [1 - \exp(-(\sum_i \rho c_i \mu_i)^B t f)]}{(\sum_i \rho c_i \mu_i)^B t f [1 - \exp(-(\sum_i \rho c_i \mu_i)^A t f)]} .....(4.6).$$

In practice the calculation of ACF as described above is inaccurate because t cannot be determined accurately and values of μ_i reported in the literature, specially of light elements, might be inaccurate [136]. Therefore parameterless methods of absorption correction have been proposed which do not require the explicit knowledge of t and μ_i, and are described in the next sections.
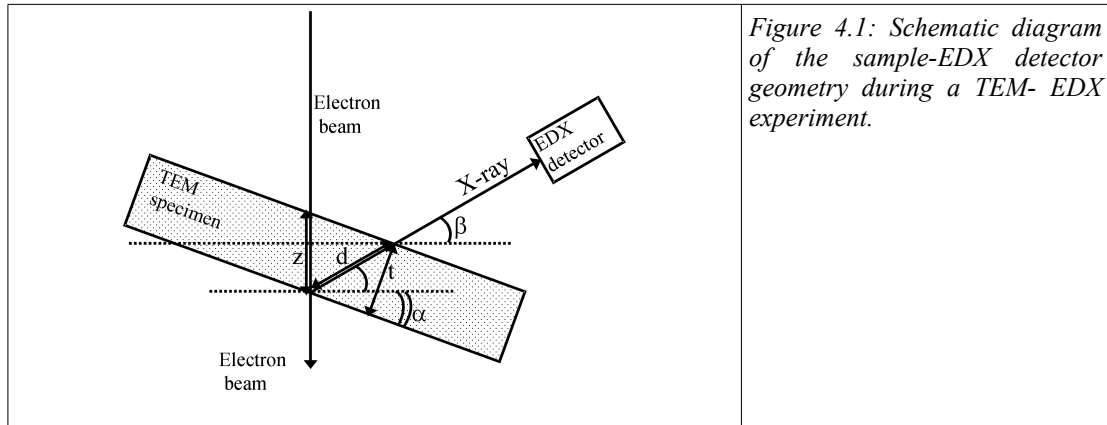
Figure 4.1: Schematic diagram of the sample-EDX detector geometry during a TEM- EDX experiment.

4.2.2   Parameterless methods of x ray absorption correction in TEM samples

4.2.2.1   Horita et al's method:

A parameterless method was given by Horita et al. [137] by using the approximation that all the x-rays are generated at one-half of the sample thickness, which yields the following simplified relation between the measured x-ray intensity ratio (I_A/I_B) and absorption corrected x-ray intensity ratio (I_{A0}/I_{B0}):

$$\frac{I_A}{I_B} = \frac{I_{A0}}{I_{B0}} \exp\left(-[(\sum_i \rho c_i \mu_i)^A - (\sum_i \rho c_i \mu_i)^B] t f \right) ......(4.7).$$

Taking the logarithms on both sides of the above relation gives,

$$\log \frac{I_A}{I_B} = \log \frac{I_{A0}}{I_{B0}} + (constant)\, t \,......(4.8).$$

The thickness t in the above equation can be replaced by the intensity (I_R) of one of the high energy x-rays emitted by the sample, which is proportional to t.

About 10 different EDX measurements are made either at areas of different thickness or, at the same area but with different sample tilt. The absorption corrected x-ray intensity ratio I_{A0}/I_{B0} is obtained by plotting log I_A/I_B versus I_R, and extrapolating the graph to $I_R = 0$. No explicit thickness measurement is required. However it is essential that the specimen is homogenous and the beam current remains constant during about 10 EDX measurement that are required to draw log I_A/I_B versus I_R plots.

4.2.2.2   *Eibl's method:*

Another parameterless method was given by Eibl [138][136][139]. A transmission coefficient was defined as the ratio of the intensity measured with absorption switched on divided by intensity measured with absorption switched off:

$$T_A(t) = \frac{I_A}{I_{A0}} = \frac{intensity\,with\,absorption\,on}{intensity\,with\,absorption\,off} = \frac{1 - \exp(-(\sum_i \rho c_i \mu_i)^A t f)}{(\sum_i \rho c_i \mu_i)^A t f} \,...(4.9).$$

In a distance defined as x-ray absorption length (XAL):

$$XAL = 1/(\sum_i \rho c_i \mu_i)^A \,......(4.10),$$

the characteristic x-ray intensity of element A is reduced by a factor of 1/e. A small XAL means more x-ray absorption in the sample.

When written in units of XAL, the magnitude of the x-ray path length in the sample is given by,

$$d = t\, f\, (\sum_i \rho c_i \mu_i)^A \,......(4.11),$$

and the transmission coefficient function becomes

$$T(d) = \frac{1 - \exp(-d)}{d} \,......(4.12).$$

As pointed out by Eibl [138], this change of unit enables a material independent understanding of the x-ray absorption.

Experimental procedure for acquiring TEM-EDX spectra is similar to that in Horita's method. Two EDX measurements with x-ray path lengths d_1 and d_2 are made either at areas of different thickness or at the same area but with different sample tilt.

The transmission coefficients for the x-ray path lengths (d_2) and (d_1) cannot be determined experimentally because the x-ray intensity with no absorption (I_{A0}), cannot be determined experimentally. But, if there exist a high energy x-ray of intensity (I_R), which is negligibly absorbed in the sample, then $I_{A0} \propto I_R$, and the ratio between the transmission coefficients for x-ray path lengths (d_2) and (d_1) can be determined from the measured x-ray intensities for the x-ray path lengths d_2 and d_1 respectively. Therefore,

$$\left[\frac{T(d_2)}{T(d_1)} \right]_{exp} = \frac{(I_{A2})/(I_{A02})}{(I_{A1})/(I_{A01})} = \frac{(I_{A2})/(I_{R2})}{(I_{A1})/(I_{R1})} \,......(4.13),$$

is determined experimentally. This is the most important idea of the Eibl's method.

Additional experimental information is used to express d_2 in terms of d_1,

$$d_2 = K\, d_1 \,......(4.14).$$

In the case of EDX spectra acquired at different sample tilts, the geometrical relationship between the d_2 and d_1 is used to determine K. In the case of EDX spectra acquired at different thicknesses, relative thicknesses obtained by acquiring zero-loss EELS spectra are used to determine K In case a constant-current electron beam is available, no additional experiment is required and the intensity I_R, itself can be used to determine K.

From equation 4.12 and 4.14 we get

$$\left[\frac{T(d_2)}{T(d_1)}\right]=\frac{1}{K}\frac{1-\exp(-Kd_1)}{1-\exp(-d_1)} \quad ......(4.15).$$

By equating equation 4.13 and 4.15 one gets

$$\frac{1}{K}\frac{1-\exp(-Kd_1)}{1-\exp(-d_1)}=\frac{(I_{A2})/(I_{R2})}{(I_{A1})/(I_{R1})} \quad ......(4.16),$$

which can be solved numerically to obtain d_1. d_2 is then obtained from equation 4.14. Transmission coefficients and absorption corrected x-ray intensities are then obtained using equations 4.12 and 4.9.

Eibl's method has the following advantages in comparison to Horita et al's. Method.

(i) Eibl's method uses an accurate expression (equation 4.12) for transmission coefficient. Horita et al. on the hand assume that all the x-rays produced at the middle of the specimen which is equivalent to using the following approximation for transmission coefficient,

$$\frac{1-\exp(-d)}{d} \approx \exp(-d/2)......(4.17).$$

(ii) Eibl's method unlike Horita et al's method does not require constant electron beam current.

(iii) Eibl's method, unlike that of Horita et al's does not require background subtraction as the background is cancelled out in the ratio of $(I_A/I_R)_1$ and $(I_A/I_R)_2$.

4.2.3   Zeta factor method

In the Eibl's and Horita et al's method , the quantitative analysis, after absorption correction is carried out using Cliff-Lorimer equation (equation 4.3). Recently a new zeta-factor method [140], with an in-built absorption correction, has been proposed. Explicit measurement of sample thickness is not required.

In a thin film sample, the characteristic x-ray intensity, I_A can be assumed to be proportional to mass-thickness (ρt), wt. Fraction of element A (C_A) and the electron dose (D_e). Therefore one can write,

$$\rho t=\zeta_A\frac{I_A}{C_A D_e}......(4.18),$$

where, ζ_A is the proportional factor and is called zeta factor for characteristic x-rays of element A. Similarly,

$$\rho t=\zeta_B\frac{I_B}{C_B D_e}......(4.19).$$

From equations 4.18 and 4.19 and assuming binary system where $C_A + C_B =1$, one gets

$$\rho t=\frac{\sum_{j=A,B}\zeta_j I_j}{D_e};\quad C_A=\frac{\zeta_A I_A}{\sum_{j=A,B}\zeta_j I_j};\quad C_B=\frac{\zeta_B I_B}{\sum_{j=A,B}\zeta_j I_j}......(4.20),$$

which are taken to be initial values.

The absorption correction is integrated as per equation 4.4, by using the mass absorption coefficients from the literature and the initial values of ρt, C_A and C_B obtained in equation 4.20 to yield the absorption corrected values,

$$\rho t = \frac{\sum_{j=A,B} \zeta_j I_j / T_j}{D_e}; \quad C_A = \frac{\zeta_A I_A / T_A}{\sum_{j=A,B} \zeta_j I_j / T_j}; \quad C_B = \frac{\zeta_B I_B / T_B}{\sum_{j=A,B} \zeta_j I_j / T_j} \quad ......(4.21),$$

where, T_j is the transmission coefficient defined in equation 4.9. Further refinement is done by iteration.

Zeta factors are obtained by applying equation 4.18 to standard thin film sample of pure element or multielement samples for whom the absorption and fluorescence effects can be neglected.

Major advantages of zeta factor method are

(i) Zeta factors are easier to determine than Cliff-Lorimer factors because pure element thin films can be used as standards. Pure element thin films are easy to synthesize and their compositon does not change during thinning to electron transparency or as a result of beam damage. Additionally x-ray absorption in pure-element standards is small and can be neglected.

(ii) The absorption corrected composition and the mass thickness can be obtained simultaneously in a single measurement.

Disadvantages of zeta factor method are,

(i) measurement of electron dose is a prerequisite. However, many TEMs including the one used in this work are not equipped with a Faraday cup to measure the electron dose.

(ii) Mass absorption coefficients are still required, which specially for light element x-rays might not be known sufficiently accurately.

4.3   Experimental

Quantitative TEM-EDX analysis of MgB_2 samples was carried out using Zeiss 912Ω TEM (see chapter 2), equipped with an Si(Li) EDX detector (Oxford Instruments) with ultra-thin window (ATW2). Schematic diagram of the EDX detector - sample in TEM is shown in Figure 4.1. The sample is normally tilted by 20 degrees (angle α) towards the detector to minimise the x-ray path length in the sample. Other acquisition parameters like, acquisition time, spot size, process time are given in Table 9.6. The EDX spectra were acquired and quantitatively evaluated using INCA software.

Sample 4 and 5 of chapter 3 have been selected for the TEM-EDX analysis. Sample 4 has a homogenous and stoichiometric chemical composition, as shown by SEM and EPMA analysis (Chapters 3 and 6), and is therefore used as a standard. Sample 5 is used as an experimental sample of unknown composition. The synthesis of these sample was described in chapter 3. TEM samples for EDX analysis were prepared by conventional method described in chapter 2.

4.4   Results

A series of TEM-EDX spectra were acquired at positions of increasing sample thickness, indicated in the bright-field image (Figure 4.2 (a)) of a colony of standard sample 4 with a known chemical composition [116]. B-K_α x-ray peaks of these spectra, after normalisation at the Mg-K_α peak are shown in (Figure 4.2 (b)). The height of the B-K_α x-ray peak decreases with increasing sample thickness because of the preferential absorption of the B-K_α x-rays in the sample. Similarly the decrease in I_B/I_{Mg} (Table 4.2) with increase in sample thickness in grain 7 and 8 of sample 5 indicates preferential absorption of B-K_α x-rays.

The absorption correction was carried out by parameterless method of Eibl discussed in 4.2 by using a matlab script given in section (9.2.3). The ratios of the B-K_α peak to Mg-K_α peak in-

tensity $(I_B/I_{Mg})_0$ for the standard sample 4 and sample 5, after correcting for the absorption of B-K_α x-rays, are given in Table 4.1. and Table 4.2 respectively.
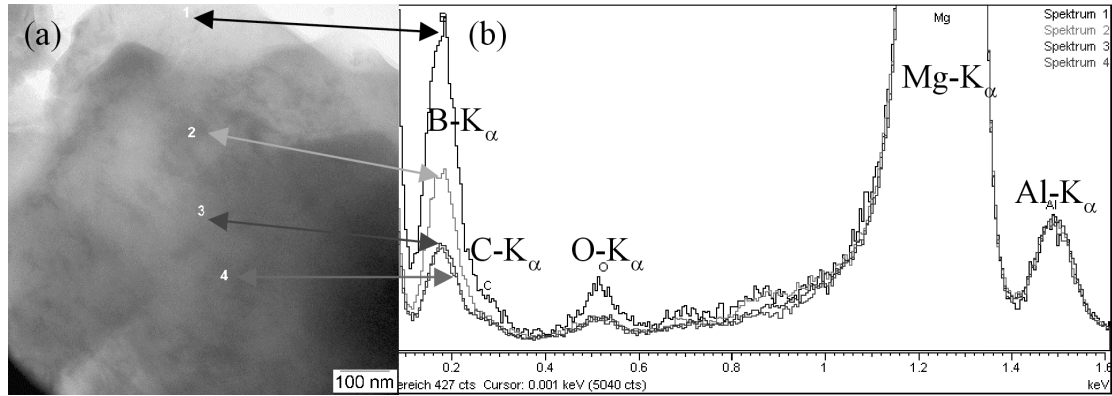
Figure 4.2: (a) TEM bright-field image of the MgB$_2$ sample (sample 4 of chapter 3) used for EDX spectroscopy, (b) EDX-spectra acquired at positions of increasing sample thickness indicated in (a)

Table 4.1: Quantitative evaluation of the thickness series of TEM-EDX spectra in standard sample 4, to determine Cliff-Lorimer factor k_{B-Mg}

Spectrum	IB	IO	IMg	$(I_B/I_{Mg})_0$	k_{B-Mg}	B/Mg mole fraction ratio	O/Mg mole fraction ratio	B mole fraction (at.%)	O mole fraction (at.%)	Mg mole fraction (at.%)
sample 4: thickness series 1										
1	5310	910	122920			2.000	0.018	66.26	0.61	33.13
3	5906	1470	447123	0.110	8.69	2.000	0.008	66.49	0.27	33.24
4	5914	1160	474782	0.110	8.72	2.000	0.006	66.53	0.20	33.27

Table 4.2: Table for the quantitative TEM-EDX analysis of sample 5 with absorption correction of B-K_α x-rays.

Spectrum	IB	IO	IMg	$(I_B/I_{Mg})_0$	kB-Mg	B/Mg mole fraction ratio	O/Mg mole fraction ratio	B mole fraction (at.%)	O mole fraction (at.%)	Mg mole fraction (at.%)
sample 5: thickness series grain 7										
1	3886	5586	76037	0.147	8.71	2.680	0.183	69.37	4.74	25.89
2	7763	4324	185735	0.126	8.71	2.285	0.058	68.35	1.73	29.92
3	9743	4819	281526	0.123	8.71	2.230	0.043	68.14	1.30	30.56
4	10363	10105	422159	0.122	8.71	2.220	0.060	67.69	1.82	30.49
sample 5: thickness series grain 8										
1	1885	1966	17044		8.71	2.230	0.288	63.39	8.18	28.43
2	7239	3527	137755	0.126	8.71	2.280	0.064	68.19	1.91	29.91
3	7235	6922	202426	0.128	8.71	2.320	0.085	68.13	2.50	29.37
4	9797	6146	335980	0.123	8.71	2.230	0.046	68.08	1.39	30.53

The Cliff-Lorimer factor k_{B-Mg} was determined to be 8.71 by applying Cliff-Lorimer equation (equation 4.3) to standard sample 4. $(I_B/I_{Mg})_0$ for sample 4 was taken from Table 4.1. C_B and C_{Mg} were determined by EPMA analysis reported in chapter 3 and they correspond to stoichiometric MgB$_2$.

The B/Mg mole fraction ratio in sample 5 was then determined using the Cliff-Lorimer equation (equation 4.3). The O/Mg mole fraction ratio was determined, again by the Cliff-Lorimer method, but the absorption of O-K_α x-rays in MgB$_2$, which is six times smaller than that of B-K_α x-rays, was not considered. For O and Mg, theoretical Cliff-Lorimer factors given in the INCA software [128] were used. Finally the absolute values of B, O and Mg mole fractions are determined by setting their sum equal to 100 at.%.

The quantitative EDX -analysis of sample 5 is summarised in Table 4.2 The B mole fraction of sample 5, with and without absorption correction is plotted as a function of sample thickness (in units of Mg-K_α x-ray counts) in Figure 4.3. Without absorption correction the B mole fraction decreases with increasing sample thickness, whereas with absorption correction the B mole fraction is independent of the sample thickness.

The O-K_α x-ray intensity is plotted as a function of sample thickness (in units of Mg-K_α counts) in Figure 4.4. O-K_α x-ray intensity in sample 4 is almost independent of specimen thickness, while O-K_α x-ray intensity in sample 5 increases with increasing sample thickness.
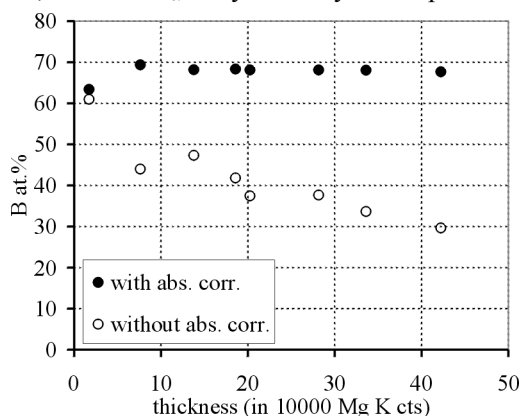
Figure 4.3: Quantitative B analysis using TEM-EDX, with absorption correction (●) and without absorption correction (o) of B-K_α x-rays, at different thicknesses in sample 5
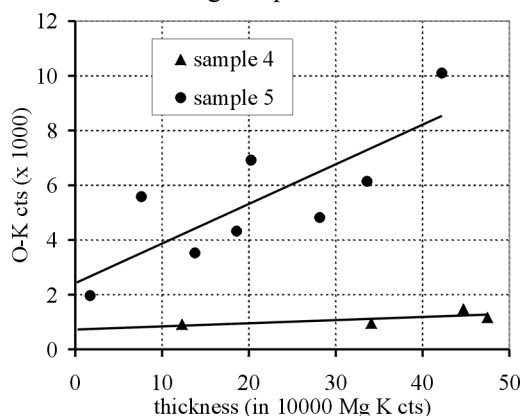
Figure 4.4: O-K_α x-ray intensity in the TEM-EDX spectra acquired at different thicknesses (in units of Mg-K_α counts) of samples 4 and 5.

4.5   Discussion

The MgB$_2$ colonies in sample 4 were known to have a homogenous chemical composition of stoichiometric MgB$_2$ (Chapter 3 and 6). Therefore the decrease in the B-K_α x-ray intensities in Figure 4.2 can only be attributed to the preferential absorption of B-K_α x-rays. To confirm this, transmission coefficient for B-K_α and Mg-K_α x-rays, defined in equation 4.9, are plotted (Figure 4.5) as a function of t using matlab script given in (9.2.4). The mass absorption coefficients of B-K_α and Mg-K_α x-rays in Mg and B were taken from the compilation of Zchornack [141]. The specimen density was calculated from the crystallographic unit cell information. These data and the x-ray absorption lengths are summarised in Table 4.3. The geometry factor f =1.56, is used, which corresponds to the sample-detector geometry used in TEM-EDX experiments as described in section 4.2.1. The plots predict significant preferential absorption of B-K_α x-rays. In a 120 nm thick sample more than 50% of the B-K_α x-rays, but less than 2% of the Mg-K_α x-rays are absorbed in the sample. This highlights the need for absorption correction of B-K_α x-rays and justifies the use of Mg-K_α x-rays as a relative measure of sample thickness (under the condition of constant current in the beam).

The thickness dependence of the B mole fraction could be eliminated after correcting for the absorption of B-K_α x-rays (Figure 4.3). B-rich secondary phases like MgB$_4$ and MgB$_7$ are known to exist in the MgB$_2$ matrix. Absorption corrected TEM-EDX analysis is essential to identify these secondary phases.

The O-K_α x-ray intensity versus thickness plots (Figure 4.4) for sample 4 and 5 enable to differentiate between the surface and bulk oxidation. The O-K_α x-ray intensity in sample 5 increases with increase in sample thickness, which indicates that oxidation in sample 5 is a bulk effect. The O-K_α x-ray intensity in sample 4 does not increase with increasing thickness which indicates that bulk oxidation in sample 4 is negligible in comparison to sample 5. O-K_α x-ray intensity extrapolated to zero thickness, gives a measure of surface oxidation in sample 4 and 5. From (Table 4.1),

and (Table 4.2) it can be seen that about 1 and 4-8 at.% of oxygen is found at thin regions of sample 4 and 5 respectively. The lower O mole fractions in sample 4 compared to sample 5 can be explained. Sample 4 is an ex-situ sample prepared from pre-reacted MgB_2. Negligible fraction of B-rich secondary phases is found in sample 4 and the MgB_2 phase formation is complete. The TEM-EDX measurements were made from a MgB_2 colony [116], which is a dense arrangement of well formed MgB_2 grains of 200-1000 nm size. There is little unreacted Mg in the bulk of the MgB_2 colonies which can oxidise, which explains the low oxygen mole fraction in sample 4. In agreement with these TEM-EDX results, the SEM-EDX quantification of such colonies also showed very less oxygen (~ 1 at.%) [116]. On the other hand, sample 5 is prepared by powder in tube technique by annealing at 600°C , a highly reactive mechanically alloyed mixture of Mg and B powder, prone to oxidation due to the air trapped in the tube. In agreement with these TEM-EDX results the SEM-EDX measurement showed about 4 at.% of oxygen in sample 5 [73].
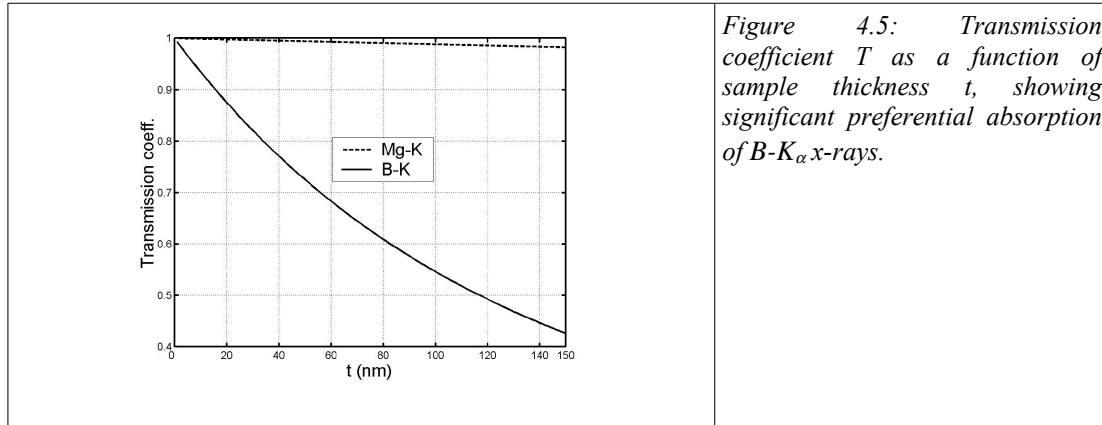
Figure 4.5: Transmission coefficient T as a function of sample thickness t, showing significant preferential absorption of B-K_α x-rays.

Table 4.3: Mass absorption coefficients and x-ray absorption lengths of B-K_α and Mg-K_α x-rays in MgB_2

X-ray	X-ray energy [eV]	μ_B [cm^{2}g^{-1}]	μ_{Mg} [cm^{2}g^{-1}]	ρ_{MgB2} C_B [gcm^{-3}]	ρ_{MgB2} C_{Mg} [gcm^{-3}]	XAL[nm]
B_Ka	183.3	3350	59500	1.24	1.4	114.7
Mg_Ka	1253.6	645	500	1.24	1.4	6674.06

The advantages and limitations of Eibl's and Zeta factor method were discussed in section 4.2. In this work only Eibl's method is used because the measurement of probe current in the electron beam was not possible in our microscope. It also does not require the knowledge of mass absorption coefficients. Eibl's method is however prone to inaccuracies due to local variations in the shape of the sample, because at-least two EDX measurements at different sample tilts or at different sample thicknesses are required. On the other hand, Zeta factor method requires only one EDX measurement and therefore less prone to inaccuracies due to local sample shape variations, but explicitly requires mass absorption coefficients, which for B-K_α x-rays might be inaccurate. Therefore, the possibility of comparing the TEM-EDX quantification of MgB_2 samples by Eibl's method with that by Zeta factor method should be explored.

Quantitative TEM-EDX spectroscopy described in this chapter was essential for a reliable interpretation of ESI elemental maps like those in Figure 3.12, which usually suffer from artefacts due to multiple scattering. Quantitative TEM-EDX spectroscopy should be applied to determine the exact chemical composition of B-rich secondary phases smaller than 1 μm (the lateral resolution of the SEM-EDX).

Chapter 5

5   Al-alloyed MgB₂: correlation of superconducting properties, microstructure, and chemical composition [10]

5.1   Introduction

The electronic structure of MgB_2 (see chapter 2) consists of p_{x-y} orbitals which interact strongly with the in-plane vibrations of boron atoms giving rise to large superconducting energy gap $\Delta_\sigma = 6.8$ meV, and p_z orbitals which are not strongly coupled with phonons giving rise to a smaller superconducting energy gap $\Delta_\pi = 1.8$ meV[33][47][23][30][50].

    Such a peculiar electronic structure offers unique chance to modify the superconducting properties by substitution of either the B or Mg lattice sites [142][62][143]. Therefore the Al-alloyed samples were synthesised by two step solid state reaction described later. The residual resistivity (ρ_0) at 40 K, measured by four-probe method was found to be 2.5 ±0.5 $\mu\Omega$cm for the pure sample and less than 24±2 $\mu\Omega$cm for the largest Al-alloyed sample. Resistivity of the pure sample is comparable to that of single crystals and indicates the excellent quality of these samples. Recently, Putti et al.([144] [145]) have studied the upper critical field (B_{c2}) of the Al-alloyed MgB_2 and given a theoretical explanation for the decrease in B_{c2}.

    Most of the investigations on Al-alloyed MgB_2 show degradation[146][147] of the superconducting properties except that of Berenov et al.[148] who reported a slight increase in J_c for low levels of Al doping. The microstructure of the Al-alloyed MgB_2 which also could be the reason for the decrease of B_{c2} in Al-alloyed samples, has however not been investigated in detail so far. TEM studies of Song et al. [149] on non-alloyed samples prepared by the same procedure as for the samples investigated in this study, showed the presence of 150 nm sized MgB_2 nanodomains with a slightly different lattice parameters inside a few MgB_2 grains. Also MgB_7 nano-precipitates of size 1-5 nm were found in about 2-3% of the MgB_2 grains. Slusky et al. [146], Zandbergen et al. [150] and Li et al.[151] from their x-ray diffraction (XRD) and TEM investigations found that for Al concentrations > 3.33 at.%, a second MgB_2 phase with a longer c lattice parameter is formed. Recently, XRD and high resolution TEM investigations in $Mg_{1-x}Al_xB_2$ single crystals with $x > 0.1$ indicated the presence of a non-superconducting $MgAlB_4$ phase [152]. Putti et al.[153] who annealed the mixture of elemental B, Mg , and Al for longer times did not detect such phase transformation using XRD. TEM investigations were not performed. Higher order magnesium-boride secondary phases, expected to form due to the evaporation of highly volatile Mg [4] were not detected in the above investigations [146],[153], [151]. However considering that very few grains out of a large number of grains in the sample are analysed by TEM and low x-ray scattering for light elements, both TEM and XRD might not detect the presence of secondary phases of higher magnesium borides. Investigations using the electron beam techniques like EPMA and TEM which are sensitive to light elements and have spatial resolution of 1 μm and 10 nm respectively [8] might reveal the microstructure of Al-alloyed MgB_2 to be quite complex. In fact, TEM investigations by Song et al. [149] on similarly prepared pure samples showed the presence of 1-5 nm sized MgB_7 nanoprecipitates. Similarly, our recent investigations [8],[114] on MgB_2 ceramics show that, they contain secondary phases of higher magnesium borides and MgO precipitates in the matrix of MgB_2. Neutron powder diffraction technique is also sensitive to light elements and Hinks et al. [36] detected MgB_4 secondary phases in MgB_2.

    It is still unclear how Al is accommodated in the possibly complex microstructure of MgB_2 on the sub-micrometer length scale. So far, Al concentration, was either assumed to be same as

the Al concentration that was taken in the reaction mixture for the synthesis, or was determined indirectly from T_c and XRD analysis. But MgB_2 is known to be a line compound [36] and both the above estimations may not represent the true Al concentration in the end product MgB_2. This chapter attempts to quantitatively determine the chemical composition of secondary phases and matrix using SEM and EPMA, and of the MgB_2 grains on the nanometer scale using TEM.

5.2   Experimental

5.2.1   *Al-alloyed MgB₂ synthesis*

Al-alloyed MgB_2 was prepared in a two step process. In the first step Mg-Al alloys are prepared with aluminium mole fractions of 0, 3.33, 6.66 and 10 at.% for samples 1 to 4 respectively. In the second step cylindrical piece of Mg-Al alloy and crystalline B powder (325 mesh) are put in Ta crucibles, welded in argon and closed in quartz tubes. The quartz tube is then placed in a vertical furnace which is at 850-900°C; after one hour the temperature is raised and maintained at 1000°C for 100 hours.

5.2.2   SEM and EPMA

SEM and EPMA samples were prepared by the conventional metallographic method described in section (2.1.4). The sample surfaces were then coated by carbon to improve electrical conductivity and immediately brought into electron microprobe and SEM. To protect the sample from decomposing into $Mg(OH)_2$ [131] powder , it was necessary to use ethanol instead of water during the sample preparation process.

EPMA by wavelength-dispersive x-ray spectroscopy (WDX) was performed with a JEOL Superprobe 8900 RL operated at 15 keV primary energy with a probe current of 15 nA. Sample surfaces had to be polished very well and the so called "area intensity mode of measurement" had to be used to obtain precise quantitative analysis [9] for boron, which suffers from strong absorption and chemical shift of B-K_α x-ray peak. Number of counts in the x-ray peaks was ~ $5x10^4$, which results in a counting precision of 1%. Heterogeneity of the sample affects the EPMA quantification. For metallic boron used as a standard, the B-content varied between 98.07 and 101.17 wt.%. SEM analysis was performed using a SEM-FEG Philips XL 30 operated at 10 kV.

5.2.3   TEM

TEM sample are prepared by the powder method described in section 2.2.5. A small piece of sample 3 ($Mg_{0.8}Al_{0.2}B_2$) was crushed in a silica mortar, dispersed in ethanol and then placed onto a carbon foil supported by a copper grid. Thin electron transparent grains on these foils were investigated by a LEO 912 TEM, operated at 120 kV. An Energy dispersive x-ray (EDX) detector equipped with an ultra-thin window was used to acquire EDX spectra which were analysed using INCA 4.01 software package [128] from Oxford Instruments. B-K_α x-rays because of their low energy are strongly absorbed in the sample (Figure 5.8 (b)). Because of the difficulties in the determining the local thickness of the specimen absorption of x-rays was not corrected. Mg-K_α and Al-K_α x-ray energies being almost equal , undergo similar absorption effect. The fluorescence yield decreases with decreasing atomic number. The number of counts in the area under B-K_α peak was therefore only ~100 while that under the Mg-K_α peak is ~6600. The counting precision of Mg-K_α, Al-K_α, and B-K_α is 1.3 %, 2.5%, and 7.9% respectively. Evaluation of B-K_α peak is further complicated by the closely lying C-K_α peak. The C-K_α peak arises due to the cracking of residual gases at thin regions of the samples when hit upon by electron beam. Therefore only Mg-K_α and Al-K_α x-rays have been used for the quantitative analysis using TEM-EDX. The typical EDX acquisition conditions are given in Table 5.1.

Table 5.1.Acquisition conditions for EDX in TEM

Specimen tilt θ	15°
Spot size	25-40 nm
Measurement time	50 s
Integrated no. of counts under Mg-K_α peak	~6600
Resolution at B-K_α	55 eV
Spectrum energy range	1-10 keV
Energy /channel	5 eV

5.3 Results

5.3.1 Superconducting and normal state properties

Behaviour of superconducting properties namely, upper critical field (B_{c2}), T_c, superconducting transition width (ΔT_c), and normal state properties (ρ_0, *a*, *c*) of Al-alloyed MgB_2 have been recently investigated by Putti et al. [144],[145] and summarised in Table 5.2. B_{c2} was determined by magnetoresistance measurement. T_c was defined as $(T_{90\%}+T_{10\%})/2$ and ΔT_c defined as $= T_{90\%}-T_{10\%}$, where $T_{90\%}$ and $T_{10\%}$ are temperatures corresponding to 90% and 10 % of the resistive transition.

T_c decreases while ΔT_c increases with increasing Al concentration as shown in Figure 5.1(a). B_{c2} decreases with increasing Al concentration [144], [145]. The variation of ρ_0 (Figure 5.1(a)) with Al mole fraction is linear until aluminium concentration in sample 3, thereby obeying the Nordheim rule [154]. ρ_0 of sample 4 however is higher than expected. Lattice parameter *c* which is the distance between the adjacent B-planes decreases at the rate of 1.15 pm/at.% Al with increasing Al mole fraction (Figure 5.1(b)). In contrast the in-plane lattice parameter *a* decreases only by 1.3 pm for an Al mole fraction of 7.62 at.%.
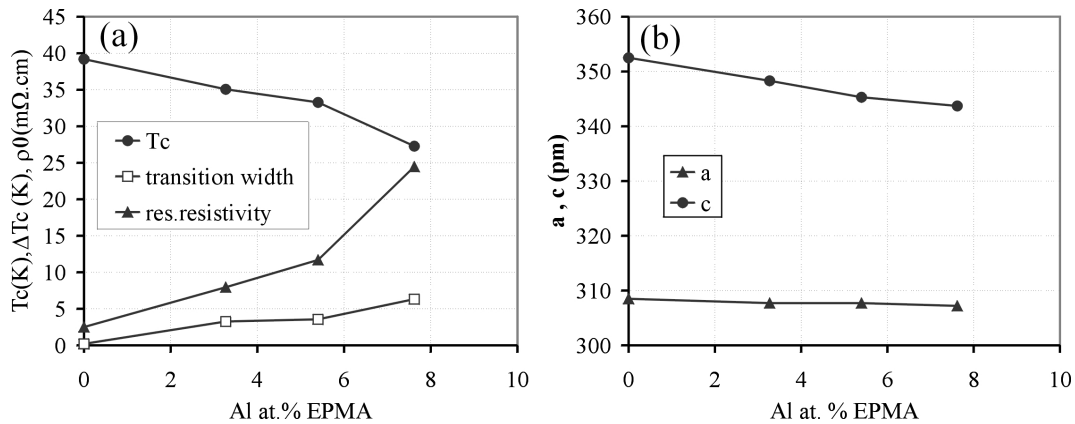
Figure 5.1: Variation of T_c(●), ΔT_c(□), and ρ_0(▲) at 40 K with Al at. % determined by EPMA. (b) Variation of lattice parameters a(▲) and c(●) with Al at. % determined by EPMA.

Table 5.2.Superconducting properties of pure and Al alloyed MgB_2

Sample No.	Nominal Composition	T_c (K)	ΔT_c (K)	ρ_0 ($\mu\Omega cm$)	a (pm)	c (pm)	Al at.% EPMA	Al at.% Nominal
1	MgB_2	39.19	0.2	2.5	308.5	352.5	0	0
2	$Mg_{0.9}Al_{0.1}B_2$	35.06	3.26	7.95	307.7	348.3	3.27	3.33
3	$Mg_{0.8}Al_{0.2}B_2$	33.27	3.56	11.69	307.7	345.3	5.4	6.67
4	$Mg_{0.7}Al_{0.3}B_2$	27.27	6.32	24.47	307.2	343.7	7.62	10.0

5.3.2 Microstructural analysis

Al- alloying of MgB_2 changes not only its superconducting properties but also its microstructure. In fact, the changes in superconducting properties could well be the consequence of the changes

in microstructure. These microstructural changes were investigated by SEM , EPMA and TEM. Secondary and backscattered electron images were used to identify the phases followed by EPMA measurements to yield the quantitative chemical composition of the phases in pure (sample 1) and Al-alloyed MgB_2 (samples 2-4).

Quantitative analysis of light elements, specially B needs special attention because of high absorption and chemical shifts of x-ray lines and peak shape alterations. Recently, Wenzel et al. [9] have successfully applied the EPMA technique to quantitatively analyse MgB_2 compounds. Extremely well polished surfaces and the area intensity measurement mode of operation were the key to yield precise chemical composition of MgB_2 compounds. Similar methodology has been used to analyse the present samples. Porous areas and non-planar surfaces give rise to artefacts in data evaluation yielding totals of element weights smaller or larger than 100 ± 5 %. Such data were not taken into consideration. Further data evaluation is done by converting the weight fractions into mole fractions. Although the characteristic x-rays of the constituent elements are generated within similar volumes, B-K_α x-rays from only the top 100 nm of the sample are emitted, unlike Mg- K_α and Al- K_α x-rays which come from depths upto few µms. Consequently, quantitative EPMA analysis of such Mg-B compounds is highly sensitive to sample heterogeneity.

5.3.2.1   Pure MgB_2

Figure 5.2(a) shows a secondary electron image of the surface of the pure MgB_2 sample. Island-like dark areas that are 2-10 µm in size (indicated by "arrows" and hereafter referred to as "large secondary phases") can be seen within grey area (hereafter referred to as "matrix"). The large secondary phases constitute about 4-5 % of the total surface area of the specimen, which means less than 1% of the sample volume. The matrix is planar and dense. 5-15 µm sized voids are seen (indicated by "1"), some of which (indicated by "2") are filled by 5-10 µm large particles. EDX spectra acquired from such particles showed strong Mg-K_α and O-K_α peaks. These particles might be Mg hydroxide [131], formed due to the reaction of traces of unreacted magnesium with water in ambient atmosphere. They are confined to the sample surface and are not likely to be the characteristic feature of the bulk microstructure. Figure 5.2(b) shows the magnified image of the dark region marked in Figure 5.2(a). Due to the ion milling of the sample surfaces, areas with B-rich secondary phase yield a topographic contrast and can be easily identified also in secondary electron images.
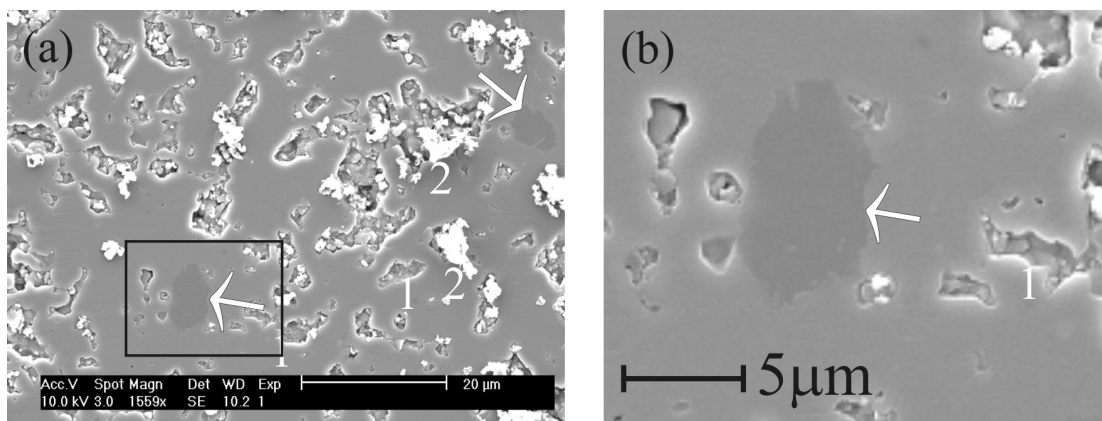
Figure 5.2: (a) SEM secondary electron image of sample 1. Dark regions , voids, and regions with hydroxide growth are indicated by "arrows", "1", and "2" respectively. (b) A magnified view of the portion marked in (a).

The results of quantitative chemical analysis of the matrix and dark regions by EPMA are shown in Figure 5.3(a,b) and summarised in Table 5.3. Correlation diagrams of B-Mg and B-O mole fractions show the matrix composition to be close to MgB_2. The oxygen mole fraction in the matrix is 0.24 at.%. Similar analysis of dark regions using 3 measurements showed B to Mg mole

fraction ratio to be 7.99. Dark phases contained a smaller average oxygen mole fraction of 0.09 at. %.
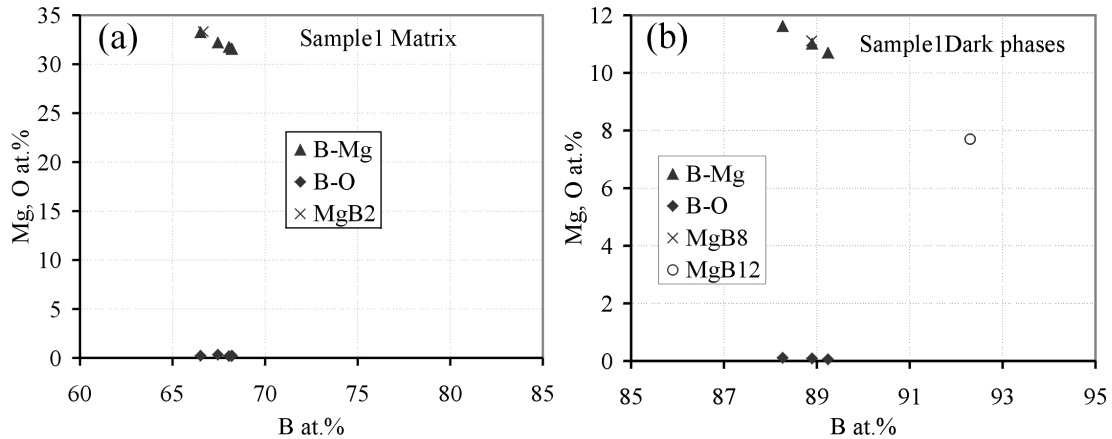
Figure 5.3: Correlation diagram of B-Mg (▲) and B-O (♦) mole fractions from EPMA of (a) the matrix and (b) the large secondary phases of sample 1. The ideal position of MgB_2, MgB_8 and MgB_{12} are also indicated for reference.

Table 5.3. B, Mg, O mole fractions obtained by EPMA of matrix and secondary phases in sample 1 with a nominal composition of MgB_2.

		B at.%	Mg at.%	O at.%
Matrix	Mean	67.68	32.07	0.24
	Std.dev.	0.72	0.71	0.06
Large sec.phase	Mean	88.80	11.11	0.09
	Std.dev.	0.49	0.47	0.03

5.3.2.2   Al-alloyed MgB_2

Sample 2 is lowest Al-alloyed with a nominal composition of $Mg_{0.9}Al_{0.1}B_2$. A back- scattered electron image (Figure 5.4(a)) of this sample shows bright matrix containing 10-20 μm sized secondary phases. A magnified image of one such region is shown in Figure 5.4(b). The large secondary phases are themselves found to be heterogeneous, i.e. they consist of 5-10 μm sized dark regions (indicated by "arrow" in Figure 5.4(b)) embedded in the background of faint dark region. In addition, 1-3 μm size dark secondary phases (indicated by "arrowheads" in Figure 5.4(b) and hereafter referred to as "small secondary phases") are found with a density of ~5 x 10^6 cm^{-2} around the dark regions and with slightly larger densities away from the dark regions. The volume fraction of these secondary phases can be estimated to be less than 3 %.

Table 5.4: B, Mg, Al, O mole fractions obtained by EPMA from matrix and secondary phases in sample 2 with a nominal composition Mg0.9Al0.1B2.

		B at.%	Mg at.%	Al at.%	O at.%
Matrix	Mean	67.52	28.94	3.27	0.26
	Std.dev.	0.93	1.13	0.94	0.03
Large sec. phase	Mean	90.78	8.46	0.67	0.10
	Std.dev.	0.22	0.25	0.02	0.04

The results of quantitative chemical analysis of the matrix and large secondary phases by EPMA are shown in Figure 5.5(a,b) and summarised in Table 5.4. Correlation diagrams of B-Mg, B-O, and B-Al mole fractions plotted from 7 measurements show that the matrix composition is $(Mg,Al)B_2$ (Figure 5.5(a)). The Al mole fraction in the matrix is determined to be 3.27 at. % . Similar chemical analysis of dark regions using 3 measurements showed B to (Mg,Al) mole frac-

tion ratio to be 9.95. The Al mole fraction in the large secondary phase is 0.67 at.%. Al to Mg mole fraction ratio is 0.11 in the matrix and 0.08 in the large secondary phases.
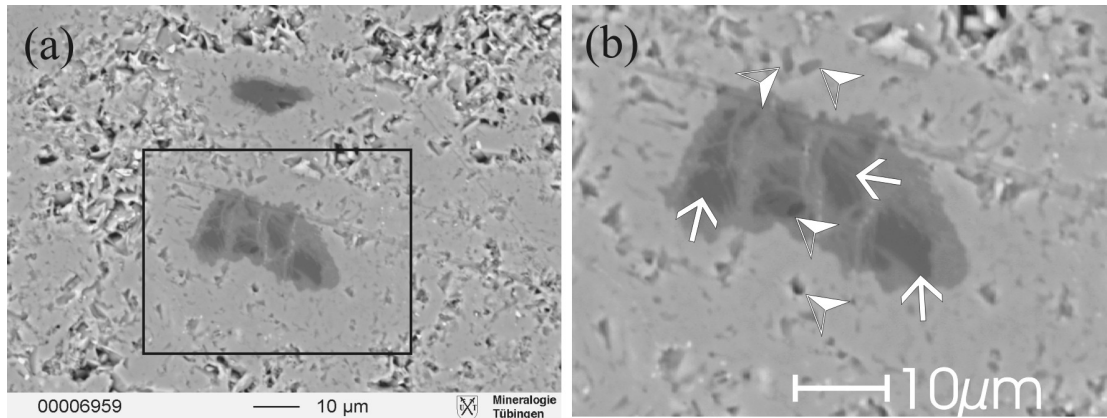
Figure 5.4: (a) EPMA backscattered electron image of sample 2 . (b) A Magnified image of the area marked in (a). Arrows and the arrow heads, respectively, indicate the large secondary phases inside dark regions and the small secondary phases.
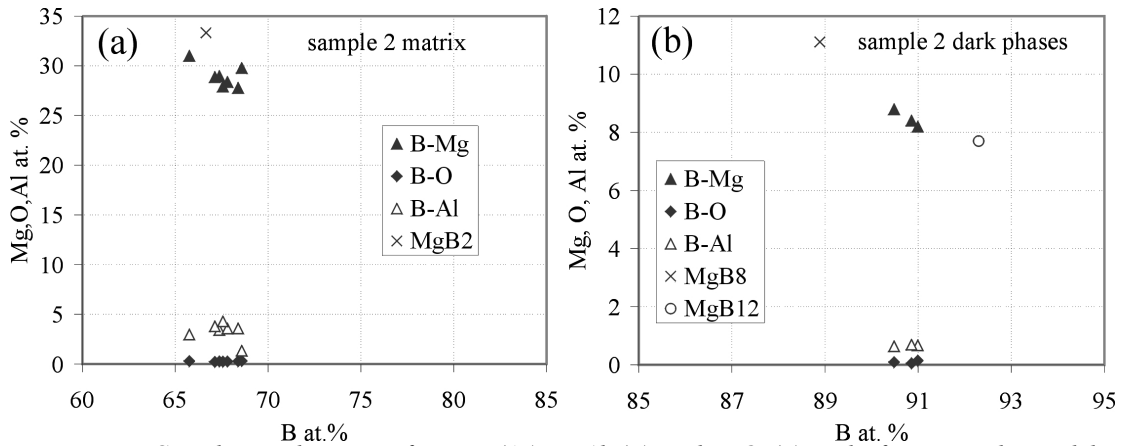
Figure 5.5: Correlation diagram of B-Mg (▲), B-Al (△) and B-O (♦) mole fractions obtained by EPMA of (a) the matrix and (b) large secondary phases of sample 2. The ideal position of MgB_2, MgB_8 and MgB_{12} are also indicated for reference.

Sample 3 is moderately Al-alloyed and has a nominal composition of $Mg_{0.8}Al_{0.2}B_2$. Secondary electron image (Figure 5.6(a)) of this sample shows the microstructure to be qualitatively similar to that of sample 2. However, the sizes of the large secondary phases and the dark regions in them have grown to 20-30 μm and 15-20 μm, respectively, while the size of small secondary phases has decreased. The local density of these small secondary phases has also decreased in the areas around the large dark regions and increased in regions away from the large secondary phases. The average density of small secondary phases is smaller than for sample 2. The volume fraction of the total amount of secondary phases can be estimated to be less than 4 %.

The results of quantitative chemical analysis of the matrix and large secondary phases by EPMA are shown in Figure 5.7(a,b) and summarised in Table 5.5. The results are similar to those of sample 2. The B to (Mg,Al) mole fraction ratio in the large dark phases has increased to 10.73. Al mole fraction has increased to 5.4 at.% in the matrix. In the dark phase, however, the Al content has decreased to 0.5 at.%. The Al to Mg mole fraction ratio is 0.20 in the matrix and 0.06 in the large secondary phases. Oxygen mole fraction in both matrix and large secondary phase is again very small.

In addition, microstructure and composition of sample 3 was analysed by TEM. Most of the grains are oriented close to [-1-22] pole about 35° from the [001] pole. Figure 5.8(a) is a centred dark field image of a typical MgB_2 grain, acquired under nearly two beam conditions with a (011)

reflection strongly excited. Distinct diffraction contrast (thickness fringes and bend contours) enable the grain size to be determined as ~1 μm. A corresponding high magnification bright field image is shown in Figure 5.8(b). No precipitates are seen. It should however be noted that only 5 out of the numerous randomly distributed grains were investigated.

For quantitative analysis 29 EDX spectra from various grains were acquired. Because of the difficulties(see experimental section) in B-K_α x-ray peak evaluation, identification of the $(Mg,Al)B_2$ matrix and $(Mg,Al)B_{7+\delta}$ secondary phases was not possible using B-K_α x-rays. However, the EPMA finding, that the Al to Mg mole fraction ratio in $(Mg,Al)B_2$ matrix (0.20) is different from that in $(Mg,Al)B_{7+\delta}$ secondary phases (0.06), can be used to identify the phases of grains from the Mg-K_α and Al-K_α x-ray intensities in TEM. 26 grains were thus found to be of $(Mg,Al)B_2$ phase. Mg and Al mole fractions are calculated from the TEM-EDX spectra, assuming the B mole fraction to be 66.67 at.% and a Mg-Al correlation diagram (Figure 5.9(a)) is plotted. Applying the similar technique to the EPMA data the composition of the matrix was recalculated and is also indicated (filled circle) in the Figure 5.9(a). The agreement between the chemical compositions of the $(Mg,Al)B_2$ matrix, determined independently by TEM-EDX and EPMA-WDX after eliminating the B quantification errors is worth noting. Thus the matrix phase was quantitatively analysed using TEM-EDX and the results are summarised in Table 5.5.
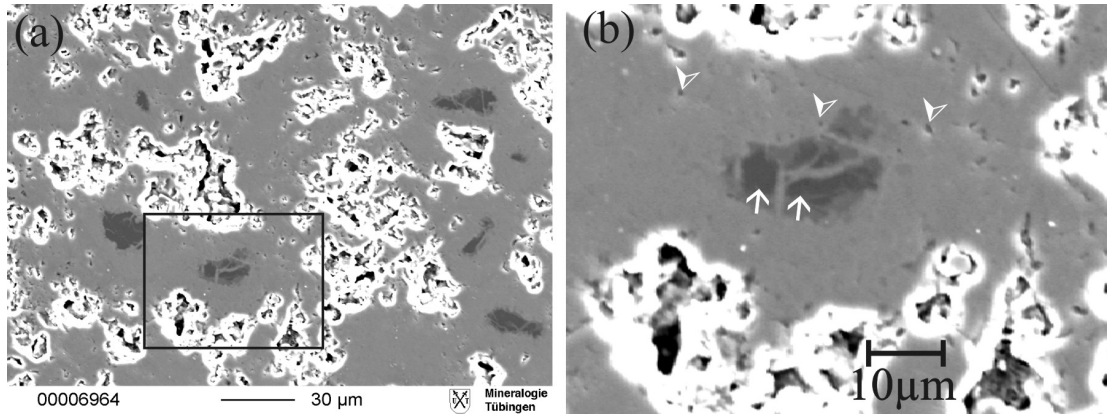
Figure 5.6: (a) EPMA secondary electron image of sample 3. (b) Magnified image of the area marked in (a). Arrows and the arrow heads, respectively, indicate the large secondary phases inside dark regions and, the small secondary phases.
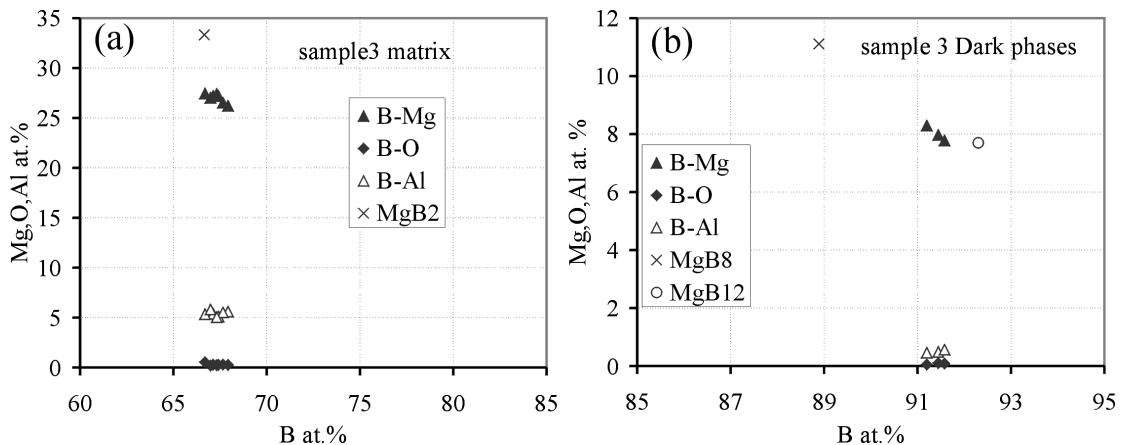
Figure 5.7: Correlation diagram of B-Mg (▲), B-Al (△) and B-O (♦) mole fractions from EPMA of (a) the matrix (b) the large secondary phases of sample 3. The ideal position of MgB_2, MgB_8 and MgB_{12} are also indicated for reference.
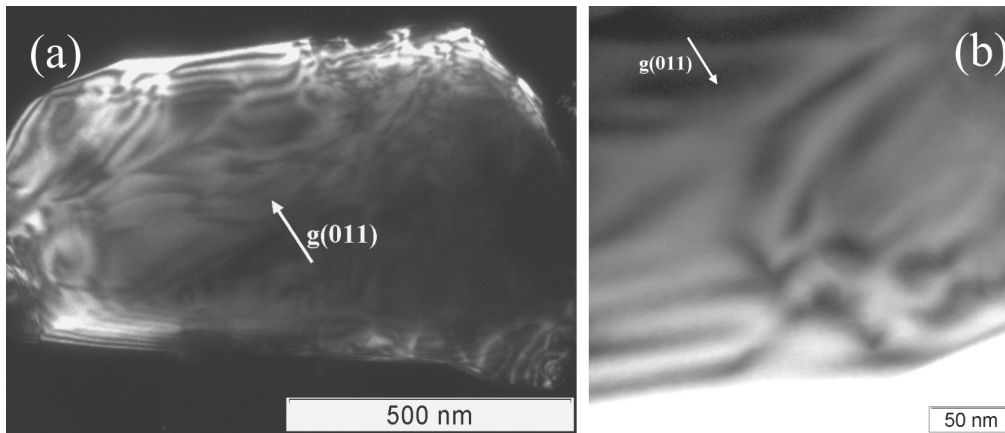
Figure 5.8: TEM-dark field (a) and bright field (b) image of MgB₂ grain under two beam conditions.
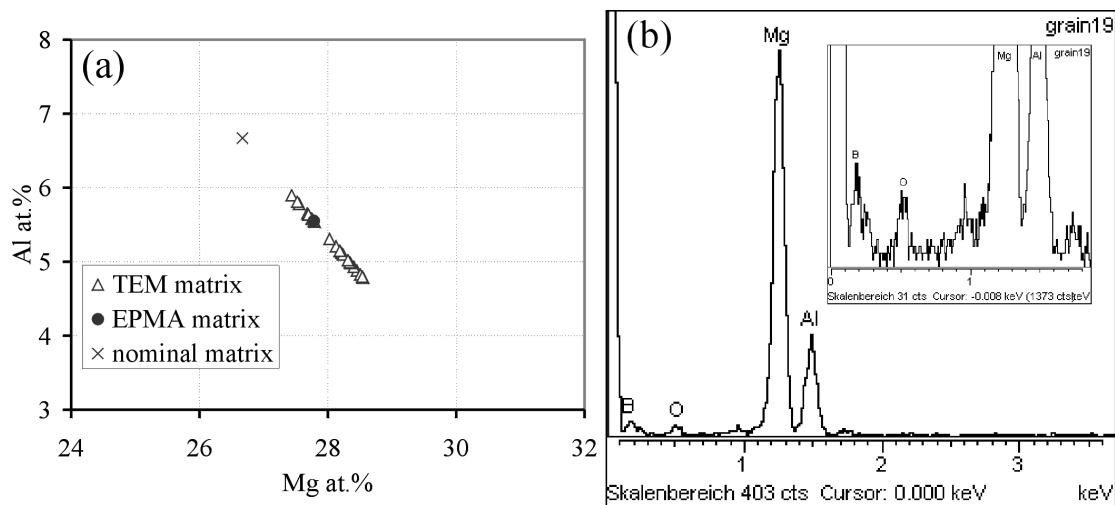
Figure 5.9: (a) Correlation diagram of Al-Mg mole fractions determined using TEM-EDX spectra (Δ) and EPMA quantification of matrix (●) of sample 3. The ideal position of nominally alloyed MgB₂ (□) is indicated for reference. (b) A typical TEM-EDX spectrum.

Table 5.5: B, Mg, Al, O mole fractions obtained by EPMA and TEM-EDX from matrix and EPMA from secondary phases in sample 3 with a nominal composition Mg0.8Al0.2B2.

		B at.%	Mg at.%	Al at.%	O at.%
Matrix (EPMA)	Mean	67.31	27.00	5.40	0.29
	Std.dev.	0.41	0.46	0.27	0.11
Matrix(TEM)	Mean	66.67	27.78	5.55	-
	Std.dev.	0.00	0.37	0.37	-
Large.sec.phase (EPMA)	Mean	91.41	8.01	0.50	0.08
	Std.dev.	0.19	0.26	0.05	0.03

Sample 4 is maximum Al-alloyed and has a nominal composition of $Mg_{0.7}Al_{0.3}B_2$. A secondary electron image (Figure 5.10(a)) of this sample shows the microstructure to be similar to that of the Al-alloyed sample 2 and 3. However, the density of large secondary phases has increased and their size has increased further to 20 - 40 μm. These large secondary phases, as can be seen in the magnified image (Figure 5.10(b)), now contain a large dark core. The regions close to large secondary phases are almost free of small secondary phases. It is out of trend that the overall density of small secondary phases is significantly larger for this particular sample as can be seen in Figure 5.10(a). The total volume occupied by the secondary phases is estimated to be less than 4 % of the total volume of the sample.

The results of quantitative chemical analysis of the matrix and dark regions by EPMA are shown in Figure 5.11(a,b) and summarised in Table 5.6. The scatter in the correlation points in the dark region has strongly reduced compared to sample 3, and B to (Mg,Al) mole fraction ratio has increased to 11.14. This should be seen together with the fact that 30-40 μm sized dark regions are now mostly composed of a 30 μm sized dark core. The Al mole fraction in the matrix has increased to 7.62 at.% and to 0.9 at.% in the large secondary phases. Al to Mg mole fraction ratio is 0.32 in the matrix and 0.12 in the large secondary phases.
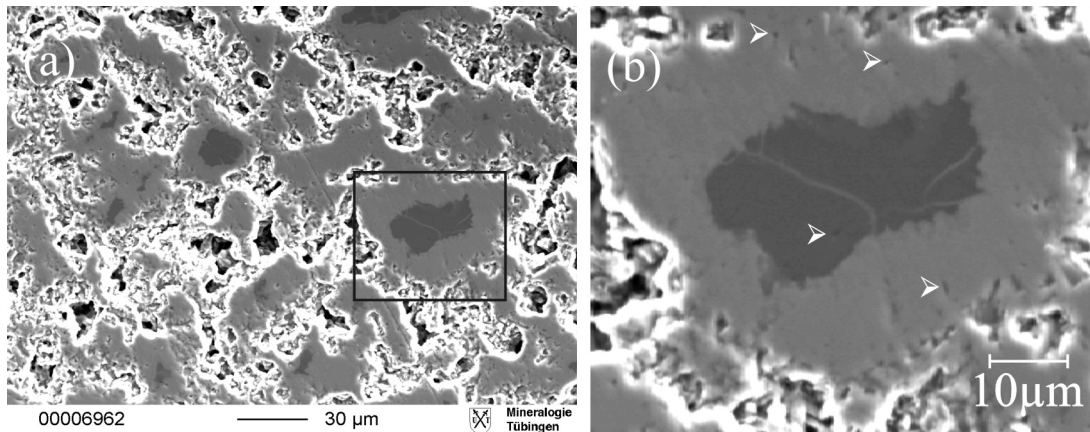
Figure 5.10: (a) EPMA secondary electron image of sample 4. (b) A Magnified image of the area marked in (a). A large secondary phase consisting of a dark region is seen. Arrow heads indicate the small secondary phases.
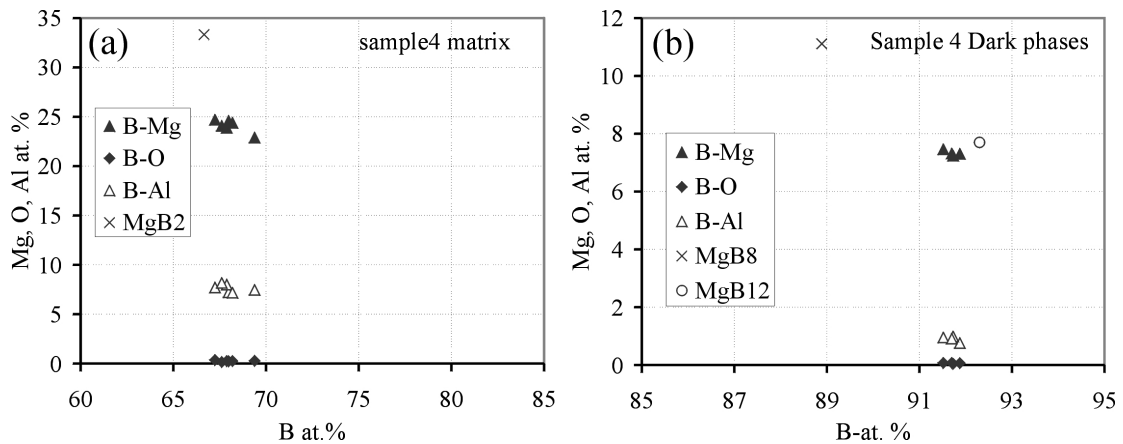
Figure 5.11: Correlation diagram of B-Mg (▲), B-Al (△) and B-O (♦) mole fractions from EPMA in (a) the matrix and (b) large secondary phases of sample 4. The ideal positions of MgB₂, MgB₈ and MgB₁₂ are also indicated for reference.

Table 5.6: B, Mg, Al, O mole fractions obtained by EPMA from matrix and secondary phases in sample 4 with a nominal composition Mg0.7Al0.3B2.

		B at.%	Mg at.%	Al at.%	O at.%
Matrix	Mean	68.05	24.08	7.62	0.25
	Std.dev.	0.73	0.66	0.41	0.07
Large.sec.phase	Mean	91.71	7.33	0.90	0.06
	Std.dev.	0.15	0.09	0.10	0.01

5.4   Discussion

5.4.1   *Microstructure of Pure MgB$_2$*

The analysis of pure MgB$_2$ (sample 1) using electron beam techniques proved that it consists of 10 µm sized secondary phases embedded in the matrix of MgB$_2$. Matrix is found to be slightly Mg deficient by about 1 at.% which is in accordance with findings of Bellingeri et al.[155] and Hinks et al [36]. The Mg to B mole fraction ratio in the large secondary phases is (1:8). The compound MgB$_8$ has not been reported in the literature, the composition of secondary phases must therefore be MgB$_7$ plus an excess of boron and can be written as MgB$_{7+\delta}$.

Hypothetical [4] and calculated [5] phase diagrams show that for Mg mole fraction >33 at.%, MgB$_2$ is stable for temperatures less than 1545 °C at atmospheric pressure. The formation of secondary phases is not predicted by the phase diagram. The annealing temperature of 1000 °C is smaller than the calculated decomposition temperature[5] by about 545 °C. Hink et al. [36] who annealed their samples at a lower temperature of 850 °C also found MgB$_4$ secondary phases in their samples. Annealing temperature is thus not likely to initiate the formation of MgB$_{7+\gamma}$ secondary phases.

The other factor which can initiate the formation of higher boride secondary phases is the lower effective Mg mole fraction. Considering the volatility of Mg and its relatively low melting point 649 °C, this is more likely to be the case and has been experimentally confirmed by Brutti et al. [7][24]. The diffusion of Mg into the B grains and the evaporation of Mg are the two important processes that drive the reaction kinetics and determine the quantity and composition of the phase products. The relatively higher annealing temperature (1000 °C) and longer annealing time (100 hours) ensure that diffusion of Mg into the smaller (< 44 µm ; 325 mesh) B grains that we used, is complete and there is little unreacted B. The result is therefore the formation of MgB$_8$ secondary phase. Eyidi et al.[8] who used similar annealing temp (950 °C) but shorter annealing time (2 hours) and larger (< 250 µm ; 60 mesh) B grains found MgB$_{12}$ secondary phases. The diffusion of Mg is thus not complete and there is more unreacted B present.

Also intriguing is the absence of intermediate secondary phase MgB$_4$ in our and Eyidi et al.'s [8] investigations, while such MgB$_4$ secondary phases have been detected by Hink et al. [36]. Here it seems that apart from smaller Mg mole fraction the effect of annealing temperature has also to be considered. The annealing temperature in the Hink's investigation was lower by about 150 °C. The depletion of effective Mg mole fraction in their case is predominantly due to the oxidation of Mg and the lower annealing temperatures thus favour the formation of MgB$_4$ secondary phases. Our EPMA results showed oxygen mole fractions less than 0.29 at. %, oxidation of Mg is thus negligible and the Mg depletion is primarily due to its evaporation. The higher annealing temperature and annealing time thus favour the formation of a MgB$_7$ secondary phases directly without the formation of MgB$_4$ secondary phases. Such a simultaneous existence of MgB$_2$ and MgB$_{7+\delta}$ is not possible according to the published phase diagrams [4], [5]. It should however be noted that these are the calculated phase diagrams and they have not yet been precisely verified experimentally [7].

5.4.2   *Microstructure of Al-alloyed MgB$_2$*

SEM images and EPMA quantitative measurements showed that Al-alloyed MgB$_2$ consists of the (Mg,Al)B$_2$ matrix, large secondary phases and small secondary phases. The lattice parameters *a* and *c* decrease at the rate of 1.15 pm/at.% Al and 0.17 pm/at.% Al, respectively. This can be used to determine the Al-mole fraction in the sample by simply measuring the lattice constant using XRD without having to perform EPMA measurements. The distance between adjacent boron planes (*c*) is significantly reduced in comparison to the in-plane B-B distance (*a*) which remains almost constant on Al-alloying. This indicates that alloying takes place by substituting Mg atoms by Al atoms. Subsequently, if Al plus Mg mole fractions versus B mole fraction correlation plots are made (Figure 5.12(a)), the data points from the matrix almost coincide with MgB$_2$. The stand-

ard deviations in Al mole fractions in tables 4, 5, and 6 can be taken as a measure of inhomgeneit-ies in the Al distribution, although they suffer from poor statistics. The Al mole fractions in the matrix of largest alloyed sample for example vary by about 1 at.% when the average Al mole frac-tion is 7.62 at.%. The Al distribution is thus quite inhomogenous on the micrometer scale.

Investigation on the nanometer scale using TEM revealed the grain size of sample 3 to be ~ 1 μm. TEM-EDX investigations found similar Al inhomogeneity even on the scale of 40 nm. In fact Zandbergen et al.[150] who annealed their samples at lower temperature (800 °C) and shorter an-nealing time, found a much larger Al inhomogeneity in their samples. The Al distribution in the $(Mg,Al)B_2$ grains is thus not homogenous. Although our preliminary investigation using TEM bright and dark field imaging did not detect Al precipitates (Figure 5.8(b)) in the grains, their ex-istence in other grains cannot be ruled out. Because of its great importance to the superconducting properties, analysis of coherence length sized precipitates, using TEM will have to be carried out on ion etched samples The Al mole fractions in the matrix determined by TEM-EDX and EPMA-WDX agree well with each other; but are significantly smaller than the nominal Al mole fractions.

Embedded in the matrix are 20-40 μm sized large secondary phases and 1-3 μm sized small secondary phases. The size and number density of the large secondary phases increases with in-creasing Al alloying. Their composition is determined to be $(Mg,Al)B_{7+\delta}$, the mole fraction of ex-cess boron being 2.95, 3.73, and 4.14 at.% for samples 2,3 and 4 respectively. Likewise the dis-tinct faint and dark regions seen in the large secondary phases (Figure 5.4(b)) must also be due to the varying amounts of excess boron. The increase in excess boron (δ) with increasing Al concen-tration can be explained if the diffusion of Mg is hindered by Al alloying and cannot compensate the loss of Mg due to evaporation in the dark regions transforming them into a $(Mg,Al)B_{11}$ phase.

The larger secondary phases yielded smaller Al mole fractions relative to Mg. This might be due to the different crystal structure (orthorhombic for MgB_7). Again Al plus Mg mole fraction versus B mole fraction correlation points lie on the line joining the hypothetical MgB_8 and MgB_{12} compositions(Figure 5.12(b)). Therefore, even in the large secondary phases the Al is likely to be alloyed by substitution of Mg lattice atoms.

After the publication of our work [10] on Al-alloyed MgB_2, Zambano et al. [156]studied the Al-alloyed MgB_2 samples annealed at low (850 °C) and high (1200 °C) annealing temperature us-ing x-ray diffraction. They found that Al is inhomogenously distributed in sample annealed at low temperature and homogeneously distributed in sample annealed at higher temperature because of the complete diffusion of Al into the MgB_2 grains.
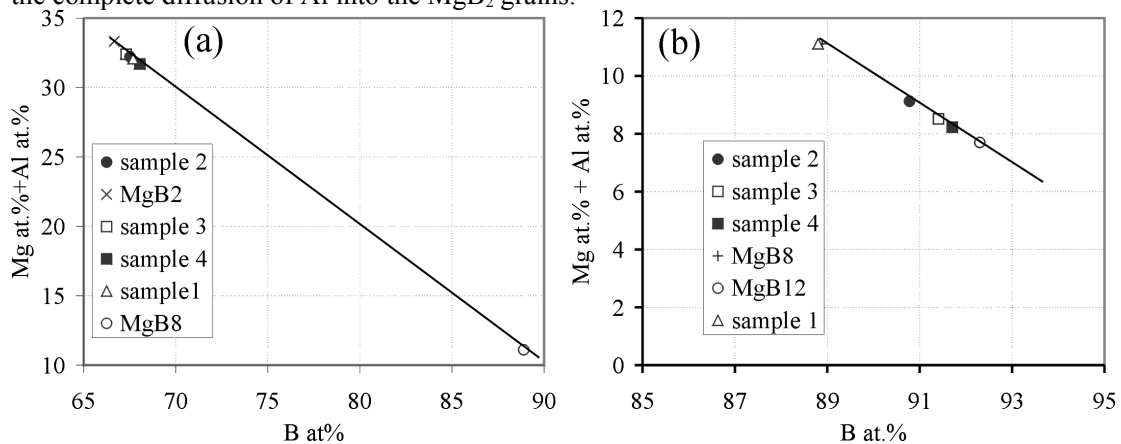
Figure 5.12: Correlation diagram of mean B mole fractions versus sum of mean Mg plus Al mole fractions of the matrix (a) and the large secondary phases (b) for samples 1 (Δ), 2 ($\bullet$), 3 ($\square$) and 4 ($\blacksquare$). The ideal position of MgB_2, MgB_8 and MgB_{12} are also indicated for reference.

5.4.3   Correlation of Al alloying on superconducting properties.

Thanks to the small fraction of the secondary phases, their contribution can be neglected, and the normal and superconducting properties presented by the samples can be attributed to the matrix.

As it can be seen from Figure 5.1(a), T_c decreases at the rate of 1.97 K/at.% with increase in Al mole fraction and is in accordance with the findings of other investigators reviewed in Buzea et al. [14]. The T_c versus Al mole fraction curve is in agreement with the calculations of Kortus et al. [157] which considered both, the decrease in density of states and increase in interband scattering with increasing Al-alloying.

ΔT_c increases with increasing Al mole fraction and is related to the inhomogeneities in the Al-distribution. The ΔT_c for sample 3 for example is 3.56 K. The EPMA and TEM-EDX measurements on sample 3 show that maximum variation in the Al mole fractions is 0.77 at.%. This predicts a ΔT_c of 1.21 K which is less than the experimentally observed value of 3.56 K. It should however be noted that the inhomogeneities determined by EPMA and TEM-EDX suffer from poor statistics as measurement from only ~ 10 grains are considered.

The residual resistivity ρ_0 increases linearly with the Al mole fraction at the rate of about 2 $\mu\Omega$cm /at.% Al until sample 3. The residual resistivity ρ_0 of sample 4 is higher than the value expected by the Nordheim rule [154]. This might be due to the reduction of the density of states plus the increase of scattering centres both being introduced by Al alloying. With Al alloying, the plasma frequencies of π bands increase, while the plasma frequencies of σ bands decrease. However substitutions in the Mg planes affect the scattering rate of π than that of σ bands. In this complex situation the right behaviour of residual resistivity is not predictable. Putti et al. [144] explained the anomalous behaviour of the upper critical field which decreases with Al-alloying by assuming that Al-substitution in Mg sites does not affect the impurity scattering in σ bands: in this framework σ carriers give the main contribution to the electrical conductivity and the increase of resistivity could be related to the filling of σ bands with Al alloying.

5.5   Summary and Conclusions

Low resistivity Al-alloyed MgB_2 samples with a T_c ~39 K were prepared by solid state reaction of Mg-Al alloy and crystalline boron. No phase separations were detected upto the highest Al concentration. The microstructure consists of ~15 μm and ~2 μm sized secondary phases embedded in the matrix of $(Mg,Al)B_2$. Aluminium is incorporated into the 1 μm sized MgB_2 grains by substitution of Mg lattice atoms, causing T_c and c to decrease at a rate of 1.56 K and 1.15 pm per at. % of Al alloying. This data may be used to determine the actual Al concentration which was found to be smaller than the nominal Al concentration. The Al distribution in the grains is inhomogenous, which at least partially accounts for the increase in ΔT_c with Al-alloying. The ρ_0 increased linearly with Al mole fraction, obeying the Nordheim rule till a Al mole fraction of 5.4 at. %.

The composition and size of secondary phases was governed by diffusion and evaporation of magnesium. The diffusion of Al seems to be smaller than that of Mg and Al-alloying hinders the diffusion of Mg. Annealing temperature, annealing time, boron grain size and Al mole fraction thus determine the size and composition of secondary phases. The composition of large secondary phases is found to be $Mg(Al)B_{7+\delta}$, with the mole fraction of excess boron (δ) increasing from 0.99 at.% in pure sample to 4.14 at.% in hiest alloyed sample approaching composition $(Mg,Al)B_{11}$. The size and density of secondary phases increased with increasing Al concentration but its volume is less than 4 % and is not likely to affect the bulk superconductivity.

Chapter 6

6   MgB₂ multifilamentary tapes: microstructure, chemical composition and superconducting properties[116]

6.1   Introduction

Synthesis of MgB$_2$ is easy and economically viable routes for the synthesis of MgB$_2$ wires and tapes of long lengths have been developed [158] [159]. Critical current densities of 2.5 x 10^4 Acm^{-2} at 4.2K, 10T [160] or higher than 10^4 Acm^{-2} at 20K, 5T were measured. An irreversibility field of B*(20K)=10T was determined at 4.2K [161], the same as for Nb-Ti . Therefore , it is the goal that MgB$_2$ replaces Nb-Ti in cryogen-free low-field applications, such as MRI . It has a potential also for high field applications both at the liquid He and in cryogen-free systems [63], [162]. Further enhancement in J$_c$ and critical fields is possible by optimising the microstructure of MgB$_2$.

Using a percolation model Eisterer et al. [163] [164]have recently suggested, that the critical current density in MgB$_2$ wires is governed by (i) the upper critical field B$_{c2}$ and (ii) the anisotropy of B$_{c2}$ [165]. It is well known that B$_{c2}$ can strongly vary (15 – 70 T) [63]in MgB$_2$ and can be increased by various methods, e.g. neutron and ion irradiation, C doping etc., introducing structural disorder. The correct determination of B$_{c2}$ in wires and tapes requires elimination of the sheath material, which is a substantial problem for multifilament conductors.

Because of the anisotropy of B$_{c2}$ even a homogenous poly-crystalline MgB$_2$ conductor will show granularity at higher magnetic fields [163],[164]. As will be shown in this chapter the microstructure of MgB$_2$ shows significant granularity and is not homogenous. This extends the validity of a percolation model towards smaller magnetic fields.

Defects on the nanometer scale e.g. dislocations, grain boundaries and precipitates can act as flux pinning centres and enhance the critical current density (J$_c$). The microstructure of MgB$_2$ bulk [166] [8] and MgB$_2$ tapes [114] was analysed by TEM. It was found that in spite of its simple crystal structure, MgB$_2$ offers a wide range of microstructure parameters that can be optimised in order to control and enhance its superconducting properties.

In this work the microstructure of the MgB$_2$ core and the MgB$_2$-Ni sheath interface of the multifilamentary tape cut from a 1600 meters-long tape produced by Columbus Superconductors [83] has been analysed by EPMA (Electron Probe Microanalyser), SEM and TEM.

6.2   Experimental

Multifilamentary Ni sheathed tapes are produced in lengths up to 1.6 km by the powder-in-tube technique using pre-reacted (i.e. ex-situ) MgB$_2$ powders. Such tapes have a copper core for the thermal stabilisation, surrounded by fourteen Ni sheathed superconducting filaments with a Fe barrier in order to prevent the diffusion of Cu into Ni (Figure 6.1). After several steps of cold deformation yielding dimensions of 3.65 x 0.65 mm^2, annealing at 980°C was performed.
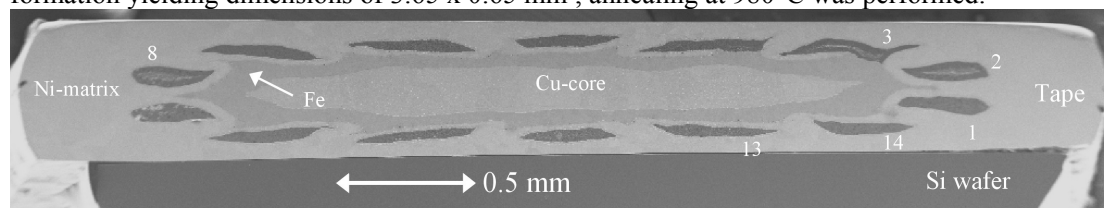
Figure 6.1: SEM-overview image of the tape in cross section. The Cu core, the Fe diffusion barrier, fourteen MgB$_2$ filaments and the Ni matrix are shown. A Si wafer is glued on one side of the tape.

Superconducting characterization i.e. T_c and J_c measurement of pieces cut from such a long tape has been performed. Current-voltage (I-V) characteristics have been measured in a cryogen-free test facility operating at temperatures between 12 and 80 K, with magnetic fields up to 1.6 T and currents up to 250 A.

The secondary electron images and the EDX (Energy Dispersive X-ray) spectra were obtained using a Jeol JSM 6500F SEM.. A sample for the SEM analysis was prepared by gluing a 3 mm piece of tape to a similarly sized Si wafer using M-bond as described in section 2.2.4 (Figure 6.1). The same sample was also used for EPMA analysis by Wavelength-Dispersive X-ray spectroscopy (WDX), performed with a Jeol Superprobe 8900 RL operated at a primary energy of 15 keV with a probe current of 15 nA. Further details about the EPMA analysis of Mg-B compounds are given in Wenzel et al. [9].

The TEM analysis was performed using a ZEISS-912 analytical TEM (see section 2.3.4.for details). Images and diffraction patterns were acquired digitally using the EsiVision software [167]. The EDX spectra were acquired and processed using the INCA software [128]. The quantitative analysis of the spectra was performed by the Cliff-Lorimer method. User defined values of 17.360 and 2.250 [114] which gave reliable MgB_2 mole fraction ratios close to 2 in thin regions of the sample were used as Cliff-Lorimer factors for B-K_α and O-K_α x-rays . The Cliff-Lorimer factor of Mg-K_α x-rays (1.076) was not changed. Absorption of B-K_α x-rays was, however, not explicitly taken into account. Samples for TEM analysis were prepared in the conventional manner as described in section 2.3.5.

Great care was taken to avoid carbon contamination during the sample preparation process both for SEM and TEM. Also artefact induced oxidation of the samples have to be avoided. Chemical analysis in the SEM, EPMA and TEM allows to assess the quality of the samples. Carbon and oxygen free regions of samples were prepared and analysed by SEM, EPMA and TEM and show that no artefacts are introduced in the preparation process.

6.3 Results

6.3.1 Superconducting properties

In Figure 6.2 the transport critical current density in magnetic fields of 0, 0.5 and 1 T is reported as a function of the temperature, measured with the magnetic field perpendicular to the plane of the tape. T_c of 36.5 K and J_c of 2.0 x 10^5 Acm^{-2} at 20 K and 1 T is obtained. Similar $J_c(B)$ curves were obtained for samples cut from 6 different places in the 1.6 km long, copper stabilised tape [83]. This indicates that the $J_c(B)$ curves are representative of the whole length of the tape and are reproducible.
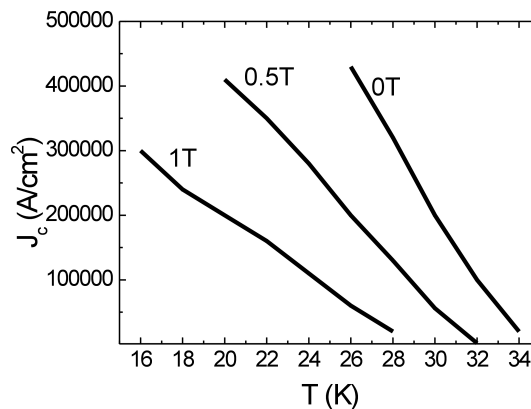
Figure 6.2: Transport critical current density as a function of temperature at 0, 0.5 and 1 T.

6.3.2 Microstructure of the MgB_2 core

SEM images of the MgB_2 core of the filaments are shown in Figure 6.3 (a and c). Typically the size of the MgB_2 colonies, i.e. arrangement of several well connected grains, is found to vary

between 0.5 and 6 μm. Sub-micrometer sized voids are also observed. Dark phases, i.e. higher borides of MgB_4, MgB_7 were found at the centres of a few extremely large colonies as shown in Figure 6.3 (a). The volume fraction of such phases is however small and were observed in only three of the fourteen filaments.
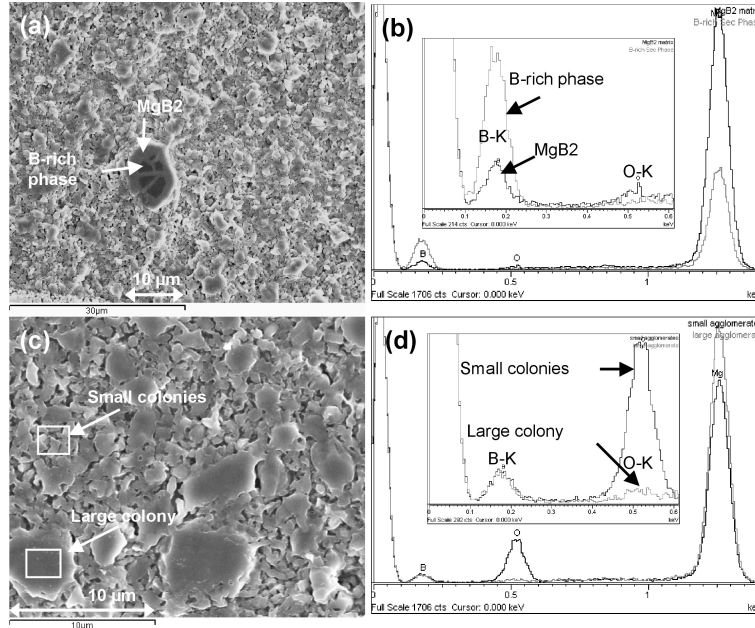
Figure 6.3: SEM images of the cross-section of a tape showing (a) B-rich phase and the MgB_2 matrix, (c) large and small MgB_2 colonies. The SEM-EDX spectra obtained from the regions indicated in (a) and (c) are shown in (b) and (d) respectively. Portions of the spectra around $B-K_\alpha$ and $O-K_\alpha$ peaks are shown magnified in the insets.

The SEM-EDX spectra acquired from the regions indicated in Figure 6.3 (a and c) are shown in Figure 6.3 (b and d) and the elemental quantification is given in Table 6.1. It can be seen that the cores of the large colonies have a B/Mg mole fraction ratio close to 2 and the oxygen mole fraction is ~ 1 at.%. In the spectrum obtained from a region containing many small MgB_2 colonies, a large (~ 16 at.%) oxygen mole fraction is found. The dark phases shown in Figure 6.3(a) were found to be boron-rich phases with boron to magnesium mole fraction ratio of about 8.

Table 6.1: SEM-EDX quantification of the MgB_2 matrix and B-rich phases in large (~5 μm) colonies, and small (~1 μm) colonies.

	B at.%	O at.%	Mg at.%	B at.%/ Mg at.%
MgB_2	66.01	0.91	33.08	2
B-rich phase	89.2	0.19	10.61	8.41
Large colony	65.21	1.14	33.64	1.94
Small colonies	56.75	17.36	25.89	2.19

Precise chemical composition of the MgB_2 matrix in the core of the filaments was determined using EPMA. Metallic boron was used as a standard. In order to avoid the effects of chemical shifts in the positions of $B-K_\alpha$ peak, and to increase the number of $B-K_\alpha$ x-ray counts, the so-called area intensity measurement mode [9] was used. Five measurements were performed at the centres of the ~ 5 μm large MgB_2 colonies and the B, O, and Mg mole fractions are given in Table 3.3 of chapter 3. Correlation diagrams of Mg and O mole fractions versus B mole fractions are given in Figure 6.4. The measured Mg and B mole fractions are close to that of stoichiometric MgB_2, indicated by a filled circle. The average value of the B/Mg mole fraction ratio is 2.02 and the average mole fraction of oxygen is ~0.5 at.%.

TEM bright-field image of a MgB_2 colony at low magnification is shown in Figure 6.5 (a). Grains 1 and 2 inside a 5 μm colony are clearly identified by diffraction contrast. A dark field image (at a higher magnification) of grain 1 acquired under a two-beam diffraction condition with a

(101) reflection strongly excited is shown in Figure 6.5 (b). Long straight dislocations are seen with an average spacing of ~ 0.1 μm which corresponds to a dislocation density of 1×10^{10} cm^{-2}. Figure 6.6 (a and b) are bright and dark-field images of another MgB$_2$ grain under two beam conditions, 15 to 70 nm sized precipitates are seen. From the TEM dark-field images, the size of a typical MgB$_2$ grain was found to be between 0.5 to 1 μm, but many MgB$_2$ grains of the size between 30 to 200 nm were also observed.
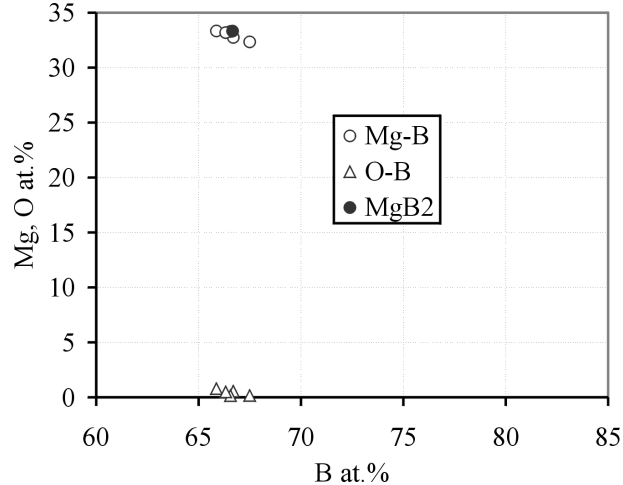
Figure 6.4: Correlation diagrams of Mg-B (○) and O-B (Δ) mole fractions of ~ 5 μm large MgB$_2$ colonies determined using EPMA. Stoichiometric MgB$_2$ composition is indicated by (●)
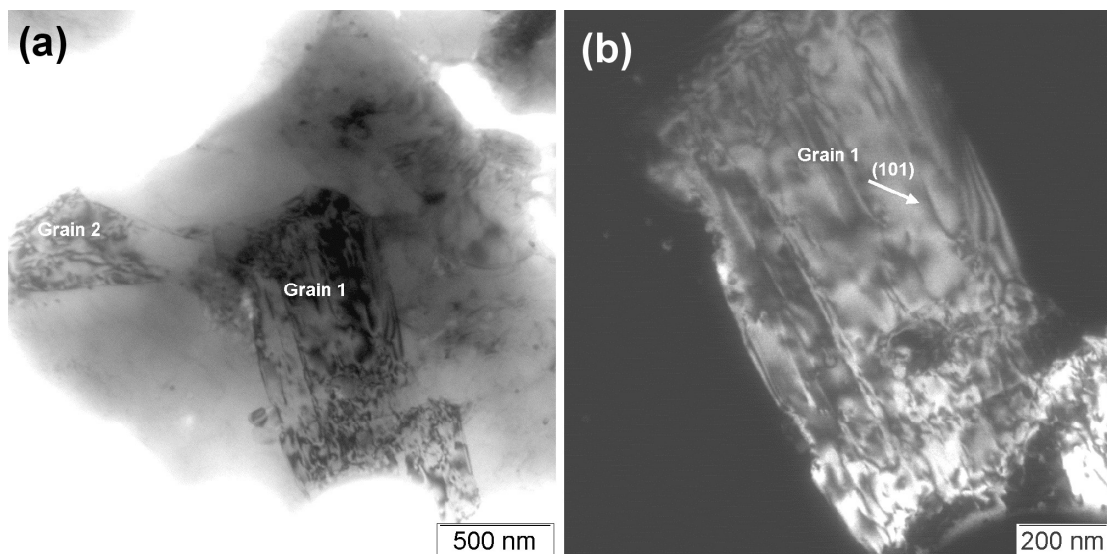
Figure 6.5: (a) TEM bright field image of a MgB$_2$ colony showing grains with different diffraction contrast.(b) Corresponding dark field image of grain 1 at higher magnification.

The chemical composition of the precipitates and the oxide layers indicated in Figure 6.6 (a) was determined from the EDX-spectrum shown in Figure 6.6 (c), and is summarised in Table 6.2 . The high O/Mg mole fraction ratio indicated the precipitate to be MgO and the oxide layer to be a mixture of MgO and Mg(OH)$_2$.
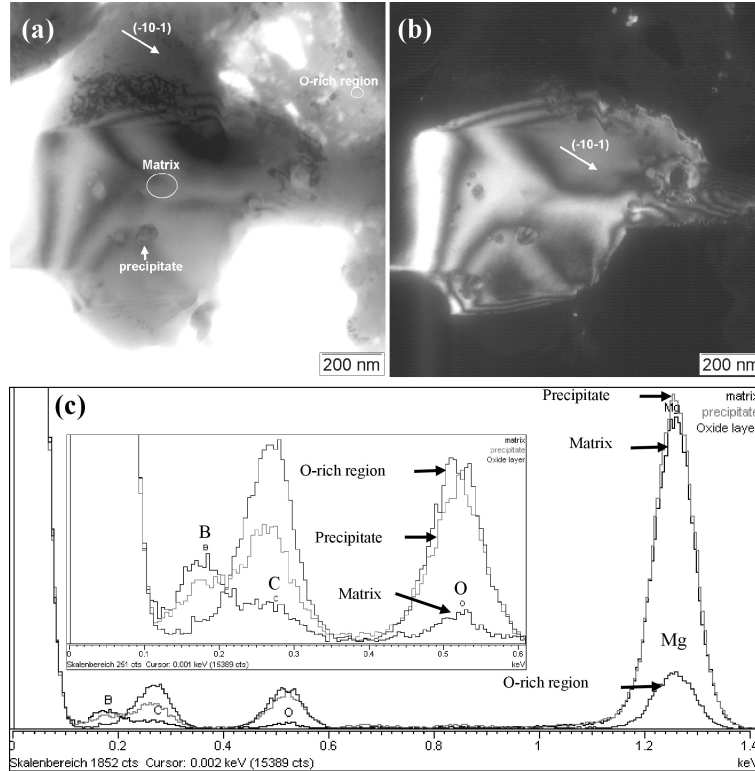
Figure 6.6: (a) TEM bright- field image showing MgO precipitate and oxygen-rich region. (b) The corresponding TEM-dark field image. (c) TEM-EDX spectra from matrix, MgO precipitate and oxide layer.

Table 6.2: O/Mg mole fraction ratios determined from the TEM-EDX quantification of the matrix, precipitate and O-rich region indicated in Figure 6.6(a).

Spektrum	Oat.% / Mg at.%
matrix	0.04
precipitate	0.23
oxide	1.64

6.3.3   Microstructure of the MgB$_2$-Ni interface

A backscattered electron image of the MgB$_2$-Ni interface acquired in EPMA is shown in Figure 6.7 (a). A reaction zone consisting of ~6 μm wide inner layer and ~4 μm wide outer layer is seen. Up to 1 μm large voids are concentrated on both sides of the inner layer.

The chemical composition of the reaction layers at the Mg-Ni interface was determined using WDX analysis in EPMA. The elemental analysis of the reaction zone is even more difficult because of the severe absorption of B-K$_\alpha$ x-rays in Nickel. Secondly the low energy x-ray lines of Ni lie close to the B-K$_\alpha$ x-ray lines, because of which, B-K$_\alpha$ x-ray intensity cannot measured in area intensity mode as was done for MgB$_2$ in the core of the filament. Therefore a MgB$_2$ ceramic was used as a standard for the calibration of B-K$_\alpha$ x-ray peak position. Thirteen EPMA measurements were acquired from the inner and outer reaction layers and the B, O, Mg and Ni mole fractions are given in Table 6.3. B-Mg, B-Ni and B-O correlation diagrams are plotted in Figure 6.7 (b). Three different intermetallic compounds of B, Mg and Ni are found. The composition of the inner reaction layer is, however, not homogenous. Along the flat sides of the filament the inner reaction layer has a composition of MgB$_2$Ni$_{2.9}$ and contains ~ 1.13 at. % of oxygen, while at the edges it has significantly boron-deficient composition of MgB$_{0.6}$Ni$_2$ and contains 2.25 at.% of oxy-

gen. The outer layer has a homogenous composition of $MgB_{3.3}Ni_{10}$ and a contains 0.09 at.% of oxygen.
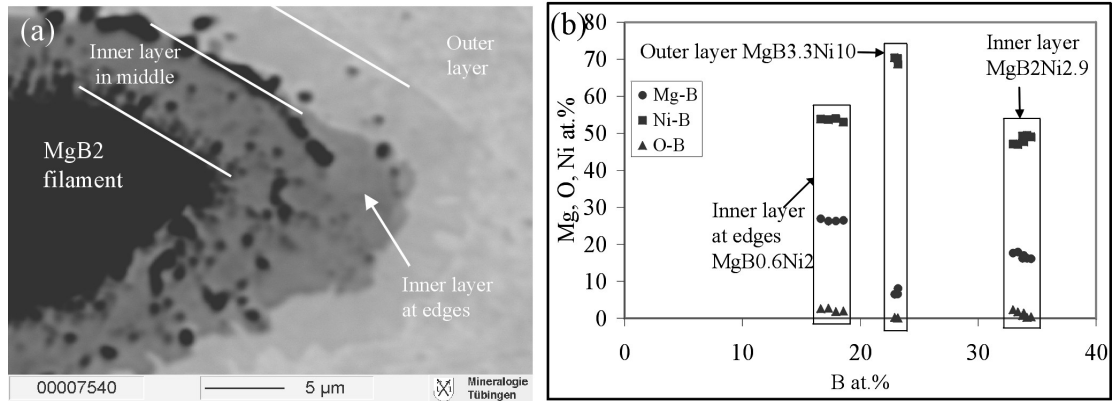
Figure 6.7: (a) Back scattered electron image of the reaction zone at the MgB_2-Ni interface of a MgB_2 filament. (b) Correlation diagrams of Mg-B (●), Ni-B(■) and O-B(▲) mole fractions determined using EPMA.

Table 6.3: EPMA-WDX quantification of the MgB_2-Ni interface reaction layers shown in Figure 6.7 (a)

	B at.%	O at.%	Mg at.%	Ni at.%
Inner layer				
1	33.37	1.72	17.92	47
2	34.15	0.23	16.21	49.41
3	33.87	1.4	16.99	47.74
4	34.49	0.39	16.1	49.02
5	33.77	0.73	16.23	49.27
6	32.96	2.31	17.63	47.11
mean	33.77	1.13	16.85	48.26
Inner layer at edges				
7	18.57	1.91	26.48	53.04
8	17.93	1.78	26.29	54
9	17.3	2.72	26.27	53.71
10	16.65	2.6	26.91	53.85
mean	17.61	2.25	26.49	53.65
Outer layer				
11	23.17	0.04	6.57	70.22
12	23.2	0.02	8.07	68.71
13	22.92	0.19	6.5	70.39
mean	23.1	0.09	7.05	69.7

TEM bright field image and the diffraction patterns of the MgB_2-reaction zone interface are shown in Figure 6.8 (a). Diffraction patterns were obtained from the upper part "MgB_2" in Figure 6.8 (a) and confirmed the presence of MgB_2. TEM-EDX spectra acquired at the regions indicated in bright-field image are shown in Figure 6.8 (b). Spectrum 21 is a typical MgB_2 spectrum. Spectrum 20, however, shows a reduced Mg peak and a prominent Ni peak. O/Mg and Ni/Mg mole fraction ratios determined from the quantitative analysis of the spectra are given in Table 6.4 .
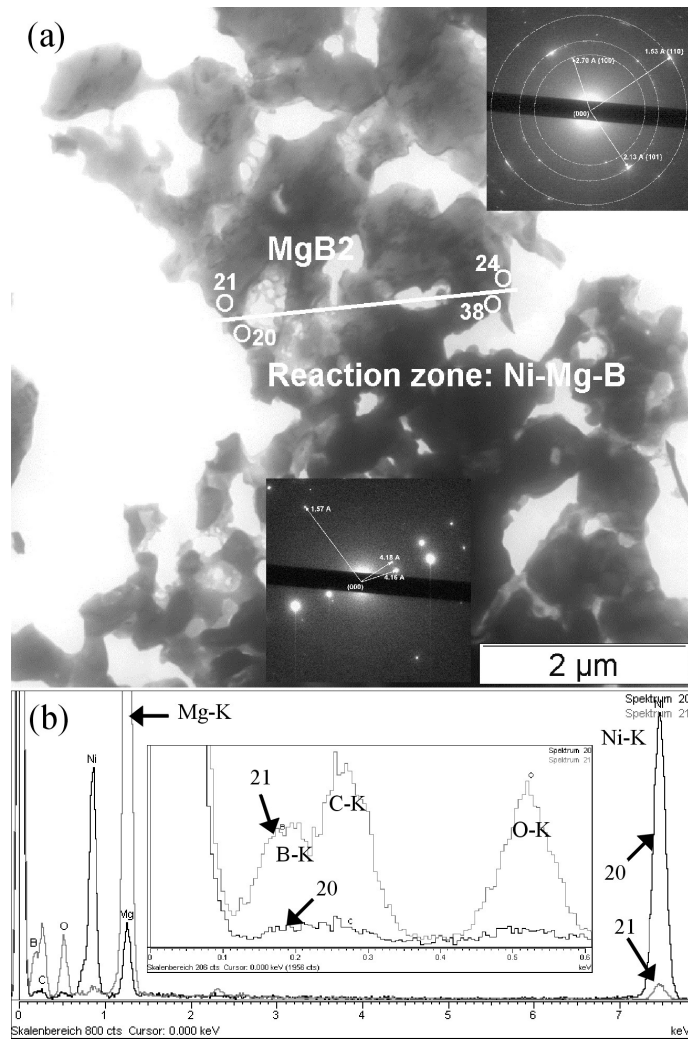
Figure 6.8: (a) TEM bright-field image of the MgB$_2$-reaction zone interface. TEM diffraction patterns are shown in the inset. (b) TEM-EDX spectra from the MgB$_2$ (spectrum 21) and from the reaction zone (spectrum 20). Portions of the spectra around B-K$_\alpha$ and O-K$_\alpha$ are shown magnified in the inset.

Table 6.4: O/Mg and Ni/Mg mole fraction ratios in the MgB$_2$ and the reaction zone, determined using TEM-EDX.

Spektrum	O at.% / Mg at.%	Ni at.% / Mg at.%
Spectrum 21 (matrix)	0.17	0.02
Spectrum 21 (reaction zone)	0.08	3.91

6.4   Discussion

6.4.1   Microstructure and chemical composition of MgB$_2$ core

SEM and TEM images of the MgB$_2$ core show that the MgB$_2$ in the filaments is porous only on the sub-micrometer scale. The MgB$_2$ colonies are structurally well connected to each other and to the Ni sheath. The size of the MgB$_2$ colonies varied from 1 to 6 μm (Figure 6.3(c)). Comparing these SEM images with those of the starting MgB$_2$ powders (not shown here), it was evident that the MgB$_2$ colonies had grown in size and the structural connectivity between the colonies had improved mostly during the annealing of cold drawn tapes.

The typical grain size determined using TEM bright and dark-field images (Figure 6.4 and Figure 6.5) was 0.5 to 1 μm. However, numerous grains with sizes between 30 to 200 nm were also found. Such a wide distribution of grain sizes means that, although the average grain size is

large (0.5 to 1 μm), numerous grain boundaries are still present and could significantly contribute to the possible grain boundary pinning. Long straight dislocations with a density of 1 x 10^{10} cm^{-2} and 15-70 nm sized MgO precipitates were found in some of the grains, which can act as pinning centres.

SEM and TEM EDX analysis prove that non superconducting layers, which appear as oxide layers in SEM and TEM samples, are present at the surface of the MgB$_2$ colonies. Amorphous layers at grain boundaries were also reported by Zhu et al. [166] who also identified them to be rich in Mg and O. The origin of the formation of such layers is not understood. In spite of such layers, J$_c$ as high as 2.0 x 10^5 Acm^{-2} have been reached at 20K, 1T (see Figure 6.2). The critical current density of the MgB$_2$ tapes might increase if these layers could be removed. Detailed analysis of these layers by advanced electron microscopy techniques namely x-ray elemental mapping in SEM and TEM, and electron spectroscopic imaging highlights the granular character of the microstructure, allows to obtain the oxygen distribution and will be described in chapter 8.

6.4.2 Microstructure and chemical composition of the MgB$_2$-Ni reaction layer

A reaction zone with a total width of 10 μm is formed at the MgB$_2$-Ni interface as seen in Figure 6.7 (a). Efficient transfer of heat from the MgB$_2$ core to the surrounding metallic sheath is essential in order to transport critical current densities > 10^5 Acm^{-2}. The characterisation of the reaction zone at the MgB$_2$-Ni interface was therefore important. Using WDX analysis in EPMA the composition of the major portion of the inner reaction layer was determined to be MgB$_2$Ni$_{2.9}$ and an intermetallic phase with a similar composition of MgB$_2$Ni$_3$ [168] was reported in the literature. At the elongated edges, however, the inner reaction layer has a highly boron-deficient composition of MgB$_{0.6}$Ni$_2$. The anisotropy of boron distribution in the inner layer is likely to be due to the anisotropy in the stresses applied during the final cold deformation steps. The 1 μm voids on both sides of the inner reaction layer might be due to vacancy formation during the diffusion processes, i.e. the Kirkendall effect [169]. The outer layer was found to have a composition of MgB$_{3.3}$Ni$_{10}$ while a phase reported in the literature has a composition of MgB$_2$Ni$_{6.7}$ [170]. Bellingeri et al. [155] determined the chemical composition of a reaction layer at the Ni-MgB$_2$ interface in their monofilamentary tapes using neutron diffraction and found it to be MgB$_2$Ni$_{2.5}$, another intermetallic phase of B, Mg and Ni , which has also been reported in the literature [171]. Depending upon their thermal conductivity, these intermetallic phases would affect the heat transfer from the MgB$_2$ core to the surrounding metallic sheath and cryogen. The thermal conductivity of these intermetallic phases of B, Mg and Ni have not so far been reported in the literature.

6.4.3 Correlation of superconducting properties and microstructure

For the investigated tapes the transition temperature T$_c$ and the critical current density J$_c$ was measured over a large range of magnetic fields and temperatures. However, B$_{c2}$ of the multifilamentary tapes was not measured and, therefore, the its role on J$_c$ cannot be discussed here.

The transport critical current density 2.0 x 10^5 Acm^{-2} at 20 K and 1 T of the multifilamentary tapes reported in this chapter is comparable to the inductive J$_c$ of multifilamentary strands of Sumption et al. [159], and higher than the J$_c$ of the monofilamentary tapes [172].

The J$_c$ of the multifilamentary tapes studied here relates to the microstruture in the following three points:

(1) *Density of pinning defects.*

Our investigations showed the grain size to vary between 30 to 1000 nm and many grains showed dislocations with a density of 1 x 10^{10} cm^{-2}. Fabrication of the tapes involves plastic deformation in the form of cold drawing and rolling. The fractioning of the MgB$_2$ grains and the introduction of defects like dislocations is thus likely to happen. In addition, 15-70 nm MgO precipitates were also found. The relatively large coherence length of MgB$_2$, about 10 nm, means that most of these defects can act as flux pinning centres.

(2) *Granularity and grain size.*

Granularity was identified in the microstructure of the multifilamentary tapes. Dense colonies with diameters of 1-6 μm were identified in a porous matrix. In the porous matrix the size of the voids is smaller than 1 μm. Non-superconducting oxide layers were found at the surface of the MgB_2 colonies. Therefore, granularity exists because of two reasons, (i) structural granularity as shown in this chapter and (ii) granularity due to the B_{c2} anisotropy as discussed in [163], [164].

The J_c of the multifilamentary tapes shows a strong field dependence even in the 1 T regime: J_c at 20 K is reduced by a factor of 2 when the field is increased from 0.5 T to 1 T. Preliminary investigations by Braccini et *al.* [172] showed that due to ball milling of starting precursor powders, the J_c of their monofilamentary tapes increased and the anisotropy in the field dependence of the J_c decreased.

Recently Häßler et al.[73] have reported a very much improved field dependence of the J_c (5.0×10^4 Acm^{-2} at 20 K , 3 T) by using mechanically alloyed, fine grained MgB_2. It is assumed that J_c and its field dependence would be further improved for the multifilamentary tapes by decreasing the grain size of the MgB_2 and by eliminating the non-superconducting layers at the surface of the colonies.

(3) *Thermal stability.*

The central copper core in the tapes ensures that the heat generated at the local hot spots is efficiently transferred to the cryogen. The undesirable situation in which partial quenching by hot spots occurs is thus prevented, even when large superconducting currents are transported. Intermetallic layers were formed at the MgB_2-Ni interface and might reduce the transfer of heat generated by local hot spots.

6.5   Summary and Conclusions

Thermally stabilised multifilamentary MgB_2 tape carrying critical current densities of 200000 Acm^{-2} at 20 K and 1 T were produced over a length of 1.6 km. The transition temperature T_c and the critical current density J_c was measured over a large range of magnetic fields and temperatures. However, B_{c2} was not measured.

For SEM, EPMA and TEM sample preparation, carbon contamination was reduced to a minimum by (i) resin free preparation (ii) ion etching (iii) immediate transfer to the microscope after preparation. A quick, reliable and standard-less method of B-quantification using SEM-EDX was established for the analysis of MgB_2 wires and tapes.

MgB_2 filaments in the tapes are found to be granular, yielding colonies (dense arrangement of grains) in a porous matrix. The size of the MgB_2 colonies varied between 1 to 6 μm. The B to Mg mole fraction ratio in the MgB_2 colonies is close to 2 and O mole fraction is less than 1 at.%. The colony size and their structural connectivity with each other is increased in comparison to the initial MgB_2 powder mostly during post-cold drawing annealing.

Non-superconducting layers were found at the surfaces of MgB_2 colonies, which might limit the critical current density. These layers appear as oxide layers in SEM and TEM samples. The typical size of the MgB_2 grains was between 0.5 to 1 μm, but numerous MgB_2 grains of the size between 30 to 200 nm were also observed because of the fractioning of MgB_2 grains during cold rolling. Dislocations with a density of 1×10^{10} cm^{-2} and 15-70 nm sized precipitates were observed. These grain boundaries, dislocations, precipitates can act as flux pinning centres in these tapes. A 10 μm reaction zone in the form of intermetallic phases of Mg, B and Ni is formed at the MgB_2-Ni interface.

Reduction of the MgB_2 grain size by milling of starting MgB_2 powder and reduction of non-superconducting layers around MgB_2 colonies could further enhance the critical current density because of improved pinning and connectivity.

Chapter 7

7   MgB$_2$ bulk and tapes prepared by mechanical alloying: influence of the boron precursor powder[73]

7.1   Introduction

The preparation of MgB$_2$ samples including the characterization of the superconducting properties has been widely discussed in the literature [14].

The properties of the MgB$_2$ powders (phase fraction, grain size) depend, on the preparation parameters but also on the quality of the precursor powders. Influence of the quality of the precursor powders on the MgB$_2$ was first reported by Ribeiro et al. [173] and Zhou et al. [174] and showed that the results of different groups are not comparable without the characterisation of the used boron precursor powder.

Chen et al. [175] recently analysed the boron precursor powders using SEM and x-rays. Crystalline x-ray peaks were found in some powders specified to be amorphous, while boron oxide peaks were found in some other boron powders. In general the "amorphous" powders have a smaller grain size and are characterised by a higher reactivity in comparison to the "crystalline" boron powders. The bulk samples prepared with these powders show higher critical current densities.

While considering the quality of the starting elemental powders, it is necessary to distinguish between impurities which reduce the MgB$_2$ phase by reacting with either Mg or B and those which do not [142] [176]. Furthermore, the crystal structure of the boron precursor powder affects the kinetics of the MgB$_2$ formation and consequently also the superconducting properties [175].

Mechanical alloying is a special in-situ technique, which produces MgB$_2$ from the elemental powders. Mg and B are filled in a milling vessel and milled in a planetary ball mill. During this high-energy milling a partial reaction to MgB$_2$ takes place [177] [178] [179]. A similar technique was used by other groups [180] [181], but the amount of MgB$_2$ formation and grain size reduction is likely to be smaller, since short milling times were applied. The resulting nanocrystalline powder consists of MgB$_2$, Mg, B, MgO and some worn out material from the milling tools e.g. tungsten carbide. This precursor powder is highly reactive and tapes can be prepared at relatively low temperatures (500-600°C) by the powder-in-tube technique (PIT) [182] [183][184].

The influence of the impurities of the boron precursor powder on the microstructure and superconducting properties of tapes and ceramics prepared by mechanical alloying will be discussed in this chapter. Electron beam techniques like SEM, EPMA and TEM are very sensitive to the analysis of light elements and have recently been applied by Eyidi et al. for the microstructural analysis of MgB$_2$ ceramics [8] and tapes [114]. In this work the microstructure analysis of the ceramics and tapes is carried out using SEM-EDX while detailed TEM investigation of the microstructure will be reported elsewhere. The problem of the quality of the precursor powders is not limited to mechanical alloying, and is important for other *in-situ* techniques also.

7.2   Experimental

7.2.1   Characterisation of the powders

The following starting materials were used: Mg powder from *Goodfellow* (99.8% "*nominal purity*", 250 μm maximum grain size) and three different boron precursor powders with nominal purities of 99% (B-a) and 95-97% (B-b) from *STREM* and 95-97% (B-c) from *Fluka*. The grain size

of all boron precursor powders was smaller than 20 μm. The nominal purity specified by the suppliers has, however, limited relevance, since the non-metallic impurities are not included.

For characterisation of the content of non-metallic impurities (C, O, S, N) in the Mg and B precursor powders, as well as in the milled powder, the carrier gas hot-extraction analysis (CGHE) with inert (O, N – using TC436-DR, *Leco*) and reactive (C, S – using EMIA 820V, *Horiba*) atmosphere was used. The samples for analysis were filled in tin capsules within a glove box.

Other metallic impurities like Mg, K, Na and Si were analysed by Spark Source Mass Spectroscopy (SSMS, using MS7 from *AEI*). The contents of the elements Mg, B and W within the mechanically alloyed precursors were determined by Inductively Coupled Plasma – Optical Emission Spectroscopy analysis (ICP-OES, using IRIS from *Thermo*). The thermal behaviour of the mechanically alloyed precursor powder was investigated by differential scanning calorimetry under argon atmosphere with a heating rate of 20 K/min using a Netzsch DSC404.

7.2.2   Preparation of precursor powders, bulk samples and tapes

To prepare precursor powders by mechanical alloying (MA), Mg and B (in the stoichiometric ratio of 1:2, the Mg content of the boron precursor powders was not taken into account) were milled for 50 hours in a planetary ball mill. Repeated fractioning of powder particles and partial formation of MgB_2 takes place via a solid state reaction. More details of this technique have been described in recent papers [177][178]. For the high-energy milling, tungsten carbide (WC) milling tools with cobalt binder were used. The milling was done in Ar atmosphere. In the subsequent processing steps the exposure of the MA powder to air was kept to a minimum.

The MA powders are further processed in different ways to bulk samples and tapes. The bulk samples were prepared by hot-pressing of MA powder. In a vacuum chamber, uniaxial pressure of 640 MPa was applied at 700°C for 10 minutes on MA powder (300 mg), which yielded a disk with a diameter of 10 mm and a thickness of about 1 mm.

As the first step of the PIT-processing of tapes, rods of the precursor powder were prepared by cold isostatic pressing at 350 MPa. The rods were filled into Fe tubes with 10 mm outer and 6 mm inner diameter, which were deformed by shape rolling, drawing and flat rolling to mono-filamentary tapes of about 0.35 mm thickness and 3.5 mm width. Typical values of the filling factor (core area : overall area) of mono-filamentary tapes were in the range of 0.31 – 0.37. The tapes embedded in an oxygen gettering foil were heat treated at temperatures between 500 and 650°C for 3h under Ar atmosphere.

7.2.3   Microstructure and electrical characterisation of bulk samples and tapes

A Jeol JSM 6500F SEM and Zeiss 912Ω TEM (see chapter 2 for details) have been used for electron microscopy analysis. The grain size, crystallinity and impurities of the boron precursor powders were determined using analytical SEM and TEM. Secondary electron imaging and EDX in SEM has been used to study cracks, voids and B-rich secondary phases in MgB_2 bulk and tapes. The reliability and reproducibility of the SEM-EDX analysis for B quantification was checked using a MgB_2 tape prepared by Grasso et al. [116] as a standard and by EPMA measurements [10]. Thus, the dark boron-rich secondary phases and the grey MgB_2 matrix could be identified in the SEM images and were used to estimate the volume fraction of B-rich secondary phases in MgB_2 bulk and tapes. The chemical composition of boron-rich secondary phases (hereafter referred to as B-rich phases) is either $MgB_{4+\delta}$ or $MgB_{7+\delta}$. SEM and TEM sample preparation of powders, ceramics and tapes is described in chapter 2. Carbon contamination during sample preparation and during EDX analysis was minimised.

The phase composition, grain sizes and internal stresses were determined by x-ray diffraction Rietveld analysis using a X'Pert PW 3040 x-ray diffractometer from *Philips*.

The critical temperature T_c was determined by temperature and magnetic field dependent resistance measurements using the Physical Property Measurement System (PPMS, from *Quantum Design*). T_c is reported as the temperature at which the resistance dropped to 50% of the resistance at $T_{c,onset}$. From these measurements, the superconducting transition width ΔT_c and the critical field B_{c2} and B_{irr} was determined. Transport critical current densities (J_c) of the tapes were determined by the standard four probe method using the 1µV/cm electric field criterion. The measurements were carried out at 4.2 and 20 K, in fields up to 14 T applied parallel to the plane of the tapes. J_c of the bulk samples was determined from the magnetic measurements using the Bean model [70].

Depending on the boron precursor powder B-a, B-b and B-c, the samples were labelled as follows: mechanically alloyed powders M-a, M-b and M-c, the hot pressed bulk samples S-a, S-b and S-c and tapes T-a, T-b and T-c.
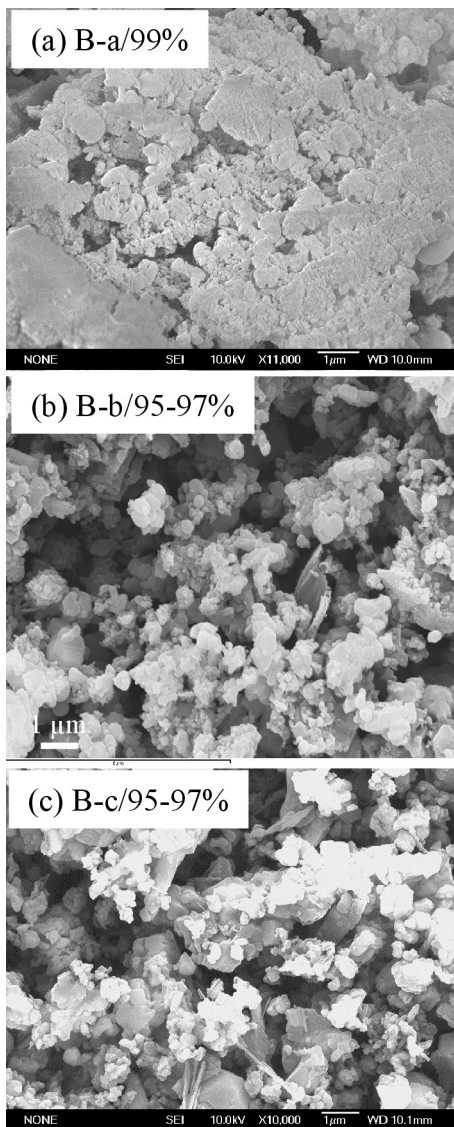
Figure 7.1: SEM images of boron powders of (a) B-a, (b) B-b and (c) B-c.
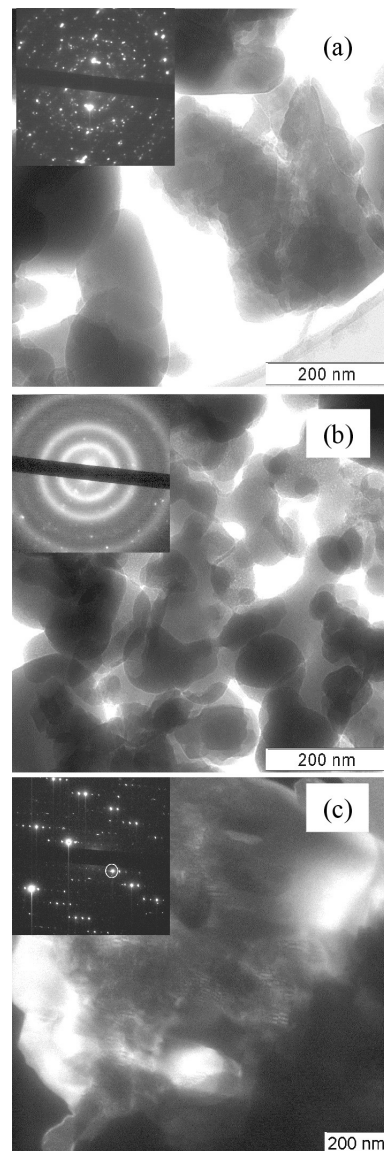
Figure 7.2: TEM bright-field images of (a) crystalline (b) nanocrystalline grains of boron powder B-a. (c)TEM dark-field image of grains in boron powder B-c. The corresponding diffraction patterns are shown in the inset.
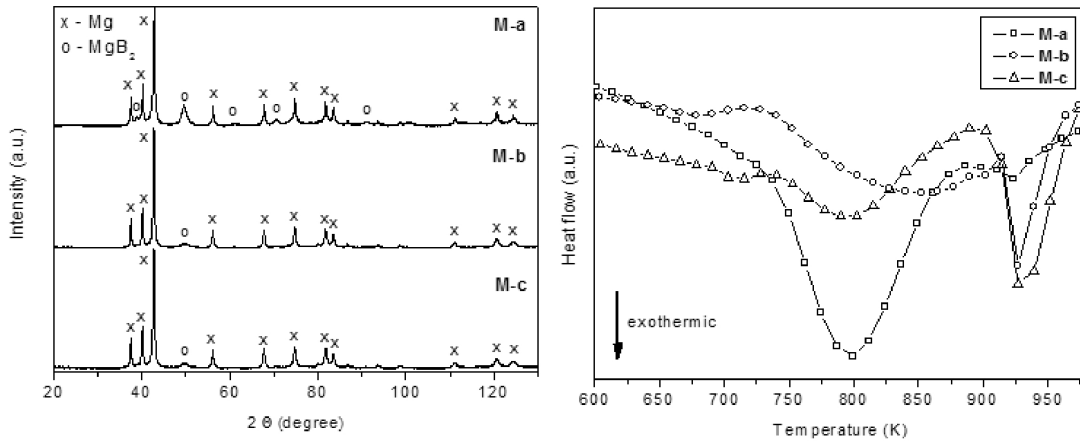
Figure 7.3: XRD measurement of the mechanically alloyed powder with different boron powders.

Figure 7.4: DSC-curves of mechanically alloyed powders prepared with different boron qualities

7.3 Results and Discussion

7.3.1 Elemental boron precursor powders

The experimentally determined impurities, the grain size and crystallinity, together with the nominal purity specified by the suppliers, of three different boron precursor powders B-a to B-c, are summarised in Table 7.1. Mg is the most frequent impurity, probably in the form of MgO, followed by alkali and alkaline earth metals like Na, K, Ca and Si. Oxygen and carbon were found to be the main non-metallic impurities. The oxygen content of the boron precursor powder with highest nominal purity, B-a, is higher than in B-c, which has a nominal purity of only 95-97%. It is however important to note that the *nominal purity* specified by the supplier considers only the metallic impurities. It is very important that also the non-metallic impurities are taken into account to correctly correlate the precursor powder purity with the material properties.

Table 7.1: Nominal purity, impurities, grain size and crystallinity of boron precursor powders from different suppliers.

Boron powders	B-a	B-b	B-c
Supplier	STREM	STREM	Fluka
Batch number	B2401051	B1371092	371465/1
Nominal purity (%)	99	95-97	95-97
Impurity contents determined by SSMS and CGHE			
Metallic impurities	Mg 400, Na 80, Si 41,	Mg 7300, Si 2600, Ca 840,	Mg 4900, K 1500, Na 310,
(µg/g)	Ti 9	Na 590	Si 300 (all others <100)
C (wt.%)	0.25	0.35	0.29
O (wt.%)	3.55	3.31	1.87
Microstructure analysis using SEM and TEM			
Average grain size (nm)	~110	~300	~500
Crystallinity	Crystalline + Nanocrystalline	Crystalline + Nanocrystalline	Crystalline
Ref. figure	1a/2a	1b/2b	1c/2c

The grain sizes of the boron precursor powders B-a, B-b and B-c were estimated from the SEM images in Figure 7.1(a-c) and confirmed by TEM imaging and diffraction (Figure 7.2). EDX microanalysis in SEM and TEM was used to qualitatively identify the impurities in boron powders. Type B-a has crystalline grains of size ~110 nm (Figure 7.2(a)) and nanocrystalline grains which are strongly agglomerated (Figure 7.1(a) and Figure 7.2(b)) . Mainly Mg and O but also some K, Ca, F impurities were detected in the nanocrystalline grains. Relatively less impurities were found in the crystalline grains. B-b is similar to B-a, but contains larger grains. B-c is

very different from B-a and B-b as it has large crystalline grains and contains relatively smaller amounts of Mg and O impurities although its *nominal purity* is only 95%. All the boron precursor powders investigated in this study were specified to be amorphous. The electron diffraction patterns of Figure 7.2, however, clearly show that the boron powders are either nanocrystalline or crystalline.

7.3.2   Mechanically alloyed powder

Mechanically alloyed MgB_2 precursor powders M-a, M-b, and M-c were prepared using B-a, B-b, and B-c respectively. The carbon and oxygen weight fractions in the milled powder are summarised in Table 7.2. It can be seen that the carbon weight fraction did not increase during the MgB_2 preparation by mechanical alloying. During the preparation process W and Co were introduced additionally, but their weight fractions were determined by ICP-OES analysis to be < 0.01 wt.%.

Using x-ray diffraction (Figure 7.3), the phase fractions of Mg, MgB_2 and WC phases were determined and are summarised in Table 7.2. The phase fraction of MgB_2 in M-a is 1.5 times of that in M-b and M-c. This indicates that the reactivity of the boron precursor powder B-a is larger than B-b and B-c. The microstructure of the mechanically alloyed MgB_2 is nano-crystalline. The lattice parameters in M-a and M-c correspond to an undistorted lattice cell, whereas in M-b the lattice constant *c* is smaller indicating strain.

Table 7.2: Impurity analysis using CGHE and structural analysis using x-ray diffraction of mechanically alloyed powders.

Mechanically alloyed powder	M-a	M-b	M-c
B nominal purity (%)	99	95-97	95-97
Milling time (hours)	50	50	50
Impurity analysis using CGHE			
C (wt.%)	0.154	0.121	0.191
O (wt.%)	3.37	3.74	1.84
Structural analysis using XRD			
Lattice parameter *a* (nm)	0.3085	0.3086	0.3087
Lattice parameter *c* (nm)	0.3523	0.349	0.3519
Ratio *c / a*	1.142	1.131	1.140
Grain size (nm)	4	2	5
MgB_2 phase content (wt.%)	47	30	31
Mg phase content (wt.%)	53	70	68
WC phase content (wt.%)	-	-	1
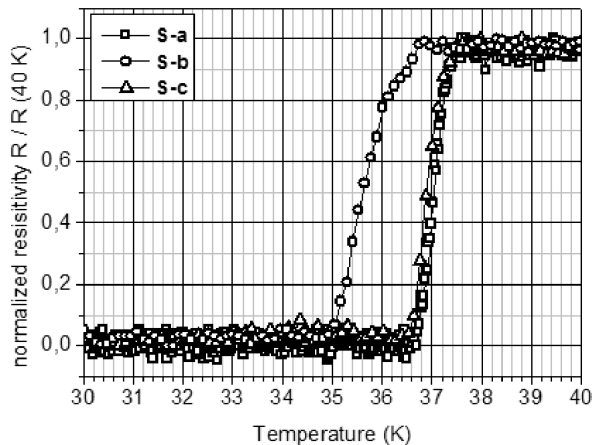
Figure 7.5: Resistive transition curves of bulk samples.
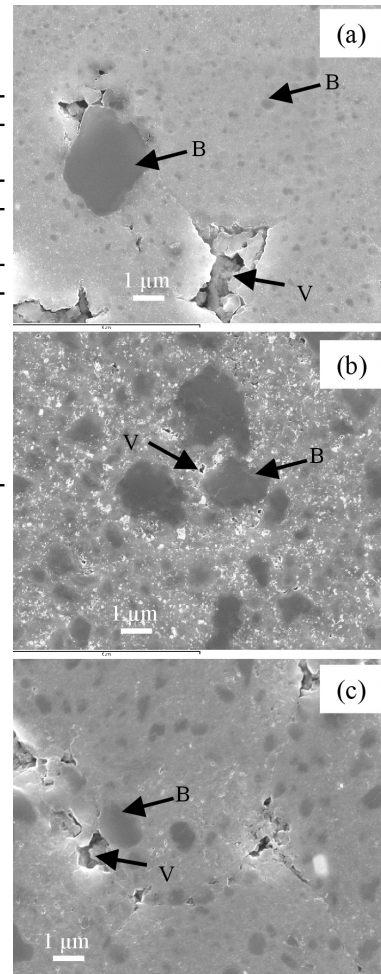
Figure 7.6: SEM images in plan-view of hot pressed bulk samples (a) S-a, (b) S-b and (c) S-c. The B-rich phases and voids are indicated by B and V respectively.

Figure 7.4 shows the DSC-curves of three different mechanically alloyed powders during heating. It can be seen that the reaction of Mg and B takes place in two steps, one at about 500°C, the other at about 650°C. For the powder M-a the main DSC-peak occurs at a lower temperature and only a small peak occurs at about 650°C. For M-b and M-c the situation is opposite. This is in agreement with the x-ray diffraction result indicating that the reactivity of powder M-a is larger compared to M-b and M-c. All measured DSC-peaks belong to the MgB_2 formation and are not due to phase transitions or other chemical reactions.

7.3.3   Bulk samples

Bulk samples S-a, S-b, and S-c were prepared using different mechanically alloyed powders (M-a, M-b, M-c) by hot pressing at 700°C and 640 MPa for 10 minutes. During hot pressing Mg and B nearly completely react to form MgB_2, which is sintered to about 90% of the theoretical density. A comparison of the microstructure and superconducting properties of these samples is given in Table 7.3.

Table 7.3: Synthesis parameters, structural analysis by x-ray diffraction, microstructure analysis by SEM-EDX, and superconducting properties of hot pressed bulk samples.

Bulk sample	S-a	S-b	S-c
B nominal purity (%)	99	95-97	95-97
Annealing temp. (°C)	700	700	700
Pressure (MPa)	640	640	640
Structural analysis using x-ray diffraction			
Lattice parameter a (nm)	0.3085	0.3086	0.3086
Lattice parameter c (nm)	0.3525	0.3523	0.3523
Ratio c / a	1.143	1.142	1.142
Grain size (nm)	19	58	65
MgB_2 phase content (wt.%)	95.2	85.0	94.8
Mg phase content (wt.%)	-	3.5	<1
MgO phase content (wt.%)	4.8	11.2	5.0
WC phase content (wt.%)	<1	<1	<1
Microstructure analysis using SEM-EDX			
Void size (μm)	5-30	5-15	5-30
B-rich phases: Size (nm)	~200 nm	~1000	600
B-rich phases: Volume fraction (vol%)	<3	~10	~3
O mole fraction (at.%)	~2.5	5	2.5
Superconducting properties			
T_c (K)	36.8	35.6	37.0
ΔT_c (K)	0.6	1.5	0.6
B_{c2} at 0K (T)	22	18	22
B_{irr} at 0K (T)	16	12	16
J_c at 20 K, 1 T (A/cm²)	$4,7 \cdot 10^5$	$2,5 \cdot 10^5$	$4,0 \cdot 10^5$

The grain size of S-a is about 20 nm and is confirmed also by preliminary TEM investigations. In comparison the grain size of S-b and S-c are three times bigger. These grain sizes are one order of magnitude smaller than the MgB_2 grain sizes reported of ceramics , wires and tapes prepared by other groups [8][114][116]. Using x-ray phase analysis, sample S-b was found to contain 11.2 wt% of MgO and 3.5 wt.% of unreacted Mg. In comparison the MgO wt.% in sample S-a and S-c is smaller by a factor of 2 and the Mg content is less than 1 wt.%.

The effect of the boron precursor powder on microstructure of the hot pressed bulk samples S-a, S-b and S-c is shown in the SEM images in Figure 7.6(a-c). In the MgB_2 matrix of all the samples B-rich phases are identified by EDX. The average size of the B-rich phases is largest (~1 μm) for S-b and constitute ~ 10 % of the sample volume. In comparison the volume fraction of B-rich phases in S-c is ~ 3 % and still smaller in S-a. Bulk samples S-a and S-c contain 5-30 μm large voids. Although the grain size and reactivity of the boron precursor powders are different, the microstructure of samples S-a and S-c is similar due to the high temperatures used during hot pressing. The oxygen mole fraction in the MgB_2 matrix of S-a and S-c was determined by EDX to

be ~ 2.5 at.% and twice as much in S-b. A large number of sub-micrometer sized bright particles are seen in the SEM image of S-b (Figure 7.6(b)), which are MgO secondary phases. This agrees with the higher MgO phase fraction found by x-ray diffraction of S-b. The oxygen mole fraction in the bulk samples is not entirely proportional to the oxygen weight fractions in the boron powders, since extra oxygen is introduced during the hot pressing. The mechanically alloyed powers M-b and M-c have a higher Mg content in comparison to M-a, which may partly oxidise. Therefore, during the subsequent annealing, the oxygen content in S-b and S-c increases more than the oxygen content of S-a.. As a result, S-a and S-c have similar oxygen mole fractions, although B-a contains a larger oxygen weight fraction than B-c.

The T_c, the critical field B_{c2}, B_{irr}, and the critical current density J_c shown in Figure 7.5, Figure 7.7 and Figure 7.8 respectively, is summarised in Table 7.3. The T_c (~37 K), ΔT_c (0.6 K), B_{c2} (22 T at 0 K) and B_{irr} (16 T at 0 K) of S-a and S-c are similar, although the J_c of S-a is slightly higher than that of S-c. In comparison S-b shows a decreased T_c, with a broad superconducting transition ($\Delta T_c = 1.5$ K), decreased B_{c2} and J_c smaller by a factor of about 2. Better superconducting properties of S-a and S-c can be explained by the dominant MgB_2 phase and the lower oxygen mole fraction in S-a and S-c. J_c of S-a decreased less rapidly at higher fields, which might be attributed to the increased grain boundary pinning because of the smaller grain size of S-a. The J_c of S-a is higher than the J_c of bulk MgB_2 with ZrO_2 additives reported recently [185]. Detailed TEM investigation of the microstructure will be necessary to explain the J_c of the various samples. In conclusion, boron precursor powders like B-a, with smaller grain size and low metallic impurities are most appropriate for the synthesis of bulk MgB_2 by hot pressing.
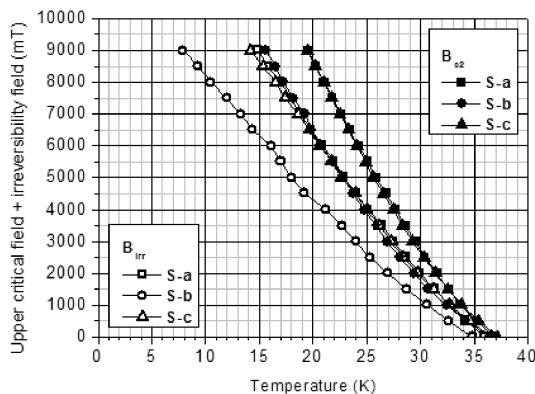
Figure 7.7: Upper critical fields B_{c2} and irreversibility fields Birr of bulk samples estimated from R(T,B)-curves.
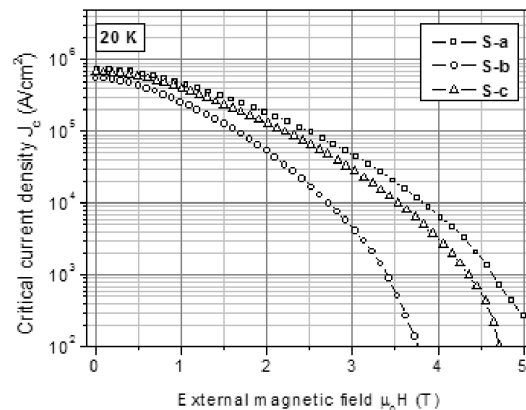
Figure 7.8: Critical current densities J_c of bulk samples at 20 K calculated from magnetisation measurements using the Bean model.

7.3.4 Tapes

For the fabrication of tapes powders M-a and M-c were used. During the fabrication of Fe sheathed tapes work hardening takes place. Therefore, several annealing steps at temperatures between 450°C and 500°C are necessary for the secondary recrystallisation of the Fe sheath. The powder M-a is more reactive than M-c and reacts at temperatures close to 500 °C to form MgB_2 as suggested by the DSC analysis in Figure 7.4. Therefore a partial MgB_2 formation takes place in tape T-a during the several annealing steps of the wire drawing process. The MgB_2 grains are heavily deformed in the next drawing step and therefore refined to smaller sizes. At the same time, a hardening of the wire core and a strong agglomeration of grains (size about 10 μm) are seen in the metallographical image (Figure 7.9(a)) of the as deformed tape T-a. In comparison the microstructure of filaments of the tape prepared with powder M-c is more homogeneous (Figure 7.9(b)).
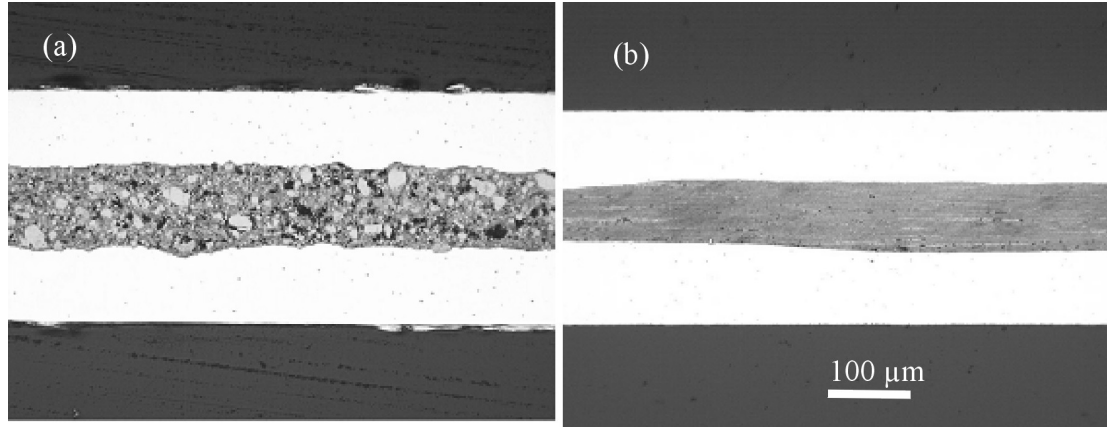
Figure 7.9: Metallographical images of the as deformed but not annealed tapes T-a and T-c.

Low and high magnification SEM images of the annealed tapes T-a1, T-a2 and T-c1, T-c2 are shown in Figure 7.10 (a-d). Tape T-a1 and T-a2 were synthesised using powder M-a and annealed at 500°C and 650°C respectively. Tapes T-c1 and T-c2 were prepared from powder M-c and annealed at temperatures 500°C and 600°C. The superconducting properties and the size of the B-rich phases, cracks and voids in the MgB_2 matrix of the tape estimated from the SEM images are summarised in Table 7.4.

Table 7.4: Synthesis parameters, microstructure analysis by SEM-EDX and superconducting properties of tapes.

Tapes	T-a1	T-a2	T-c1	T-c2
B nominal purity (%)	99	99	95-97	95-97
Annealing temp. (°C)	500	650	500	600
Microstructure analysis using SEM-EDX				
Cracks (width, length) (μm)	1,30	0.2, 2	0.2, 2	1.3, 50
Void size (nm)	~ 90	~ 90	$60 - 1000$	$60 - 1000$
B-rich phase: grain size (nm)	50-500	100-250	50 - 3000	250 - 3000
B-rich phase: Vol.fraction (%)	~ 2	< 2	~ 20	~ 4
O mole fraction (at.%)	~ 7	~ 6	~ 2	~ 3
Superconducting properties				
T_c (K)	29.5	32.5	27.5	36.5
$\Delta T_{c\,(K)}$	0.5	0.7	2.8	1.0
J_c at 20 K, 3 T (A/cm^2)	-	$5,0 \cdot 10^4$	-	$5,5 \cdot 10^4$

In tape T-a1 B-rich phases have grain sizes between 50 to 500 nm and are found in the MgB_2 matrix. Most of the B-rich phases are however small and constitute less than 2 % of the sample volume. In tape T-a2, annealed at 650 °C, the B-rich phase fraction is further reduced. In tape T-c1, the grain size of B-rich phases are 50 nm to 2 μm and the volume fraction is 20 %. The formation of MgB_2 is incomplete at the annealing temperature of 500°C because of the lower reactivity and large grain size of the boron powder B-c. In tape T-c2 the 50 to 200 nm sized B-rich grains have completely reacted to MgB_2 and the B-rich phase fraction has decreased to 4%, because of the higher annealing temperature of 600°C. Oxygen mole fraction is 3 at.% in T-c2 and twice as much in T-a1 and T-a2, which corresponds qualitatively to the oxygen ratio in the powders M-a and M-c. The extra oxygen might be introduced during the wire and tape preparation especially during the preparation of the precursor rod by cold isostatic pressing.

Cracks are found in all tapes due to the heavy deformation during the drawing process. Tape T-a1 has 1 μm wide and $\sim$ 30 μm long cracks lying in the plane parallel to the length of the tape and perpendicular to the plane of the tape. It also contains $\sim$ 90 nm sized voids. In tape T-a2 which is annealed at a higher temperature of 650 °C, the size and density of cracks is reduced in comparison to T-a1. The tape T-c1 contains cracks parallel to the rolling direction of the tape. Very few $\sim$ 90 nm sized voids are observed. The microstructure of tape T-c2 is similar to that of T-c1, however the size and density of the cracks and voids has increased after annealing at higher

temperature. In conclusion tapes (T-c1 and T-c2) prepared using boron precursor powders (B-c) contain larger cracks and voids, which increase with annealing temperature. In contrast the size of the cracks in tapes T-a1 and T-a2 prepared using small sized boron grains (B-a) decreases with increasing annealing temperature. Therefore, the grain size of the boron precursor powder affects the formation of cracks in tapes. Another factor for the crack formation could be the higher reactivity of the powder M-a. Therefore, significant amount of MgB_2 is already formed in T-a1 and T-a2 during the intermediate annealing steps required to reduce the work hardening. On the other hand in tapes T-c1 and T-c2, most of the MgB_2 formation takes place during the final annealing step after the rolling. The associated higher shrinkage of the material, therefore, might give rise to cracks in the regions of lower density.
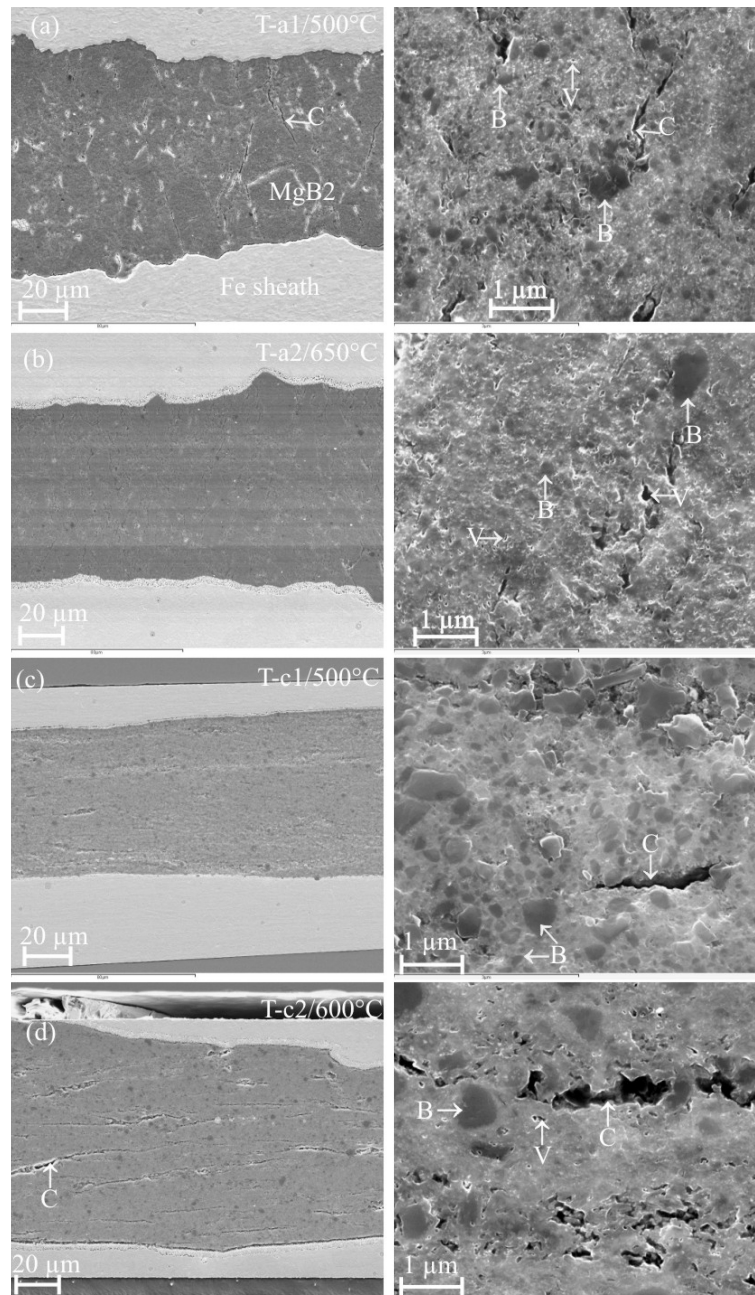
Figure 7.10: Low-magnification (left) and high-magnification (right) SEM images of Fe-sheathed tapes (a) T-a1, (b) T-a2, (c) T-c1 and (d) T-c2 after final annealing in cross-section. The cracks, B-rich phases and voids are indicated by C, B and V respectively.

The differences in the microstructure of the tapes observed in the SEM images are reflected also in the superconducting properties summarised in Table 7.4. The lower T_c and J_c of T-c1 in comparison to other tapes are related to the suppressed MgB_2 phase formation. The T_c of T-a2 is lower than that of T-c2 by about 4 K (Figure 7.11) and can be attributed to the higher oxygen mole fraction in it. The decrease in T_c could also be due to oxygen and carbon [157] contamination during the formation of tapes. The irreversibility field B_{irr} of the tape T-c increased from about 7T to 16T at 4.2 K when the annealing temperature was increased from 500°C to 600°C (Figure 7.12). In contrast the other J_c versus B curves of T-a show only small differences (which are in the range of the measurement error) for the annealing temperature in the range of 500 to 650°C. A possible cross over at 10 T in the J_c versus B curves (Figure 7.12) of T-a2 and T-c2 has to be confirmed by measurements at lower fields. The J_c of T-c2 is likely to be limited by the large density of cracks and a slightly higher B-rich phase fraction in comparison to T-a2. TEM analysis of pinning defects like grain boundaries, dislocations and precipitates [22][114] formed due to oxygen and other impurities is essential for a better understanding of the J_c of these tapes. The J_c of 5.0 x 10^4 A/cm^2 (at 20K, 3T) of the tapes investigated in this work are significantly higher than the tapes reported recently [23][186], and highlights the importance of mechanical alloying for enhancing the J_c of MgB_2 superconductors.

At this stage it is not possible to decide which of the two boron precursor powders B-a and B-c is more appropriate for the tapes. The main advantage of powder B-a is its higher reactivity, which yields compact tapes synthesised at about 500°C. Advantage of powder B-c is the higher T_c of the tapes due to the lower oxygen content. However powder B-c requires higher annealing temperatures and results in a large density of cracks in the tapes which probably limits J_c.
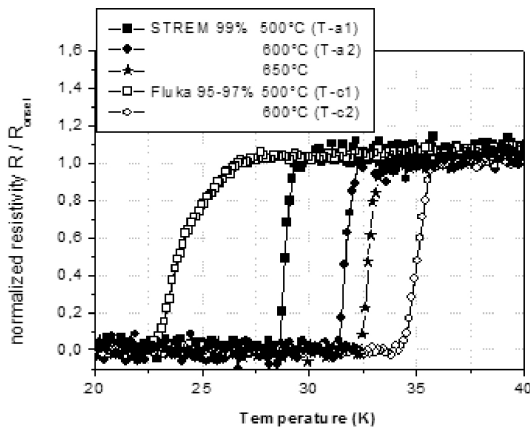
Figure 7.11: Resistive transition curves of tapes T-a and T-c, prepared with precursors M-a and M-c.
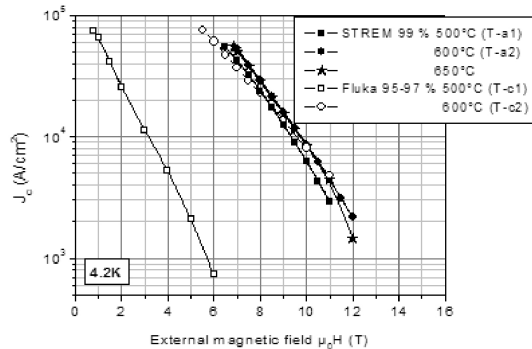
Figure 7.12: Critical current densities of tapes T-a and T-c at 4.2 K.

7.4   Summary and conclusions

Mechanically alloyed MgB_2 powders were used to synthesise MgB_2 bulk by hot pressing and tapes by PIT technology. The influence of the quality of the boron precursor powder on the microstructure and superconducting properties of MgB_2 bulk was studied. Nominal purity, which considered only the metallic impurities, was not sufficient for the characterisation of the quality of the boron precursor powders. Therefore, the non-metallic impurities e.g. O were determined using CGHE, in addition to the metallic impurities determined using SSMS and ICP-OES. The oxygen impurity in the boron precursor powder B-a was found to be highest although it had the highest nominal purity i.e. 99%. The average grain size and impurities of the boron precursor powders of different quality are determined using analytical SEM and TEM. Boron precursor powders B-a, B-b and B-c have an average grain size of ~110, 300 and 500 nm, respectively. Although x-ray

diffraction analysis shows boron precursor powders to be amorphous, electron diffraction patterns reveal them to be nanocrystalline or crystalline. Using DSC the boron precursor powder B-a was found to be most reactive and therefore a significant fraction of MgB_2 phase is formed already during mechanical alloying and during drawing of the tapes.

The grain size in the MgB_2 bulk samples was found to be small because of the mechanical alloying. The bulk samples prepared from B-a contain the largest MgB_2 phase fraction and show the highest J_c of 4.7×10^5 Acm^{-2} at 20 K and 1 T. Boron precursor powders like B-a, with smaller grain size and less metallic impurities are most appropriate for the synthesis of bulk MgB_2 samples by hot pressing. At this stage it is not possible to decide which of the two boron precursor powders B-a and B-c is more appropriate for the tapes. The main advantage of B-a is its higher reactivity because of which compact tapes can be synthesised at about 500°C. However oxygen is introduced during synthesis of tapes, resulting in a significantly reduced T_c. B-c yields a higher T_c and lower oxygen content in the synthesised tapes. It requires higher annealing temperatures and results in large density of cracks in the tapes, which probably limit J_c. The J_c of 5.0×10^4 A/cm^2 (at 20K, 3T) of the tapes investigated in this work are significantly larger than the J_c of the tapes reported in the literature. This underlines the importance of mechanical alloying for enhancing the J_c of MgB_2 tapes.

Chapter 8

8 Microstructure-critical current density model for MgB₂ wires and tapes

8.1 Introduction

At the present stage, the J_c's and resistivities of different MgB₂ superconductors, differ by orders of magnitude, the reasons for which are not fully understood.

Rowell in a review article [49] analysed the resistivity of a large number of MgB₂ single crystals, bulk samples, thin films and one wire prepared by the diffusion of Mg into the B wire. Large variations were found in the residual resistivity (at 50 K) of these samples, the minimum being 0.4 μΩcm and maximum being 1560 μΩcm. Various models like reduction in the effective current carrying cross-sectional area of the sample and Josephson junction model of the grain boundaries, were proposed to explain the increase in resistivity and decrease in J_c. Transport J_c (at zero field) of only one sample was discussed and the importance of more transport J_c measurements was underlined. MgB₂ wires and tapes prepared by the technologically important PIT technique were not considered.

Eisterer et al. [134] studied the correlation of electrical resistivity on the T_c, B_{c2} and J_c of MgB₂ wires prepared in-situ by the PIT technique. The residual resistivity was increased by neutron irradiation, carbon doping or lower processing temperature, which led to increase in B_{c2}, which in turn was shown to be the main reason for the improvement in J_c. The effectively conducting cross section of the MgB₂ filaments was found to be only one third of the geometrical cross section of filaments in pure MgB₂ wires and one sixth of the geometrical cross section in SiC added MgB₂ wires. The effect was attributed to the structural granularity, but the microstructure of these wires was not analysed in detail.

In this chapter we report the transport J_c's of a large number of wires and tapes and their correlation to the microstructure, which was investigated using the advanced electron microscopy methods described in chapter 3.

8.2 Experimental

The MgB₂ wires and tapes were prepared by different variants of the powder in tube (PIT) technique. The deformation technique, precursor powders, annealing temperatures, superconducting transition temperature (T_c), upper critical field (B_{c2}) and critical current density (J_c) of samples 1-6 are given in Table 8.1. The synthesis of the samples and measurement of their superconducting properties was carried out by the partner institutes within the HIPERMAG project.

The T_c was determined by resistivity (ρ) versus temperature (T) measurements. The J_c's were measured by transport measurements using the 1 μVcm⁻¹ criteria.

Advanced electron microscopy techniques were used to study the microstructure of MgB₂ wires and tapes. Advanced electron microscopy involves a combined SEM and TEM analysis with contamination free sample preparation, chemical mapping with good counting statistics and advanced chemical quantification as described in chapter 3. Schematic diagram of the steps involved in the microstructure analysis of MgB₂ wires and tapes is shown in Figure 3.1. These methods yield quantitative reliable data of the relevant microstructure parameters given in Table 8.1

Table 8.1: T_c, magnetic field for 10^4 Acm^{-2} current density (B*), critical current density at zero field (J_{c0}), magnitude of the reciprocal of the slope of the log $J_c(B)$ plot (B_p), synthesis method, powder, annealing temperature /time (θ), colony size (S), volume fraction of B-rich phases (f), oxygen mole fraction and MgB$_2$ grain size (g) of samples 1-6.

#	T_c (K)	J_{c0} Acm^{-2}	B_p (T)	B* (T)	Synthesis technique	Powder	θ (°C/ h)	S (μm)	f (%)	O (at. %)	g (nm)
1	36.5	1x10^6	2.03	9.6	MA	Mg (gf)+2B (fluka)	600/3	-	1.4	3.75	25
2	32.5			9.7	,,	Mg (gf)+2B (strem)	650/3	15	0.5	9.34	20
3	33.7	3.3x10^5	2.5	9.0	RWIT	Mg(aa) +2B (Geneva) +11.3 mol% SiC (aa)	650/0. 5	-	2.7	10.4	35
4	35.5	2.6x10^5	1.95	6.5	,,	Mg+2B+11.3 mol% SiC (ox-ford)	650/0. 5	-	4.6	15.46	75
5	36.5	5.0x10^6	0.79	4.9	14-fila.	MgB$_2$ (Lamia)	980	6	~0	14.57	500
6	38.7	3.1x10^5	1.32		HE+TAR	MgB$_2$ (aa)+1.5 mol% SiC	950/0. 5	3	1.1	8.89	150

notes: MA (Mechanical Alloying [73]); RWIT (Rectangular wire in tube ; see [79][127]); 14-filament (see reference [116]); HE+TAR (Hydrostatic extrusion and two axial rolling) [111]; gf (good fellow); aa (Alpha Aesar); abcr (ABCR GmbH)

8.3   Results and discussion

8.3.1   Superconducting properties

The T_c's of samples 1-6 is given in Table 8.1. T_c's of the ex-situ samples 5-6 are higher than the T_c's of in-situ and mechanically alloyed samples 1-4. Sample 6 has the highest T_c (38.7 K) while sample 2 and 3 have lowest T_c's of 32.5 and 33.7 K respectively.

$J_c(B)$ curves of samples 1-6 are shown in Figure 8.1. Mechanically alloyed samples show the highest J_c at high fields (> 5T) among the samples 1-6, which is about 3 times smaller than the J_c of SiC added MgB$_2$ wires of Dou et al. [56]. A large scatter is observed in the J_c's of different wires. At 7 T, the J_c of sample 2 is about 100 times larger than sample 5. Similarly the field dependence of the J_c varies from sample to sample. Sample 3 shows the best field dependence and. Sample 5 shows the most rapid decrease in J_c with increase in magnetic field.
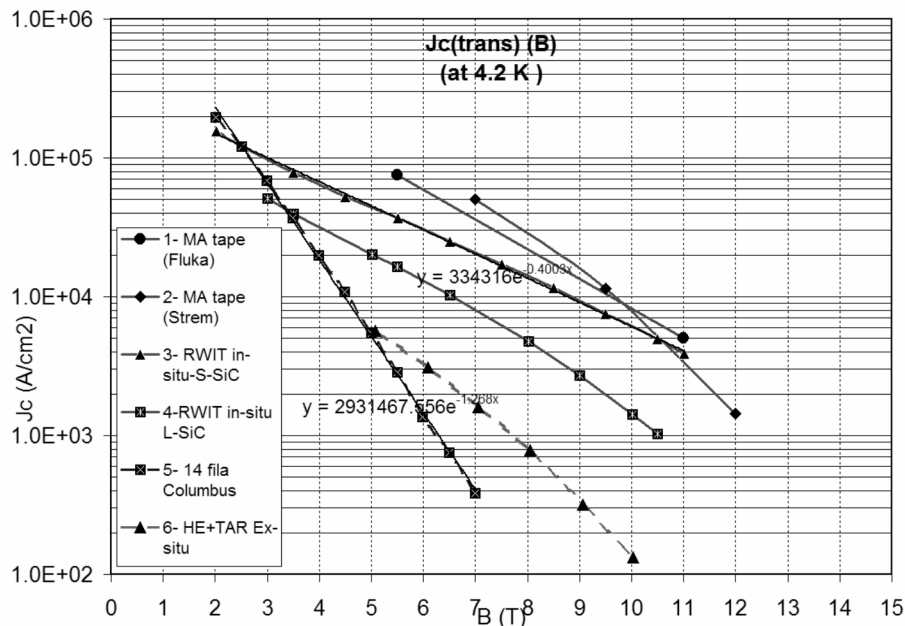
Figure 8.1: J_c (B) plots of samples 1 to 6 at 4.2 K from transport measurments.

8.3.2 Microstructure analysis

The SE (secondary electron) images and the corresponding RGB (Mg-O-B) or RGB (Mg-Si-B) images of the SEM-EDX elemental maps are shown in Figure 8.2. The volume fraction of B-rich secondary phases, size of MgB_2 colonies and O mole fraction summarised in Table 8.1 were obtained by SEM analysis as described in chapter 2 and 3. TEM dark-field images (Figure 8.2) yield the grain size of the MgB_2 filaments.

SE images of mechanically alloyed sample 1 and 2 show very few cracks and are dense. Sample 1 shows 1.4 % B-rich secondary phases (which appear blue in the RGB (Mg-O-B) image), indicating inhibited MgB_2 phase formation. Sample 2 shows dense and pure MgB_2 colonies embedded in an oxygen rich granular MgB_2 matrix. A colony is a dense arrangement of several MgB_2 grains.

SE images of in-situ samples 3 and 4 show a large density of cracks and voids on the 1-10 μm length-scale. RGB (Mg-Si-B) images show highest volume fraction (3.1 %) of Mg_2Si secondary phases and 2.7 % volume fraction of B-rich secondary phases in sample 3. On the other hand, sample 4 has smaller volume fraction (1%) of Mg_2Si but highest volume fraction (4.6 %) of B-rich secondary phases. A TEM bright field image of the nanocrystalline SiC powder, used for the preparation of samples 3 and 4 is shown in Figure 8.3(a). These particles, originally thought to be incorporated as pinning centres, react with Mg to form μm sized Mg_2Si secondary phases (Figure 8.3(b)). The carbon released during the formation of formation of Mg_2Si is doped into the MgB_2 matrix [56]. T_c of sample 3 is suppressed because of the enhanced C-doping in this sample.

SE images of the ex-situ samples 5-6 and STEM dark-field image (Figure 8.4(a)) of sample 5, show 2-6 μm large dense regions in a granular matrix with voids. RGB (Mg-O-B) image shows the dense regions to be MgB_2 colonies and the granular matrix to be rich in oxygen. A schematic diagram of such a colony formation is shown in Figure 8.4(b) and is found to be a universal feature of all ex-situ samples.

TEM dark-field images of samples 1-6 are shown in Figure 8.3(c). The grain size of mechanically alloyed samples 1-2 and in-situ samples 3-4 is in the range of 15-100 nm. The grain size is of the order of the coherence length of MgB_2 and yields reduction of T_c. The MgB_2 grain size in ex-situ samples 5-6 is significantly larger (100-1000 nm) than in in-situ or mechanically alloyed samples.

Secondary phases on the sub-micrometer scale in samples 3-6 were studied using STEM-EDX and ESI elemental mapping as described in chapter 3. Sample 3 showed 50-400 nm large grains of crystalline Mg_2Si and highest density of 100-200 nm large grains of amorphous B-rich secondary phases embedded in the MgB_2 matrix. The granular matrix in sample 5 showed 200 nm wide oxide layers between the MgB_2 grains. Sample 6 with SiC additives showed 50 nm wide oxide and $MgSi_xO_y$ layers between the MgB_2 grains.

8.3.3 J_c-microstructure correlation model

J_c of MgB_2 wires and tapes (Figure 8.1) is influenced by B_{c2} and microstructure (Figure 8.5 and Table 8.2). Microstructure affects J_c because of the structural granularity and crystal defects on the coherence length scale of MgB_2 namely grain boundaries, dislocations and precipitates, which can act as pinning centers [126]. The structural granularity arises due to inhibited MgB_2 phase formation and due to the formation of secondary phases (B-rich secondary phases, Mg_2Si) and oxide layers at grain boundaries.

Weeren [69]used J_{c0} (the extrapolated J_c at 0 field) and B_p (magnitude of the reciprocal of the slope of the logarithmic $J_c(B)$ plot) to characterise the influence of connectivity (structural granularity) and pinning respectively on J_c. Higher J_{c0} and B_p would yield enhanced $J_c(B)$. B* (the magnetic field at which the J_c drops to 1×10^4 Acm^{-2}) is a technologically relevant parameter which depends on the J_{c0} and B_p. Values of these three parameters for samples 1-6 are included in Table 8.1.

The J_c-microstructure correlation model is used to explain the order of magnitude differences in the J_c of samples 1-6. The model consists of 1) MgB_2 grain size, 2) oxygen mole fraction, 3)

volume fraction of B-rich secondary phases and 4) colony size, which are summarized in Table 8.1 for samples 1-6.
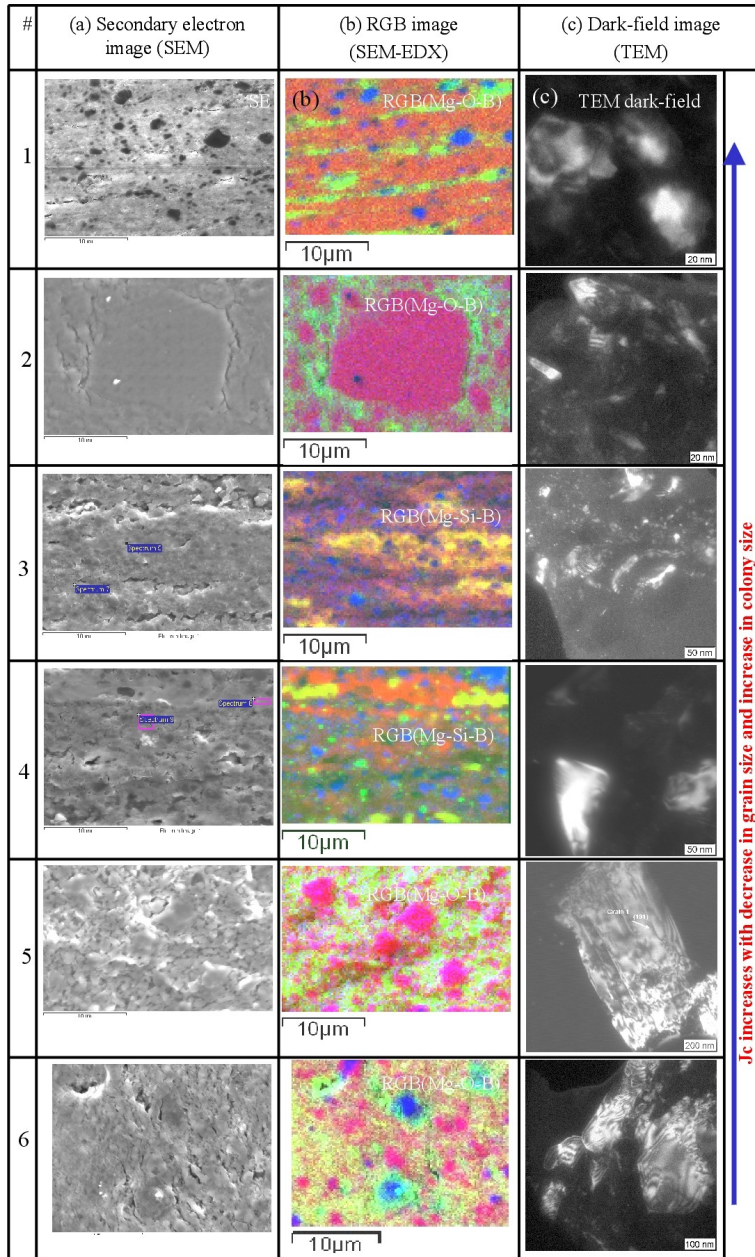
Figure 8.2: (a) secondary electron images and

(b) the corresponding RGB(Mg-O-B) or RGB(Mg-Si-B) images of samples 1-6.

(c) TEM dark field images showing MgB₂ grain size in samples 1-6. (note: dark-field image of sample 2 was acquired from a similarly prepared bulk sample)

Figure 8.3: a) TEM bright-field image of nanocrystalline SiC powder (b) RGB (Mg-Si-B) image showing Mg₂Si secondary phase.
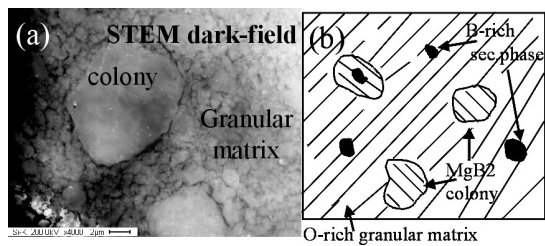
Figure 8.4: (a) STEM dark-field image of sample 5. (b) Schematic of the microstructure of ex-situ MgB₂

The correlation diagram of the B_p versus MgB_2 grain size in samples 1 and 3-6 is plotted in Figure 8.6(a). The B_p is clearly seen to increase with decrease in grain size, indicating MgB_2 grain boundaries to be excellent pinning centres. The size of the dislocations at the grain boundaries is approximately equal to the lattice constant (~0.3 nm for MgB_2). How these grain boundaries pin the approximately 10 nm (coherence length) large vortices in MgB_2 is not well understood. Strain field at the grain boundaries might contribute in the grain boundary pinning as pressure is known to suppress the T_c of MgB_2 at a rate of 0.2-2 K(GPa)$^{-1}$ [14]. Anisotropy in B_{c2} might also play a role in grain boundary pinning and has been reported for Nb_3Sn (p.89 [71])

The correlation diagrams of the J_{c0} versus O mole fraction (Figure 8.6(b)), and J_{c0} versus volume fraction of B-rich secondary phases (Figure 8.6(c)) in mechanically alloyed samples 1 and in-situ samples 3-4 show that connectivity increases with decrease in O mole fraction and B-rich secondary phase fraction. The correlation diagram of J_{c0} versus colony size (Figure 8.6(d)) in ex-situ samples shows that connectivity increases with increase in colony size. These results are summarised in Table 8.2.

The high J_c of mechanically alloyed tapes (samples 1-2) is attributed to the high J_{c0} due to the dense microstructure and high B_p due to the enhanced grain boundary pinning because of their small MgB_2 grain size. The J_c is likely to be further enhanced by reducing the volume fraction of B-rich secondary phases in sample 1 and increasing the volume fraction of MgB_2 colonies in sample 2.

Sample 3 shows the best field dependence of J_c i.e. high B_p, which can be attributed to the enhanced grain boundary pinning due to small MgB_2 grain size and, enhanced B_{c2} as well decreased B_{c2} anisotropy due to carbon doping. Besides MgB_2 doping with C, addition of SiC contributes significantly to the formation of Mg_2Si and B-rich secondary phases and a large density of such secondary phases of size 200 nm (Figure 3.12) to 2 μm (Figure 8.2(b)) were observed in sample 3. This has a favourable effect of forming of normal-superconducting interfaces which can act assist in pinning [71] [72]. However, these secondary phases also yield structural granularity, which results in smaller J_{c0} and limits the J_c enhancement in SiC-added MgB_2 wires.

Very high B_{c2} of 42 T and microstructure similar to that of sample 3, was observed in MgB_2 bulk and tapes with SiC additives by Zhu et al [117] and Matsumoto et al [187]. The J_c of these samples was reported to be a complex balance between connectivity, B_{c2} and flux pinning induced by grain boundaries and precipitates.

Sample 5 a 14-filament tape with a copper core, shows high J_{c0}, because of the large 6 μm colonies (Figure 8.4(a)) yielding good connectivity and thermal stability due to the copper core. The rapid decrease in J_c of sample 5 with increase in B is reflected in the low value of B_p and is explained by poor grain boundary pinning, due to large MgB_2 grain size (Figure 8.2(c)) [116].

The low J_c of samples 6 is attributed to the large volume fraction of the oxygen rich granular matrix (Figure 8.2(b)). MgB_2 grains in the MgB_2 matrix are surrounded by about 50 nm wide oxide or $MgSi_xO_y$ layers yielding poor connectivity which is reflected in the low value of J_{c0}. The field dependence of J_c i.e. B_p is however improved in comparison to sample 5 because of enhanced grain boundary pinning due to smaller (about 200 nm) size of MgB_2 grains (Figure 8.2(c)) and also because enhanced B_{c2} and decreased B_{c2} anisotropy by carbon doping due to SiC additives.

Using a percolation model Eisterer et al. [163] [164]have recently suggested, that the critical current density in MgB_2 wires is governed by (i) the upper critical field B_{c2} and (ii) the anisotropy of B_{c2} [165]. Because of the anisotropy of B_{c2} even a homogenous poly-crystalline MgB_2 conductor will show granularity at higher magnetic fields [163],[164]. It was shown in this thesis that the microstructure of MgB_2 shows significant granularity and is not homogenous. This extends the validity of a percolation model towards smaller magnetic fields.

To summarise, the high J_c of MgB_2 wires, inspite of the substantial structural granularity, can be attributed to the unique features of superconductivity in MgB_2: the 10 nm coherence length, variable B_{c2} and the anisotropy in B_{c2}. The large variations in the J_c of MgB_2 wires and tapes could be attributed to the variations in the microstructure affecting the structural granularity (connectivity) and pinning[71] [72].
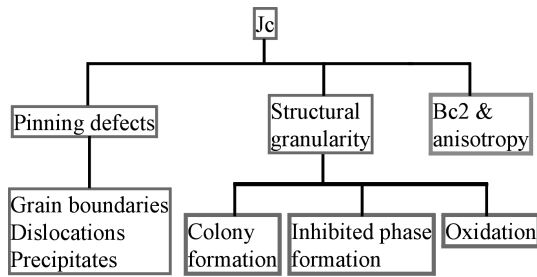
Figure 8.5: Schematic diagram of the factors affecting J_c.

Table 8.2: Microstructure parameters and their effect on J_c

Variation in microstructure parameter	Effect on J_{c0} or B_p
Decrease in MgB$_2$ grain size (increase in pinning)	B_p Increases
Decrease in oxygen mole fraction (increase in connectivity)	J_{c0} Increases
Increase in colony size (increase in connectivity)	J_{c0} Increases
Decrease in volume fraction of B-rich secondary phases (increase in connectivity)	J_{c0} Increases
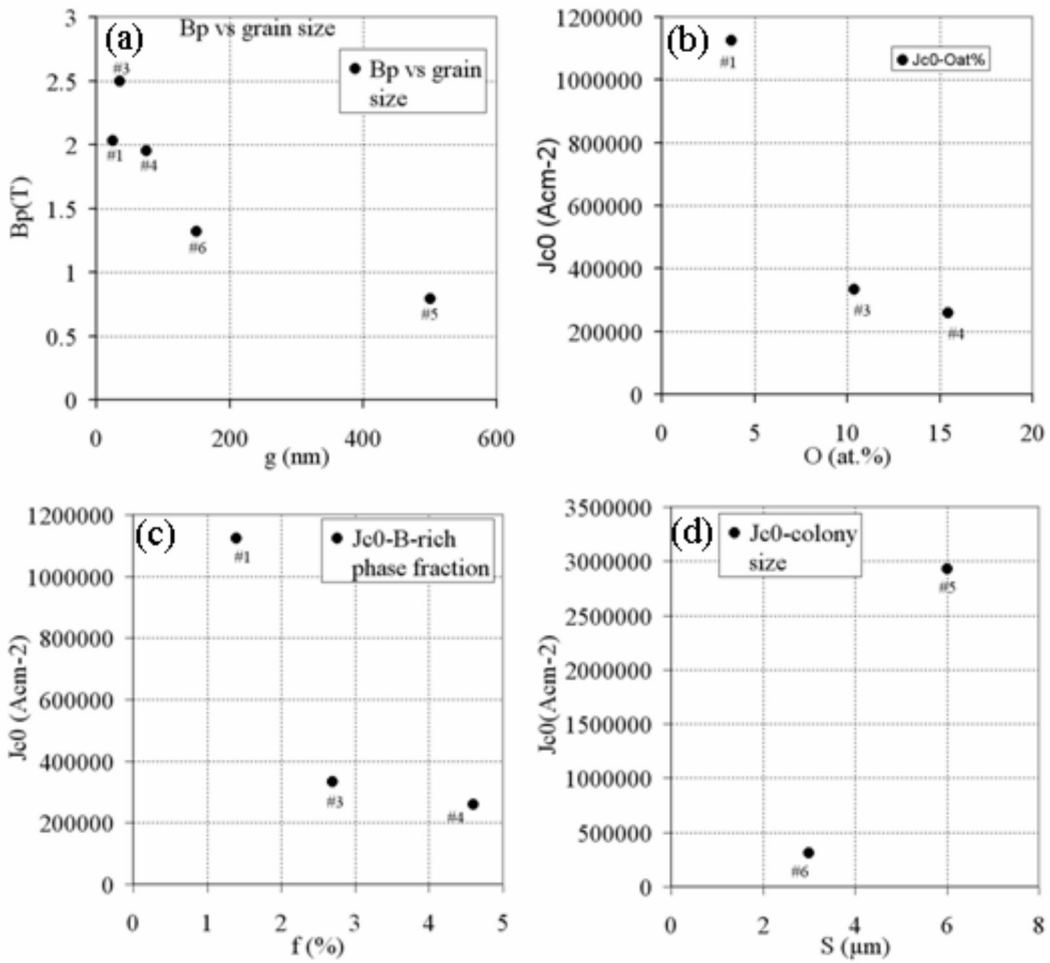
Figure 8.6: correlation diagrams of (a) B_p versus MgB$_2$ grain size for sample1 and 3-6, (b)J_{c0} versus O mole fraction for samples 1,3 and 4, (c) J_{c0} versus volume fraction of B-rich secondary phases for samples 1,3 and 4, and (d) J_{c0} versus colony size for samples 5-6.

9 Appendix

9.1 Acquisition conditions and microscope specifications

9.1.1 Specifications of SEM and EPMA

Table 9.1: Instrument specifications of SEM and EPMA

	SEM	EPMA
Name of instrument	Jeol JSM 6500F	Jeol Superprobe 8900 RL
Gun	Schottky Field Emission	Thermionic emission
Extraction voltage at the Gun	3 kV	-
Filament current	2.21 A	-
Accelerating voltage	10 kV (Range: 0.5 to 30 kV)	15 kV
Emission current	~67 µA (max: >100 µm)	-
Detector	EDX: Si(Li) with ultra thin window (ATW2) from Oxford	WDX crystal spectrometer:LDEB for B-K_α, TAP for Mg and Al-K_α and LDE1H for O-K_α x-rays.
Detector calibration	Set once for all by the manufacturer using standards	Set by the user using standards before every experiment
Standards for detector calibration of different x-rays	B-K_α: Metallic Boron, Mg-K_α: Metallic Mg	B-K_α: Metallic Beta Boron, Mg-K_α: synthetic MgO
Probe current	1-18 arbitrary units (range:30 pA to 200 nA)	15 nA
Vacuum at Gun	~ 3.2 x 10-8 Pa	-
Vacuum in Specimen chamber	~ 8.1 x 10-7 Pa	3x10-4 Pa
Magnification	10x to 500kx	40x to 300kx
Detectors for conventional imaging	SE, BSE	SE, BSE
Lateral resolution of SE imaging	~5nm	~6nm
Lateral resolution of x-ray microanalysis	1 µA	1 µA

9.1.2 Acquisition conditions for the quantitative x-ray microanalysis of MgB₂ using using SEM and EPMA

Table 9.2: Acquisition conditions for the quantitative x-ray microanalysis of MgB$_2$ using using SEM (Jeol JSM 6500F) and EPMA (Jeol Superprobe 8900 RL)

Name of instrument	Jeol JSM 6500F	Jeol Superprobe 8900 RL
Accelerating voltage	10 kV	15 kV
Probe current	18 arbitrary units (range:30 pA to 200 nA)	15 nA
Objective aperture	2§	1
Working distance*	10 mm	11 mm
Scanning mode	area mode or spot mode	Spot mode (beam size<1 µm)
Spectrum energy range	0-10 kV	-

Name of instrument	Jeol JSM 6500F	Jeol Superprobe 8900 RL
Live time	100 s	16 s at $Mg-K_\alpha$ and 30 s at $O-K_\alpha$ peak positions ;4 minutes across the $B-K_\alpha$ peak window.-
Counts per second	~6000-8000	-
Process time	4	-
$B-K_\alpha$ Peak to background ratio	11	~36
Integrated no. of counts under $B-K_\alpha$ peak	~4800	~25000
Relative statistical error in B counts	1.4 %	0.6 %
FWHM at $B-K_\alpha$ peak	68 eV	7.5 eV
Total no. of counts under $Mg-K_\alpha$ peak	~225700 (integrated)	50000
Relative statistical error in Mg counts	0.2 %	0.4 %

§ The Beam blanking plates are to be positioned completely out
*The distance between the objective lens and the sample surface (Focal length of objective lens)

9.1.3   Acquisition conditions for the SEM-EDX elemental mapping of MgB_2

Table 9.3: Acquisition conditions for the SEM-EDX elemental mapping of MgB_2 using Jeol JSM-6500F

Accelerating voltage	10 kV
Probe current	18 arbitrary units (range:30 pA to 200 nA)
Objective aperture	2§
Working distance*	10 mm
Scanning mode	area mode or spot mode
Spectrum energy range	0-10 kV
Live time	1500 s-2500 s
Counts per second	~6000-8000
Process time	4
Number of pixels in the elemental map	128 pixels x 88 pixels
Total $Mg-K_\alpha$ x-ray counts per pixel	600
Relative statistical error in Mg counts	4.1%
Total $B-K_\alpha$ x-ray counts per pixel	20
Relative statistical error in B counts	22.4%

§ The Beam blanking plates are to be positioned completely out
*The distance between the objective lens and the sample surface (Focal length of objective lens)

9.1.4 Detailed specifications of the TEMs: Zeiss 912Ω and Zeiss Libra 200FE (200kV FEG)

Table 9.4: Detailed specifications of the TEMs: Zeiss-912Ω and Zeiss-Libra (200 kV FEG)

	Zeiss 912	Zeiss Libra
General parameters		
Accelerating Voltage	60, 80, 100, 120	120, 200
Gun	LaB_6, Thermionic	ZrO/W-Schottky Field Emission
Filament current	3.4 A (maximum 3.59 A)	2.34 A (1760 K)
Emission current	1-14 µA(maximum 50 µA)	Upto 55 µA
Detectors	Si(Li) EDX detector with ultra thin window (ATW2) from Oxford instruments (detects $B-K_\alpha$ x-rays) + Omega spectrometer	Si(Li) EDX detector from EDAX (cannot detect $B-K_\alpha$ x-rays)+ Omega spectrometer + HAADF detector
STEM capability	No	Yes
Illumination system		
Lenses	3 condensor lenses + objective lens condensor(C-O)	3 condensor lenses + objective lens condensor(C-O)
Koehler illumination	yes	yes
Probe size (Area of illumination in TEM mode)	1-75 µm	-
Illumination aperture	0.01-5 mrad	0.01-20 mrad
Smallest probe size in (Spot illumination mode)	1.6 nm	0.5 nm
Condenser aperture	0(completely out),1, 2(600 µm), 3 (37.5 µm), 4 (37.5 µm), 5 (20 µm)	0(completely out),1,2,3 one of these apertures is 7 hole aperture(10, 19, 38, 75, 150, 300 and 600 µm)
Stray aperture	0(completely out),1(-),2(-),3(200 µm)	Objective aperture 5
Specimen stage		
Goniometer	Side entry	Side entry
Coordinates of specimen movement	X,y,z, theta (tilt around the axis of sample holder), Phi (tilt around the axis perpendicular to the axis of sample holder and optic axis	X,y,z, theta (tilt around the axis of sample holder), Phi (tilt around the axis perpendicular to the axis of sample holder and optic axis
tilt	Theta = ± 60°; Phi= ±30°	Theta = ± 30°; Phi= ±30°
Specimen holder	Low background (EDX) holder made of Be	Low background (EDX) holder made of Be
Imaging system		
Lenses	Objective lens+projective lens system I + Omega spectrometer+projective lens system II	Objective lens+projective lens system I + Omega spectrometer+projective lens system II
Objective lens point to point resolution	0.37 nm	0.24 nm
Objective lens focal length	3.6 mm	1.7 mm
Objective lens Cc	2.7 mm	1.2 mm
Objective lens Cs	2.7 mm	1.2 mm

	Zeiss 912	Zeiss Libra
Objective aperture	0 (completely out),1 (13.45 mrad, 90 μm), 2 (8.09 mrad, 60 μm), 3 (3.45 mrad, 30 μm)	0 (completely out) -5 (completely in); Multihole apertures (80-10 μm)
SAD aperture	0 (completely out), 1 (100 μm), 2 (20 μm), 3(20 μm)	0 (completely out), 1 (40 μm), 2 (20 μm), 3(5 μm)
Magnification (selected area mode)	3.15 kx to 250 kx	10 kx to 500 kx
Camera length (selected area diffraction mode)	290-7200 mm	12 to 3000 mm
Spectrometer		
Lenses	4 sector magnets + one corrector element	4 sector magnets + 7 corrector element
Spectrometer entrance apertures	0 (completely out), 1(1500 μm), 2 (800 μm), 3 (100 μm)	0 (completely out), 1(800 μm), 2 (500 μm), 3 (100 μm)
Slit apertures	1-100 μm	
Spectrum Magnification	19.5 x to 315 x	20x to 315 x
Energy loss range	1-2500 eV	0-3500 eV
FWHM at zero loss peak	~ 1 eV	< 0.7 eV
EDX detector		
Type	Si(Li) EDX detector with ultra thin window (ATW2) (detects $B\text{-}K_\alpha$ x-rays)	Si(Li) EDX detector (cannot detect $B\text{-}K_\alpha$ x-rays)
Manufacturer	Oxford Instruments	EDAX
Detector surface	30 mm^2	-
Operating temperature	Liquid Nitrogen	Liquid Nitrogen
Image and spectrum acquisition system		
CCD camera image resolution	1024 pixels x 1024 pixels	1024 pixels x 1024 pixels
CCD camera image depth	14 bit	14 bit
Image and EELS acquisition software	ESIVISION	WinTEM+Digital micrograph
EDX acquisition software	INCA	EDAX Genesis
Vacuum system		
Vacuum system	Rotary pump+Molecular turbo pump+Ion getter pump	Rotary pump+Molecular turbo pump+Ion getter pump
Vacuum in column	1×10^{-7} mbar	1.58×10^{-7} mbar
Vacuum at Gun	4×10^{-7} mbar	1.74×10^{-9} mbar
Vacuum at Camera	1×10^{-6} mbar	1.75×10^{-6} mbar

9.1.5   Acquisition conditions for diffraction contrast imaging of MgB$_2$ using Zeiss-912Ω

Table 9.5: Acquisition conditions for the Transmission Electron Microscopy of MgB$_2$ using Zeiss 912Ω and Zeiss Libra

Condenser aperture	3
Objective aperture	3
Energy width of slit aperture	20 (eV)

Condenser aperture	3
Preferred (hkl) refelections	{002},{011}and {110}
Excitaiton error (s) for brightfield image	Slightly >0
Excitaiton error (s) for dark-field image	0
Pixel intensity	8000
Acquisition time	1
Camera binning	1

9.1.6   Acquisition conditions for quantitative TEM-EDX analysis of MgB$_2$ using Zeiss-912Ω

Table 9.6: Acquisition conditions for the quantitative TEM-EDX analysis of MgB$_2$ using Zeiss-912Ω

Filament current	3.4 A
Extraction voltage	-
Specimen tilt	20°
Condenser aperture	3
Objective aperture	0
Stray aperture	3
Spot size	~ 50 nm
EDX acquisition software	INCA
Counts per second	~ 2000
Acquisition time	100 s
Process time	4 or 5
B-K$_\alpha$ Peak to background ratio	19
Integrated no. of counts under B-K$_\alpha$ peak	~5300
Relative statistical error in B counts	1.4 %
FWHM at B-K$_\alpha$ peak	83 eV
Total no. of counts under Mg-K$_\alpha$ peak	~122900 (integrated)
Relative statistical error in Mg counts	0.3 %

9.1.7   Acquisition conditions for the STEM-EDX elemental mapping of MgB$_2$ using Zeiss Libra

Table 9.7: Acquisition conditions for the STEM-EDX elemental mapping of MgB$_2$ using Zeiss Libra

Filament current	2.34 A (1760 K)
Extraction voltage	4.4 kV
Specimen tilt	10°
Condenser aperture	3
Objective aperture	5
Stray aperture	5 (objective)
Spot size	8-10 nm
EDX acquisition software	EDAX Genesis
Counts per second	~5000

Filament current	2.34 A (1760 K)
Acquisition time	~14 minutes
Image resolution of chemical maps	256 pixels x 200 pixels
Dwell time	1 ms/pixel
No of frames	16
Total Mg-K_α x-ray counts per pixel	80
Relative statistical error in Mg counts	11.2 %

9.1.8   Acquisition conditions for the EFTEM-ESI elemental mapping using Zeiss-912Ω and Zeiss-Libra

Table 9.8: Acquisition conditions for EFTEM-ESI elemental mapping using Zeiss-912Ω and Zeiss-Libra

	Zeiss 912	Zeiss Libra
Filament current	3.4 A	2.34 A (1760 K)
Emission current	10 µA	-
Extraction voltage	-	4.4 kV
Condenser aperture	3	1
Spectrometer entrance aperture	2	smallest
Slit width	15 eV	10-20 eV
Magnification	Upto 12.5 K	Upto 50 K
Objective aperture	2 (semi-angle 8.09 mrad)	3(20 mm diameter at 567mm camera length; semi-angle 1.76 mrad)
Acquisition time	B:2s; C: 2 s; O : 3.2 s	B:3s; C:8s; O:30 s
Illumination angle (marad)	B:1.6; C:2; and O: 2	-
MIS aperture	4	
Camera binning(software)	2x2	2x2
Background estimation method	Three window power law	Three window method
Background subtraction method	Difference	Difference
Signal in B-K ESI	~ 400 cts	1000
Background in the B-K difference ESI	~ 2600 cts	3000
Signal to Background ratio in B-K difference ESI	0.15	0.33
B-K ESI Signal in vacuum at a distance of 50 nm and 200 nm from the edge of the sample	57 and 1 cts	100 and 70 cts
Elements used for RGB images	B, C and O	B, C and O

9.1.9   Acquisition conditions for the EELS analysis of MgB$_2$ using Zeiss-912Ω

Table 9.9: Acquisition conditions for the EELS analysis of MgB$_2$ using Zeiss-912Ω

Wide range PEELS of MgB$_2$ using Zeiss 912

Emission current	10 μA
Objective aperture	2 (8.1 mrad)
MIS	0
Emission current	10 μA
Objective aperture	2 (8.1 mrad)
MIS	0
Spot size	~8 , ~50, ~100 nm for low energy, middle energy and high energy loss window
Spectrometer entrance aperture	3
Spectrum magnification	19.5x
Energy range	160-1510 (4 frames)
Acquisition time	Automatically chosen (~10 s per frame)
Image/Diffraction mode	Diffraction?
Integration width	~250 eV (maximum is 250 eV); The width is to be set as per the B-K edge width. Quantification is extremly sensitive to the intgration width.
Background fit approximation	Power law (exponential law does not fit specially for B-K edge)

B-K core loss EELS of MgB_2 using Zeiss 912	
Emission current	10 μA
Objective aperture	3
Entrance aperture	3
Diffraction / Image	Diffraction
Spectrum magnification	63x
Spot size	100 nm
Acquisition time	1s x 10
Signal	610
Signal to background ratio	0.5

Mg-K core loss EELS of MgB_2 using Zeiss 912	
Emission current	10 μA
Objective aperture	2
Entrance aperture	3
Diffraction / Image	Image
Spectrum magnification	63x
Spot size	100 nm
Acquisition time	1s x 20
Signal	139
Signal to background ratio	4.09

Low loss EELS of MgB_2 using Zeiss 912	
Emission current	1 μA
Objective aperture	3
MIS	3
Entrance aperture	3
Diffraction / Image	Diffraction
Spot size	10 nm
Spectrum magnification	63x
Acquisition time	100 ms x1

Specimen thickness	<0.5 MFP (~160 nm)

9.2   Matlab scripts

9.2.1   Matlab code for the quantitative phase analysis of SEM-EDX elemental maps

```
%***Quantitative phase analysis of SEM-EDX elemental maps

%***I:\balaji auf D\Balaji\Hipermag\HIPERMAG-till-2007-09-30\Dresden-Häßler\20050002-2006-06-07-
Jeol6500F-Fluka 600\Auswertung\5000x8\CHI_Mg_B.m

Mg = imread('Mg.jpg');%greyvalues(0-255) are read in mxn matrix Mg

Mg_double=double(Mg);% converts numeric class uint8 array to double array

B = imread('B.jpg');%greyvalues(0-255) are read in mxn matrix B

B_double=double(B);
   CHI=zeros(256);%256x256 matrix
   HIS_B=zeros(1,256);
   HIS_Mg=zeros(1,256);
   [m,n]=size(Mg);
for I=1:m
  for J=1:n
  i_act=((B_double(I,J)))+1;% adding 1 to grey value range of boron image pixel
  j_act=((Mg_double(I,J)))+1;
     CHI(i_act,j_act)= CHI(i_act,j_act)+1;%incrementing the number of pixels with B grey value (i_act)...
     % and Mg grey value (j_act)
     HIS_B(i_act)=HIS_B(i_act)+1;%incrementing the number of pixels with grey value (i_act) in B image
     HIS_Mg(j_act)=HIS_Mg(j_act)+1;
   end
end
pixelrowvector=sum(CHI);%sum of all the pixels in the image calculated by summing CHI

pixeltotal=sum (pixelrowvector');

MAXROW = max(CHI);%row of maxima made from maxium in each column of CHI

MAXEL=max(MAXROW')

CHIN=CHI/MAXEL;% normalised CHI

%********************Displaying Mg-B CHI

colormap('gray');

clims=[0,8];

imagesc(CHI,clims);

xlabel('Magnesium','FontSize',16)

ylabel('Boron','FontSize',16)

title('\it{Mg-B CHI}','FontSize',16)

%********************Defining Blue mask for Boron rich secondary phase Blue

gB1lower=150 ;

gB1upper=256;

gMg1left=1;

gMg1right=150;
```

```
%****Incoporating masks for B-rich seconary phases in the Blue channel
CHINB=CHIN;
CHINB(gB1upper,gMg1left:gMg1right)=ones(1,gMg1right-gMg1left+1);
CHINB(gB1lower,gMg1left:gMg1right)=ones(1,gMg1right-gMg1left+1);
CHINB(gB1lower:gB1upper,gMg1left)=ones(gB1upper-gB1lower+1,1);
CHINB(gB1lower:gB1upper,gMg1right)=ones(gB1upper-gB1lower+1,1);
%***Calculating area and volume of B-rich secondary phases
Ar_B_rich=0;
for gB1=gB1lower:gB1upper%B-rich phase
   for gMg1=gMg1left:gMg1right
     Ar_B_rich=Ar_B_rich+CHI(gB1,gMg1);%no. of  pixels having B-rich secondary phase composition
 end
end
Ar_image=pixeltotal
Ar_B_rich
vol_B_rich= (Ar_B_rich/(m*n))^(1.5)*100%volume fraction of B_rich sec. in percent
%**************plotting histogram of boron elemental map
plot(HIS_B)
xlabel('B grey value','FontSize',16)
ylabel('no. of pixels','FontSize',16)
title('\it{Histogram}','FontSize',16)
%**************plotting histogram of Mg elemental map
plot(HIS_Mg)
xlabel('Mg grey value','FontSize',16)
ylabel('no. of pixels','FontSize',16)
title('\it{Histogram}','FontSize',16)
%***plottig B-Mg CHI with blue mask for B-rich sec. phases (such a CHI is weak in intensity)
CHIRGB = cat(3,CHIN,CHIN,CHINB);
image(CHIRGB);
xlabel('Magnesium','FontSize',16)
ylabel('Boron','FontSize',16)
title('\it{Mg-B CHI}','FontSize',16)
%*******creating sythetic map of B-rich sec. phase
for i_act=1:m
   for j_act=1:n
     if ((B_double(i_act,j_act) >= gB1lower)&(B_double(i_act,j_act) <= gB1upper)&  ...
  (Mg_double(i_act,j_act) >= gMg1left) & (Mg_double(i_act,j_act) <= gMg1right));
     ct(i_act,j_act)=1;
     end
   end
end
colormap('gray');
clims=[0,1];
imagesc(ct,clims);
```

9.2.2   Matlab script to calculate extinction lengths of MgB₂

%***Matlab script to calculate extinction length of MgB2

%***I:\balaji auf E\balaji\Matlab Programmes\MgB2ExtDist120kV.m

%***calculating dhkl

h=[0]

k=[0]

l=[2]

a=[3.08489];%in Angstroms

c=[3.52107];%in Angstroms

dhkl=[4/(3*a^2)*(h^2+h*k+k^2)+(l^2)/(c^2)]^(-0.5)%in Angstroms

%***Calculation of wavelength, speed and mass of electrons considering relativistic effects

c0= 2.99792458*10^8 % speed of light in units of ms^-1

% m*c0^2= m0*c0^2+e*U; conservation of energy ;

e=1.6021892*10^-19 % charge of electron in units of coulombs;

U=120000 % accelerating voltage in V;

m0=9.10953*10^-31 % rest mass of electron in kg

beta = (1-(1/(1+e*U/(m0*c0*c0)))^2)^0.5% relativistic correction factor for velocity = beta= (v/c0)

gamma = (1-beta^2)^-0.5 %gamma = m/m0

hp= 6.62617*10^-34 %Plancks constant in units of Watt*second^2

Lambda=hp/((m0*gamma)*(beta*c0));% wavelength of 120 kV electron beam in meters

Lambda=Lambda*10^10%wavelength in Angstroms

%***calculating atomic electron scattering factors of B and Mg

a_Mg=[2.2682,1.8025,0.8394,0.2892];%in Angstroms

b_Mg=[73.6704,20.1749,3.0181,0.4046];%in Angstrom^2

F_Mg= 0;%in Angstroms

a_B=[0.9446,1.3120,0.4188,0.1159];

b_B=[46.4438,14.1778,3.2228,0.3767];

F_B=0;%in Angstroms

for e=1:4

F_Mg=[F_Mg+a_Mg(e)*exp(-b_Mg(e)*(0.5/dhkl)^2)];

F_B=[F_B+a_B(e)*exp(-b_B(e)*(0.5/dhkl)^2)];

end

F_Mg

F_B

%***calculating kinematical structure factor of MgB2

F_MgB2=(F_Mg+F_B*exp(2i*pi*(h*1/3+k*2/3+l*1/2))+F_B*exp(2i*pi*(h*2/3+k*1/3+l*1/2)))*gamma

%***calculating extinction length of MgB2

Extinctiondistance=pi*(3^0.5/2*a^2*c)/(Lambda*F_MgB2)% in Angstroms

Table 9.10: atomic scattering factor (f) of B and Mg,and kinematical structure factor (F) and extinction lengths of MgB₂ for first few refelections.

(hkl)	d(nm)	f_B(nm)	f_{Mg}(nm)	F_{MgB2}(nm)	ξ_{MgB2}(nm)
(001)	0.35211	0.18635	0.27902	0.11568	235.3

(010)	0.26716	0.14726	0.21013	0.07763	350.6
(101)	0.21283	0.11368	0.16243	0.34094	79.83
(002)	0.17605	0.08758	0.12980	0.37657	72.28
(110)	0.15424	0.07128	0.11058	0.31259	87.08
(-102)	0.14700	0.06583	0.10431	0.04752	572.76

9.2.3 Matlab code for the parameterless absorption correction of B-K$_\alpha$ x-rays for the quantitative TEM-EDX analysis of MgB$_2$

Calcualtion of k-factor

% Calcualtion of k factors using a thickness series of TEM-EDX spectra acquried on a standard MgB2 sample

%G:\balaji auf E\balaji\stic backup 2007-08-06\Matlab scripts for chapter 4\k_factor.m

% Standard MgB2 sample = sample 4 of chapter 3 with Stoichimetric MgB2 composition

%k-Faktor Mg as given in INCA software

kMg_wt=1.076

%Atommassen

A_B=10.811;

A_Mg=24.305;

%Atomprozente von B und Mg in MgB2

Cat_B=2/3*100

Cat_Mg=1/3*100

%Gewichtsprozente von B und Mg in MgB2

Cwt_B=100*(Cat_B*A_B)/(Cat_B*A_B+Cat_Mg*A_Mg)

Cwt_Mg=100*(Cat_Mg*A_Mg)/(Cat_B*A_B+Cat_Mg*A_Mg)

%Messung dünne Stelle

global t1 I1_B I1_Mg

t1=122920

I1_B=5310   %Integrierte Counts B

I1_Mg=122920   %Integrierte Counts Mg

%Messung dicke Stelle

global t2 I2_B I2_Mg

t2=447123   %Probendicke in Mg-K counts or EELS mean free path

I2_B=5906   %Integrierte Counts B

I2_Mg=447123   %Integrierte Counts Mg

% Calculation of specimen thickness in units of B-K XAL

d1_B=fzero('d1find',2)% the function d1find is defined elsewhere in the directory

d2_B=t2/t1*d1_B

% Calculation of absorption corrected B-K x-ray intensities

I10_B= I1_B/T_d(d1_B)%the function d1find is defined elsewhere in the directory

I20_B= I2_B/T_d(d2_B)

%***Determination of k-factors

%kB-Mg factors when compositions are mesured in at.%

kB_Mg_at_1= (Cat_B/Cat_Mg)*(I1_Mg/I10_B)

kB_Mg_at_2= (Cat_B/Cat_Mg)*(I2_Mg/I20_B)

kB_Mg_at=(kB_Mg_at_1+kB_Mg_at_1)/2

%kB-Mg factors when compositions are mesured in wt.%

kB_Mg_wt_1= (Cwt_B/Cwt_Mg)*(I1_Mg/I10_B)

kB_Mg_wt_2= (Cwt_B/Cwt_Mg)*(I2_Mg/I20_B)

kB_Mg_wt=(kB_Mg_wt_1+kB_Mg_wt_1)/2

kB_wt=kB_Mg_wt*kMg_wt

Quantitative analysis of a MgB2 sample of unknown chemical composition

% Calcualtion of wt. fraction and mole fractionn ratios of B and Mg in MgB2 sample of unknown composition

%G:\balaji auf E\balaji\stic backup 2007-08-06\Matlab scripts for chapter 4\quantification.m

%Atommassen

A_B=10.811;

A_Mg=24.305;

%Atomprozente von B und Mg in MgB2

Cat_B=2/3*100

Cat_Mg=1/3*100

%Gewichtsprozente von B und Mg in MgB2

Cwt_B=100*(Cat_B*A_B)/(Cat_B*A_B+Cat_Mg*A_Mg)

Cwt_Mg=100*(Cat_Mg*A_Mg)/(Cat_B*A_B+Cat_Mg*A_Mg)

%Messung dünne Stelle

global t1 I1_B I1_Mg

t1=122920

I1_B=5310   %Integrierte Counts B

I1_Mg=122920   %Integrierte Counts Mg

%Messung dicke Stelle

global t2 I2_B I2_Mg

t2=447123   %Probendicke in Mg-K counts or EELS mean free path

I2_B=5906   %Integrierte Counts B

I2_Mg=447123   %Integrierte Counts Mg

% Calculation of specimen thickness in units of B-K XAL

d1_B=fzero('d1find',2)% the function d1find is defined elsewhere in the directory

d2_B=t2/t1*d1_B

% Calculation of absorption corrected B-K x-ray intensities

I10_B= I1_B/T_d(d1_B)%the function d1find is defined elsewhere in the directory

I20_B= I2_B/T_d(d2_B)

%***Determination of mole fraction ratio of B and Mg

Cat_B_by_Cat_Mg_at_1= kB_Mg_at *(I10_B/I1_Mg)% the k-factor is determined using standard sample elsewhere in directory

Cat_B_by_Cat_Mg_at_2= kB_Mg_at *(I10_B/I1_Mg)

%***Determination of wt. fraction ratio of B and Mg

Cwt_B_by_Cwt_Mg_at_1= kB_Mg_wt *(I10_B/I1_Mg)%the k-factor is determined using standard sample elsewhere in directory

Cwt_B_by_Cwt_Mg_at_2= kB_Mg_wt *(I10_B/I1_Mg)

Matlab function used to find the sample thickness at thin place in units of B-K XAL using fzero function

%function to be used to find the sample thickness at thin place in units of B-K XAL using fzero function

%G:\balaji auf E\balaji\stic backup 2007-08-06\Matlab scripts for chapter 4\d1find.m

function dsolution=d1find(d);

global t1 I1_B I1_Mg t2 I2_B I2_Mg

dsolution=T_d(t2/t1*d)/T_d(d)-(I2_B/I2_Mg)/(I1_B/I1_Mg);

Matlab function defining transmission coefficient

%Transmission coeffcient

%G:\balaji auf E\balaji\stic backup 2007-08-06\Matlab scripts for chapter 4\T_d.m

function Td=T_d(d);

Td=(1-exp(-d))./d;

9.2.4   Matlab script for the transmission coefficients of B-K$_\alpha$ and Mg-K$_\alpha$ x-rays in MgB$_2$

%This script calculates the Transimssion coeeficient for BK and MgK x-rays in MgB2

%I:\balaji auf E\balaji\stic backup 2007-08-06\Matlab scripts for chapter 4\Trans_coeff_MgK_BK.m

t=[0.00:1:150.00]%nm

f=1.56

MgK_xrayabslength=6672.63%nm

BK_xrayabslength=114.68%nm

d_MgK=(f/MgK_xrayabslength)*t

d_BK=(f/BK_xrayabslength)*t

TMgK=(1-exp(-d_MgK))./d_MgK

TBK=(1-exp(-d_BK))./d_BK

plot (t,TMgK,t,TBK)

xlabel('t (nm)','FontSize',16)

ylabel('Transmission coeff.','FontSize',16)

Bibliography

[1] Jones M E, Marsh R E. *Journal of American Chemical Society*, **76**:1434, 1954.

[2] Nagamatsu J, Nakagawa N, Muranaka T, Zenitani Y, Akimitsu J. *Nature*, **410**:63, 2001.

[3] Spear K E. *Rrefractory materials (ed. Aper A M, Academic press, New York)*, 1976.

[4] Predel B. *Landolt-Boernstein new series (ed. Madelung O, Springer, Berlin)*, **IV/5b**:29, 1992.

[5] Liu Z K, Schlom D G, Li Q, Xi X X. *Appl. Phys. Lett.*, **78**:3678, 2001.

[6] Braccini V. *Superconducting behaviour of bulk MgB2: dependence of critical temperature, irreversibility line and upper critical field on the normal state properties, Ph.D. thesis, University of Genova*, 2003.

[7] Brutti S, Ciccioli A, Balducci G, Gigli G, Manfrinetti P, Palenzona A. *Appl. Phys. Lett.*, **80**:2892, 2002.

[8] Eyidi D, Eibl O, Wenzel T, Nickel K G, Giovannini M, Saccone A. *Micron*, **34**:85, 2003.

[9] Wenzel T, Nickel K G, Glaser J, Meyer H J, Eyidi D, Eibl O. *Phys. Stat. Sol. a*, **198**:374, 2003.

[10] Birajdar B, Wenzel T, Manfrinetti P, Palenzona A, Putti M, Eibl O. *Supercond. Sci. Technol.*, **18**:572, 2005.

[11] Grivel et al. *Supercond. Sci. Technol.*, **19**:96, 2006.

[12] Nayab-Hashemi A A, Clark J B. *Bull. Alloy phase diagrams*, **5**:584, 1984.

[13] Predel B. *Landolt-Boernstein new series (ed. Madelung O, Springer, Berlin)*, **IV/5h**:89, 1997.

[14] Buzea C, Yamashita T. *Supercond. Sci. Technol.*, **14**:R115, 2001.

[15] *Internatinal tables for crystallography, ed. Hahn T (D. Riedel Publishing company, Boston)*, **A**:584, 1952.

[16] Jorgensen J D, Hinks D G, Short S. *Phys. Rev. B*, **63**:224522, 2001.

[17] An J M, Pickett W E. *Phys. Rev. Lett.*, **86**:4366, 2001.

[18] Naslain R, Guette A, Barret M. *J. Solid State Chem.*, **8**:68, 1973.

[19] Guette A et al . *J. Less-Comm. Met.*, **82**:325, 1981.

[20] Brutti S et al. *Intermetallics*, **10**:811, 2002.

[21] Markowsky L Y et al. *J. Gen. Chem. USSR*, **25**:409, 1955.

[22] Nayeb-Hashemi A A, Clark J B. i*n: Phase diagram of binary magnesium alloys (Metals park (OH) ASM International)*, 43, 1988.

[23] Kortus J, Mazin I I, Belashchenko K D, Antropov V P, Boyer L L. *Phys. Rev. Lett.*, **86**:4656, 2001.

[24] Mazin I I, Antropov V P. *Physica C*, **385**:49, 2003.

[25] Dahm T. *in "Frontiers in Superconducting Materials" edited by Narlikar A V (Berlin, Springer)*, 983, 2005.

[26] Yelland E A, Cooper J R , Carrington A , Hussey N E, Meeson P J, Lee S, Yamamoto A, Tajima S. *Phys. Rev. Lett.*, **88**:217002, 2002.

[27] Mazin I I, Kortus J. *Phys. Rev. B*, **65**:180510, 2002.

[28] Carrington A et al. *Phys. Rev. Lett.*, **91**:037003, 2003.

[29] Tsuda S et al. *Phys. Rev. Lett.*, **91**:127001, 2003.

[30] Souma S, Machida Y, Sato T, Takahashi T, Matsui H, Wang S C, Ding H, Kaminski A, Campuzano J C, Sasaki S, Kadowaki K. *Nature*, **423**:65, 2003.

[31] Muranaka T et al. *in "Frontiers in Superconducting Materials" edited by Narlikar A V (Berlin, Springer)*, 937, 2005.

[32] Zehetmayer M et al. *Phys. Rev. B*, **66**:052505, 2002.

[33] Choi H J, Roundy D, Sun H, Cohen M L, Louie S G. *Phys. Rev. B*, **66**:020513, 2002.

[34] Canfield P C, Crabtree G W. *Physics Today*, 34, March 2003.

[35] Budko S L, Lapertot G, Petrovic C, Cunningham C E, Anderson N, Canfield P C. *Phys. Rev. Lett.*, **86**:1877, 2001.

[36] Hinks D G, Claus H, Jorgenesen J D. *Nature*, **411**:457, 2001.

[37] Wang Y, Plackowski T, Junod A. *Physica C*, **355**:179, 2001.

[38] Bouquet F et al. *Phys. Rev. Lett.*, **87**:047001, 2001.

[39] Yang H D et al. *Phys. Rev. Lett.*, **87**:167003, 2001.

[40] Giubileo F et al. *Phys. Rev. Lett.*, **87**:177008, 2001.

[41] Tsuda S et al. *Phys. Rev. Lett.*, **87**:177006, 2001.

[42] Szabo P. *Phys. Rev. Lett.*, **87**:137005, 2001.

[43] McMillan W L. *Phys. Rev.*, **167**:331, 1968.

[44] Allen P B, Dynes R C. *Phys. Rev. B*, **12**:905, 1975.

[45] Carbotte J P. *Rev. Mod. Phys.*, **62**:1027, 1990.

[46] Liu A Y, Mazin I I, Kortus J. *Phys. Rev. Lett.*, **87**:087005, 2001.

[47] Choi H J, Roundy D, Sun H, Cohen M L, Louie S G. *Nature*, **418**:758, 2002.

[48] Schopohl N, Scharnberg K. *Solid State Comm.*, **22**:371, 1977.

[49] Rowell J M. *Supercond. Sci. Technol.*, **16**:R17-R2, 2003.

[50] Mazin I I, Anderson O K, Jepson O, Dolgov O V, Kortus J, Golubov A A, Kuzmenko A B, van der Marel D. *Phys. Rev. Lett.*, **89**:107002, 2002.

[51] Patnaik et al. *Supercond. Sci. Technol*, **14**:315, 2001.

[52] Angst M et al. *Phys. Rev. Lett.*, **88**:167004, 2002.

[53] Eltsev Y et al. *Phys. Rev. B*, **65**:140501, 2002.

[54] Lyard L et al. *Phys. Rev. B*, **66**:180502, 2002.

[55] Welp U et al. *Phys. Rev. B*, **67**:012505, 2003.

[56] Dou S X, Shcherbakova O, Yeoh W K, Kim J H, Soltanian S, Wang X L, Senatore C, Flukiger R, Dhalle M, Husnjak O, Babic E. *Phys. Rev. Lett.*, **98**:097002, 2007.

[57] Zehetmayer M et al. *Phys. Rev. B*, **70**:214516, 2004.

[58] Putti M et al. *Appl. Phys. Lett.*, **86**:112503, 2005.

[59] Dahm T, Schopohl N. *Phys. Rev. Lett.*, **91**:017001, 2003.

[60] Gurevich A. *Phys. Rev. B*, **67**:184515, 2003.

[61] Golubov A A, Koshelev A E. *Phys. Rev. B*, **68**:104503, 2003.

[62] Gurevich A et al. *Supercond. Sci. Technol.*, **17**:278, 2004.

[63] Braccini V et al.. *Phys. Rev. B*, **71**:012504, 2005.

[64] Mannhart J. *Physics of high-temperature superconductors (Springer Series in Solid-State Sciences 106, Springer-Verlag Berlin 1992)*, 367, 1992.

[65] Larbaleister D C et al. *Nature*, **410**:186, 2001.

[66] Kambara M, Hari Babu N, Sadki E S, Cooper J R, Minami H, Cardwell D A, Campbell A M, Inoue I H. *Supercond. Sci. Technol.*, **14**:L5, 2001.

[67] Dou S X et al. *in "Frontiers in Superconducting Materials" edited by Narlikar A V (Berlin, Springer)*, 1011, 2005.

[68] Yeoh W K, Dou S X. *Physica C*, **456**:170, 2007.

[69] van Weeren H. *Magnesium Diboride Superconductors for Magnet Applications, Ph.D. thesis, University of Twente, ISBN 978-90-365-2519-0*, 2007.

[70] Bean C P. *Rev. Mod. Phys.*, **36**:31, 1964.

[71] Ullmaier H. *Irreversible Properties of Type II Superconductors ; Springer Tracts in Modern Physics 76 (Springer-Verlag, New York)*, 1975.

[72] Dew-Hughes D. *Philos. Mag.*, **30**:293, 1974.

[73] Haessler W, Birajdar B, Gruner W, Herrmann M, Perner O, Rodig C, Schubert M, Holzapfel B, Eibl O, Schultz L. *Supercond. Sci. Technol.*, **19**:512, 2006.

[74] Shields T C et al. *Supercond. Sci. Technol.*, **15**:202, 2002.

[75] Mikheenko P, Bevan A I, Abell J S. *Journal of Physics: Conference series*, **43**:535, 2006.

[76] Canfield P C, Budko S L, Finnemore D K. *Physica C*, **385**:1, 2003.

[77] Goldacker W, Schlachter S I. *in "Frontiers in Superconducting Materials" edited by Narlikar A V (Berlin, Springer)*, 1049, 2005.

[78] Pachla W et al.. *Supercond. Sci. Technol.*, **18**:552, 2005.

[79] Kovac P et al. *Supercond. Sci. Technol.*, **20**:771, 2007.

[80] Sumption M D et al. *Supercond. Sci. Technol.*, **18**:730, 2005.

[81] Sumption M D et al. *Supercond. Sci. Technol.*, **19**:155, 2006.

[82] Hinks D G, Jorgenson J D, Zheng H, Short S. *Physica C*, **382**:166, 2002.

[83] Columbus Superconductors, Corso Perrone 24, 16152 Genova, Italy. *http://www.columbussuperconductors.com*.

[84] Kumakura H. *Facets*, **5 (No.3)**, 2006.

[85] Reimer L. *Scanning Electron Microscopy: Physics of Image Formation and Microanalysis (Springer-Verlag, New York)*, 1985.

[86] Goodhew P J, Humphreys J, Beanland R. *Electron Microscopy And Anaysis, Third Edition (Taylor & Francis, New York)*, 2001.

[87] Fuch E, Oppolzer H, Reheme H . *Paticle Beam Microanalysis, Fundamentals, Methods and applications (VCH, New York)*, 1990.

[88] *Quantitative Electron-probe Microanalysis ; Edited by Scott V D, Love G (Ellis Horwood Ltd. Chichester)*, 1983.

[89] Kenda A, Eibl O, Pongratz P. *Micron*, **30**:85, 1999.

[90] Philibert J. *X-ray Optics and X-ray Microanalysis (Pattee H H, Coslett V E, Engstrom A, Eds.)*, 379, 1963.

[91] Lenard P, Becker A. *Handbuck der Experimental Physik. Akad Verlayyses, Leipzig*, **14**:178, 1927.

[92] Bothe W. *Zeit. Phys.*, **54**:161, 1929.

[93] Scott V D, Love G. *Scanning*, **12**:193, 1990.

[94] Pouchou J -L, Pichoir F. *Electron probe quantitation ed. Heinrich K F J, Newbury D E (Plenum press, New York)*, 31, 1991.

[95] Duncumb P. *J. Anal. At. Spectrom.*, **14**:357, 1999.

[96] Williams D B, Carter C. *Transmission Electron Microscopy: A Text-book for Materials Science (Plenum Press, New York)*, 1996.

[97] Hirsch P, Howie A, Nicholson R B, Pashley D W, Whelan M J. *Electron Microscopy of Thin Crystals; Second Revised Edition (Robert E. Krieger Publishing Company, New York)*, 1977.

[98] Fultz B, Howe J M. *Transmission Electron Microscopy and Diffractometry of Materials (Springer, Berlin)*, 2001.

[99] Graef M. *Introduction to Conventional Transmission Electron Microscopy (Cambridge University Press, Cambridge)*, 2003.

[100] *Handbook of Microscopy: Applications in Materials Science, Solid-State Physics and Chemistry; Ed. Amelinckx S, Dyck D, Landuyt J, Tendeloo G (VCH, Weinheim)*, **I,II,III**, 1997.

[101] Doyle P A, Turner P S. *Acta Cryst.*, **A24**:390, 1968.

[102] Grivel J C et al. *Journal of Physics: Conference series*, **43**:107, 2006.

[103] Eibl O. *in Manuscript zu Vorlesung: Grundlagen und Verfahren der angewandten Elektronenmikroskopie*, : 70, 2005.

[104] Eibl O, Peranio N. *Microsc. Microanal.*, **13(suppl 3)**:352, 2007.

[105] Keyse R J et al. *Introduction to scanning transmission electron microscopy (Springer BIOS Scientific Publishers Ltd., New York, 1974)*, 1998.

[106] Eibl O. *Micron*, **30**:527, 1999.

[107] Reimer L. *Energy-Filtering Transmission Electron Microscopy (Springer-Verlag, New York)*, 1995.

[108] *Zeiss 912 Omega operating manual.*

[109] Birajdar B, Peranio N and Eibl O. *Supercond. Sci. Technol. (accepted as topical review)*,**21,** 2008.

[110] Eibl O. *Ultramicroscopy*, **69**:289-96, 1997.

[111] Pachla W, Morawski A, Kovac P, Husek I, Mazur A, Lada T, Diduszko R, Melisek T, Strbik V, Kulczyk M.

Supercond. Sci. Technol., **19**:1, 2006.

[112] Hata S, Yoshidome T, Sosiati H, Tomokiyo Y, Kuwano N, Matsumoto A, Kitaguchi H and Kumakura H. *Supercond. Sci. Technol.*, **19**:161, 2006.

[113] Yeoh W K, Kim J H, HOrvat J, Xu X, Qin M J, Dou S X, Jiang C H, Nakane T, Kumakura H, Munroe P. *Supercond. Sci. Technol.*, **19**:596, 2006.

[114] Eyidi D, Eibl O, Wenzel T, NIckel K G, Schlachter S I, Goldacker W. *Supercond. Sci. Technol.*, **16**:778, 2003.

[115] Sosiati H, Hata S, Kuwano N, Tomokiyo Y, Matsumoto A, Fukutomi M, Kitaguchi H, Komori K, Kumakura H. *Physica C*, **412-414**:1376, 2004.

[116] Birajdar B, Braccini V, Tumino A, Wenzel T, Eibl O, Grasso G. *Supercond. Sci. Technol.*, **19**:916, 2006.

[117] Zhu Y et al. *J. Appl. Phys.*, **102**:013913, 2007.

[118] Keast V J. *Appl. Phys. Lett.*, **79**:3491, 2001.

[119] Yu R C et al. *Physica C*, **363**:184, 2001.

[120] Zhu Y et al. *Phys. Rev. Lett.*, **88**:247002, 2002.

[121] Klie R F et al. *Phys. Rev. B*, **67**:144508, 2003.

[122] Klie R F et al. *Appl. Phys. Lett.*, **82**:4316, 2003.

[123] Klie R F, Zheng J C, Zhu Y, Zambano A J, Cooley L D. *Phys. Rev. B*, **73**:014513, 2006.

[124] Dou S X, Pan A V, Zhou S, Ionescu M, Wang X L, Horvat J, Liu H K, Munroe P R. *J. Appl. Phys.*, **94 (No. 3)**:1850, 2003.

[125] Birajdar B, Peranio N and Eibl O. *Microsc. Microanal. (Cambridge University Press)*, **13 (Suppl.3)**:290, 2007.

[126] Birajdar B, Eibl O, Braccini V, Grasso G, Pachla W, Herrman M, Haessler W. *Physica C, doi: 10.1016/j.physc.2007.04.121*, **460-462**:1409, 2007.

[127] Kovac P, Birajdar B, Husek I, Holubek T, Eibl O. *Supercond. Sci. Technol. (doi: 10.1088/0953-2048/21/4/045011)*, **21**:, 2008.

[128] INCA 4.05 software, 2001, Oxford Instruments.

[129] Ashcroft N W, Mermin N D. *Solid state physics (Harcourt College Publishers, London)*, 1976.

[130] Vasquez R P, Jung C U, Park Min-Seok, Kim Heon-Jung, Kim J Y, Lee Sung-Ik. *Phys. Rev. B*, **64**:052510, 2001.

[131] Serquis A, Zhu Y T, Peterson D E, Mueller F M, Schulze R K, Nesterenko V F, Indrakanti S S. *Appl. Phys. Lett.*, **80 (No. 23)**:4401, 2002.

[132] Pouchou J-L, Pichoir F. *J. de Micros. Spectrosc. Electron.*, **11 (No. 4)**:229, 1986.

[133] Takenobu T, Ito T, Chi D H, Prassides K, Iwasa Y. *Phys. Rev. B*, **64**:134513, 2001.

[134] Eisterer M, Müller R, Schöppl R, Weber H W, Soltanian S, Dou S X. *Supercond. Sci. Technol.*, **20**:117-12, 2007.

[135] Foltyn S R et al. *Nature Mater.*, **6(No.9)**:631, 2007.

[136] Eibl O. *Ultramicroscopy*, **50**:189, 1993.

[137] Horita Z, Sano T, Nemoto M. *Ultramicroscopy*, **21**:271, 1987.

[138] Eibl O. *Ultramicroscopy*, **50**:179, 1993.

[139] Eibl O. *Ultramicroscopy*, **50**:203, 1993.

[140] Watnabe M, Williams D B. *Journal of Microscopy*, **221**:89, 2006.

[141] Zschornack G. *Atomdaten für die Röntgenspektralanlyse (Springer, Berlin)*, 1989.

[142] Cava R J, Zandbergen H W, Inumaru K. *Physica C*, **385**:8, 2003.

[143] Braccini V, Cooley L D, Patnaik S, Larbalestier D C, Manfrinetti P, Palenzona A, Siri A S. *Appl. Phys. Lett.*, **81**:4577, 2002.

[144] Putti M, Braccini V, Ferdeghini C, Pallecchi I, Siri A S, Gatti F, Manfrinetti P, Palenzona A. *Phys. Rev. B*, **70**:052509, 2004.

[145] Putti M, Ferdeghini C, Monni M, Pallecchi I, Tarantini C, Manfrinetti P, Palenzona A, Daghero D, Gonnelli R S, Stepanov V A. *Phys. Rev. B*, **71**:144505, 2005.

[146] Slusky J S, Rogado N, Regan K A, Hayward M A, Khalifah P, He T, Inumaru K, Loureiro S M, Haas M K, Zandbergen H W, Cava R J. *Nature*, **410**:343, 2001.

[147] Zheng D N, Xiang J Y, Lang P L, Li J Q, Che G C, Zhao Z W, Wen H H, Tian H Y, Ni Y M, Zhao Z X. *Physica C*, **408**:136, 2004.

[148] Berenov A, Serquis A, Liao X Z, Zhu Y T, Peterson D E, Bugoslavsky Y, Yates K A, Blamire M G, Cohen L F, MacManus-Driscoll J L. *Supercond. Sci. Technol.*, **17**:1093, 2004.

[149] Song X, Braccini V and Larbalestier D C. *J. Mater. Res.*, **19**:2245, 2004.

[150] Zandbergen H W, Wu M Y, Jiang H, Hayward M A, Haas M K, Cava R J. *Physica C*, **366**:221, 2002.

[151] Li J Q, Li L, Liu F M, Dong C, Xiang J Y, Zhao Z X. *Phys. Rev. B*, **65**:132505, 2002.

[152] Karpinski J et al.. *Phys. Rev. B*, **71**:174506, 2005.

[153] Putti M, Affronte M, Manfrinetti P, Palenzona A. *Phys. Rev. B*, **68**:094514, 2003.

[154] Rossiter P L. *The electrical resistivity of Metals and Alloys (Cambridge University Press, Cambridge)*, : 222, 1991.

[155] Bellingeri E, Malagoli A, Modica M, Braccini V, siri A S, Grasso G. *Supercond. Sci. Technol.*, **16**:276, 2003.

[156] Zambano A J et al. *Supercond. Sci. Technol.*, **18**:1411, 2005.

[157] Kortus J, Dolgov O V, Kremer R K. *Phys. Rev. Lett.*, **94**:027002, 2005.

[158] Grasso G et al. *Appl. Phys. Lett.*, **79**:230, 2001.

[159] Sumption M D et al. *Supercond. Sci. Technol.*, **18**:961, 2005.

[160] Yamada H et al. *Appl. Phys. Lett.*, **84**:1728, 2004.

[161] Kumakura H et al. *Supercond. Sci. Technol.*, **18**:1042, 2005.

[162] Sumption M D et al. *Appl. Phys. Lett.*, **86**:092507, 2005.

[163] Eisterer M, Krutzler C, Weber H W. *Journal of Applied Physics*, **98**:033906, 2005.

[164] Eisterer M, Zehetmayer M, Weber H W. *Phys. Rev. Lett.*, **90**:247002, 2005.

[165] Zehetmayer M, Eisterer M, Jun J, Kazakov S M, Karpinsi J, Birajdar B, Eibl O, Weber H W. *Phys. Rev. B*, **69**:054510, 2004.

[166] Zhu Y, Wu L, Volkov V, Li Q, Gu G, Moodenbough A R, Malac M, Suenaga M, Tranquada J. *Physica C*, **356**:239, 2001.

[167] ESIVISION 3.2 software. *Soft Imaging System GmbH*, 2002.

[168] Gross K J, Zuettel A, Schlapbach L. *Alloys Compounds*, **274**:234, 1998.

[169] Smallman R E. *Modern Physical Metallurgy, (London: Butterworths)*, :147, 1985.

[170] Stadelmaier H H, Draughn R A, Hofer G. *Metallk.*, **54**:640, 1963.

[171] Jung W. *Naturf. b*, **32**:1371, 1977.

[172] Braccini V et al. *private communication*, 2005.

[173] Ribeiro R A, Budko S L, Petrovic C, Canfield P C . *Physica C*, **385**:16, 2003.

[174] Zhou S, Pan A V, Horvat J, Qin M J, Liu H K. *Supercond. Sci. Technol.*, **17**:S528, 2004.

[175] Chen S K, Yates K A, Blamire M G, MacManus-Driscoll J L. *Supercond. Sci. Technol.*, **18**:1473, 2005.

[176] He T, Cava R J, Rowell J M. *Appl. Phys. Lett.*, **80, No. 2**:291, 2002.

[177] Gumbel A, Eckert J, Fuchs G, Nenkov K, Muller K H, Schultz L. *Appl. Phys. Lett.*, **80**:2725, 2002.

[178] Gümbel A, Perner O, Eckert J, Fuchs G, Nenkov K, Müller K - H, Schultz L. *IEEE Trans. Appl. Supercond.*, **13**:3064, 2003.

[179] Perner O, Eckert J, Häßler W, Fischer C, Müller K - H, Fuchs G, Holzapfel B, Schultz L. *Supercond. Sci. Technol.*, **17**:1148, 2004.

[180] Matsumoto A, Kumakura H, Kitaguchi H, Hatakeyama H, Yamada H, Kirakawa M. *Proc. ASC (Jacksonville, USA) 5MG02*, 2004.

[181] Sumption M D et al. *Supercond. Sci. Technol.*, **17**:1180, 2004.

[182] Haessler W, Rodig C, Fischer C, Holzapfel B, Perner O, Eckert J, Nenkov K, Fuchs G. *Supercond. Sci.*

Technol., **16**:281, 2003.

[183] Fischer C, Rodig C, Häßler W, Perner O, Eckert J, Nenkov K, Fuchs G, Wendrock H, Holzapfel B, Schultz L. *Appl. Phys. Lett.*, **83**:1, 2003.

[184] Fischer C, Häßler W, Rodig C, Perner O, Behr G, Schubert M, Nenkov K, Eckert J, Holzapfel B, Schultz L. *Physica C*, **406**:121, 2004.

[185] Bhatia M, Sumption M D, Collings E W, Dregia S. *Appl. Phys. Lett.*, **87**:042505, 2005.

[186] Feng Y, Zhao Y, Pradhan A K, Zhou L, Zhang P X, Liu X H, Ji P, Du S J, Liu C F, Wu Y, Koshizuka N. *Supercond. Sci. Technol.*, **15**:12, 2002.

[187] Matsumoto A et al. *Appl. Phys. Lett.*, **89**:132508, 2006.

List of Tables

List of Figures

List of Acronyms and Symbols

Acronyms

ACF	Absorption correction factor
ARPES	Angle resolved photo emission spectroscopy
BSE	Back scattered electron
CGHE	Carrier gas hot extraction
CHI	Concentration histogram
CPP	Counts per pixel
CTFF	Continuous tube filling and forming
DSC	Differential scanning calorimetry
EDX	Energy dispersive x-ray spectroscopy
EELS	Electron energy loss spectroscopy
EFTEM	Energy filtered transmission electron microscope
EPMA	Electron probe microanalysis
ESI	Electron spectroscopic imaging
FEG	Field emission gun
FS	Fermi surface
HAADF	High angle annular dark field
HE	Hydrostatic extrusion
ICP-OES	Inductively coupled plasma-optical emission spectroscopy
MA	Mechanically alloying
PIT	Powder in tube
RGB	Red-Green-Blue
RWIT	Rectangular wire in tube
SEM	Scanning electron microscope
SESAM	Sub-Electron volt Sub-Angstrom Microscope
SSMS	Spark Source Mass spectroscopy
STEM	Scanning transmission electron microscope
TAR	Two-axial rolling
TEM	Transmission electron microscope
WDX	Wavelength dispersive x-ray spectroscopy
XAL	X-ray absorption length

Superconducting and normal state properties

α_a, α_c	Thermal expansion coefficients of MgB_2 along a and c axis
$\alpha_T, \alpha_B, \alpha_{Mg}$	Total, boron, and magnesium isotope effect coefficient respectively
B_{c1ab}, B_{c1c}	Lower critical field parallel to ab plane, Lower critical field along c axis
B_{c2ab}, B_{c2c}	Upper critical field parallel to ab plane, upper critical field along c axis
Bi-2223	$(Bi,Pb)_2Sr_2Ca_2Cu_3O_{10}$
$\Delta_\pi, \Delta_\sigma$	Superconducting energy gap on π band, on σ band
B_{irr}	Irreversibility field
λ	Electron phonon coupling strength
λ_{ab}, λ_c	Penetration depth in the ab plane, along c axis
M_i	Atomic mass of element i
ρ	Resistivity

T_c	Superconducting transition temperature
U_{11}, U_{33}	Debye-Waller factors parallel and perpendicular to the basal plane
$V_0(\Delta P/\Delta V)$	Bulk modulus
ω_{ln}	Logarithmic average of phonon frequencies
YBCO	$Yba_2Cu_3O_x$
μ^*	Electron-electron interaction
ξ_{ab}, ξ_c	Superconducting coherence length in the ab plane, along c axis

Crystal structure and diffraction contrast imaging

(hkl), ([uvw])	Lattice plane (direction) with Miller indices h, k, l
{hkl} and <uvw>	Lattice planes and directions equivalent to (hkl) and [uvw] respectively
a,c	Lattice parameters
d_{hkl}	Interplanar spacing for (hkl) planes
G_{hkl}, (g_{hkl})	Diffraction beam (Diffraction vector) corresponding to hkl diffraction spot
hkl	Diffraction spot corresponding to a specific (hkl) plane
s, s$_{eff}$	Excitation error, Effective excitation error
ξ_0, ξ_g	Extinction length for direct beam, Extinction length for G_{hkl} diffracted beam

Quantitative SEM-EDX and TEM-EDX analysis

α	Sample tilt with respect to the normal to the optic axis
A	Absorption correction
a_A	Probability of k_α transition in atom of element A
β	Detector take off angle
C_A	Weight fraction of element A
d	Magnitude of x-ray path length written in units of x-ray absorption length
D_e	Electron dose
ε	EDX detector efficiency
f	Geometry which on multiplying with t gives x-ray path length in the sample
F	Fluorescence correction
$\phi(\rho z)$	Depth distribution of x-ray intensity induced by primary ionisation
I_A	Integrated number of counts (intensity) measured in the x-ray peak of element A
I_{A0}	Absorption corrected intensity of characteristic x-rays of element A
k_{A-B}	Cliff-Lorimer factor of element A relative to element B
Q	Ionisation cross section
ρ	Sample density
R	Backscatter loss factor
S	Stopping power
t, z	Specimen thickness
T	Transmission coefficient
ω	Fluorescence yield
Z	Atomic number correction
z	Specimen thickness
ζ_A	Zeta factor of element A
μ	Mass absorption coefficient

Acknowledgement

Eidesstattliche Versicherung

Ich erkläre hiermit, dass ich die zur Promotion eingereichte Arbeit mit dem Titel "Correlation of superconducting properties and microstructure in MgB_2 using SEM, EPMA and TEM" selbständig verfasst, nur die angegebenen Quellen und Hilfsmittel benutzt und wörtlich oder inhaltlich ubernommene Stellen als solche gekennzeichnet habe. Ich versichere an Eides statt, dass diese Angaben wahr sind und dass ich nichts verschwiegen habe. Mir ist bekannt, dass die falsche Abgabe einer Versicherung an Eides statt mit Freiheitsstrafen bis zu drei Jahren oder mit Geldstrafe bestraft wird.

Weiterhin erkläre ich, dass bisher kein Promotionsversuch unternommen wurde.

Tübingen, den   13. November 2007

List of publications

Publications during Ph.D. thesis

Peer reviewed papers

1. **Birajdar B**, Peranio N, Eibl O, "Quantitative electron microscopy and spectroscopy of MgB$_2$ wires and tapes" S*upercond. Sci. Technol.* **21**, (2008) (topical review, in print)

2. Kovac P, **Birajdar B**, Husek I, Holubek T, Eibl O, "Stabilized in situ rectangular MgB2 wires: the effect of B purity and sheath materials" *Supercond. Sci. Technol.* **21**, 045011 (2008)(doi:10.1088/0953-2048/21/4/045011)

3. **Birajdar B,** Eibl O, "Microstructure-critical current density correlation model for MgB$_2$ wires and tapes" *Journal of Physics: Conference Series* **97**, 012217 (2008) (doi:10.1088/1742-6596/97/1/012217)

4. **Birajdar B,** Peranio N, Eibl O, "Advanced electron microscopy methods for the analysis of MgB$_2$ superconductor" *Journal of Physics: Conference Series* **97**, 012246 (2008) (doi:10.1088/1742-6596/97/1/012246)

5. **Birajdar B,** Eibl O, Braccini V, Grasso G, Pachla W, Herrmann M, Häßler W, "Correlation of superconducting properties and microstructure of MgB$_2$ wires and tapes" *Physica C* **460-462**, 1409 (2007)

6. Haessler W, Herrman M, Birajdar B, Rodig C, Schubert M, Holzapfel B, Eibl O, Schultz L, "Superconducting MgB$_2$ tapes prepared using mechanically alloyed nanocrystalline precursor powder" I*EEE Transactions on Applied Superconductivity* **17** No. 2, 2919 (2007)

7. **Birajdar B**, Braccini V, Tumino A, Wenzel T, Eibl O, Grasso G, " MgB$_2$ multifilamentary tapes: microstructure, chemical composition and superconducting properties" *Supercond. Sci. Technol.* **19**, 916 (2006)

8. Häßler W**, Birajdar B**, Gruner W, Herrmann M, Perner O, Rodig C, Schubert M, Holzapfel B, Eibl O, Schultz L, "MgB$_2$ bulk and tapes prepared by mechanical alloying: influence of the boron precursor powder" *Supercond. Sci. Technol.* **19**, 512 (2006)

9. Grivel J C, Eibl O, **Birajdar B**, Andersen N H, Abrahamsen A, Pinholt R, Grasso G, Hässler W, Herrmann M, Perner O, Rodig C, Pachla W, Kováč P, Hušek I, Mikheenko P, Abell S and Homeyer J, "Combined X-ray and electron microscopy study of MgB$_2$ powders, wires and tapes" *Journal of Physics: Conference Series* **43**, 107 (2006)

10. **Birajdar B**, Wenzel T, Manfrinetti P, Palenzona A, Putti M, Eibl O, "Al-alloyed MgB$_2$: correlation of superconducting properties, microstructure and chemical composition" *Journal of Physics: Conference Series* **43**, 484 (2006)

11. **Birajdar B**, Wenzel T, Manfrinetti P, Palenzona A, Putti M, Eibl O, "Al-alloyed MgB$_2$: correlation of superconducting properties, microstructure and chemical composition" *Supercond. Sci. Technol.* **18**, 572 (2005) [Selected among highlights of 2005]

12. Zehetmayer M, Eisterer M, .Jun J, .Kazakov S M, .Karpinski J, **Birajdar B**, Eibl O, Weber H W, "Fishtail effect in neutron-irradiated superconducting MgB_2 single crystals" *Phys. Rev. B* **69**, 054510 (2004)

Conference papers

1. Birajdar B, Peranio N, Eibl O, "Advanced Electron Microscopy of SiC added MgB_2 wires and tapes" *Microsc. Microanal. (Cambridge University Press)*, **13** (Suppl. 3), 286 (2007)

2. Birajdar B, Peranio N, Eibl O, "Quantitative B-analysis using EDX in SEM and TEM" *Microsc. Microanal. (Cambridge University Press)*, **13** (Suppl. 3), 290 (2007)

Conference Abstracts

1. Birajdar B, Peranio N, Kováč P, Pachla W, Eibl O, **"Correlation of critical current denstiy and microstructure in SiC added MgB_2 wires"** in 71st Annual meeting and DPG spring meeting of the division of condensed matter, Regensburg, Germany, 26th –30th March 2007, page 657

2. Birajdar B, Pachla W, Morawski A, Grasso G, Häßler W, Eibl O, **"Electron microscopy investigation of superconducting MgB_2 tapes and wires"** In Microscopy Conference (6 th Dreiländertagung), Davos, Switzerland 28th August- 2nd September 2005, page 74

3. Birajdar B, Eisterer M, Karpinski J, Weber H W, and Eibl O, **"TEM Imaging of Neutron Irradiation Induced Pinning Defects in MgB_2 Single Crystals"** at Microscopy Conference (6 th Dreiländertagung), Davos, Switzerland 28th August- 2nd September 2005, page 264

Publications before Ph.D. thesis

Peer reviewed papers

1. **Birajdar B I**, Shende S V, Joag D S, "Adsorption studied of Chromium on W (110) plane by Probe-Hole Field Emission Microscopy" *Surface Science* **505**, 285 (2002)

2. **Tondare** V N, **Birajdar B I,** Pradeep N, Joag D S, Lobo A and Kulkarni S K, "Self-assembled Ge nanostructures as field emitters" *Applied Physics Letters,* **77(15)**, 2394 (2000)

Curriculum Vitae

Personal data	Mr. Balaji I. Birajdar Date and place of birth: 31/12/1976, Kamjalga (India) Nationality: Indian

School

1982-1987 (primary schooling)	Primary school, Kamjalga
1987-1994 (Secondary and higher secondary schooling, CBSE)	Sainik School, Satara

University

7/1994-7/1997 (Bachelor of Science:Physics, Chemistry, Mathematics)	M. U. College, Udgir, (Dr. B.A.M. University, Aurangabad)
7/1997-7/1999 (Master of Science: Physics)	Dept. of Physics, Dr. B.A.M. University, Aurangabad Prof. Shah, Prof. Patil, Dr. Bichile, Dr. Deshmukh, Dr. Behere, Dr. Khirade

Associate fellow

8/1999-10/2001	Dept. of Physics, University of Pune, Pune Project:"study of submono/mono/multilayer adsorption of 3d transition metals on tungsten field emitters" Prof. D. S. Joag

Pre-Ph.D. courses and training

2/2002-4/2003	Institute of Applied Physics, University of Tuebingen Prof. Eibl, Prof. Schopohl, Prof. Muether, Prof. Kleiner, Prof. Wharam, Prof. Dahm

Ph.D. thesis

4/2003-11/2007	Institute of Applied Physics, Prof. Dr. O. Eibl, Eberhard-Karls University of Tuebingen "Correlation of superconducting properties and microstructure in MgB_2 using SEM, EPMA and TEM"

Tuebingen